POLITECNICO DI MILANO
DEPARTMENT OF STRUCTURAL SEISMIC AND GEOTECHNICAL ENGINEERING
DOCTORAL PROGRAMME IN 2012

ON THE LOAD INDUCED THERMAL STRAIN FOR PLAIN AND STEEL FIBER REINFORCED CONCRETE SUBJECTED TO UNIAXIAL LOADING

Doctoral Dissertation of:
Thomaz Eduardo Teixeira Buttignol

Supervisor:
Prof. Marco di Prisco

Co-supervisor:
Prof. Matteo Colombo

Tutor:
Prof. Roberto Paolucci

The Chair of the Doctoral Program:
Prof. Roberto Paolucci

2016

(This page intentionally left blank)

Summary

The thesis aims to investigate transient creep in concrete structures. In the first part, transient creep theoretical fundaments are introduced and discussed. A new semi-empirical model in terms of LITS, which can be adopted for plain or steel fiber reinforced concrete, is proposed. A comparison among different empirical models is carried out. The proposed semi-empirical model is compared both with experimental results and empirical models from other authors, demonstrating its reliability.

The experimental investigation of transient creep was carried out by means of steel fiber reinforced concrete cast in 2005. In order to analyze the effects of long-term aging on the material, a mechanical characterization was performed on SFRC beams. The mechanical characterization aims to observe changes in concrete tensile properties, especially the residual post-cracking tensile strength, due to long-term aging. For this purpose, flexural tests together with indirect tensile tests by means of Double Edge Wedge Splitting (DEWS) procedure were performed. The results of ten-year-old specimens are compared with the ones obtained at one-year-old.

The numerical investigation was developed by means of a 2D three-phase mesoscopic analysis, using finite element modeling (FEM). A parametric analysis is carried out in order to validate the numerical model and estimate its sensitivity due to different aggregate distributions and variations on the mechanical properties of the concrete phases. The path dependence is analyzed on preloaded and pre-heated specimens. LITS is uncoupled by recognizing the influence of the aggregate geomechanical properties decay due to the temperature increase ($LITS_{agg}$), the matrix thermomechanical properties evolution as function of temperature ($LITS_{mat}$) and the effect of the boundary conditions (thermal expansion restraint imposed by the sustained compressive load) on concrete ($LITS_{bc}$). A comparison between numerical and the proposed LITS semi-empirical model results is performed in order to further validate the model.

Creep tests at high temperature were carried out in preloaded and pre-heated cylindrical specimens cored from the beams after the mechanical characterization. A comparison between the experimental results and the new LITS (Load Induced Thermal Strain) semi-empirical model proposed in the thesis is carried out. A prediction of creep at high temperature on pre-heated specimens (basic creep) is performed by introducing in the Kelvin-Voigt model a temperature adjusted parameter that takes into account the effect of high temperature on creep. The path dependence is analyzed by comparing the experimental results obtained from the difference between creep in

preloaded and pre-heated specimens with $LITS_{bc}$ function derived in the numerical investigation. A prediction of creep at high temperature on preloaded specimens (LITS during heating and basic creep during constant temperature) is developed both by means of the proposed LITS semi-empirical model and by introducing the effect of the boundary conditions ($LITS_{bc}$) in the adapted Kelvin-Voigt model. Finally, significant results on the reversible mechanical properties of SFRC subjected to high temperature and a sustained compressive load are highlighted. The limits of validity of the proposed LITS semi-empirical model when used to predict SFRC behavior are discussed.

Keywords: steel fiber reinforced concrete (SFRC), transient creep, load induced thermal strain (LITS), high temperature, bending, constitutive model, aging, double edge wedge splitting (DEWS), tensile behavior.

Acknowledgements

The author would like to thank CNPq (Conselho Nacional de Desenvolvimento Científico e Tecnológico) for its financial support through a PhD research scholarship.

I am grateful to my advisor, prof. Marco di Prisco, who gave me this opportunity and made this PhD possible. His valuable contributions throughout this research were much appreciated.

I would like to thank prof. Matteo Colombo, who was always available and accessible to help solving my questions and doubts and who made possible the execution of the experimental tests at high temperature.

An acknowledgement to the technicians of the laboratory of Politecnico di Milano-Lecco campus, Marco Perego and Andrea Stefanoni, for their support during the experimental campaign.

I am especially grateful and in debt to my wife, who firmly supported me during all these years and delayed her own projects to be by my side.

(This page intentionally left blank)

Contents

(This page intentionally left blank)

List of figures

List of tables

(This page intentionally left blank)

Notations and symbols

Uppercase letters

E_0 = Asymptotic Modulus of Elasticity of the creep compliance function

E_c = Modulus of Elasticity

E_T = Modulus of Elasticity at high temperature

E_d = Dynamic Modulus of Elasticity

E_{sec} = Secant Modulus of Elasticity

F_{sp} = Splitting force

G_f = Fracture Energy

J = Creep compliance function

J_{LITS} = LITS compliance function

$J_{LITS,tc}$ = thermo-chemical LITS compliance function

$J_{LITS,tm}$ = thermomechanical LITS compliance function

$J_{LITS,agg}$ = compliance function related to the contribution of aggregate geomechanical properties decay to LITS

$J_{LITS,mat}$ = compliance function related to the contribution of matrix thermomechanical properties decay to LITS

$J_{LITS,bc}$ = compliance function related to the effect of the boundary condition on concrete

LITS = Load induced thermal strain

$LITS_{tc}$ = LITS thermo-chemical strain which includes the contribution of matrix performance on temperature

$LITS_{tm}$ = LITS thermomechanical strain which includes the contribution of aggregates performance on temperature and concrete thermal expansion restraint

$LITS_{agg}$ = LITS strain related to the contribution of aggregate geomechanical properties decay

$LITS_{mat}$ = LITS strain related to the contribution of matrix thermomechanical properties decay

$LITS_{bc}$ = LITS strain related to the contribution of the effect of the boundary condition on the specimen (thermal expansion restraint)

Lowercase letters

f_c= characteristic concrete cylinder compressive strength

f_t = characteristic concrete tensile strength

$f_t(T)$ = characteristic concrete tensile strength at high temperature

$f_c(T)$ = characteristic concrete compressive strength at high temperature

f_{cm} = mean concrete cylinder compressive strength

f_{ctm} = mean concrete tensile strength

f_{fl}= flexural strength

f_{Fts}= characteristic tensile residual strength at SLS (w=0.5 mm)

f_{Ftu}= characteristic tensile residual strength at ULS (w=2.5 mm)
$f_{r1,k}$ = FRC post-cracking strength for a CMOD equal to 0.50mm
$f_{r3,k}$ = FRC post-cracking strength for a CMOD equal to 2.50mm
l_{cs} = characteristic structural length
q_{tm} = LITS semi-empirical thermomechanical function
q_{tc} = LITS semi-empirical thermo-chemical function
q_{agg} = LITS semi-empirical aggregate function
q_{mat} = LITS semi-empirical matrix function
q_{bc} = LITS semi-empirical function related to the thermal expansion restraint
ttc = transitional thermal creep
v_{el}= ultrasonic wave velocity
w/c = water-cement ratio

Greek letters

α = coefficient of concrete thermal expansion
β_{tm} =LITS semi-empirical thermomechanical parameter
β_{tc} =LITS semi-empirical thermo-chemical parameter
ε_c = concrete compressive strain
ε_{cT} = concrete compressive strain at high temperature
ε_{c1} = strain at ultimate stress in uniaxial compression
$\varepsilon_{c1,\theta}$ = strain at ultimate stress in uniaxial compression at high temperature
$\varepsilon_{cu1,\theta}$ =ultimate strain at high temperature
ε_c^T = reversible thermal strain
$\varepsilon_{c,irr}^T$ = irreversible thermal strain
ε_{ci}^m = reversible mechanical strain
$\varepsilon_{c,irr}^m$ = irreversible mechanical strain
ε^c = total strain
ε^{el} = elastic strain
ε^{bc} = basic creep
ε^{cr} = creep strain
ε^{dc} = drying creep
ε^{sh} = shrinkage
ε^{th} = free thermal strain
ε^{tr} = transient creep
ε^{ttc} = transitional thermal creep
φ = creep coefficient
ρ = concrete specific weight
ν = Poisson ratio
η = viscosity parameter

CHAPTER 1

Introduction

1.1 The engineering problem

Transient creep is developed in concrete structures subjected to fire, leading to large and irrecoverable deformations. It is especially important in reactor pressure vessels, tunnels, tall buildings and bridges. High deformations imposed by transient creep strains during fire on concrete columns submitted to high load levels can cause the failure. Tunnel line segments can be subjected to large stresses, especially on the joints as a result of large concrete transient creep strains, which can lead to premature failure. Reactor pressure vessels can have the service-life reduced due to microcracking or crack propagation. In prestressed concrete structures, large strains can lead to steel relaxation and the loss of prestress. This phenomenon is especially important in prestressed bridge deck, piers and girders.

Fiber incorporation in the concrete mix can contribute to reduce concrete damage during fire. In the case of transient creep, few researches were carried out in polypropylene (PP) fiber reinforced concrete. PP fibers, on one hand, contributes to control the spalling effect, but, on the other hand, increases transient creep strains due to the increase in concrete porosity resulted from fibers melting and burn. Steel fibers, instead, could be adopted as a solution to provide a reduction of concrete damage during fire and also reduce transient creep values in tension. However, no research on transient creep with this material has been performed yet. It is worth mentioning that, in the case of tunnels, steel fibers could be used to prevent or delay the failure of the concrete segment lines, helping to increase the safety. In reactor pressure vessels, fibers could increase the structural service life.

The prediction of transient creep involves a lot of uncertainties due to its complex mechanisms of activation. Transient creep is seated in the cement paste and occurs due to water evaporation (drying creep) and CSH dehydration. Above 400ºC, transient creep is accelerated by the aggregate geomechanical properties decay. There is also a thermal mismatch between aggregate expansion and cement paste shrinkage after 150ºC, leading to concrete microcracking. Design specifications of transient creep are still needed. For example, Eurocode 2 [1] considers transient creep effects implicit in the model formulation. The available models described in literature are based on an empirical approach and are fitted by taking into account relatively few experimental test results.

1.2 Transient creep in concrete structures

Concrete structures exposed to high temperatures are submitted to a complex hydro-physical-chemical transformation. In this situation, creep plays a vital role in concrete mechanical behavior. In normal conditions, at room temperature, creep is developed due to a mechanical process (sustained load) in the concrete matrix. It occurs at the cement paste level, as function of the internal moisture condition, and has an aging and a non-aging component. The former is a result of concrete hydration and the latter is due to the continuous self-equilibrium of micro-stresses Bazant et al [2] in the nano-porous microstructure of CSH (Calcium-Silicate-Hydrate). At high temperatures this process is accelerated due to concrete drying and dehydration, leading to higher deformations.

According to Sabeur et al [3], there are two different types of strain components at high temperature. One is the hygro-thermal strain, a stress free component, resulted from material thermal expansion at aggregate level and hygral shrinkage at the cement paste level, which occurs due to both concrete drying and dehydration. The other is the thermal-creep strain, a stress induced component, resulted from physical and chemical transformations which leads to a rearrangement of the concrete microstructure.

It is important to say that creep, at high temperature, can be divided into two main components, i.e.: basic creep, which occurs at constant temperature and after all concrete physical-chemical reactions have taken place; and transient creep, which is developed during heating. Transient creep encompasses drying creep, resulted from free water loss, and dehydration creep, which occurs due to physically and chemically bound water loss in the CSH layers. Above 400°C, the aggregates start to play an important role due to thermochemical changes in their microstructure, leading to higher transient creep strains. Transitional thermal creep (ttc) is commonly defined as dehydration creep and includes the effect of the aggregates.

Drying creep, according to Benboudjema et al [4], corresponds to the additional strain observed when concrete is stressed together with a change in the internal moisture state. Its asymptotic value is reached at 110ºC, as shown in Figure 1, and is a result of evaporable free water loss, generated by fluid transport due to internal pore-pressure differentials.

According to Sabeur et al [5], dehydration is the driving process of transitional thermal creep (ttc), which occurs beyond 110°C, due to the loss of CSH adjoined and bound water (CSH dehydration). Moreover, as shown in Figure 2, ttc is quasi-instantaneous. Using a thermo-gravimetric analysis (TGA), Sabeur et al [5] observed that concrete mass loss continued after the attainment of the established temperature level, confirming that dehydration is a process which needs time to occur.

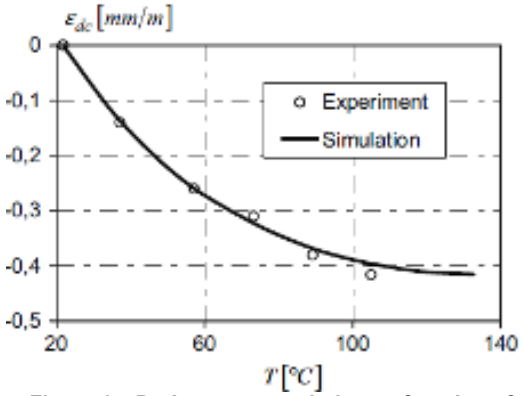

Figure 1 – Drying creep evolution as function of temperature.

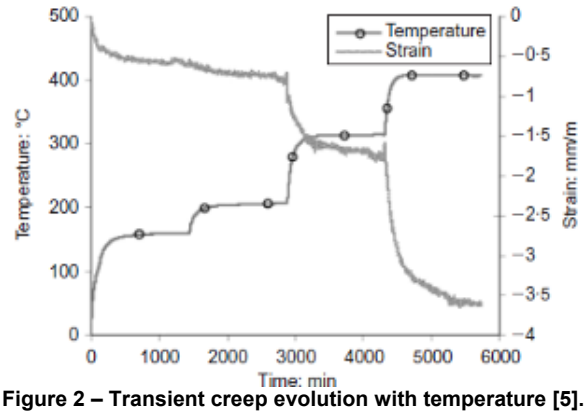

Figure 2 – Transient creep evolution with temperature [5].

It is important to underline that transient creep strains are coupled with other thermomechanical strain components and, thus cannot be directly measured in laboratory. The experimental procedure is carried out in two distinct phases with constant heating rate. The first test is developed without load to measure concrete thermal strains. Another identical test applying a constant load is performed to measure the total strain. The difference between the two strain values, disregarding the initial elastic deformation computed at room temperature, defines the so called LITS (Load Induced Thermal Strain), which is the sum of transient creep and thermomechanical strain components.

1.3 Thesis objectives

In order to analyze creep behavior at high temperature, steel fiber high-strength concrete (SFHSC) beams from Colombo [6], cast in 2005, were used.

A new LITS semi-empirical model is proposed, recognizing concrete as a heterogeneous biphasic material (aggregates and matrix). The model is based on two variables dependent respectively on the aggregate volume and the cement content and on two compliance functions dependent on the temperature. The compliance functions correspond to concrete thermomechanical (matrix damage, aggregate degradation and thermal expansion restraint due to the applied load) and thermochemical (concrete drying and dehydration) properties evolution during heating.

In order to derive the new LITS semi-empirical model, an analysis of transient creep fundamental aspects is developed. Transient creep physical-chemo-mechanical properties are detailed. Experimental results from literature are compiled, including several types of concrete (NSC, HSC, SCC, UHPC) with different ages (from 3 months to 5 years), moisture conditions (saturated, dried, cured at room conditions), aggregate types (siliceous, calcareous, basalt and recycled), heating rates and load levels. The semi-empirical LITS model is compared with experimental results obtained from literature and with other empirical models, demonstrating its reliability.

The mechanical characterization of the material was carried out in order to observe the change in material mechanical properties, especially the residual post-cracking tensile strength due to long-term aging. For this purpose, flexural tests together with indirect tensile tests by means of Double Edge Wedge Splitting (DEWS) procedure were developed.

The results of four-point bending (4PB) tests of 1-year-old beams from Colombo [6] are presented and a comparison between the mean values of 4PB tests considering 1-year-old and 10-year-old specimens are shown, demonstrating a pronounced increase in the peak and in the serviceability limit state (SLS) residual strengths, followed by a relatively small increase in the ultimate limit state (ULS) residual strength. The material classification according to fib Model Code 2010 of 1-year-old and 10-year-old specimens is carried out. The objective is to observe possible changes in the material class through the years. The tensile constitutive law is obtained according to the fib Model Code 2010 and a plane section (PS) prediction in bending is performed taking into account the constitutive law of the material. The values are compared with the results of the bending tests, showing the reliability of the PS analysis and the effectiveness of the back analysis method to identify FRC tensile post-peak response.

The numerical analyses were developed using a 2D three-phase mesoscopic model in the finite element software Abaqus. A parametric analysis was carried out in order to validate the numerical model and observe its sensitivity due to different aggregate distributions and variations on the mechanical properties of the concrete phases (matrix, inclusions and interfacial transition zone). The path dependence was analyzed on preloaded and preheated specimens in order to observe the effects of the boundary conditions on LITS. In order to better understand the different sources of transient creep strains, LITS was uncoupled taking into account the performance of the matrix at high temperature ($LITS_{matrix}$), the aggregate geomechanical properties decay as function of the temperature increase ($LITS_{aggr}$) and the effects of the boundary conditions on concrete ($LITS_{bc}$). The results demonstrated that concrete thermal expansion restraint imposed by the sustained compressive load plays a very important role both on LITS. A comparison between the numerical results and the semi-empirical LITS model proposed was also carried out.

The hot tests were carried out using an electric oven in preloaded and pre-heated cylindrical specimens. The experimental results are compared with the LITS semi-empirical model proposed in the thesis. A prediction of creep at high temperature on pre-heated specimens (basic creep) is performed by introducing in a Kelvin-Voigt model a temperature adjusted parameter that takes into account the effect of high temperature on creep. The path dependence is analyzed by comparing the experimental results obtained from preloaded and pre-heated specimens. The difference between the two results can be attributed to the effect of the boundary conditions on concrete. A comparison between $LITS_{bc}$ power function derived in the numerical investigation and the experimental results is carried out. A prediction of creep at high temperature on preloaded specimens (LITS during heating and basic creep at constant temperature) is developed both by means of the proposed LITS semi-empirical model and by introducing the effect of the boundary conditions ($LITS_{bc}$) in the adapted Kelvin-Voigt model.

1.4 Organization of the thesis

The thesis is divided in nine chapters. Chapter 1 presents an introduction to the subject, which includes the engineering problem, transient creep aspects in concrete structures and the main topics analyzed during the PhD program.

Chapter two describes the state of the art in concrete structures subjected to fire, including creep behavior at room and high temperatures.

Chapter three details the formulation of the proposed LITS semi-empirical model and the validation of the model with other experimental tests.

Chapter four presents the whole PhD program, describing the thesis objectives and main contributions.

Chapter five shows the results of the steel fiber reinforced concrete mechanical characterization and long-term aging effects on the material by comparing the experimental results in bending and in tension of specimens with 1-year-old and 10-years-old.

Chapter six presents the 2D three-phase mesoscopic modeling and the numerical results.

Chapter seven describes the experimental results of creep at high temperature in preloaded and pre-heated specimens.

Chapter eight discusses the experimental results obtained from the creep tests at high temperature.

Chapter nine presents the main conclusions and provides future perspectives for further analyses.

(This page intentionally left blank)

CHAPTER 2

State of the art

2.1 Concrete Properties at High Temperatures

Concrete exposed to high temperatures are prone to chemical and physical transformations. In microscopic scale, concrete is subjected to drying, dehydration and pore-pressure build-up. In mesoscopic level strain incompatibilities between the aggregate expansion and the cement paste shrinkage are developed. At the macroscopic level, concrete is susceptible to thermal expansion, cracking formation and spalling activation. These thermo-hydro-chemical phenomena are responsible for concrete damage and degradation and are influenced by the temperature history (previous fire exposure, maximum temperature reached, heating rate). The type of load applied (compression, tension, bending) during heating influences concrete creep behavior, which is accelerated at high temperatures.

According to Kim et al [7], during the heating process, concrete thermal mismatch starts around 110ºC. In general, until 90ºC, both cement paste and aggregate are in expansion. However, at 110ºC the cement paste starts to shrink, while the aggregate continues to expand. At this temperature level, concrete dries out due to free water evaporation.

Between 300ºC and 600ºC, aggregates start disintegration depending on their physical constituents. Portlandite ($Ca(OH)_2$), a cement paste constituent which composes about 20% of the mass of the hydrated cement, and calcite ($CaCO_3$), the basic constituent of limestone aggregate, are decomposed into lime (CaO), as shown respectively in Eq. 1 and Eq. 2. The thermal decomposition of calcium carbonate ($CaCO_3$) above 500ºC releases carbon dioxide (de-carbonation), generating calcium oxide.

$$Ca(OH)_2 \leftrightarrow CaO + H_2O \quad (1)$$

$$CaCO_3 \leftrightarrow CaO + CO_2 \quad (2)$$

Further concrete rehydration, during the cooling phase, leads to CaO greatly expansion due to its reaction with water, producing $Ca(OH)_2$ and causing concrete cracking and crumbling. Free calcium materials, such as aluminate and siliceous (pozzolana) cement based ones, contribute to reduce this problem. For example, pozzolana slow chemical reaction with water controls heat rate release and temperature inside the structure during early age hydration.

Among all thermochemical reactions, calcium-silicate-hydrate (CSH) chemistry is very important to understand concrete physical microstructure properties evolution during

heating and cooling, since it occupies around 50% of the cement paste volume. According to Allen et al [8], concrete behavior is largely related to the CSH gel viscoelastic response to the load stress level (creep) and relative humidity changes (drying shrinkage). This, according to Bazant et al [2], is due the fact that creep is directly related to the long-term relaxation of self-equilibrated micro-stresses in the CSH nano-porous microstructure.

CSH is formed due to the expansion reaction of both cement constituent minerals larnite (C2S) and alite (C3S) in contact with water (concrete aging). This expansion is not followed by concrete volume change and, as a result, causes a reduction in the capillary pore system and in the concrete permeability. The interconnected gel creates a continuous phase, isolating free water within its nanostructure interlayer. Moreover, CSH strong Van der Walls force leads to high water adsorption on its surface, as shown in Figure 3.

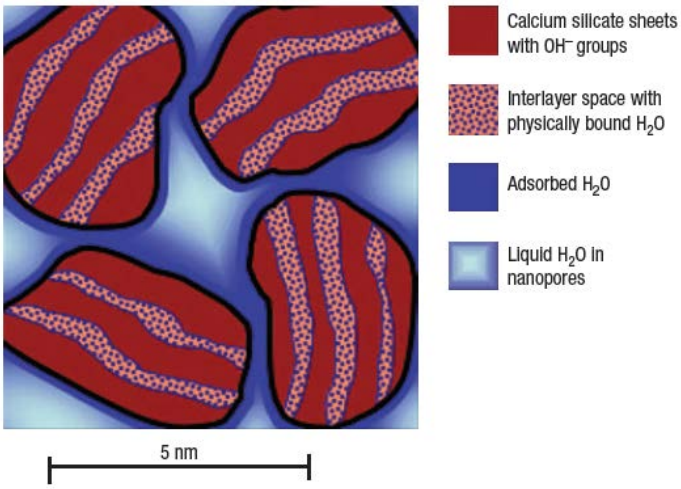

Figure 3 – CSH gel microstructure overview [8].

It is worth mentioning that larnite has low reactivity and is responsible for concrete late strength, while alite is highly reactive, being responsible for concrete early strength. Their chemical reactions with water produce CSH and portlandite, as shown in Eq. 3 and Eq. 4.

$$2Ca_2SIO_4 + 4H_2O \rightarrow 3CaO \cdot 2SiO_2 \cdot 3H_2o + Ca(OH)_2 \quad (3)$$

$$2Ca_3SIO_5 + 6H_2O \rightarrow 3CaO \cdot 2SiO_2 \cdot 3H_2o + 3Ca(OH)_2 \quad (4)$$

According to Alonso and Fernandez [9], concrete drying due to heating up to 250ºC, removes most of the CSH physically bound water (dehydrated CSH), as shown in Eq. 5. Above 200ºC, CSH is progressively decomposed into new calcium silicates (C2S and C3S), as shown in Eq. 6, releasing the chemically bound water and reducing concrete binding properties. Beyond 750ºC, there is a complete disintegration of the CSH gel.

$$CSH_{dehydrated} = (CaO)_aSiO_2(H_2O)_b \rightarrow (CaO)_aSiO_2(H_2O)_{b-c} \quad (5)$$

$$CSH_{dissolution} = (CaO)_aSiO_2(H_2O)_b \rightarrow \beta(CaO)SiO_2 + H_2O \quad (6)$$

Hence, concrete thermochemical transformations during heating are directly related to dehydration due to the loss of physically and chemically bound water. Figure 4 shows a thermal gravimetric analysis (TGA) of NSC cubic specimens from Arioz [10] experiment, where three endothermic peaks can be observed. The first one is at 114ºC, as a result of the cement paste dehydration due to physically bound water loss. The second peak occurs at 490ºC originated from the calcium hydroxide dissociation peak. And the third peak, at 743ºC, can be related to the second step of CSH gel dehydration and its complete dissociation.

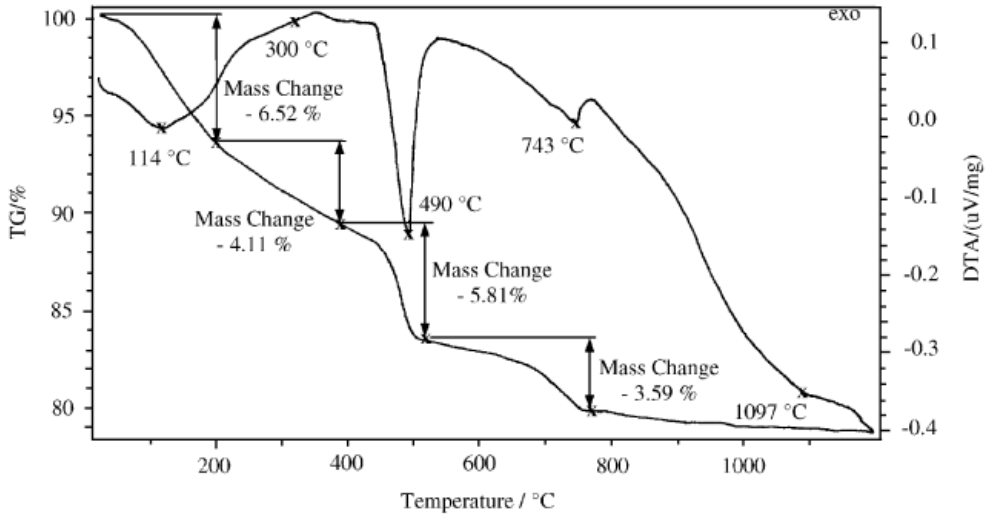

Figure 4 – Thermo-gravimetric analysis of NSC [10].

Analyzing concrete radial temperature differences, Khoury et al [11] observed two peak values due to specimen's drying and dehydration: The first one at 160ºC, due to moisture loss, and the other at 550ºC, as a result of the $Ca(OH)_2$ dissociation.

Thermal stresses effects, according to Khoury et al [11], can be limited both by reducing the heating rate, which produces lower residual stresses at the surface layer, and the cylindrical specimen's radius, which reduces radial temperature differentials. And very low stresses produces a balance between concrete expansion and bowing effects. In laterally restrained members that are free to rotate, there is a bowing dominance in respect to concrete expansion.

Doubling the heating rate doubles the thermal gradient magnitude. In turn, a slow heating rate increases free water loss (Khoury et al, [11]).

In RC beams subjected to fire, the catenary action (tensile membrane action) counterbalances the flexural stiffness depletion.

Thermal strains, as stated by Thienel and Rhostasy [12], are largely dependent on the type and quantity of aggregates, as shown in Figure 5.

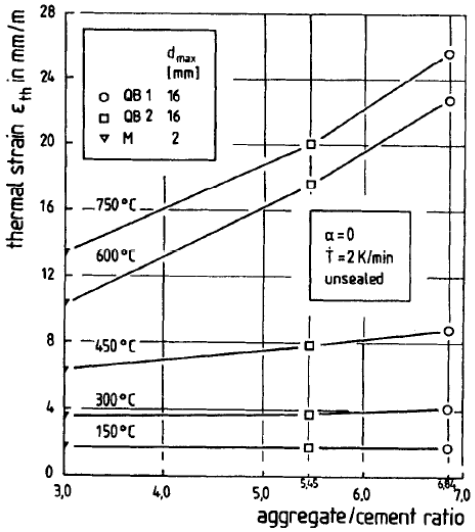

Figure 5 – Aggregate effect on concrete thermal strains [12].

Concrete hydration can be enhanced by curing in autoclave at a constant temperature of 180ºC. This technique is adopted for precast elements to guarantee better concrete stability against creep and shrinkage.

Water-cement (w/c) ratio plays an important role on concrete thermal and mechanical properties. For example, an increase in the modulus of elasticity (stiffness) is observed in correspondence to a decrease in the w/c ratio. Moreover, concrete thermal expansion is inversely proportional to the moisture content.

In relation to concrete structural behavior, Giaccio and Zerbino [13] affirm that a concrete structure heated under a sustained compressive load is less affected in relation to structures submitted to tensile or flexural loading, since the last ones are more prone to cracking.

According to Kim et al [14], compressive strength of preloaded specimens slowly decreases because crack is reduced by the restrained effects of preloading.

2.1.1 Fracture Energy

Fracture energy is defined as the energy required to open a unit area of crack surface and is determined by calculating the area under the load vs. deflection curve. The contribution of the structure's own weight is directly related to the area under the tail of the curve. Specifications to determine fracture energy of mortar and concrete structures can be found on RILEM 50-FMC [15].

According to Nielsen and Bicanic [16], until approximately 300ºC, an increase in the release of fracture energy is observed, from which point a progressive decrease begins due to the excessive concrete thermal damage, as shown in Figure 6. One plausible explanation for fracture energy increase (up to 50% between 300ºC and 400ºC), according to Nielsen and Bicanic [16], is the tortuous cracking propagation which follows aggregates contour.

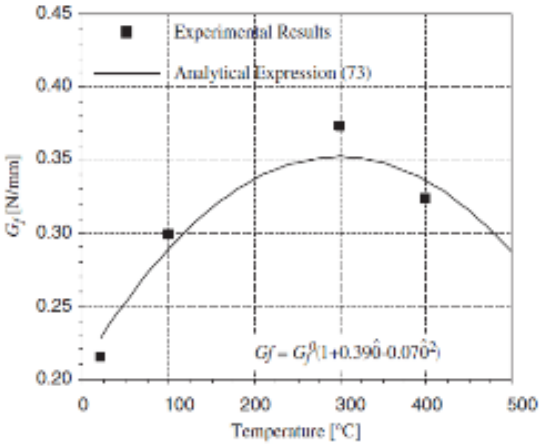

Figure 6 – Fracture energy variation with temperature [16].

Bamonte and Gambarova [17] found, for self-compacting concrete (SCC), a smaller increase in the fracture energy as function of temperature in relation to vibrated concrete, as shown in Figure 7.

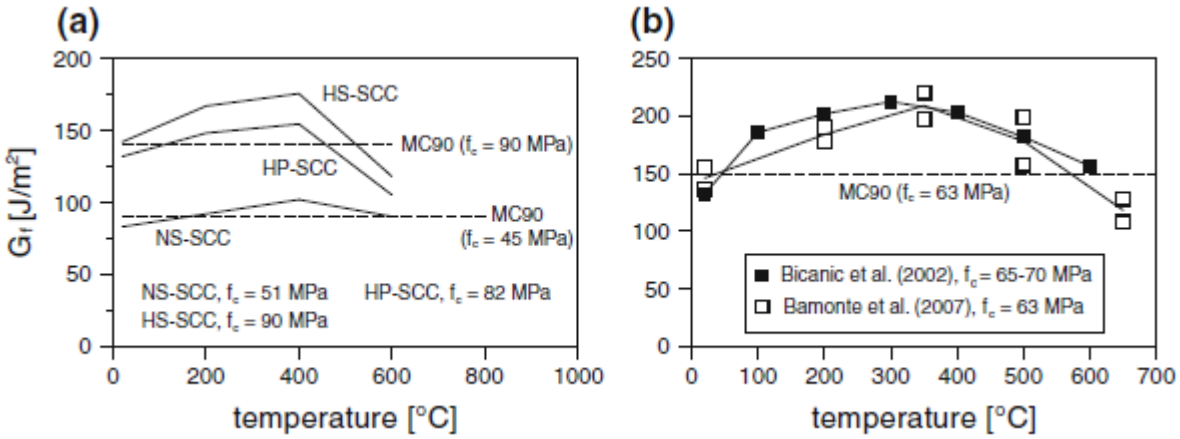

Figure 7 – Residual fracture energy as function of temperature for SCC and others results for ordinary concrete [17].

In Peng et al [18] experiments, after heating, fracture energy values in FRC specimens were much higher in comparison to plain concrete. Peng et al [18] attribute the results to both fibers pull-out mechanism triggered during the fracturing process and aggregate interlock, which, for plain concrete, is the sole resisting mechanism.

Nielsen et al [16] demonstrated that specimens cured in autoclave, at 105ºC, presented a higher fracture energy in relation to specimens cured at room temperature.

Yu et al [19] draw attention to the lack of available literature regarding fracture energy parameters, which are very important to structural and numerical analyzes in post-fire situations.

2.1.2 Cooling and Recurring

Water cooling at room temperature creates a denser microstructure compared to air curing, in part due to concrete rehydration, and also produces slightly lower residual stresses.

According to Reis et al [20], there is a partial recovery of concrete strength during the cooling phase, which can increase up to 20% for a maximum heating between 500ºC and 600ºC, as shown in Figure 8.

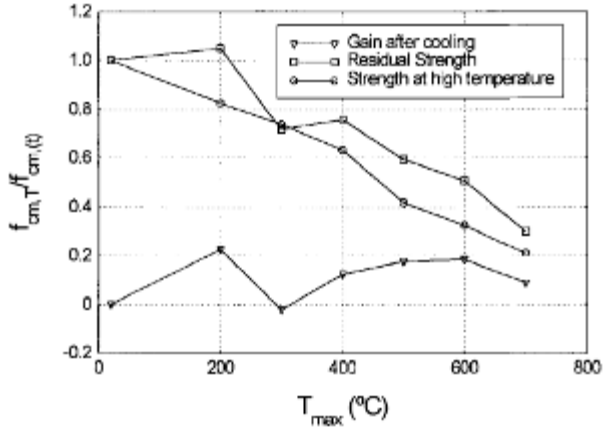

Figure 8 – Normalized concrete strength at high temperature [20].

According to Poon et al [21], concrete strength and durability recovery depend on the type of aggregate, time of heat exposure, the recovery method and its duration. In Poon et al [21] experiments, the best recovery was obtained with slag concrete with fire brick aggregates at 500ºC exposure. In this case, according to Poon et al [21], there was a recovery up to 90% after a 90-day curing.

As stated by Yu et al [19], most of the rehydration process occurs during the first seven days. During this period, voids are filled by hydrated cement grains and calcium oxide components. Rehydration forms long irregular fibers of CSH gel mingled with etringite and CH crystals.

Figure 9 shows concrete morphology beyond 800ºC heating-cooling cycle followed by water curing.

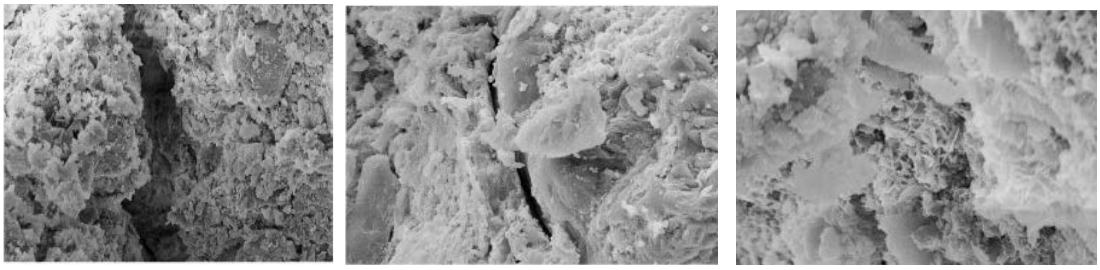

Figure 9 – Concrete morphology above a 800ºC thermal cycle with water curing for 7 days and 28 days [21].

According to Yu et al [19], concrete recovery is applicable to structures with moderate damage. A higher residual strength and durability is achieved with a 600ºC heating in comparison with a concrete heated up to 800ºC. Yu et al [19] also state that water

curing is better and faster than air cooling. Moreover, HSC presents better recovery than NSC due to its denser microstructure which helps to fill in concrete cavities.

Regarding crack opening, Yu et al [19] observed that in most of the cylindrical specimens analyzed, after a recovery period of 56 days, surface crack widths were within the maximum limit allowed by design codes.

2.1.3 Pore-pressure and transport phenomenon

Thermo-hygral process describing the flow of a fluid in a porous medium can be expressed both by Darcy's Law concept of pressure gradient and by Fick's Law concept of diffusion and molar concentration.

As stated by Mindeguia et al [22], concrete capillary pore-pressure affects vaporization process in such a way that the smaller the pore radius, the higher the vaporization temperature. In addition, as shown Figure 10, pore-pressure changes due to pore diameter. On one hand, for very large pores no pressurization process takes place and free water evaporates at 100ºC. On the other hand, small pores exhibit high values of capillary forces in which higher temperatures are needed to extract vapor molecules from liquid water.

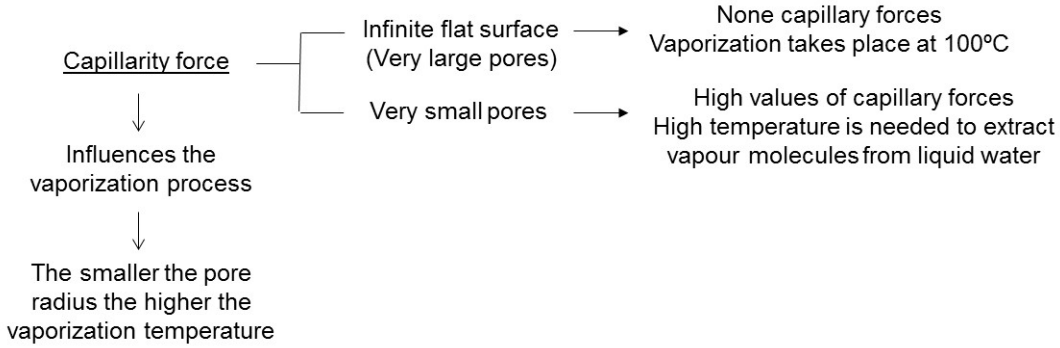

Figure 10 – Capillarity pressure in concrete.

According to Neville [23], the load applied on unsealed specimens, *per se,* causes only negligible loss of water (< 3%). And Bazant [24] states that pore humidity increase due to load application on sealed specimens is negligible.

Figure 11 shows concrete pore-pressure evolution under different temperature stages. At 105ºC vaporization process starts combined with pore-pressure increase, resulting in free water loss. High values of pore-pressure are achieved at 180ºC, from which point a progressive decline is observed. From 220ºC, a drastic pore-pressure reduction takes place.

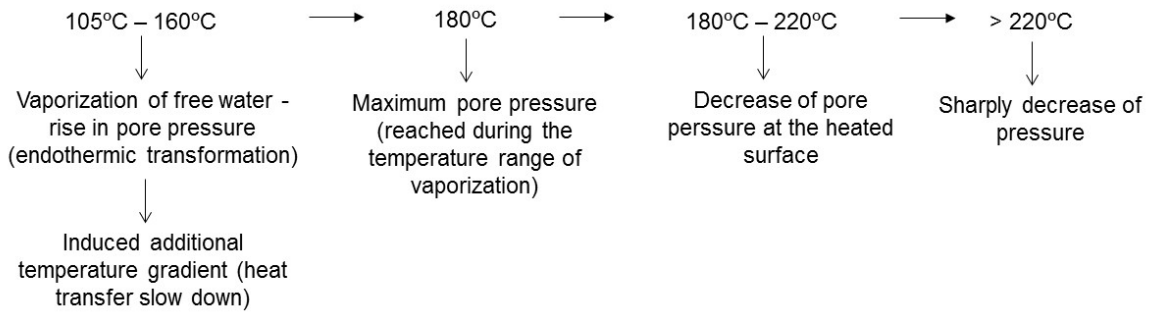

Figure 11 – Concrete capillarity pore pressure evolution according to temperature increase.

Phan [25] analyzed concrete pore-pressure evolution as function of temperature at two different sections, respectively at 25 mm (black line) and at 50 mm (blue line) from specimen's surface, as shown in Figure 12. The results demonstrated that pore-pressure decreases with specimen's depth.

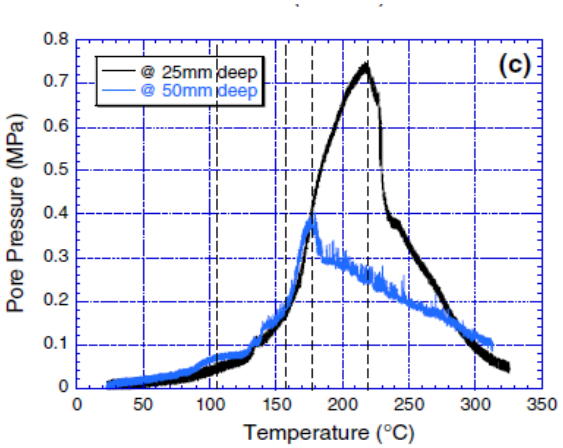

Figure 12 – Pore-pressure as function of the temperature at 25 mm and 50 mm from surface [25].

Van der Heijden et al [26] draw attention to the lack of experimental information about concrete pore-pressure and fluid transport mechanisms, which are directly related to spalling. According to Zeiml et al [27], fluids moving to the inner parts are condensed, creating a region with high water content (saturated zone) which imposes a barrier to the natural fluid flow (moisture clog). As a result, there is an increase in pore-pressure near the concrete surface which pushes the liquid water out of the specimen, causing water exudation. Due to the pore-pressure increase near the surface, violent spalling could occur.

Fu and Li [28], as shown in Figure 13, analyzed concrete pore-pressure behavior during a thermal treatment. Firstly, pore-pressure builds-up near the specimen's surface, inducing water vapor flow to concrete inner parts, which creates a saturated region as water vapor condenses. With time, there is a complete dehydration of concrete external surface, causing a fluid continuous flow (liquid and vapor) to concrete inner core.

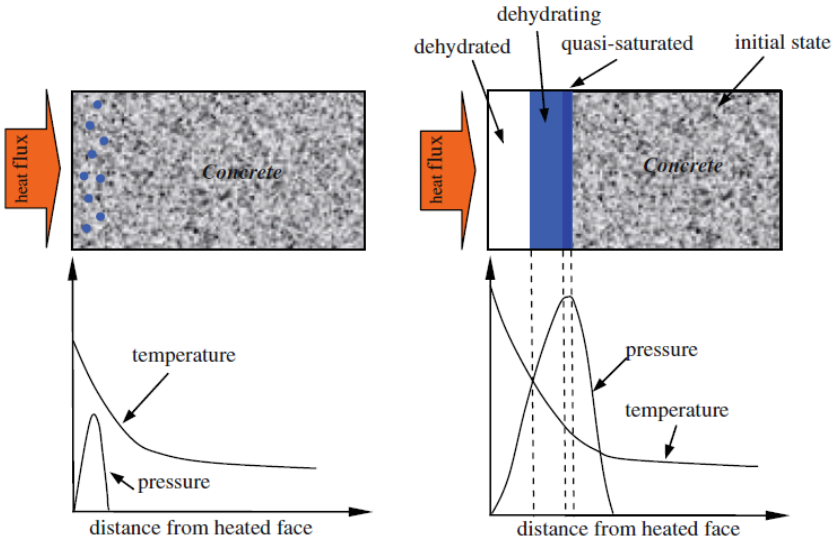

Figure 13 – Pore-pressure mechanism resulted from fluid condensation and development of a saturated zone [28].

2.1.4 Constitutive damage models

Many authors have developed and improved constitutive damage models for concrete structures submitted to high temperatures. Bendoudjema et al [4] describe a constitutive model for cracking based on an orthotropic elastic-plastic damage model considering drying shrinkage, basic creep and drying creep coupling. Sabeur and Meftah [3] propose a fully coupled thermo-hygro-mechanical model.

It is important to mention HITECO (High Temperature Concrete) research program which involved a large number of researchers to investigate and improve the knowledge of high performance concrete (HPC) and ultra-high performance concrete (UHPC) at high temperatures. As a result, a fully coupled non-linear thermo-hygro-mechanical model was developed within the software named HITECOSP (*High Temperature Concrete Spalling*).

Sa and Bendoudjema [29] compared two thermomechanical damage models (elastic-isotropic and orthotropic elastic-plastic) considering smeared crack approach. According to Sa and Bendoudjema [29], in order to predict the complex behavior of concrete mechanical properties due to both temperature and mechanical loading, three different numerical approaches can be adopted: (i) a thermo-hygro-chemo-mechanical coupling approach, involving many material parameters; (ii) a thermo-mechanical approach, assuming concrete as a homogenous material and focusing on the type of mechanical model adopted (isotropic, orthotropic, inelastic strains, etc.); (iii) and, a mesoscopic model, which recognizes concrete as a heterogeneous material and is able to give information about the complex phenomenon of micro and macro cracking development during heating.

Sa and Benboudjema [29] affirm that in order to obtain a better microcracking prediction of concrete mechanical properties one must consider strain incompatibilities at the aggregate-cement paste interface. Added to this, for a high level of temperature increase, one must include mass transfer mechanisms to the model.

Fu and Li [28] state that thermal cracking process cannot be numerically modeled without considering concrete heterogeneity and the introduction of a

thermomechanical damage model at mesoscopic level. In addition, spalling process cannot be tested numerically without considering the effects of thermal cracks.

In spite of all recent advances, Fu and Li [28] affirm that, until today, no convenient experimental method is available for obtaining the stress field during the progressive failure process.

2.1.5 The role of fibers

Lau and Anson [30] observed that, for temperatures below 400ºC, concrete strength decrease is relatively small. In general, independently of the temperature and the mixture process, until 800ºC, fibers were responsible for an increase of concrete strength between 5% and 15%. According to Lau and Anson [30], steel fibers prevented microcracking growth due to shrinkage and the applied load and provided higher tensile capacity. In addition, steel fibers contributed to reduce concrete porosity and pore diameter. Finally, Lau and Anson [30] did not observe the occurrence of violent spalling, suggesting as one plausible reason the low rate of temperature increase during the experimental tests.

According to Peng et al [18], FRC has more fracture energy, especially SFRC. Moreover, steel fibers can benefit and help concrete overcome vapor pressure build-up at high temperatures and, thus, prevent violent spalling. Chan et al [31] affirm that, until a certain limit, concrete degradation can be reduced by steel fibers addition.

Due to Biolzi et al [32] polypropylene (PP) fibers led to a small decrease of concrete mass.

In relation to pore-pressure, Kalifa et al [33] observed that PP fibers greatly contribute to pore-pressure reduction. The main reason is the premature fibers melt, as shown in Figure 14, which creates a dense network of channels, favoring fluid transport inside concrete.

PP fiber diameter, according to Heo et al [34], has a small influence in pore-pressure reduction and spalling prevention, since the latter depends more on the channels extent and connectivity created by fibers melt.

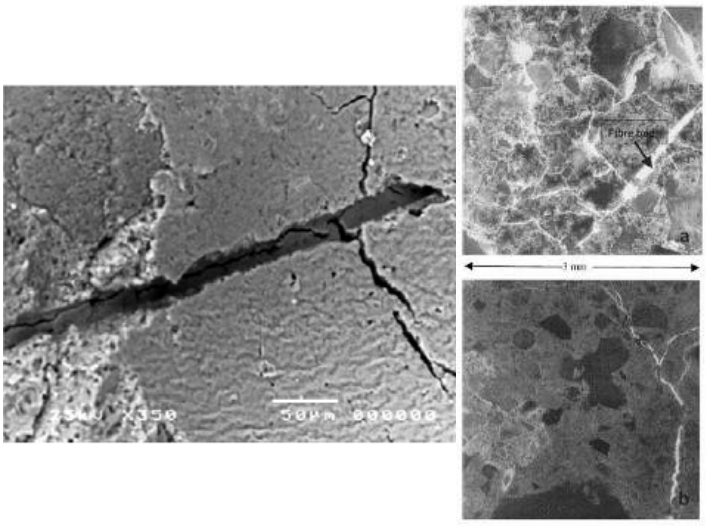

Figure 14 – Microscopic image of internal concrete channels created by fibers melt [27].

Figure 15 shows three distinct mass loss peaks in function of temperature increase. The first one is owed to PP fibers melt at 171ºC. The second one is due to fibers vaporizing at 341ºC and the third one is a result of fibers burn at 457ºC.

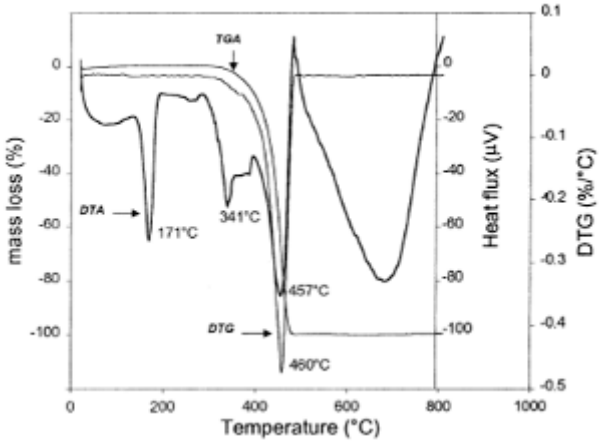

Figure 15 – Pore-pressure build up mechanism due to water vapor condensation [33].

PP fibers also contribute to an increase of concrete permeability. According to Kalifa et al [33], this contribution is higher at 200ºC than at 400ºC. Fibers contribution to fluid transport is also reduced at 400ºC as a result of concrete damage evolution due to the increase of porosity and microcracking expansion.

Biolzi et al [32] state that FRC exhibits a microcracking pattern much denser in relation to plain concrete.

Bilodeau et al [35] affirm that 12.5 mm PP fibers are significantly more efficient than 20 mm fibers to prevent spalling.

Heo et al [34] conclude that fiber quantity per concrete unit volume (n°/m^3) is more meaningful than the commonly adopted fiber weight per unit volume (kg/m^3).

2.1.6 Rheological models

Concrete mechanical behavior is characterized by a visco-elastic-plastic behavior. The elastic component is related to the recoverable instantaneous elastic strain (stress-strain relation) and the plastic component is related to the irrecoverable strain component.

One simple rheological model is the spring-dashpot analogy (visco-elasticity), in which the spring is equivalent to the stored energy in the system and the elastic behavior, and the dashpot is associated with the slow deformation (time-dependent creep strain) due to the energy release over time.

The behavior of concrete, considering its visco-elastic phase, can be represented by a combined model of a spring (elastic-linear component) and a dashpot (viscous component). Two simple linear rheological models describing this behavior are respectively the Maxwell and the Kelvin chains. The former connects linear viscous and elastic elements in series, while the latter connects in parallel, as shown in Figure 16.

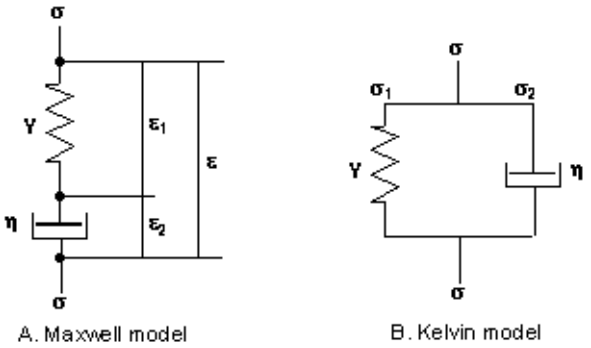

Figure 16 – Viscoelastic models.

Basic creep law is defined in Maxwell model by a linear evolution of strains Eq. 7), while in Kelvin model, creep evolution is defined by an exponential evolution law (Eq. 8).

$$\varepsilon(t) = \frac{\sigma}{E} + \frac{\sigma}{\eta}t \tag{7}$$

$$\varepsilon(t) = \frac{\sigma}{E}\left(1 - e^{-\frac{Et}{\eta}}\right) \tag{8}$$

According to Bazant [24], both Maxwell and Kelvin chains can represent the material as closely as desired, though the identification of material parameters from test data is simpler in Maxwell model.

Bazant et al [36] formulates a generalized creep law based on the microprestress-solidification theory (detailed in the next chapter), as shown in Figure 17 and described in Eq. 9, which includes recoverable elastic and irrecoverable inelastic strains (plastic and cracking), thermal strains, shrinkage and concrete viscous-elastic behavior. As stated by Bazant [24], for a good description of creep data, one must consider two distinct solidification processes, i.e., one viscoelastic strain (time-dependent) and one flow strain, which is dependent only on the applied load.

$$\varepsilon = \varepsilon^i + \varepsilon^v + \varepsilon^f + \varepsilon^{cr} + \varepsilon^{sh} + \varepsilon^T \tag{9}$$

where ε^i= instantaneous strain, ε^v= viscoelastic strain, ε^f= purely viscous strain, ε^{cr}= inelastic strain due to cracking, ε^{sh}=shrinkage, ε^T= thermal strain.

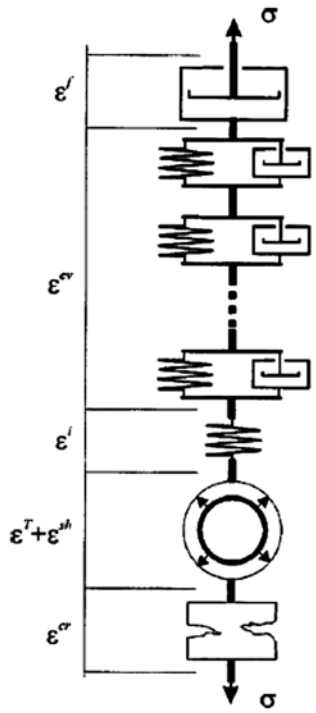

Figure 17 – Generalized concrete rheological model [36].

2.1.7 Thermal expansion

Concrete thermal expansion is the result of aggregates and cement paste volume changes. Typical values for portland cement concrete are shown in Table 1. A correlation between aggregate and concrete thermal expansion is shown in Figure 18.

Table 1 – Coefficient of thermal expansion [37]

	10^{-6}/ºC
Aggregate	
Granite	7-9
Basalt	6-8
Limestone	6
Dolomite	7-10
Sandstone	11-12
Quartzite	11-13
Marble	4-7
Cement paste	
w/c = 0.4	18-20
w/c = 0.5	18-20
w/c = 0.6	18-20
Concrete	7.4-13

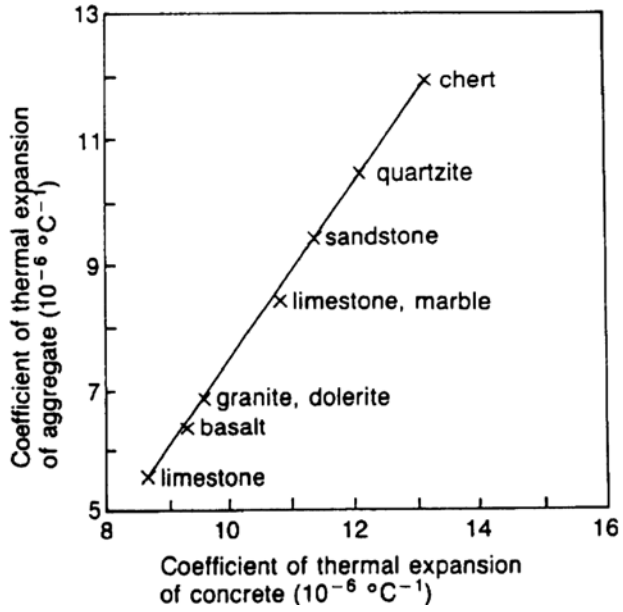

Figure 18 – Correlation between aggregates and concrete thermal expansion [38].

At high temperatures (T>110ºC), concrete thermal mismatch is developed due to aggregates expansion and cement paste shrinkage. Between 200ºC and 600ºC, a rapid increase of the thermal expansion coefficient occurs due to aggregates transformation, as one can observe from Figure 19.

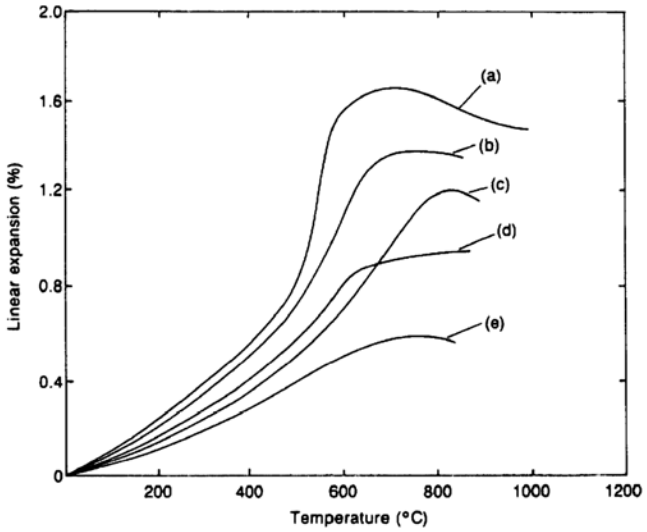

Figure 19 – Linear thermal expansion of concretes made various conventional aggregates in function of temperature: (a) quartzite; (b) sandstone; (c) limestone; (d) basalt; (e) expanded slag [38].

The addition of steel fibers changes concrete behavior, as shown in Figure 20, leading to a lower thermal expansion in relation to plain concrete up to 800ºC, when SFRC thermal expansion shows higher values.

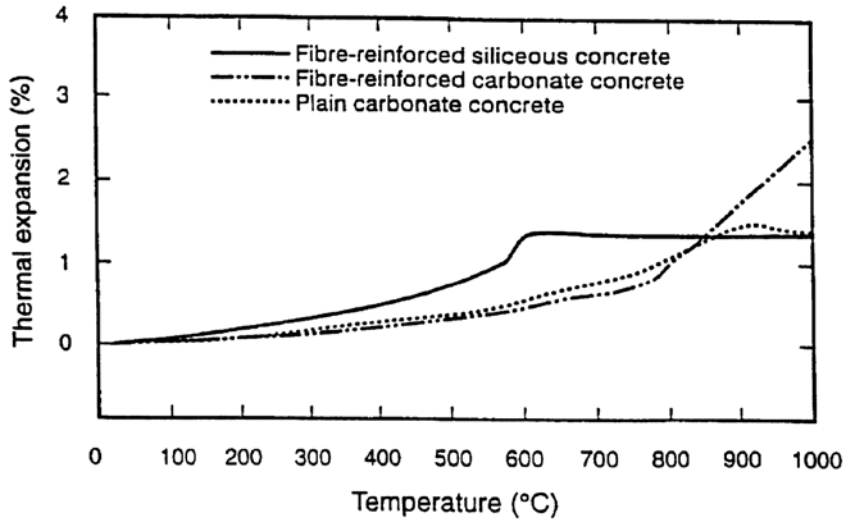

Figure 20 – Thermal expansion of two types of concrete (with and without steel fibers) as function of temperature [39].

In case of HSC, as reported by Kodur and Khaliq [40], fibers incorporation resulted in a lower thermal expansion, as shown in Figure 21. Specimens with hybrid fibers showed a very similar behavior compared to plain concrete, while the incorporation of PP fibers presented the lowest results.

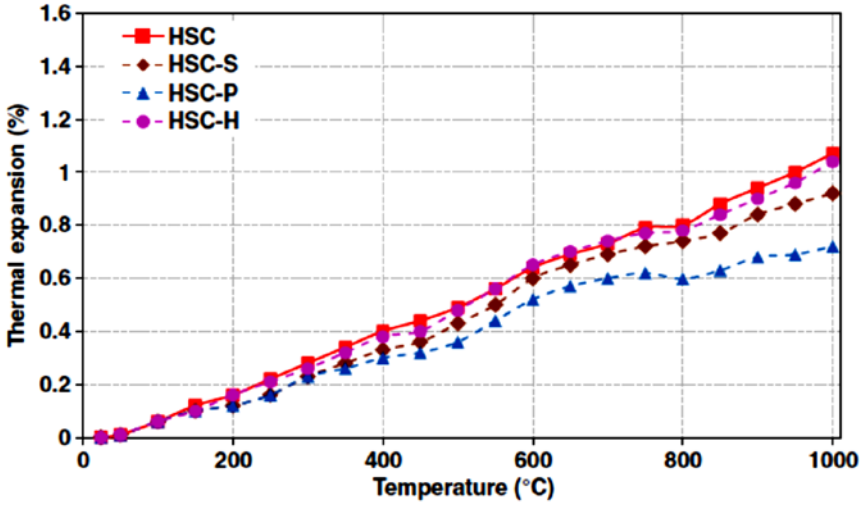

Figure 21 – Effect of fibers on HSC thermal expansion [40].

Experimental results from Hager [41] on two different high performance concrete cylindrical specimens demonstrated that most of the thermal expansion developed during heating is irrecoverable after a complete thermal cycle up to 600ºC, as one can observe in Figure 22.

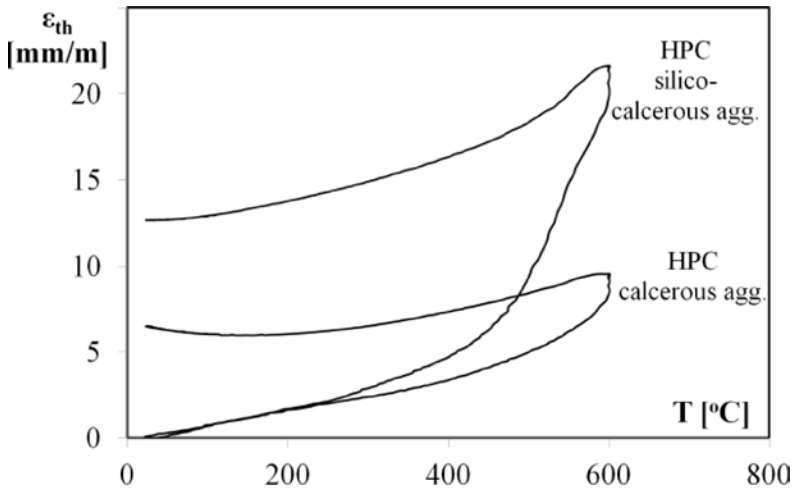

Figure 22 – Concrete thermal cycle up to 600ºC for two high performance concrete specimens [41].

Eurocode 2 [1] provides analytical equations to determine concrete thermal strains as function of temperature for concretes with siliceous and calcareous aggregates. A comparison of concrete thermal expansion using Eurocode 2 [1] and Schneider [42] results is presented in Kodur and Khaliq [40], as shown in Figure 23.

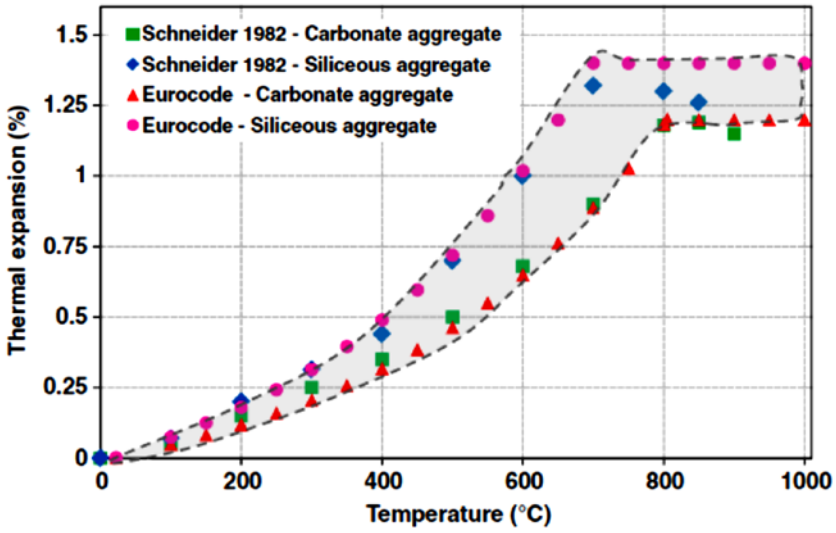

Figure 23 – Concrete thermal expansion for siliceous and calcareous aggregates [1].

It is worth mentioning that tabulated values from the literature should be adopted with precaution since they could lead to erroneous predictions of concrete structural behavior. Ellobody and Bailey [43] numerical and experimental modeling of post-tensioned concrete slabs under fire demonstrated that the coefficients of thermal expansion predicted in Eurocode 2 [1] for calcareous and siliceous concrete are inaccurate, while measured values presented in the literature have provided more accurate numbers.

2.1.8 Thermal conductivity

The coefficient of thermal conductivity depends on the aggregate and reinforcement types, moisture content, porosity and temperature.

Kahn [44] experimental investigation on both mortar and concrete thermal conductivity in dry and saturated specimens is shown in Figure 24.

Type of concrete	Thermal conductivity (W/mK)			
	Sand type I		Sand type II	
	Dry	Fully saturated	Dry	Fully saturated
Mortar	1.90	2.65	1.37	1.95
Basalt concrete	2.26	3.52	1.97	3.24
Limestone concrete	2.03	2.92	1.60	2.71
Siltstone concrete	2.21	3.61	1.91	2.90
Quartzite concrete	2.77	4.18	2.29	3.49

Figure 24 – Concrete and mortar thermal conductivity in dry and fully saturated states [44].

Eurocode 2 [1] establishes analytical equations to determine the upper and lower limits of concrete thermal conductivity for a temperature range between 20ºC and 1200ºC. Different results of thermal conductivity evolution with the temperature for NSC are shown in Figure 25, as presented in Kodur and Khaliq [40].

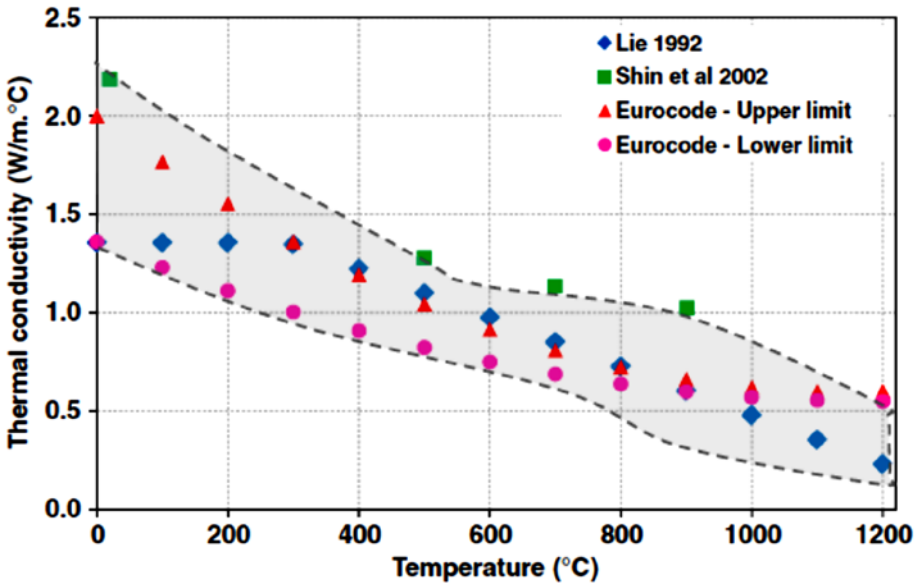

Figure 25 – Concrete thermal conductivity [40].

Kodur and Khaliq [40] analyzed, among others, the effect of steel, PP and hybrid fibers on the thermal properties of HSC. As shown in Figure 26, fibers addition does not change significantly concrete thermal conductivity up to 600ºC, from which point they present a small effect on HSC thermal conductivity. This small influence, according to

Kodur and Khaliq [40], can be attributed to CSH dehydration and the contribution of the higher thermal conductivity of steel fibers in the concrete mix.

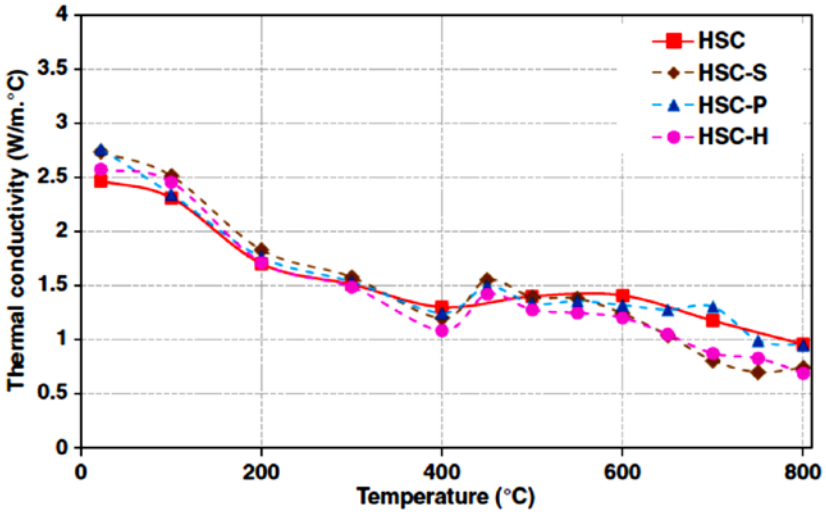

Figure 26 – Effect of fibers on thermal conductivity of HSC as function of temperature [40].

2.1.9 Specific heat

Specific heat depends on the temperature, moisture content, aggregate type and density. Eurocode 2 [1] provides analytical equations to determine the specific heat of concrete with calcareous and siliceous aggregates, in which the moisture content is implicit in the formulations. Kodur et al [40] compared the results in literature of NSC specific heat predictions, as shown in Figure 27.

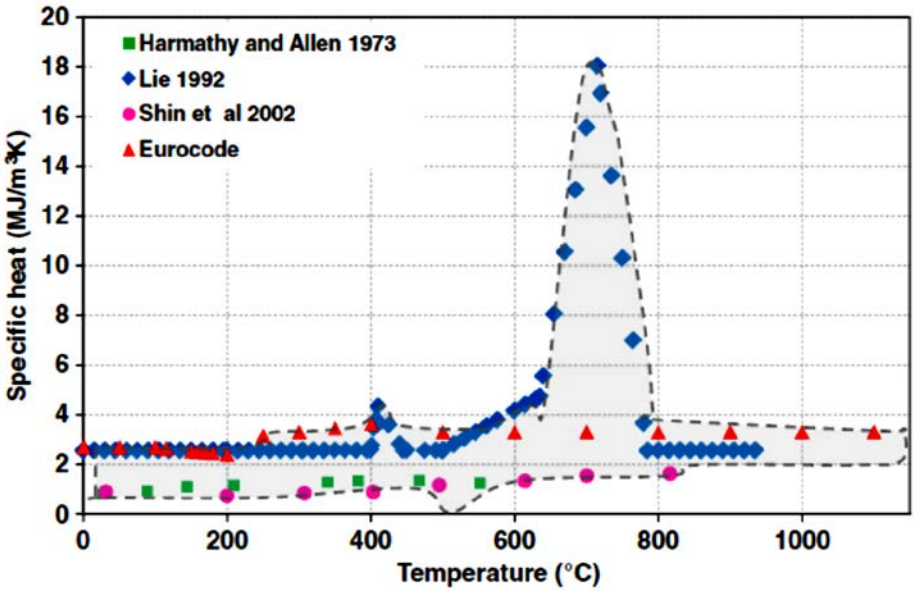

Figure 27 – NSC specific heat as function of temperature [40].

According to Kodur and Khaliq [40], the specific heat of HSC is affected by physical-chemical processes that are developed in the cement paste and aggregates above

600ºC. At this level, an enormous amount of energy is required to raise the temperature of the carbonate aggregate concrete.

The addition of fibers on HSC, according to Kodur and Khaliq [40], has a marginal effect on HSC specific heat up to 400ºC, as show in Figure 28. The reduction of the specific heat of HSC reinforced with PP fibers above 600ºC is due to polypropylene decomposition (melt and burn) which increases concrete porosity.

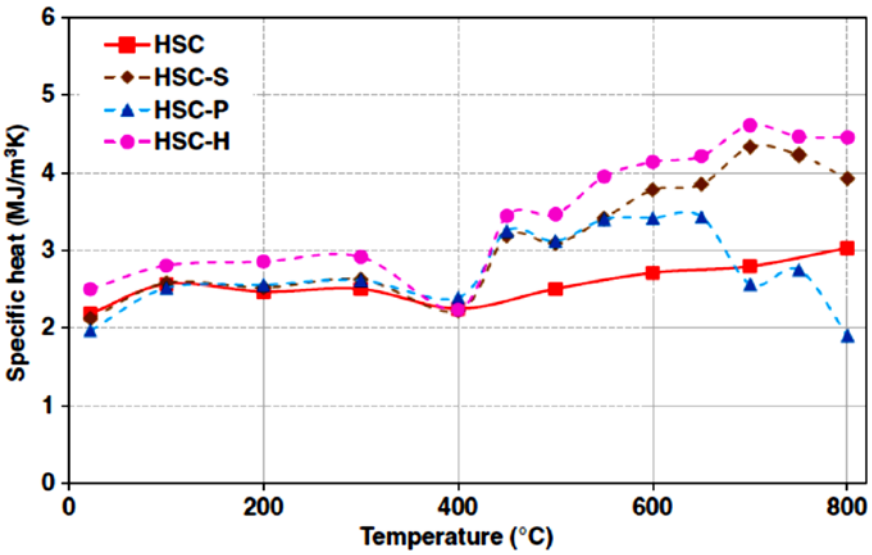

Figure 28 – Fibers effects on HSC specific heat [40].

2.1.10 Modulus of Elasticity

Due to thermal damage, concrete experiences a strength decay and a reduction in the Modulus of Elasticity (softening behavior). Comparing different experimental results and analytical models available in literature, Youssef and Meftah [45] observed a large scatter in the experimental results. Despite that, according to Youssef and Meftah [45], all predicted models for unloaded concrete demonstrated acceptable accuracy, as shown in Figure 29.

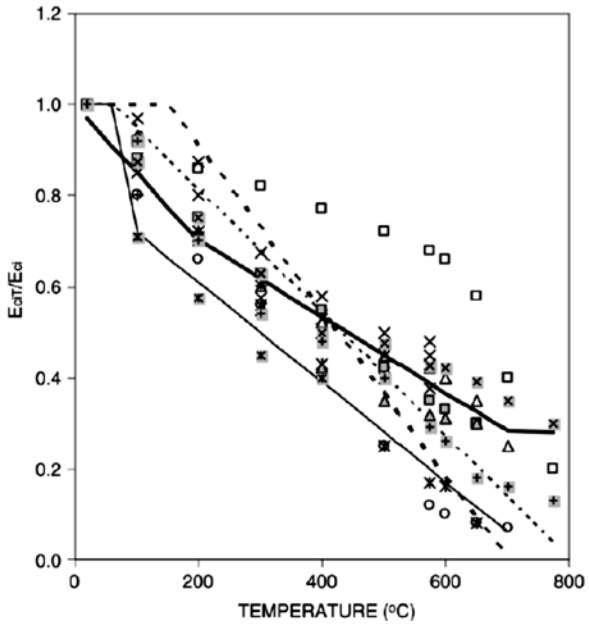

Figure 29 – Comparison of analytical models of unloaded concrete normalized Modulus of Elasticity as function of temperature [45].

Some authors provide analytical equations to account for the effect of preloading in concrete. Youssef and Meftah [45] compared the results available in literature, stating that only the models of Khenane and Baker [46], Schneider [42] and Anderberg and Thelandersson [47] demonstrate acceptable accuracy, as shown in Figure 30.

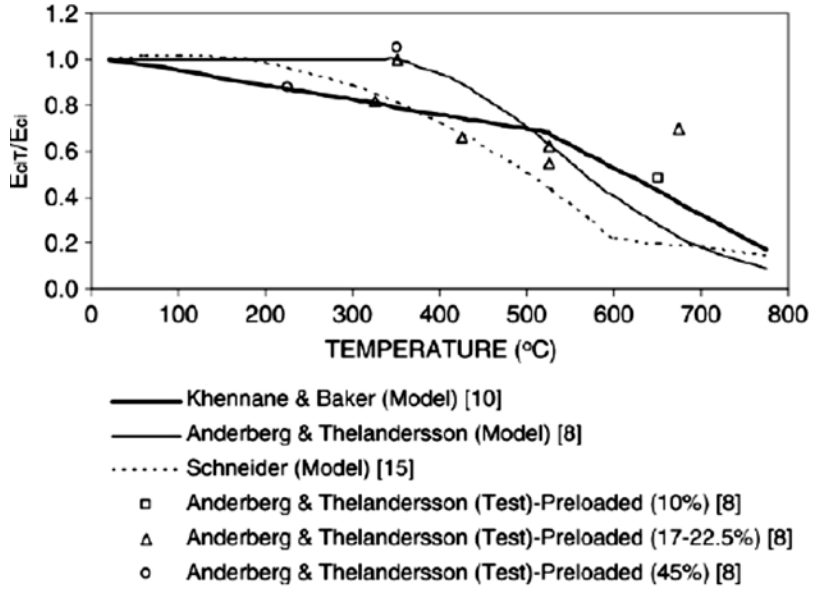

Figure 30 - Comparison of analytical models of preloaded concrete normalized Modulus of Elasticity as function of temperature [45].

Colombo [6] analyzed SFRC thermal degradation by ultrasonic wave tests before and after a complete thermal cycle of heating and cooling. In this case, the dynamic elastic modulus exhibited a quite linear decay up to 400ºC, as shown in Figure 31. Colombo [6] attributes the difference between the results at room temperature and at 200ºC to concrete drying, which causes ultrasonic wave pulses to decelerate due to concrete voids formation after water loss.

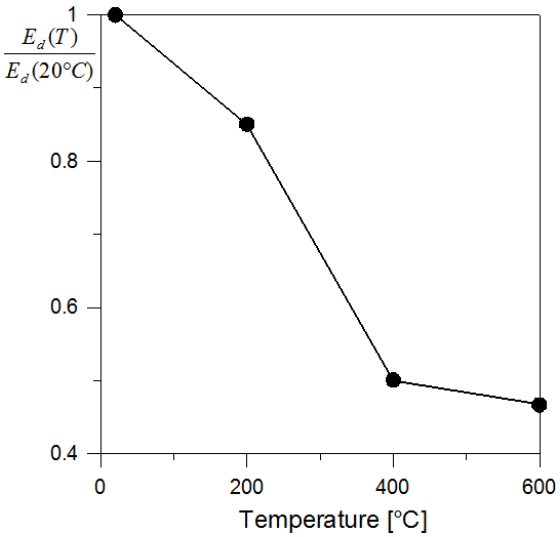

Figure 31 – Normalized Dynamic Modulus of SFRC as function of temperature [6].

Bamonte and Gambarova [17] tests on SCC both at high temperature (hot-state) and after cooling (residual), demonstrated that the residual values, up to 600°C, were higher than the hot ones, as shown in Figure 32.

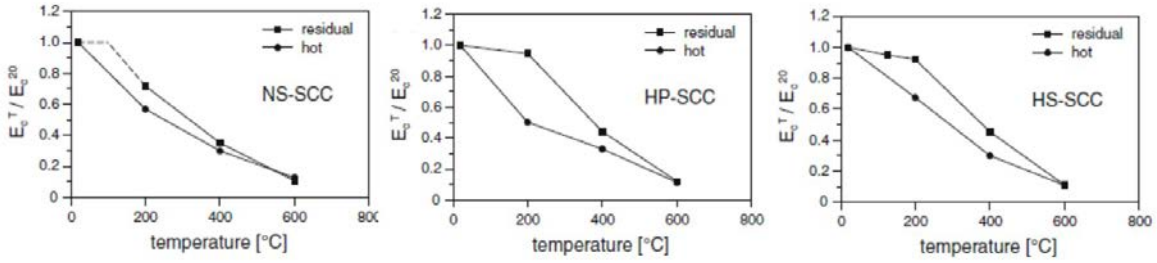

Figure 32 –Normalized Elastic Modulus as function of temperature [17].

Felicetti et al [48] analyzed hot and residual values of the Modulus of Elasticity in three different types of concrete: high-strength concrete (HSC), self-compact fiber-reinforced concrete (CRC) and reactive powder concrete (RPC). The results were similar to the ones from Bamonte and Gambarova [17], with higher values achieved after cooling.

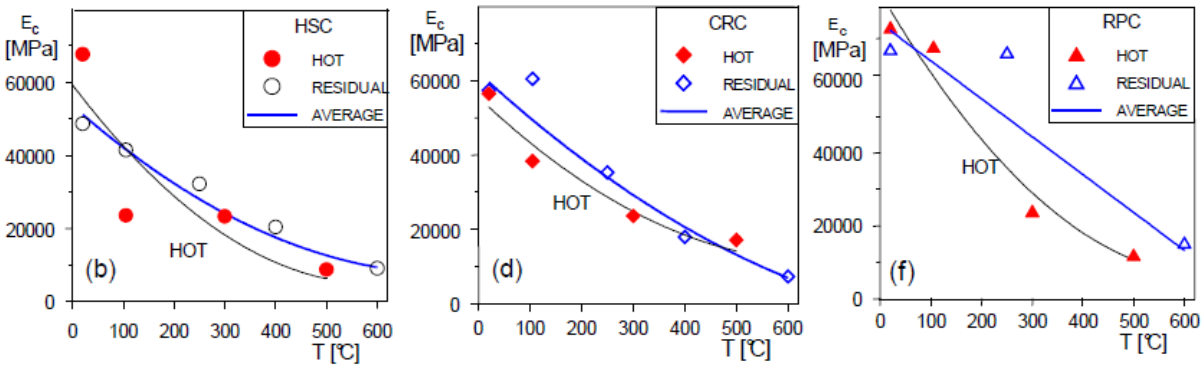

Figure 33 – Hot and residual Elastic Modulus as function of temperature [48].

2.1.11 Compressive strength

In literature, different empirical models aiming to predict concrete strength at high temperatures are available. Some of them are based on unloaded specimens, while others take into account an initial sustained compressive stress applied before heating. In turn, Eurocode 2 [1] provides tabulated data for siliceous and calcareous NSC at temperatures ranging from 20ºC to 1200ºC.

It is worth mentioning Hertz [49] model (Eq. 10), which considers the type of aggregates and takes into account the effect of the preload by multiplying the equation for the stress level. Hertz [49] states that concrete preloading reduces both microcracking and the compressive strength decay at elevated temperatures. In general, according to [49], preloaded specimens can be 25% stronger in relation to unloaded ones for compressive stresses between 0.25 f_c and 0.30 f_c.

$$f_{cT} = f'_c \left[\frac{1}{1 + \frac{T}{T_1} + \left(\frac{T}{T_2}\right)^2 + \left(\frac{T}{T_8}\right)^8 + \left(\frac{T}{T_{64}}\right)^{64}} \right] \quad (10)$$

Siliceous aggregates: $T_1 = 15000$, $T_2 = 800$, $T_8 = 570$, $T_{64} = 100000$
Lightweight concrete: $T_1 = 100000$, $T_2 = 1100$, $T_8 = 800$, $T_{64} = 940$
Other aggregates: $T_1 = 100000$, $T_2 = 1080$, $T_8 = 690$, $T_{64} = 1000$

Youssef and Meftah [45] compared some models available in literature both for unloaded and preloaded specimens, as shown respectively in Figure 34 and Figure 35.

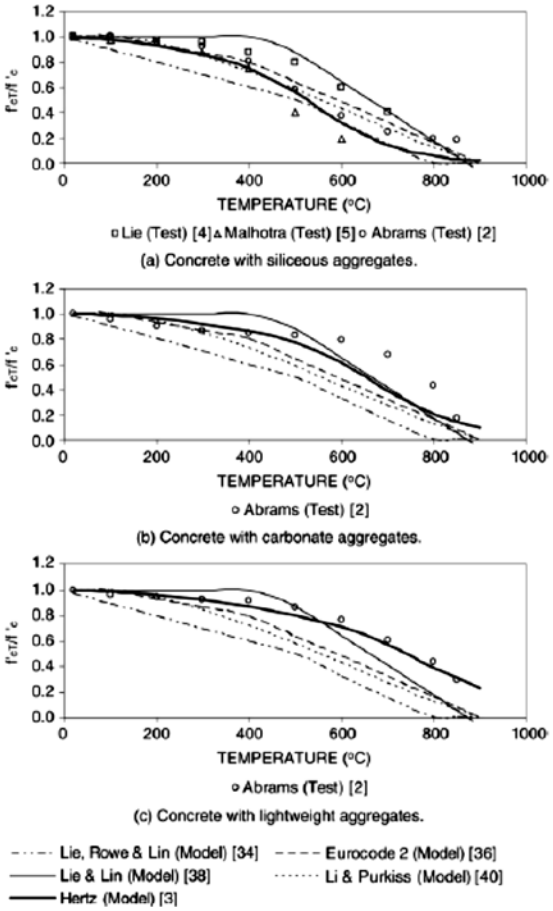

Figure 34 - Compressive strength models for unloaded concrete at elevated temperatures [45].

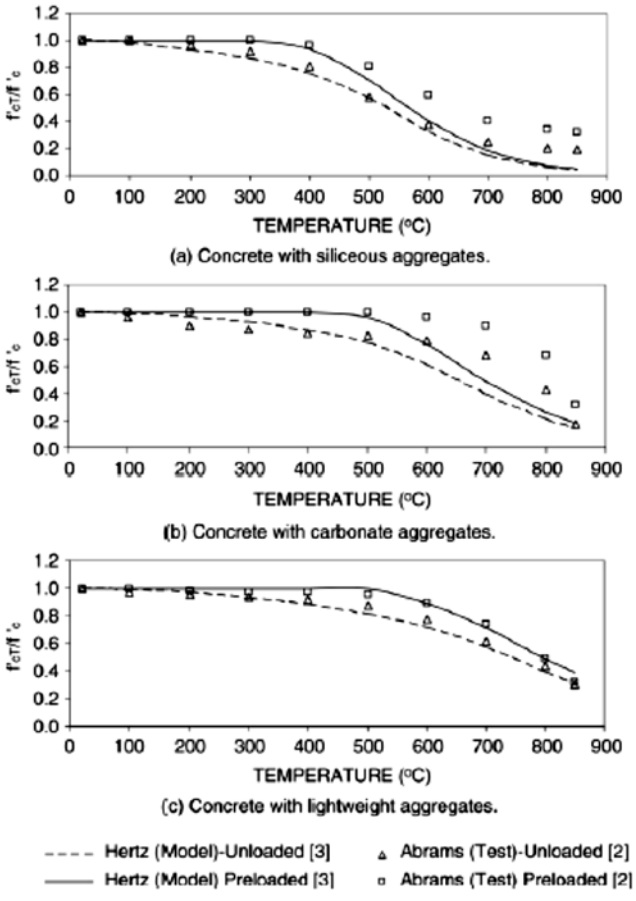

Figure 35 –Compressive strength models for preloaded concrete at elevated temperatures [45].

Bamonte and Gambarova [17] tests on SCC at high temperature have shown that concrete strength measured at hot-state was in general higher than the residual values measured after cooling. Moreover, the residual values were lower than the ones predicted with Eurocode 2 [1].

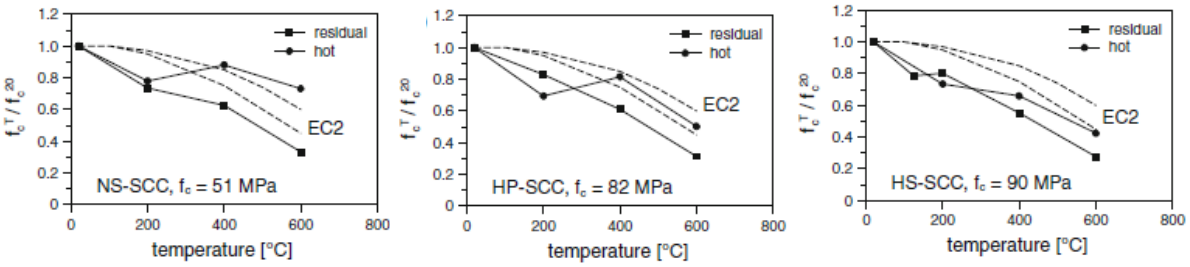

Figure 36 –Normalized compressive strength at high temperature considering hot and residual values [17].

Colombo et al [50] SFRC experimental results at different temperatures are shown in Figure 37. From the results, it is possible to notice that from 200°C to 400°C, the compressive strength decay as function of temperature is reduced. Moreover, after 400°C, the prediction of Eurocode 2 for plain concrete overestimates the results.

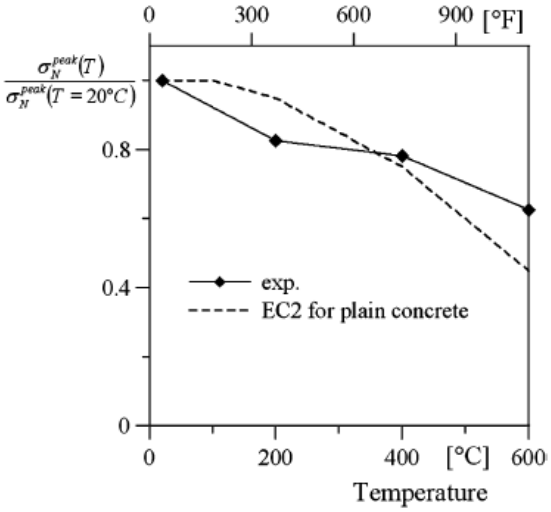

Figure 37 – Residual normalized uniaxial compressive strength as function of temperature [50].

2.1.12 Compressive strains

Eurocode 2 [1] suggest tabulated values to determine the maximum compressive strain (ε_{cu}) and the strain at maximum stress (ε_0) for different temperatures.

Anderberg and Thelandersson [47] pointed out the considerably difference between the mechanical behavior of loaded concrete under transient high temperature and under steady state conditions. In this case, as stated by Anderberg and Thelandersson [47], the compressive strains are much higher during concrete heating compared to the ones developed at constant temperature. Therefore, Anderberg and Thelandersson [47] formulated a constitutive law considering four strain components, i.e., thermal strains (including drying shrinkage), instantaneous stress-related strain, creep (constant load and temperature) and transient creep (constant load and variable temperature).

Thermal strains, according to Anderberg and Thelandersson [47], depends on the initial moisture content and, during heating, is a simple function of the temperature directly given by the measured thermal expansion curve, as shown in Eq. 11.

$$\varepsilon_{th} = \alpha(T - 20ºC) \tag{11}$$

The instantaneous stress-related strain is function of the applied load and temperature, being determined by the stress-strain curve. Among others, Li and Purkiss [51], Khenane and Baker [46], Bazant and Chern [52], Terro [53] and Schneider [42] provide analytical models to calculate ε_0 for unloaded specimens. Anderberg and Thelandersson [47], Khenane and Baker [46] and Schneider [42] also specify models for preloaded specimens

Creep strains in compression at high temperature (basic creep) in Anderberg and Thelandersson [47] were measured with a load applied after temperature stabilization. The results have shown that creep strains remained small in most of the tests compared to concrete thermal expansion. It is worth to underline that, according to Youssef and Meftah [45], this procedure does not capture realistically concrete behavior under fire conditions, since structures are subjected to varying and non-linear temperature distribution. Hence, a more appropriate strain measurement is the

transient creep, which captures concrete behavior under constant stress state and variable temperature. In this case, many authors propose empirical models which are based on experimental results. For example, Anderberg and Thelandersson [47] model is proportional both to the applied stress and the free thermal strain, while Terro [53] model accounts for the effect of the volume fraction of aggregates.

2.1.13 Compressive stress-strain relation

Eurocode 2 [1] establishes values for siliceous and calcareous NSC strength ($f_{c,\theta}$), strain at maximum stress ($\varepsilon_{c1,\theta}$) and maximum strain ($\varepsilon_{cu1,\theta}$) for a temperature range between 20ºC and 1200ºC. From these three parameters, the ascending branch of the stress-strain curve can be obtained from Eq. 12. For the descending branch, Eurocode 2 [1] allows linear (straight line) and non-linear (parabola) models.

$$\frac{3\varepsilon f_{c.\theta}}{\varepsilon_{c1,\theta}\left(2+\left(\frac{\varepsilon}{\varepsilon_{c1,\theta}}\right)^3\right)} \tag{12}$$

Youssef and Meftah [45] compared several models available in literature and proposed a new stress-strain relationship encompassing two analytical models, one based on Scott et al [54] and other based on Mander et al [55]. Both models have shown good accuracy for the ascending branch, while the former one has provided the most accurate predictions for the descending branch at different temperature degrees. In their model, transient creep was modeled using Anderberg and Thelandersson [47] empirical formula and was added to the stress-strain curve by shifting the strain at maximum stress. Figure 38 shows a comparison among Youssef and Meftah [45] model with other authors.

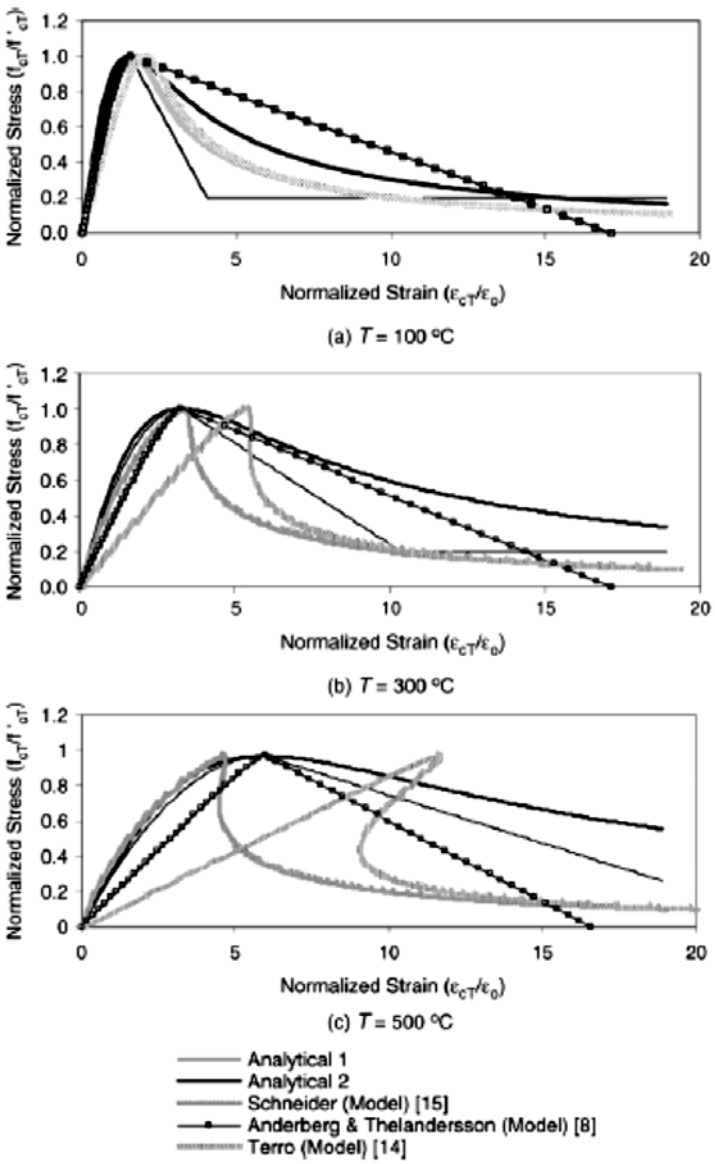

Figure 38 – Comparison of different stress-strain models considering the transient creep effect on the stress-strain curve [45].

Felicetti and Gambarova [56], based on the experimental results of high strength siliceous concrete at high temperature, proposed analytical relations regarding the peak stress (Eq. 13), Elastic Modulus (Eq. 14) and strain at peak stress (Eq. 15), where: T is the nominal temperature; T_r is the room temperature; T_u is the strength-loss temperature; ϑ is the temperature-dependent parameter (Eq. 16).

$$\frac{f_c(T)}{f_c(T=20°C)} = \frac{1-\vartheta^2}{1+\vartheta^3} \tag{13}$$

$$\frac{E_c(T)}{E_c(T=20°C)} = \frac{1-\vartheta^{1.5}}{1+\vartheta^{3.5}} \tag{14}$$

$$\frac{\varepsilon_1(T)}{\varepsilon_1(T=20°C)} = \frac{1}{1-\vartheta^{3.5}} \tag{15}$$

$$\vartheta = \frac{T - T_r}{T_u - T_r} \tag{16}$$

2.1.14 Tensile strength

The research in this area is limited according to Youssef and Meftah [45]. Some analytical models are available in literature, from which is worth mentioning Bazant and Chern [52], Terro [53] and Eurocode 2 [1]. Figure 39 shows a comparison among some models described in Youssef and Meftah [45].

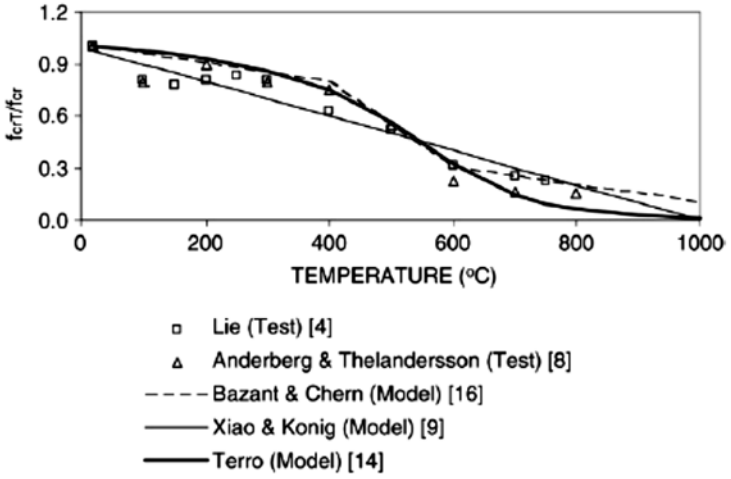

Figure 39 – Normalized tensile strength as function of temperature [45].

Euocode 2 [1] defines a parameter ($k_{c,t}$) to account for the effect of tensile strength degradation (linear decay) due to the temperature up to 600ºC, as shown in Figure 40.

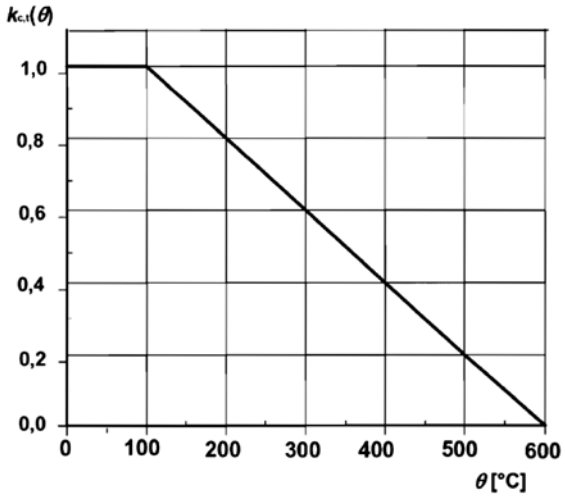

Figure 40 – Coefficient $k_{c,t}(\theta)$ allowing for tensile strength decrease at elevated temperatures [1].

Felicetti et al. [56] tests carried out on high strength concrete (HSC) and reactive powder concrete (RPC) reinforced with steel microfibers and polymeric fibers have shown similar results of the tensile strength measured at hot-state and after cooling (residual). In contrast, compact fiber-reinforced concrete (CRC) residual values were

higher in relation to the hot ones. Moreover, fiber reinforced concrete (CRC and RPC) show a lower tensile strength decay compared to plain concrete (HSC). The results are show in Figure 41.

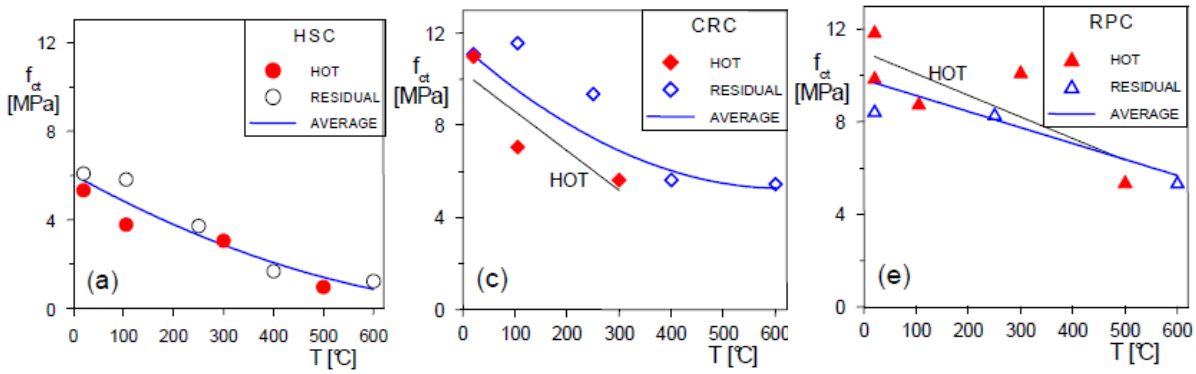

Figure 41 – Tensile strength of three different concretes at high temperature (hot and residual values) [56].

Colombo et al [50] uniaxial tensile test results on steel fiber reinforced concrete (SFRC) after a thermal cycle at different maximum temperatures is shown in Figure 42 in terms of normalized values. A prediction by means of the Eurocode 2 [1] for plain concrete shows that SFRC has a lower tensile strength decay. One important conclusion obtained from the experimental results is that fiber pull-out mechanism of FRC is less affected by the high temperature than the matrix of plain concrete.

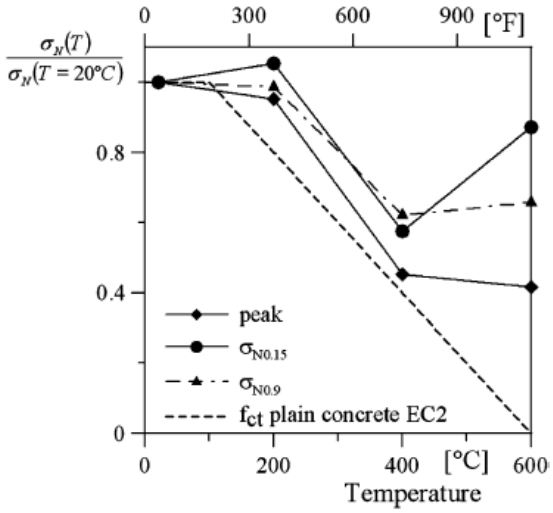

Figure 42 – Normalized tensile strength at different temperatures [50].

2.1.15 Tensile stress-strain relation

Stress-strain constitutive models in tension considering the effect of high temperature are very limited in literature. A linear relationship is widely adopted both for concrete pre-cracking and post-cracking behavior.

Youssef and Meftah [45] propose a model to describe uniaxial stress-strain relationship for concrete in tension. Before cracking, a linear stress-strain relationship is assumed and the cracking stress in direct tension is determined according to Eq. 17. Post-cracking behavior is determined according to Eq. 18, in which Collins and Mitchell [57] model was adapted to account for the reduction on both the tensile and bond strengths.

$$f_{crT} = \left(0.33\lambda\sqrt{f_c}\right)\frac{f_c}{f_{cT}} \quad (17)$$

$$f_{tT} = \frac{\propto_1 \propto_2 f_{cr}T}{1+\sqrt{500\varepsilon_{cT}}}\frac{\tau_{uT}}{\tau_{u0}} \qquad \left(\varepsilon_{cT} > \frac{f_{crT}}{E_{ciT}}\right) \quad (18)$$

2.2 Fundaments of Creep

Creep is caused by physicochemical transformations in concrete microstructure. According to Bazant [24], creep has two basic constituents at room temperature, one aging component, which reaches an asymptotic value after the end of the process of hydration, and one non-aging component, which continues to increase, and is due to long-term relaxation of self-equilibrated micro-stresses in the nano-porous microstructure of the CSH.

Bazant [24] affirms that creep is dependent on the specimen's size and shape. In addition, creep properties are significant even after many years, when the amount of cement undergoing hydration is negligible and neither the elastic modulus nor concrete strength change appreciably.

In order to evaluate the total deformation, concrete strain components (thermal, instantaneous and time-dependent mechanical) can be simply added by applying the superposition principle for stresses up to $0.4 \cdot f_c$. According to Bazant [24], after $0.4 \cdot f_c$, there is a progressive non-linearity, largely irreversible, caused mainly by gradual microcracking expansion.

At room temperature, creep has two components, basic creep and drying creep. The former occurs in sealed specimens and the latter is developed in unsealed specimens.

Creep accelerates in drying specimens due to both simultaneous loading and rapid heating or cooling. It is important to underline that, as temperature rises, creep becomes more important, eventually superseding fatigue as the likely failure criterion.

At high temperature, creep can be divided in three components: (i) basic creep, which occurs at constant temperature, after concrete physical-chemical stabilization; (ii) transitional thermal creep (ttc), which occurs during heating, continuing at constant temperature up to concrete thermal stabilization, and is due to concrete dehydration and, beyond 300ºC, also due to aggregate degradation; (iii) drying creep, which occurs during the early stages of heating and is the result of free water loss. Drying creep and ttc comprise the transient creep, while the difference between the total strain and the free thermal strains, disregarding the initial elastic deformation, constitutes the so-called Load Induced Thermal Strain *(*LITS) (Khoury, [58]), which takes into account irrecoverable mechanical strains and changes in the recoverable elastic strains due to heating.

As stated by Bazant [24], creep does not have an asymptotic value. However, its components could approach a limit for specified load and temperature conditions, as is the case of basic creep at room temperature and transient creep at high temperature.

At room temperature, creep and shrinkage experimental measurement procedures are described on RILEM TC-107 [59] and ACI Comitee 209 [60]. At high temperature, RILEM TC 129 [61] defines the standard test procedures.

The effects of creep are commonly described in terms of adimensional parameters. ACI-209 [60] defines the creep coefficient as the ratio between creep and mechanical

strain values – $\Phi(t, t_0) = \varepsilon^{cr}(t, t_0)/\varepsilon^{el}(t_0)$ – while the specific creep is defined as creep per unit stress. The advantage of the latter notation is that creep strains are kept independent of the applied load and its value can be used to estimate, under certain stress limits, creep strains at any load level. Moreover, the compliance function represents the total stress-dependent strain per unit stress and is function of the creep coefficient: $J(t, t_0) = \big(1 + \Phi(t, t_0)\big)/E_{ci}$.

It is important to observe that, according to Willam et al [62], up to 80°C, there is no noticeable change in the fundamental creep mechanism, although, at this temperature, occurs an acceleration of concrete aging and creep values are twice of the one observed at 20°C. However, at high temperature, creep parameters become also dependent of the temperature, occurring a thermo-hygro-mechanical (heating + drying/dehydration + loading) coupling effect. In addition, the stress limit is reduced due to excessive creep at lower stress levels.

2.2.1 Shrinkage

Shrinkage is dependent of concrete thermo-hygral conditions, being divided in autogeneous (sealed specimen) and drying (unsealed specimen) components. A sealed specimen, at early age, presents autogenous shrinkage due to concrete hydration. An unsealed specimen is also subjected to drying shrinkage due to free water loss. In this case, the loss of water held in the gel pores (cement paste level) is the main cause of the concrete volume change. It is worth mentioning that the loss of free-water is not responsible for an appreciable dimensional change, although the increase in the pore relative humidity in the cement paste capillary pores can give rise to concrete swelling. It is worth mentioning that cement paste shrinks more than mortar, mortar shrinks more than concrete and concrete with finer aggregates shrinks more than concrete with coarse aggregates.

During heating, there is a coupling between temperature, which leads to aggregate expansion, and pore humidity, in which concrete moisture loss induces cement paste shrinkage, resulting in a thermal mismatch which leads to concrete microcracking development.

2.2.2 Basic creep

Basic creep, at room temperature, occurs in sealed specimens under no moisture exchange with the environment. Rossi et al [63], based on acoustic emission tests, explained that the physical origins of basic creep relies on concrete microcracking which induces water vapor movement from capillaries to the microcracks, leading to capillary drying and shrinkage.

Ranaivomanana et al [64] analyses of sealed HSC specimens at room temperature showed that shrinkage plays an important role in the estimation of basic creep, particularly in the case of tensile basic creep. In this case, test results exhibited negative strain variations. As stated by Atrushi [65], this is due to the fact that, in tension, autogenous shrinkage has a high influence both in magnitude and in the rate of creep, since shrinkage is of the same magnitude of the load-dependent deformation. Moreover, Ranaivomanana et al [64] affirm that since direct tensile tests cause greater damage in the specimen, the interpretation of the results becomes more complicated due to the stronger interaction between stress-induced cracking and shrinkage strains.

Bazant et al [52] formulates a constitutive law to model basic creep effects considering constant water content and temperature conditions. The triple power law gives the creep rate (compliance function) as function of the product of power functions of the load duration, the age at loading and the current age of concrete, as shown in Eq. 19.

$$J(t,t') = \frac{\psi_1}{E_0} \frac{t'^{-m} + \alpha}{(t-t')^{1-n}\left(\frac{t}{t'}\right)^n} \tag{19}$$

where: E_0 = asymptotic modulus ($\cong 1.5 \cdot E_{28}$); n, m, ψ_1 and α = materials parameters.

At high temperature (T>100°C), basic creep (creep at high temperature) occurs in unsealed specimens (dried) with constant temperature, after all concrete physical-chemical transformations are completed. Some authors, such as Andenberg and Thelandersson [47], propose an equation to describe its effects. However, it is important to say that basic creep strains are much lower in respect to transient creep deformations. Moreover, immediately after temperature stabilization, concrete reactions continue to occur, creating a coupling behavior between basic creep and ttc, which makes the task to isolate the basic creep term more complicated.

2.2.4 Drying creep

According to Bendoudjema et al [4], drying creep corresponds to the additional deformation observed when concrete is loaded together with a change in the internal moisture state, originating the so-called Picket effect (microcracking).

Picket's paradox, as stated by Acker and Ulm [66], occurs when the hygrometric conditions acts in opposite direction on the creep rates, according to whether water content in the specimen is uniform or not. For example, a previously dried concrete exhibits no creep, whether an impermeable concrete (basic creep), with no drying, the more evaporable water it contains, the more it creeps. And a concrete that dries during loading (drying creep) creeps even more, as shown in Figure 43.

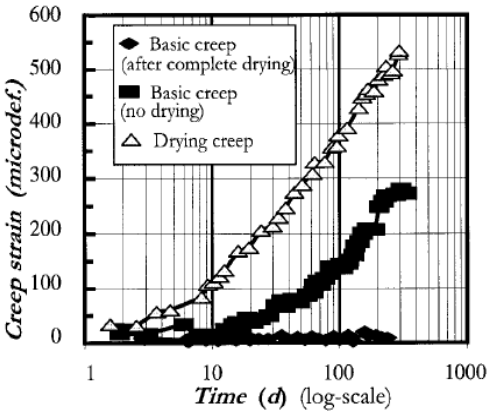

Figure 43 – Creep strains as function of time of specimens loaded in high temperature [66].

Benboudjema et al [4] say that microcracking phenomenon is the result of concrete moisture loss and can be identified when the specimen is submitted at the same time

to a sustained compressive load and drying conditions. In this case, the drying-induced microcracking is less pronounced compared to a non-loaded specimen and the measured delayed strain is greater than the sum of the elementary components (drying shrinkage and basic creep), as shown in Figure 44.

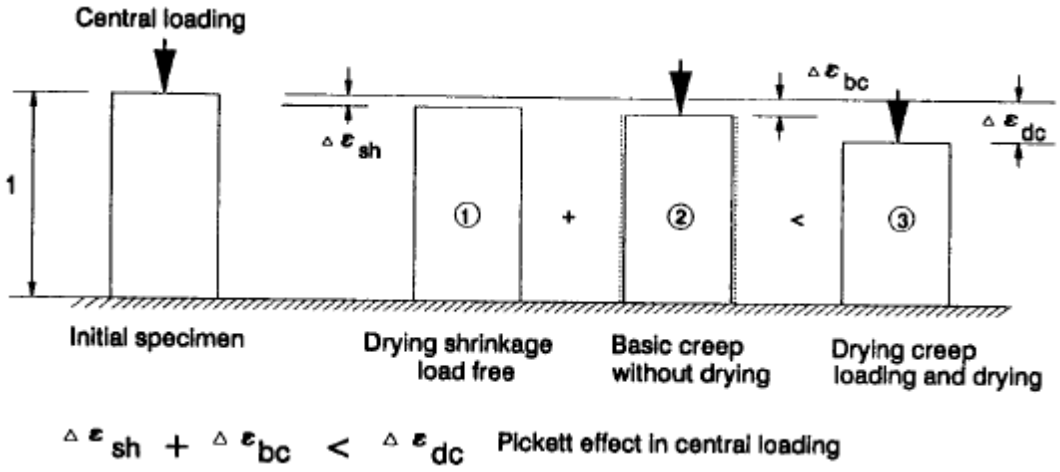

Figure 44 – Picket effect (Bazant and Carol, [67]).

Microcracking is directly related to concrete thermal gradient and inhomogeneous moisture distribution. Analyzing a free-load specimen at initial heating stage, while concrete external surface is drying and shrinking, the inner layer is wet and submitted to compressive stresses. The compressive stresses are counterbalanced by tensile stresses at the specimen's surface layer, producing microcracks, which are one of the physical explanations of drying creep. As stated by Bazant and Carol [67], since these microcracks are not fully closed, when moisture distribution reaches a uniform state, the measured shrinkage is smaller than the true shrinkage. On the contrary, a specimen under uniaxial compressive stress exhibits larger shrinkage, since the whole cross-section is in compression and microcracking is reduced. As a consequence, the apparent drying creep will be larger than the sum of the separate basic creep and shrinkage.

Bazant et al [2] propose a unified theory called microprestress-solidification theory to describe concrete creep phenomenon encompassing the short-term effect of microcracking and the long-term aging, in which creep is a result of stress-induced shrinkage. The latter is a physical explanation to describe moisture-diffusion process in concrete microstructure, which is characterized by local water transportation between capillary pores and gel pores with molecular size. The microdiffusion flux of water through the gel pores is responsible for the continuous process of separation, slip and restoration of bonds in the CSH gel, which leads to a relaxation of the shear stresses of that local site.

It is important to underline that, while microcracking effect increases and later decreases when a moisture uniform state distribution is reached, the stress-induced shrinkage continuous to increase with time, as shown in Figure 45.

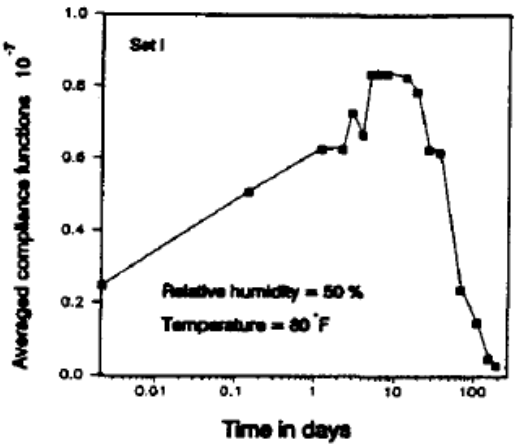

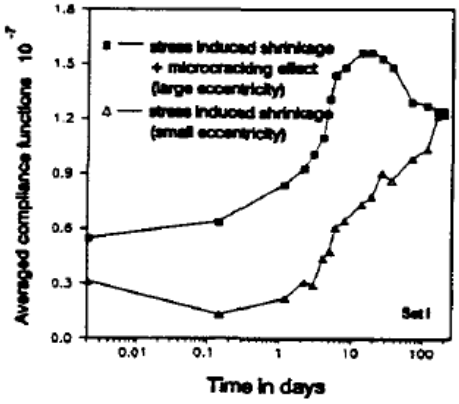

). 7 Effect of microcracking on drying creep

Fig. 6 Decomposition of different drying creep mechanisms

(a) (b)

Figure 45 – Creep mechanisms: (a) Effect of microcracking on drying creep; (b) Stress-induced shrinkage ([67]).

Bazant et al [36] includes the effects of the temperature in the microprestress-solidification theory of Bazant et al [2], taking into account microcracking and changes in the level of the microprestresses acting in the CSH structure due to temperature variations.

It is important to underline that this theory is valid for temperatures up to 100°C since, above this level, creep mechanisms change. Below 100°C, the role of temperature, due to Bazant et al [36], is twofold and causes, on one hand, the acceleration of bond breakages and restorations, and, on the other hand, it increases the hydration of the calcium-silicate-hydrates. Above 100°C, concrete dries out, ending the hydration phase (solidification process), and concrete dehydration associated with microcracking, due to thermal mismatch, prevails.

2.2.5 Creep at high temperature

At high temperature, creep is divided in two main mechanisms, one called transient creep (ε^{tr}), which occurs during the heating phase and is due to concrete drying and dehydration. The other occurs after heating, with constant temperature, and is called basic creep or generically creep at high temperature.

Transient creep describes all creep effects that takes place in concrete during heating (physical-chemical transformations), which includes drying creep and transitional thermal creep (ttc).

Drying creep (ε^{dc}), as shown in Figure 46, practically achieves its maximum value at 110ºC, with some small variations according to materials properties and boundary conditions. From that point, transient creep is almost entirely dependent of concrete dehydration, which starts at 105ºC, as shown in Figure 47.

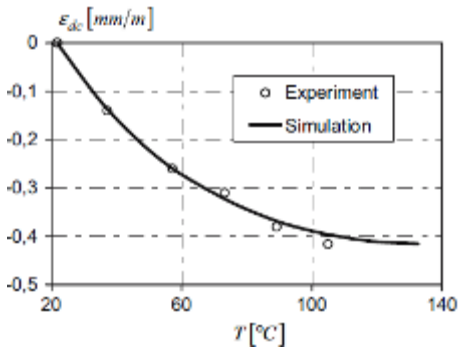

Figure 46 – Drying creep vs. temperature [5].

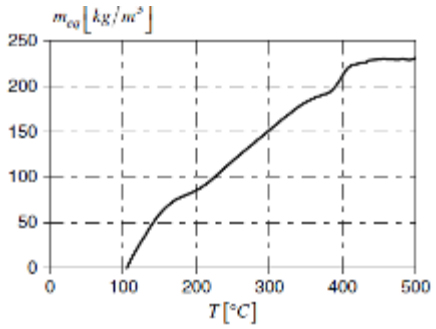

Figure 47 – Dehydration vs. temperature [5].

Transitional thermal creep, due to Thelandersson [68], is temperature-dependent, being proportional to the heating rate. It does not depend on the time of exposure to high temperature. It is developed in the first heating and does not occur again for the same maximum temperature level. Mindeguia et al [69] demonstrated that the heating scenario has a great influence on transient creep, which appeared only for temperatures higher than the maximum pre-heating one, as shown in Figure 48.

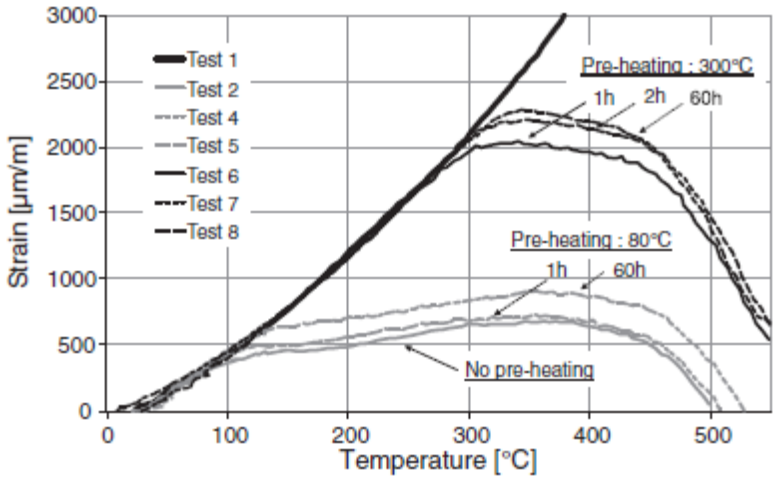

Figure 48 – Total strains of unloaded (test 1) and loaded specimens [69].

According to Sabeur et al [5], chemically bound water loss is the leading process of transitional thermal creep up to 400ºC. Figure 49 shows creep evolution with temperature.

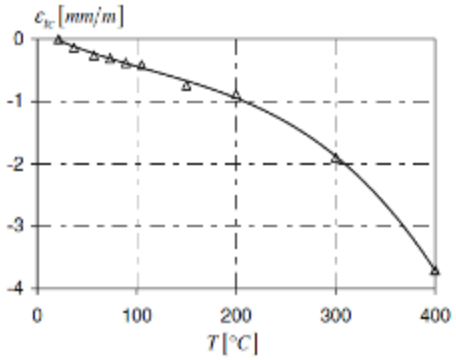

Figure 49 – LITS vs. temperature considering σ/f_c=-0.2 [5].

One important phenomenon observed by Thelandersson [68] is the path dependence (load path). As shown in Figure 50, concrete free thermal expansion is restrained when a uniaxial compressive load is applied to the specimen at the beginning of the heating process. On the contrary, if the same compressive load is applied after temperature stabilization, the sum of both mechanical and creep strains are not enough to completely counteract the free thermal strains, which indicates the important role played by the boundary conditions (thermal expansion restraint due to the applied load) to concrete total deformation.

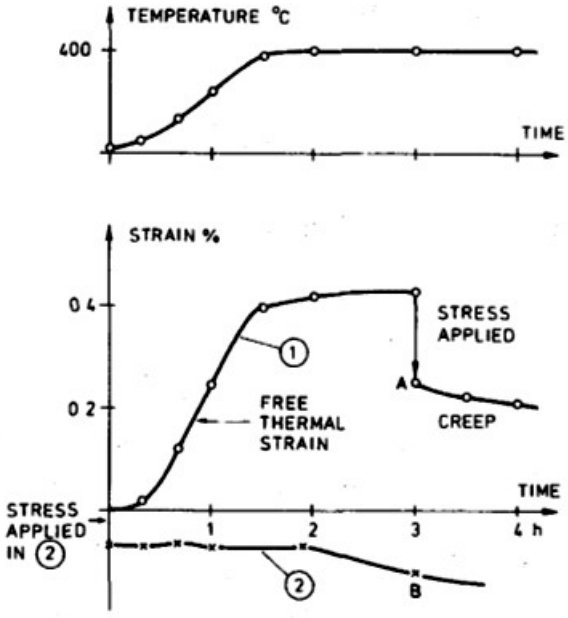

Figure 50 – Comparison between basic creep (curve 1) and transient creep (curve 2) [68].

Due to the complex concrete behavior and the coupling effects of the different strain components at high temperature, it is rather a very difficult task to uncouple the transient creep strains from other thermomechanical strain sources. For practical purposes, transient creep can be described accurately enough by concrete overall behavior. Hence, some authors (Khoury et al [11], Terro [53]) employ the term LITS (Load Induced Thermal Strains) to describe concrete stress-induced strains at high temperature, which includes transient creep and mechanical strains. LITS can be defined according to Figure 51

$$\varepsilon^c = \underbrace{\varepsilon^m_{ci}(t,t_0,T,\underline{\sigma}) + \varepsilon^T_c(T)}_{\text{rev.}} + \underbrace{\varepsilon^m_{c,irr}\left(t,T,\underline{\sigma},\frac{\partial T}{\partial t}\right) + \varepsilon^T_{c,irr}\left(T_{\max},\frac{\partial T}{\partial t}\right)}_{\text{irrev.}} + \underbrace{\varepsilon_{tc}\left(t,t_0,\frac{\partial T}{\partial t},T,w,\underline{\sigma}\right)}_{\substack{\text{transient creep}\\ \text{(irrev. strain due to sustained}\\ \text{load in preloaded specimens)}}} + \varepsilon_{sh}(t,T,RH)$$

$$\varepsilon_{LITS} = \varepsilon^c - \varepsilon^m_{ci}\left(t_0,T=20°C\right) - \underbrace{\varepsilon^T_c(T) - \varepsilon^T_{c,irr}\left(T_{\max},\frac{\partial T}{\partial t}\right)}_{\text{free thermal strain during 1st heating}}$$

$$\varepsilon_{LITS} \cong \varepsilon^m_{c,irr}\left(t,T,\underline{\sigma},\frac{\partial T}{\partial t}\right) + \varepsilon_{tc}(t,t_0,\frac{\partial T}{\partial t},T,w,\underline{\sigma}) + \Delta\varepsilon^m_{ci}\left(\underline{\sigma},t_0,T'=T-20°C\right) + \varepsilon_{sh}(t,T,RH)$$

$$\boxed{\varepsilon_{LITS} = \varepsilon^m_{c,irr}\left(t,T,\underline{\sigma},\frac{\partial T}{\partial t}\right) + \Delta\varepsilon^m_{ci}\left(\underline{\sigma},t_0,T'=T-20°C\right) + \varepsilon_{tc}\left(t,t_0,\frac{\partial T}{\partial t},T,w,\underline{\sigma}\right) + \varepsilon_{sh}(t,T,RH)}$$

where: ε^c = total strain; ε^m_{ci} = reversible mechanical strain; $\varepsilon^m_{c,irr}$ = irreversible mechanical strain; ε^T_c = reversible thermal strain; $\varepsilon^T_{c,irr}$ = irreversible thermal strain; ε_{tc} = transient creep; ε_{sh}=shrinkage.

Figure 51 – Total strain components and LITS definition.

According to Sabeur et al [5], LITS has an instantaneous component varying with temperature and fluid transportation (water and vapor) inside the specimen and other non-instantaneous and time-dependent under isothermal conditions, as shown in Figure 52. LITS is not strictly linearly related to the stress level, but can be assumed so for practical purposes. Hence, as stated by Anderberg and Thelandersson [47], LITS is proportional both to the heating rate and the stress level.

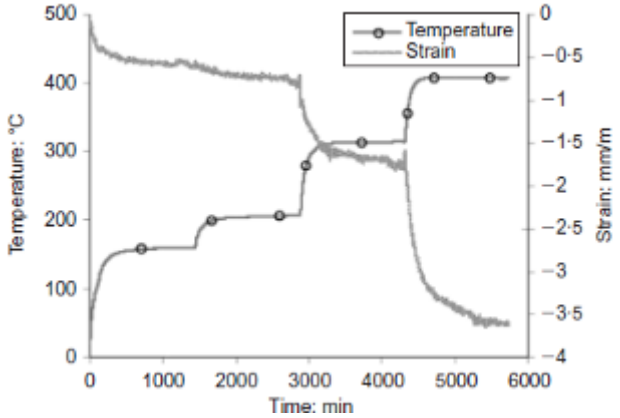

Figure 52 – LITS and temperature variation as function of time [5].

It is important to notice that the different methodologies adopted to describe creep at high temperature could lead to some confusion for those who are not familiarized with the subject. This lack of consistency in the literature is reported by Willan [62].

For clarity, this thesis adopts the term basic creep to refer to time-dependent creep that occurs at constant temperature, after all concrete physical-chemical reactions have taken place. Transient creep is defined as the quasi-instantaneous creep strain, which occurs during heating (transient phase) and is the sum of drying creep and ttc.

Immediately after the end of the heating process and before all concrete physical-chemical reactions ends, there is a coupling effect between basic creep and ttc.

LITS is the creep that occurs during concrete heating (transient creep) and includes also mechanical strains (irrecoverable strains and changes in the elastic strains due to temperature increase). It is defined experimentally by the difference between total strain, obtained from a test with a loaded specimen, and thermal strains, measured in an unloaded specimen, disregarding the initial elastic strain deformation. Transient creep is obtained by subtracting the mechanical strain sources from LITS.

Transient creep in compression is well known, with a relatively abundant literature. On the contrary, in tension, transient creep practically does not have any literature reference or test data available. Only one reference to this topic was found by the author in Mindeguia et al [69].

The lack of publications regarding transient creep in tension is probably due to the complexity of the test and the fact that the majority of the existing structures are composed of concrete and steel, and in a fire situation, concrete tensile stresses could be disregarded. As stated by Sadaoui et al [70], in simply supported beams, transient creep on the tensile surface has no significant effect since the structural response is governed by concrete cracking and steel yielding. Despite that, this is an important situation, especially in case of tunnel fires overlaid with FRC precast panels, which are subjected to tensile stresses and temperatures above 800ºC.

2.3.6 Creep in tension at room temperature

There are relatively few publications about creep in uniaxial tension compared to creep in uniaxial compression, which are focused in specific aspects, i.e., the role of creep in the durability of concrete cover layers; early age creep behavior of different cementitious materials (UHPCC, HSC, HPC); FRC material behavior at pre-peak and post-peak.

Creep in tension at room temperature seems to be governed by two mechanisms, as occurs with creep in compression, i.e, microcracking effect and stress-induced-shrinkage. However, according to Altoubat and Lange [71], fiber reinforcement reduces the effect of microcracking associated with drying. Thus, tensile creep is dominated by stress-induced-shrinkage, as shown in Figure 53. Moreover, fibers slightly reduce the contribution of stress-induced-shrinkage.

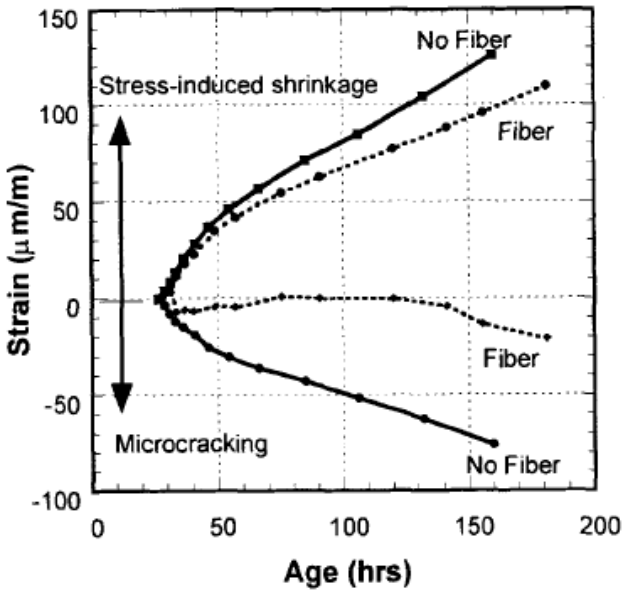

Figure 53 – Effects of tensile creep on concrete with and without fibers [71].

Altoubaut and Lange [71] propose a new methodology to separate the Picket effect of early age concrete submitted to tensile stresses. The experimental tests, shown in Figure 54, are divided in three parts, considering moist-cover (suppression of shrinkage and microcracking), sealed (uniform drying and suppression of microcracking) and unsealed specimens. The objective is to measure the effects of the stress-induced-shrinkage (difference between creep strains from moist-cover and sealed specimens) and microcracking, (obtained from the difference between total creep and basic creep strains). Basic creep is defined as the sum of the moist-cover specimen (aging component) and stress-induced-shrinkage (microprestress component).

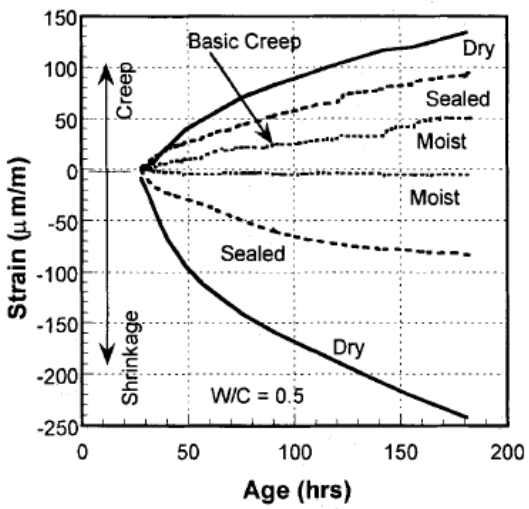

Figure 54 – Creep and shrinkage experimental results from [71].

Bissonnette et al [72] observed that tensile creep increases with the reduction of the cement paste content. The addition of fibers, on one hand, does not have much influence on drying shrinkage but, on the other hand, has a significant effect on the creep strains, which could lead to an increase of about 30% in the total creep in case

of hooked-end fibers. These results show the important role developed by the paste-aggregate and the fiber-paste interfacial areas to tensile creep behavior. Due to Bissonette et al [72], a non-negligible part of tensile creep strains could be located in these weaker and highly stressed areas, which are prone to cracking propagation.

Bissonnette et al [72] estimates that tensile creep is proportional to the applied stress up to $0.5 \cdot f_{ct}$. Basic creep, as observed in compressive creep, represents only a small percentage of the total creep.

Bissonnette et al [73] state that drying creep could be explained on the basis of a viscous-shear theory and microcracking effect. Viscous-shear is the result of the adsorbed water layers that are disturbed by both the applied load (absortion of water in the gel pores) and the evaporation process, which induce the flow of gel particles one against the other. The microcracking effect was observed indirectly by comparing the Secant Moduli of Elasticity of unsealed specimens and their companions. The results have shown a small reduction of the Elastic Modulus, thus indicating a small deterioration of the specimens.

Kovler [74] analyzed drying creep behavior under tension, showing that, at initial stage, shrinkage and drying creep do not necessarily coincide in sign with the load direction, leading to negative strain values as shown in Figure 55. In a later analysis, Kovler [75] attribute this fact (initial negative creep values and later positive) to swelling of sealed concrete which was captured in direct observations of alternative cycles of drying and sealing. Removing this effect from total creep strain, the resultant strain becomes positive with increasingly values in time.

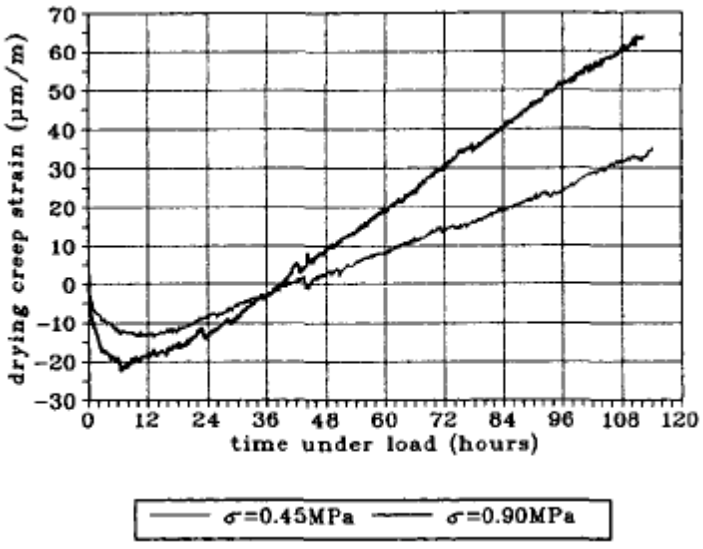

Figure 55 – Drying creep strains for different tensile stresses [74].

Reinhardt et al [76] achieved similar results of Kovler [74], but in contrast to Kovler [75], Reinhardt et al [76] explained the initial negative tensile drying creep as a result of increased concrete shrinkage. Reinhardt and Rinder [76] measured concrete humidity and found that around loaded specimens moisture loss was higher than unloaded specimens, thus concluding that shrinkage of loaded specimens is underestimated, otherwise the bump in the creep curves, shown in Figure 56, would not occur.

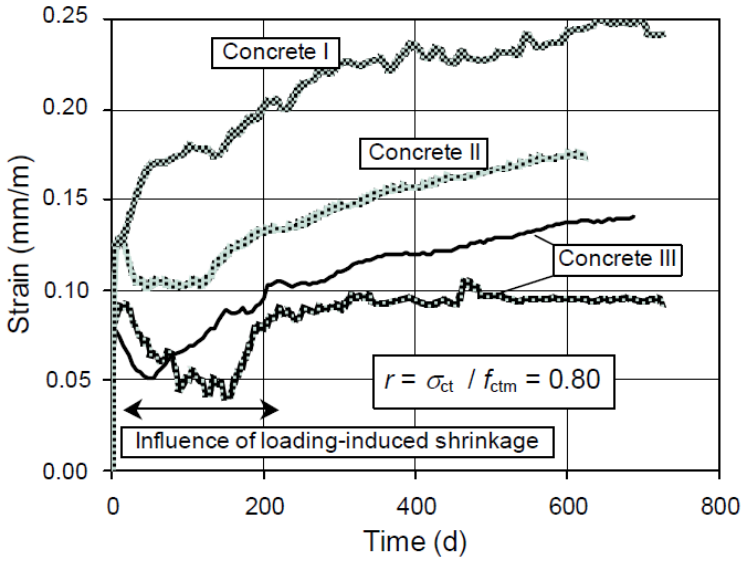

Figure 56 – Drying creep as function of time [76].

2.3 FRC Mechanical Characterization

During the last decades, a large effort was made in order to characterize fiber reinforced cementitious composites. The addition of fibers to concrete was a milestone for concrete structural design and construction. The main innovation introduced by this new cementitious composite is the ductile response obtained by the fiber pull-out effect of dispersed fibers immersed in concrete. In this system, the matrix is responsible to carry the compressive load and the fibers are responsible to carry the tensile forces alone or in companion with steel bars. On one hand, the development of new technologies of fabrication allowed the production of new types of materials (synthetic, steel, carbon), and, on the other hand, new research discoveries allowed the appearance of new types of fibers (short, long, hooked-end, straight, twisted). There were also improvements in the concrete matrix and in fibers pull-out resistance due to the addition of special binders (slurry infiltrated, fly ash, pozzolana), which improve concrete response (hardening or softening), enhances cracking control and increases fire resistance.

As a result, a completely new area of study was opened and new concrete applications were developed. FRC intrinsic properties, such as the reduction of concrete workability and fibers dispersion have for a long time studied. The problem of flowability affects structures with dense reinforcement, which creates an additional problem of preventing voids on concrete and guaranteeing the correct fibers orientation in the matrix in order to give the predicted design response. In the first case, the problem was solved with the development of new super and hyper-plasticizers, which ensure very low slump values. Also a new type of concrete (self-compacting concrete - SCC) was developed. The problem of fiber dispersion was partially solved with new casting techniques, which induce fiber orientation in predefined directions.

It is important to underline that FRC structural response (softening or hardening behavior) largely depends on the type and quantity of fibers and on the kind of test performed. For example, a material tested in uniaxial tension could develop a single crack (softening behavior in terms of σ_N-COD), while the same material in bending could be subjected to a multiple crack pattern, resulting in a hardening response in terms of load-deflection curve. In this way, Naaman et al [77] and di Prisco et al [78]

proposed to classify and explain FRC structural behavior according to different test methodologies and material response.

A very important issue of FRCC regards the procedures adopted in order to obtain the post-cracking material response. Different test procedures were developed to characterize the mechanical behavior of FRC, for example, round panel test ASTM-1150 [79], flexural tests on notched or unnotched beams (RILEM TC 162-TDF [80], UNI-11039 [81]), uniaxial direct and indirect tensile tests.

One important question regarding FRC is the material classification and characterization. This is a very important issue that is still open to debates. Different types of tests can be adopted, for example, uniaxial tensile tests, splitting (Brazilian) tests, wedge splitting tests (WST), bending tests, Barcelona test and indirect DEWS tests. Since concrete post-peak behavior is the most important characteristic of fiber reinforced cementitous composites, the experimental test should be able to capture fibers pull-out response. Notwithstanding, the tests are intrinsically very complex, as they should prevent spurious results coming from the monitoring devices and also have to minimize, as much as possible, the influence of external factors (boundary and load conditions, size effect) and internal factors (self-equilibrated stresses, premature cracking, stress redistribution and stress concentration).

Among them, the Brazilian test cannot be used to characterize FRC post-peak behavior. Only the tensile strength can be obtained by adopting some recommended test procedures as suggested by Denneman et al [82]. Other indirect tests, such as WST, BCN and flexural tests, have been largely used due to their simplicity in relation to UTT. One disadvantage of these methods is the need of a *posteriori* analysis. In order to overcome the problems related to UTT tests and, at the same time, obtain the tensile constitutive law directly without the need of an inverse analysis, DEWS [83] test was devised. In this case, a compressive load is applied at the top of the specimen and a double notch at the top and the bottom of the specimen guarantees an uncoupled stress field and a pure mode I fracture state on the ligament.

2.3.1 Tests for concrete mechanical characterization

The following tests are described in this section: flexural tests, Brazilian tests, wedge splitting test (WST), uniaxial tensile test (UTT), double edge wedge splitting (DEWS) test and Barcelona (BCN) test. It is important to underline that, independently of the test methodology, fiber orientation is of utmost importance and has a direct influence on the test results. For example, fiber distribution in small specimens is influenced by the wall effect, which limits fibers orientation. As a result, it is always better, for practical purposes, to respect as much as possible the onsite casting conditions. Moreover, the specimens used for the mechanical characterization should have the same fibers representative distribution on the section of interest, otherwise correction factors should be adopted. FRC design should take into account an orientation factor parameter, which can be disregarded only in case when a homogeneous and isotropic fiber distribution is found (Laranjeira et al, [84]).

The Wedge Splitting Test (WST) has been first proposed in Linsbauer et al [85] and developed further in Bruhwiler et al [86]. This method is relatively common for determination of the fracture properties of plain concrete. However, as stated by Logfren et al [87], in case of fiber reinforced concrete, a small number of references is found and no standard procedures exist regarding, for example, the size and shape of the specimen and the interpretation of the data. The deformations are measured in

terms of crack mouth opening displacement (CMOD). Since this is an indirect tensile test, a compressive load is applied, inducing a splitting force along the ligament. Due to the kinematics of the test, when localization occurs (crack initiation), there is a release of the potential energy from both the vertical applied load and the splitting force along the ligament. Using Finite Element Method (FEM), Logfren et al [87] calculated the contribution of the vertical load to the total work for two specimens with different sizes (small and large) and found that its contribution is about 5% to 7%. The main advantages of WST method, according to Logfren et al [87], are that the test allows the use of relatively small specimens in relation to bending tests and the utilization of relatively simpler testing equipment compared to uniaxial tensile tests (UTT). The drawbacks include the appearance of friction between the wedge and the roller bearings. There is also the need to make an inverse analysis to determine the tensile constitutive law. Experimental tests carried out by Logfren et al [87] on specimens with and without a guided notch have demonstrated that the guide notch prevented diffused cracking and appeared to increase the energy dissipated during the fracture process.

The uniaxial tensile test has the great advantage of not requiring an inverse analysis. However, the test results are affected by specimen-machine interactions. For example, fixed-end platens generate additional forces (bending moments) due to the kinematic constrains, while free-end platens allow the specimen to rotate along the vertical axis. In the former case, due to the imposed constrains in the boundary conditions, there is a higher flexural stiffness in relation to the latter case, which retards the crack propagation. A stiffer system has the tendency to deviate the cracking front from the ligament in the case of notched specimens, generating a bump in the softening branch of the stress vs. COD curve, which means that there is a higher fracture energy stored in the system in relation to free-end tensile tests. Moreover, experimental tests carried out by di Prisco et al [88] have shown that tests with free-end platens results in a slightly weaker tensile strength and a higher scattering compared to tests with fixed-end platens. Another disadvantage of uniaxial tensile tests is related to the complexity of the tests. Qian et al [89] pointed out that the specimen is sensitive to stress concentrations that arouse due to test setup misalignment. Moreover, special fixtures for the specimen ends are needed.

The Double Edge Wedge Splitting (DEWS) test is an indirect tensile test, as WST, in which a compressive load is applied to induce the development of splitting forces on the ligament. However, unlike WST, DEWS methodology does not need an inverse analysis to determine the tensile stress vs. COD curve and this is the main advantage of this type of test. In this case, a double notch both at the top and at the bottom of the specimen is created, generating a pure mode I fracture behavior and allowing the complete uncoupling of the stress field, which results in the development of an arch of compression and the concentration of tensile stresses on the ligament. It is important to underline that a crack orientation can be pre-determined by choosing the notch orientation, allowing the analysis of concrete fracture properties in any desired direction. This is particularly important for fiber reinforced cementitious composites, in which fibers orientation is of utmost importance to concrete post-cracking behavior. However, the specimen-machine interaction plays an important role. In this case, the specimen is free to develop in- and out-of-plane rotations, which results in a lower torsional stiffness in relation to UTT. Moreover, there is the effect of friction on the point of the application of the load.

The splitting (Brazilian) test is very effective to determine concrete tensile strength. In addition, the test methodology is much simpler in relation to UTT. However, the test is restricted to the elastic range. After cracking, the test cannot provide any kind of

information about concrete residual properties (Denneman et al [82]). It can, at most, be used to establish the tensile strength, as described in Denneman et al [82]. The limitations are related to the size effect and the boundary conditions, which have a direct effect on the crack propagation. After the peak strength, a secondary cracking mechanism outside the ligament appears, which is not correlated to the linear elastic stress distribution and is the result of stress redistributions after cracking. As a result, new highly stressed areas are formed on the top and on the sides of the specimen, accompanied by a relaxation of the stresses along the ligament (loading axis) (Denneman et al [82]).

The bending test was introduced in order to overcome the problems related to UTT experimental procedures. The test can be carried out adopting one (3PB) or two (4PB) point-loads in notched or unnotched (structural) beams. RILEM [80] recommends 3PB tests on notched beams, while UNI 11039 [81] adopts 4PB tests on notched beams. One of the main differences between the two types of test refers to the displacement measurements. In 4PB tests, crack tip opening displacement (CTOD) values are monitored, while in 3PB tests, the crack mouth opening displacement (CMOD) is measured. 3PB tests tend to give higher values in relation to 4PB tests due to the load scheme, span and notch dimensions (di Prisco et al [78]). Numerical analyses carried out by Ferrara et al [90] demonstrated that the concentrated load on the ligament in 3PB tests leads to a larger internal lever arm and a slightly increase in the resultants of the tensile and compressive stresses.

Montaignac et al [91] compared the results of inverse analyses on notched beams and on round panel tests. In the former case, the results were more accurate to identify FRC post-cracking behavior, although there is a tendency of an overestimation of the values for large crack widths. In the latter case, the inverse analyses had a tendency to underestimate the post-cracking strength. And the first post-peak strength, immediately after concrete cracking, was not captured due to the structural redundancy. In this case, three cracks have to be formed in order to fully activate fibers pull-out mechanism.

Among the differences between UTT and flexural tests, it is important to mention that, while, in the latter case, the entire specimen is under tension and the tensile strength is related to the maximum tensile strength capacity, in the bending test, the tensile flexural strength refers to the tensile capacity of the lowest cross-sectional stretched portion. The main disadvantage of this test is that it requires an inverse analysis. However, despite other indirect methods such as WST, a comprehensive study has been carried out during the last decades in order to simplify the analysis procedures, which culminated in the publication of simplified methods to determine FRC tensile ductile behavior, as described in RILEM TC 162-TDF [80] and *fib* Model Code 2010 [78].

Barcelona (BCN) test is an indirect tensile test based on the double punching test (Carmona et al, [92]). The test is carried out on cylindrical specimens with an aspect ratio (diameter/height) of 1 and subjected to a compressive load imposed by steel wedges centered on the top and bottom faces of the sample. The displacements are measured in terms of total circumferential opening displacements (TCOD). The so-called generalized Barcelona test [92] replaces the TCOD by axial displacement measurements between the two steel wedges. In this case, the peak and residual strengths are calculated according to UNE 83-515 [93]. The main advantages of this test includes the relatively small specimens adopted and the possibility to use

conventional testing machines. The disadvantage is that the test results do not provide a straightforward solution and a quantitative interpretation of the data is needed.

Bruhwiler et al [86] experimental results from WST, UTT and 3PB tests have shown that the fracture energy (G_f) gives identical values in all three tests if the ligament length and the concrete type are the same.

2.3.2 Inverse analyses techniques

Two main procedures are generally adopted to determine the tensile post-peak curve in terms of σ-ε or σ-COD. The most accurate method and, at the same time, more complex one, applies a step-by-step iterative solution to track FRC curve adopting a piecewise function, in which the load *vs.* deflection curve from bending tests is followed point-by-point and the error between the computed and the corresponding load is minimized by weighting functions (optimization process). The other method simplifies this procedure by previously determining the shape of the post-peak curve (generally bi-linear or tri-linear) and determining fracture parameters for the chosen solution. The prediction of the tensile constitutive law is based on a sectional analysis (cross-section equilibrium), assuming the Bernoulli law (plane sections remain plane), force equilibrium and compatibility between strains and displacements.

Many authors have proposed different methodologies based on the two main procedures described above. For example, Qian and Li [89] developed simple linear equations based on master curves. But, this model can be used only for the original specified FRC geometry and loading conditions. For other types of concrete, new master curves and equations should be created. Mobasher et al [94] propose a trilinear σ-ε constitutive model based on plane section approach with cross-sectional equilibrium and linear stress-strain distribution. The model is based on load-deflection data from bending tests and on the moment-curvature response. Displacements (stress-crack) and deformations (stress-strain) are obtained through the average response within the cracking zone.

Sousa et al [95] describe an inverse analysis procedure implemented in a software program called FIT3PB which allows the implementation of different types of σ-w curves (bilinear, trilinear, slope constant and Hordijk's model). The structural analysis is based on the cracked hinge model and includes weighting functions and an optimization process for a better correlation between three-point bending test results (P-CMOD) and the uniaxial tensile constitutive law (σ-w).

All of these methods have the great disadvantage of the necessity, in a greater or lesser extent, of the development of numerical techniques to find the solution, which restricts its wide application. In general, these methods require relatively complicated calculations. In order to overcome this problem, RILEM TC 162-TDF [80] defined simple procedures to calculate concrete fracture properties, based on a linear residual tensile stress evolution and fixed conversion factors obtained from flexural cross-sectional equilibrium and a simplified linear-perfectly plastic tensile stress distribution. However, in some cases, this model could overestimate the ductility in bending (di Prisco et al [88]; Godde et al, [96]). Moreover, the constitutive law is described in terms of σ-ε curve and cannot be obtained directly from bending tests. According to Montaignac et al [91], there is also a problem with size effect, since the increase in beam's depth increases the curvature and reduces the maximum strain. Godde et al

[96] propose new variable conversion factors, based on the compressive strength and the residual tensile flexural strength, obtained through tabulated diagrams.

A new revised model of RILEM TC 162-TDF [80] was proposed in *fib* Model Code 2010 [97] taking into account σ-COD curve rather than σ-ε. σ-COD curves are independent of the structural member size, representing the actual behavior of the specimen (Montaignac et al, [91]). The basic assumptions adopted in RILEM TC 162-TDF [80] were considered in the new *fib* Model Code 2010 [78], which includes the structural characteristic length (l_{cs}) governing the fracture process zone, a linear softening curve and a simplified elastic-perfectly plastic tensile stress distribution. In the latter case, compressive stresses after concrete cracking are disregarded and tensile stresses are averaged through the entire cross-section (stress block). The equilibrium, in terms of bending moment-curvature, is obtained through a kinematic model that considers a theoretical hinge on the top of the beam, where the curvature is delimited.

The characteristic length was originally defined in RILEM TC 162-TDF [80] as two times the crack length and in the Model Code 2010 [78] it is defined as the beam's depth for localized cracks (softening behavior) and as the distance between the cracks for a multi-cracking pattern (strain hardening). It is important noting that the characteristic length is influenced by several parameters, e.g., the type and volume of fibers, matrix strength, cross-section geometry, load level and the presence or not of steel bars. In order to overcome some of these problems, the Italian guideline [81] uses the concept of multiple characteristic lengths in the same cross-section, according to the fracture phase (microcracking, localization and macrocracking).

Recently, Amin et al [98] have proposed a bilinear post-peak constitutive model (σ-w) based on the rigid body rotation centered on the crack tip point and on the cross-sectional equilibrium taking into account the internal forces (both compressive and tensile stresses) and the neutral axis position. The displacements are defined in terms of mean COD values and the crack width is directly proportional to the distance from the neutral axis. For the first part of the curve, a transition function is assumed to take into account the progressive fibers activation.

2.3.3 FRC characteristic values

Fiber reinforced cementitious composites have distinct characteristics in relation to plain concrete and traditional reinforcement. While steel bar reinforcement in plain concrete is localized, fibers have a smeared distribution in the bulk concrete, which give fibers the pull-out resistance and concrete ductile behavior. Fibers can be oriented adopting special casting procedures, but their intrinsic random distribution, defined in terms of the orientation factor, cannot be eliminated. As a result, the standard deviation found in FRC specimens is always higher compared to plain concrete. Moreover, different amounts and types of fibers (straight, long, short, hooked-end, twisted) can give different responses (hardening or softening) and different peak strength values. Hence, contrary to plain concrete, in which the mean strength and the standard deviation are previously known, in case of FRC, due to the huge variability and also due to the fact that it is a new material, it is not possible to know in advance the coefficient of variation (V_x) for a specific type of concrete. This is an additional setback for the material characterization, since a minimum number of tests should be carried out in order to determine the characteristic value for a specified FRC.

The characteristic value (X_k), according to Eurocode [99], can be obtained with Eq. 20, where X_m is the average value, V_x is the coefficient of variation and K_m is a parameter

that depends on the number of specimens tested, the distribution adopted and by the a-priori knowledge of V_x.

$$X_k = X_m \cdot (1 - K_m \cdot V_x) \tag{20}$$

The coefficient of variation is defined as $V_x = \sigma_x / X_m$, where σ_x is the standard deviation.

Experimental tests from Logfren et al [87] have demonstrated that the coefficient of variation of uniaxial tensile tests ranged between 10% to 50%, with a tendency to have half of the expected number of fibers on the fracture area. In case of 3PB tests, the CoV varied up to 38% and, as the fiber volume increased, CoV value decreased. For WST, the maximum CoV was equal to 26%.

According to Laranjeira et al [84], a CoV larger than 20% is commonly observed in flexural tests. Carmona et al [92] found values of CoV for the residual strength reaching almost 30% in Barcelona tests. Finally, Soetens et al [100] CoV values of f_{R1} (SLS, CMOD=0.5 mm) and f_{R3} (ULS, CMOD=2.5 mm) from 3PB tests ranged between 10% to 33%.

2.3.4 FRC constitutive law according to fib Model Code 2010 [78]

The steel fiber reinforced cementitious material investigated in this thesis was classified according to *fib* Model Code 2010 [101], which assumes FRC as a homogeneous and isotropic material when fiber efficiency factor (k), which considers fibers distribution and orientation, is taken equal to 1. FRC classification takes into account the residual post-cracking tensile strength, determined from bending tests on notched beams, which are carried out according to standard procedures.

The two points that characterize the material class refers respectively to the serviceability limit (SLS; CMOD=0.5 mm; f_{r1k}) and the ultimate limit (ULS; CMOD=2.5 mm; f_{r3k}) states. The first value defines concrete characteristic strength class (from 1 MPa to 8 MPa), while a letter from “a” to “e” indicates the ratio f_{R3k}/f_{R1k} (hardening or softening behavior). An example of the material classification, according to Model Code 2010 [101], is shown in Figure 57.

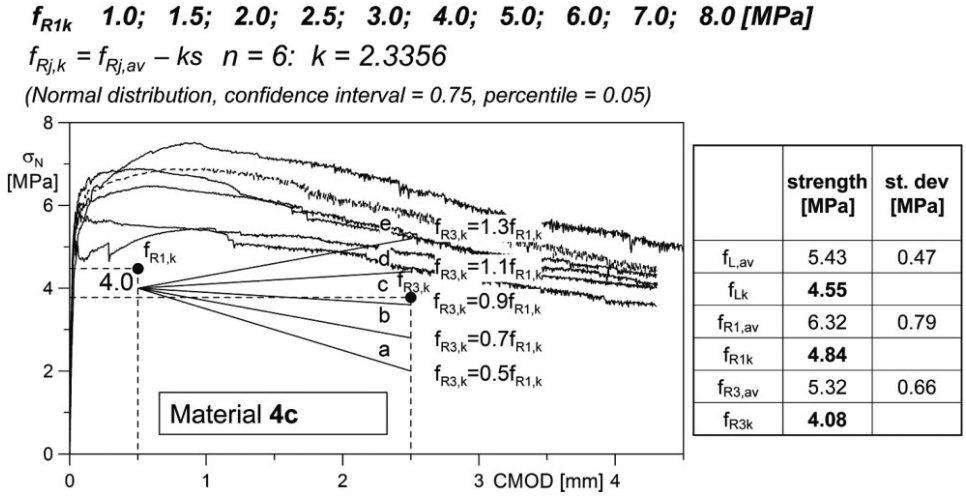

Figure 57 – Material classification according to fib Model Code 2010 [101].

FRC constitutive law can be defined according to *fib* Model Code 2010 [101], [78] (Eq. 21 and Eq. 22), which is based on the residual strengths at SLS and ULS obtained from the material classification.

$$f_{Fts} = 0.45 \cdot f_{r1} \quad (w = 0) \tag{21}$$

$$f_{Ftu} = 0.50 \cdot f_{r3} - 0.2 \cdot f_{r1} \quad (w = 2.50) \tag{22}$$

(This page intentionally left blank)

CHAPTER 3

PhD program overview

The thesis has the objective to analyze SFRC creep at high temperature both in compression and tension. In the latter case, one of the main problems regards the test setup, which requires special techniques to measure concrete displacements, especially during the post-cracking regime. Mindeguia et al [69] have successfully tested plain concrete specimens before cracking by means of uniaxial direct tensile tests. However, after cracking, no experimental test has been performed yet. In order to test FRC both before and after cracking, a new test setup was devised taking advantage of DEWS methodology. A preliminary assessment of FRC transient creep can be found in Askin and Sigin [102] master dissertation. In this study, numerical analyses were developed in order to investigate the effectiveness of DEWS tests to measure transient creep, taking into account different heating rates, load levels and specimen geometries.

The analysis of creep at high temperature in compression aims to propose a new LITS-semi-empirical model that could be adopted for design engineers to have a straightforward and preliminary prediction of LITS behavior in concrete structures subjected to a sustained uniaxial compressive load. In order to do so, the thesis is divided in three parts, focusing on the formulation of a semi-empirical model, a numerical check of the basic assumptions used in the proposed model and experimental tests on LITS to analyze experimentally the most interesting aspects that could be related to fiber contribution which are completely disregarded in the model.

In Chapter 4 experimental results from other authors are gathered in order to allow a better understanding of LITS behavior. It is worth mentioning that, during the recent years, new creep tests at high temperature with different concrete types (NSC, HSC, UHPC, FRC) and different ages (from 1 to 5 years) were carried out by distinct researchers, which allowed a better understanding of LITS phenomenon. From the experimental results obtained from others, a more viable semi-empirical model in relation to the available ones was developed by recognizing concrete as a heterogeneous material. The model is described in terms of thermomechanical (aggregate degradation and thermal expansion restraint) and thermochemical (matrix softening behavior) strains. In this way, the role played by the aggregates (increase of LITS) is recognized in the model. The effect of the age of loading is also discussed and an aged-adjusted parameter is proposed based on the best fitting of the experimental results from the literature considering 1- to 5-year-old concrete specimens and also with SFRC with 11.5-years-old experimental results carried out during the thesis. The proposed semi-empirical model is compared both with experimental results and transient creep models from other authors.

After the development of the semi-empirical model, a 2D three-phase numerical mesoscopic modeling was carried out by means of the finite element software Abaqus. The objective is to analyze the different concrete phases (aggregates and matrix) contribution to LITS. As a result, LITS is uncoupled into three components: the contribution of the aggregate geomechanical properties decay with the temperature increase ($LITS_{agg}$); the contribution of matrix thermomechanical properties evolution as function of temperature ($LITS_{mat}$); and the effect of the boundary conditions ($LITS_{bc}$) due to the thermal expansion restraint imposed on the specimen by the compressive sustained load during heating. From the numerical results, an equation that takes into account the effect of the boundary conditions ($LITS_{bc}$) is derived.

The proposed semi-empirical model was also validated by means of experimental results carried out during the thesis in 10-year-old steel fiber-reinforced concrete. The same material with 1-year-old was analyzed during Colombo [6] PhD thesis. The mechanical characterization was performed by means of compressive tests, ultrasonic wave tests, indirect tensile DEWS tests and three- and four-point bending tests. In order to verify the long-term aging effects on SFRC, the results were compared with the ones obtained by Colombo [6]. The experimental investigation on the 10-year-old material is shown in Table 2.

Table 2 – Experimental tests on the mechanical characterization of 10-year-old SFRC.

type of test	n° of tests
uniaxial compressive	1
4-point bending	9
3-point bending	9
uniaxial indirect tensile DEWS	8

After the mechanical characterization, a preliminary creep test at room temperature with a duration of three days was carried out. The experimental result was compared with the Kelvin-Voigt approach and also with Eurocode 2 [103] and Model-Code 2010.

At high temperature, creep tests had the objective to analyze LITS in preloaded specimens (the load was applied before the temperature increase), basic creep in preheated specimens (the load was applied after three hours of the temperature stabilization) and the path dependence. The tests were performed taking into account two load paths (preloaded and pre-heated specimens), two load levels ($0.2 \cdot f_{c,28}(T)$ and $0.4 \cdot f_{c,28}(T)$) and two different maximum temperatures (200ºC and 400ºC). In this way, one can expect that concrete remains in the viscoelastic regime, since the maximum load applied was below $0.4 \cdot f_c(T)$ ($0.4 \cdot f_{c,28}(T) \approx 0.3 \cdot f_c(T)$), from which an increasingly non-linearity occurs due to the progressively damage (irrecoverable strain) produced by microcracking growth in the bulk matrix.

A total of 16 tests were performed according to Table 3.

Table 3 – Description of the tests procedure at high temperature

test 1 – preloaded (x2)		test 2 – preloaded (x2)		test 3 – pre-heated (x2)		test 4 – pre-heated (x2)	
temp.	load level	temp.	load level	temp.	load level	temp.	load level
200°C	$0.2 \cdot f_{c,28}(T)$ ≈13 MPa	400°C	$0.2 \cdot f_{c,28}(T)$ ≈12 MPa	200°C	$0.2 \cdot f_{c,28}(T)$ ≈13 MPa	400°C	$0.2 \cdot f_{c,28}(T)$ ≈12 MPa
	$0.4 \cdot f_{c,28}(T)$ ≈26 MPa		$0.4 \cdot f_{c,28}(T)$ ≈24 MPa		$0.4 \cdot f_{c,28}(T)$ ≈26 MPa		$0.4 \cdot f_{c,28}(T)$ ≈24 MPa

A comparison between the experimental results in preloaded specimens and the proposed LITS semi-empirical model was carried out. From the creep values in pre-heated specimens, it was noticed that, as the temperature rises, the time of development of primary creep is reduced and creep values are increased. Based on these results, a prediction of basic creep was made by introducing in the Kelvin-Voigt model a temperature-adjusted parameter to take into account the effect of high temperature on creep. A prediction of creep in preloaded specimens during heating and at constant temperature was performed by introducing in the adapted Kelvin-Voigt model the effect of the boundary condition defined in terms of $LITS_{bc}$ as described in Chapter 6.

3.1 Preliminary assessment of transient creep in tension

An experimental test at room temperature considering a cylindrical specimen with 75 x 150 mm was also carried out as shown in Figure 58. In this particular case, after an initial crack propagation through the ligament from the top to the bottom surface, at a certain point, the crack deviates, continuing to propagate in the horizontal direction. One possible explanation is that the cylindrical specimen has a higher torsional stiffness in relation to the prismatic one. In the former case, the out-of-plane rotations are restrained, while, in the latter case, the specimen is free to develop in- and out-of-plane rotations. It is worth mentioning that the V/S (volume to surface) ratio is higher in cylindrical samples. In the experimental test, the height of the cylindrical specimen tested was twice the diameter. As a result, due to the kinematics of the test, which leads to an angular deformation and in-plane rotations during crack propagation from the top to the bottom surface, the specimen is more prone to the appearance of additional forces in form of bending moment. These two phenomena, associated with an existing flaw in the bulk concrete outside the ligament surface, could be responsible for this type of failure. As a result, more analyses should be carried out before adopting DEWS methodology in transient creep tests.

Figure 58 –Indirect tensile DEWS test in cylindrical specimen.

(This page intentionally left blank)

CHAPTER 4

LITS semi-empirical model formulation

In the literature, there are many empirical models (Diederichs [104], Terro [53], Schneider [42], Anderberg and Thelandersson [47]) that aim to describe the behavior of concrete transient creep in compression. However, the main problem is that all of them start from a limited database, usually containing few experimental tests, and, therefore, the formula and the parameters derived from the data are restricted to that small amount of samples. According to Terro [105], transient creep has not yet been thoroughly investigated: the limited database leads to mathematical model assumptions based on interpolations or extrapolations from the existing data.

Only recently an increase in the number of publications of transient creep was observed, with new experimental tests taking into account different types of concrete (HPC, UHPC, SCC, FRC). Until the last decade, only few researchers, such as Schneider, Andenberg, Thelandersson and Khoury, investigated this problem, having developed extensive experimental campaigns with important findings, such as the path dependence (Andenberg and Thelandersson, [47]) and the LITS master curve (Khoury et al, [106]).

With the increase in the number of publications and experimental test results available, it is possible to compile all these different tests into a single database, allowing the researcher a broader analysis of the transient creep phenomenon. Having that in mind, a total of 76 different transient creep tests were catalogued from Khoury [58], Andenberg and Thelandersson [47], Nielsen [107], Huismann et al [108], Tao et al [109], Mindeguia et al [110], Wu et al [111], Hager [112] and Didererichs et al [113]. The database includes several types of concrete (NSC, HSC, SCC, UHPC) with different ages (from 3 months to 5 years), moisture conditions (saturated, dried, room conditions), aggregate types (siliceous, calcareous, basalt and recycled), heating rates and load levels. A twofold objective was pursued: compare the different experimental results in order to find a correlation for transient creep evolution in different types of concrete and, based on that, derive a semi-empirical model that better fits all the test data. In order to accomplish that, first it is important to describe all the theoretical framework which underpins the mathematical formulations.

4.1 Theoretical formulations of transient creep

In the 1970's, Andenberg and Thelandersson [47] developed an extensive experimental campaign with different load paths, stress levels, heating rates and moisture conditions. Based on the test results, Andenberg and Thelandersson [47]

proposed a transient creep law which is dependent both on the temperature and on the concrete coefficient of thermal expansion.

In the 1980's, Khoury et al [106], after a broad experimental campaign with different concrete types, had defined the concept of LITS master curve which is, on one hand, independent of the aggregate type and the concrete age (after a two-month aged specimen), and, on the other hand, is linearly dependent of the applied load and the heating rate. According to Khoury et al [106] and Cheyrezy et al [114], LITS trend is similar for NSC, HSC and HPC.

In the early 1990's, Terro [105] used Khoury et al [106] test data to obtain an empirical formula based on a fourth order polynomial equation, which is directly related to the temperature and linearly dependent on the stress level and the volume of the aggregates.

Besides that, some important conclusions were attained by different researches which are summarized below.

Sabeur et al [5] affirms that dehydration is the driving process of the transient creep up to 400°C and Sabeur and Meftah [3] divided it into two components, i.e., drying creep and dehydration creep.

The addition of PP fibers (Wu et al [111], Huismann et al [108], Tao et al [109]) increase transient creep strains due to the microcracking effect.

Mindeguia et al [110] measured radial displacements and concluded that creep practically is not activated in this direction.

Gillen [115] reported that moisture conditions strongly affect transient creep strains at temperatures around 100°C.

Khoury [58] states that LITS is absent in concrete structures during a second heating cycle, up to the maximum temperature reached before.

According to Mindeguia et al [69], transient creep appears only for temperatures higher than the maximum pre-heating one. In agreement with this, Terro [105] affirms that ttc can be even eliminated by preheating.

According to Khoury [58], LITS is seated on the cement paste and, thus, is insensitive to the aggregate type up to 450°C. In addition, thermal stability depends specifically on the aggregate type. In agreement with that, Mindeguia et al [69] state that transient creep is influenced by the nature of the aggregate above 300°C.

Khoury [116] observed no significant sign of LITS or shrinkage during concrete cooling. The applied load restrains the crack-induced and other strain expansion components (Khoury, [116]).

Tao et al [109] affirms that the two most important mechanisms of transient creep activation are the CSH dehydration and the decomposition of portlandite.

Sabeur and Colina [117] found that transient creep is inversely proportional to the w/c ratio, which is directly related to concrete permeability.

Experimental tests up to 220°C from Sabeur and Colina [117] show that OC (ordinary concrete) had the smallest creep strains, followed by HSC and HPC, which developed the highest values.

Sabeur and Colina [117] observed the separation of the cement paste from the aggregates due to the development of microcracks during the cooling phase. The authors attributed this fact to the absence of transient creep strain during cooling.

Concrete complex thermo-chemo-mechanical behavior and its influence to LITS are summarized in Table 4.

Table 4 – Relationship between concrete thermomechanical behavior and LITS

Agent	Influence of temperature	Effects on concrete	LITS behavior
Aggregate volume	Thermal expansion	Thermal mismatch leading to diffused microcracks, nucleation and coalesce of cracks	Directly proportional to LITS (thermomechanical damage)
Cement paste	CSH and portlandite dehydration	Microprestress relaxation and reduction of concrete stiffness	Directly proportional to LITS (thermochemical damage)
Heating rate	Concrete thermal differentials	Development of eigenstresses inducing concrete microcracking	Inversely proportional to LITS
Compressive stress	Thermal expansion restraint	Delay of crack formation and crack opening restraint	Directly proportional to LITS
PP fibers	Fibers melting and burning	Increase of concrete porosity and microcracking	Directly proportional to LITS (thermomechanical damage)
Moisture	Concrete drying. Inversely proportional to FTS	Directly related to concrete porosity	Inversely proportional to LITS

It is worth mentioning that the heating rate is inversely proportional to transient creep. Lower heating rates reduce the thermal stresses (eigenstresses) and, as a result, concrete thermal damage. Besides, a larger time of exposure to fire increases concrete dehydration due to the reduction of the thermal gradient in the bulk concrete, increasing the transient creep strains. However, between 1°C/min to 5 °C/min, a small variation of transient creep values is observed, as stated by Andenberg and Thelandersson [47].

Concrete increased ductility can be attributed to the cement paste dehydration, which leads to CSH bond layers breakage and, under load, results in a structural readjustment within the paste in order to achieve a lower overall energy level (microprestress relaxation as described in Bazant et al, [2]).

4.2 Comparison among the empirical transient creep models

Despite concrete complex behavior, all empirical formulations reduce the problem to only two or three variables, which includes the temperature, the stress level and the moisture condition (Schneider, [42]) or the aggregate volume (Terro, [105]). This simplification is due to the fact that the test data used in the analyses do not cover the great variability of concrete mixtures. In the following, four transient creep models (Terro, [105], Schneider [42], Tao [109], Anderberg and Thelandersson [47]) are described and compared as follows:

a) Anderberg and Thelandersson [47] transient creep model is shown in Eq. 23.

$$\varepsilon_{tr} = -k_2 \times \left(\frac{\sigma}{f'_c}\right) \times \varepsilon_{th} \;\; if \; T \leq 550°C \tag{23}$$

where: σ= applied stress; f'_c= concrete compressive strength at room temperature; t= time in minutes; k_2= dimensionless constant varying between 1.8 and 2.35.

b) Schneider [42] includes also the moisture content in the formulation, as described in Eq. 24.

$$\varepsilon_{tr} = \varphi \times \frac{\sigma}{Eci_T} \tag{24}$$

$$\varphi = C_1 \times tanh[\gamma_w \times (T-20)] + C_2 \times tanh[\gamma_0 \times (T - T_g)] + C_3 \tag{25}$$

where: $\varphi(w,T)$= empirical function as defined in Eq. 25; Eci_T= Modulus of Elasticity at high temperature; $\gamma_w = (0.3 \times w^{0.5} + 2.2) \times 10^{-3}$; $w =$ water to cement ratio; $C_1, C_2, C_3, T_g, \gamma_0$= constants dependent on the type of concrete. For siliceous concrete, the constants are respectively equal to 2.50, 0.70, 0.70, 800, 0.0075.

c) Tao [109] includes one parameter to take into account NSC and HSC materials. The empirical model is the simplest one, being just in function of the temperature and the applied load as shown in Eq. 26.

$$\varepsilon_{tr} = c \cdot \left(\frac{\sigma}{f'_c}\right) \times A(T) \tag{26}$$

$$A(T) = (-2.64 \times 10^{-7} \times T^4 + 2.93 \times 10^{-4} \times T^3 - 9.45 \times 10^{-2} \times T^2 - 5.79 \times T + 270) \times 10^{-6}$$

where: $c =$ empirical function equal to 1.55 for HSC and 1.0 for NSC.

d) Terro in [53] and [105] defines creep effects at high temperature as LITS (Load Induced Thermal Strain), assuming a linear relationship between LITS and the compressive strength at room temperature, as shown in Eq. 27**.** The formula is defined for normalweight concrete with 65% of aggregate by volume. For other aggregate mixture conditions, a linear relationship is adopted as shown in Eq. 30.

$$LITS(T,\sigma) = LITS(T, 0.3f'_c) \times \left(0.0032 + 3.226 \times \frac{\sigma}{f'_c}\right) \tag{27}$$

$$LITS(T, 0.3f'_c) = A_0 + A_1 \times T + A_2 \times T^2 + A_3 \times T^3 + A_4 \times T^4 \tag{28}$$

$$LITS(T, 0.3f'_c) = 1.48 \times (B_0 + B_1 \times T + B_2 \times T^2 + B_3 \times T^3 + B_4 \times T^4 + B_5 \times T^5) \tag{29}$$

$$LITS(T,\sigma) = LITS(T, 65\%) \times \left(3.05 - 3.15 \times \frac{V_a}{100}\right) \tag{30}$$

where: $A_0, A_1, A_2, A_3, A_4$are empirical coefficients for normalweight concrete, respectively equal to: -43.87; 2.73; $6.35 \cdot 10^{-2}$; $-2.19 \cdot 10^{-4}$; $2.77 \cdot 10^{-7}$; $B_0, B_1, B_2, B_3, B_4, B_5$ are empirical coefficients for Thames gravel aggregate type, respectively equal to: -1098.50; 39.21; -0.43; $-2.44 \cdot 10^{-3}$; $-6.27 \cdot 10^{-6}$; $5.95 \cdot 10^{-9}$.

From the comparison among the semi-empirical models shown in Figure 59, it is possible to observe that Terro [105] LITS model constitutes the upper bound limit, since the transient creep deformation includes implicitly changes in the elastic strains due to the temperature increase, together with irreversible mechanical strains. The following parameters were adopted herein: σ/f_c=0.3; E_c=45 GPa; f_c=75 MPa; V_{aggr}/V_c=65%.

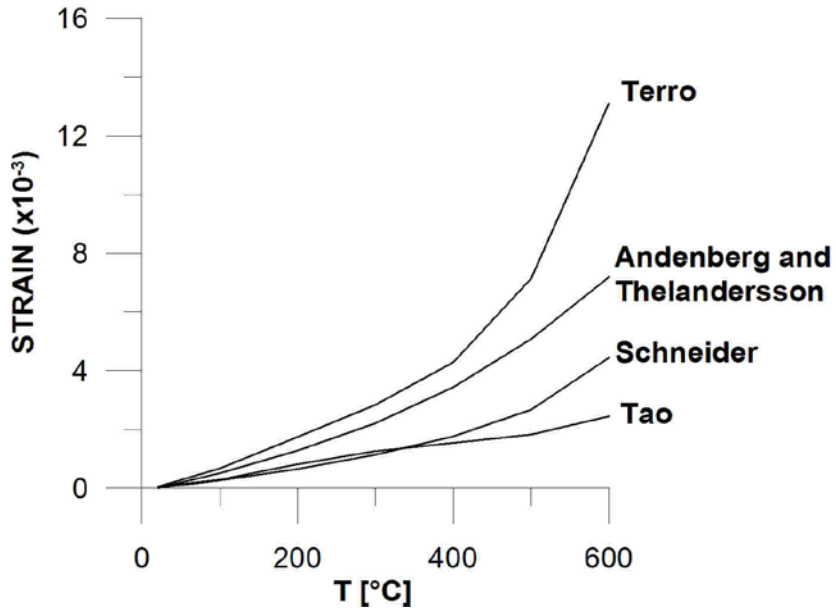

Figure 59 – Comparison of different transient creep models in compression for $0.30 \cdot f_c$.

4.3 LITS model formulation

4.3.1 Transient creep thermo-chemo-mechanical behavior

In order to describe the different LITS sources, concrete is recognized as a heterogeneous biphasic material, composed of aggregates and matrix (cement paste + fine aggregates). In this way, LITS is defined in the thesis as the sum of the thermomechanical and thermochemical strains. The former is developed in the bulk concrete (aggregates and matrix) and it is the result of microcracking, aggregate degradation and concrete thermal expansion restraint imposed by the applied load. Microcracking occurs due to thermal mismatch and increases with the amount of coarse aggregates. The aggregates are responsible for LITS acceleration above 400°C, especially due to α-β quartz phase transformation at 573°C. The thermochemical strain is seated in the cement paste (matrix), thus it is insensitive to the type of aggregates, and includes both drying and dehydration creep.

4.3.2 Preliminary assumption

The aggregates seem to play a very important role on LITS. Comparing the experimental data (Figure 60) available in the literature, it is possible to notice that an increase in the coarse aggregate volume, described as the ratio of the coarse aggregate and the binder (coarse aggregate/binder), leads to an increase in LITS values.

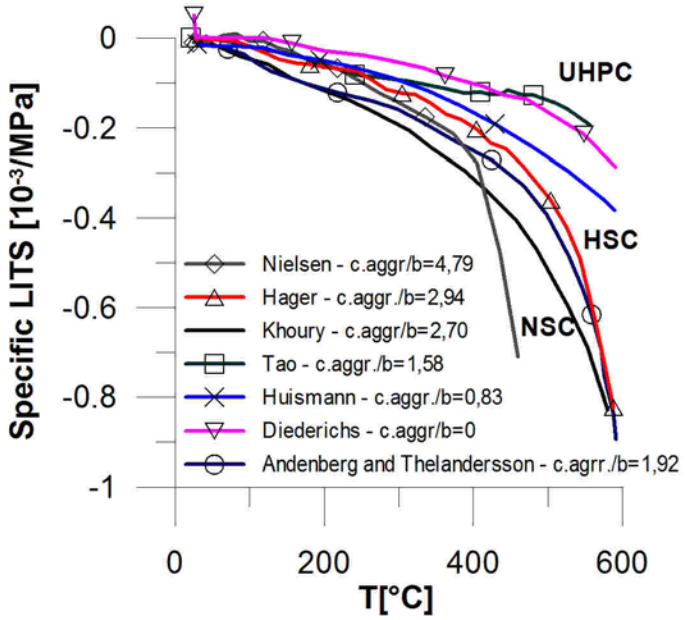

Figure 60 – Comparison of LITS among concretes with different mix design.

Moreover, this relationship seems to be logarithmic and can be mathematically expressed as $\ln(coarse\ aggregate/binder)$. In fact, solely the coarse aggregate seems to play a key role, as their expansion has a much higher effect to concrete expansion in relation to fine aggregates.

Taking advantage of LITS master curve numerically described in Terro [105] (Eq. 27), and considering an aggregate logarithmic variation, as shown in Eq. 31, it is possible to obtain a very good approximation with other experimental results, as shown in Figure 61.

$$LITS = LITS(T, 0.3f'_c) \times \left(0.0032 + 3.226 \times \frac{\sigma}{f'_c}\right) \times \ln(c.aggr/b) \quad (31)$$

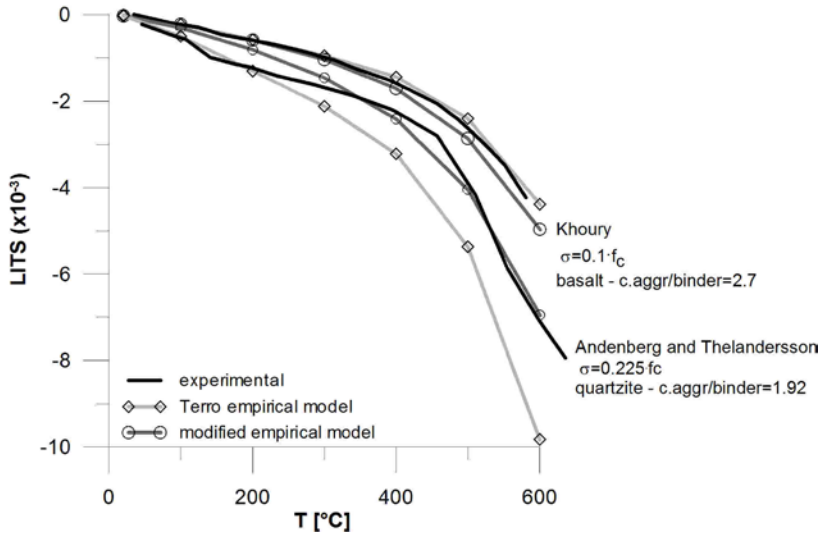

Figure 61 - Comparison of LITS considering [105] and modified [105] models.

However, this equation only works for OC and HSC with a relatively high coarse aggregate content ($\ln(coarse\ aggregate/binder) \geq 1$). Moreover, with this equation it is not possible to uncouple concrete thermomechanical and thermochemical strain

components. Hence, a new LITS equation, considering separately these two phenomena and which can be adopted for different types of plain concrete was pursued. The role of the thermomechanical and thermochemical strains are described below, followed by the description of the proposed LITS semi-empirical model proposed in this thesis.

4.3.3 LITS thermomechanical strains

In order to proper analyze transient creep, one must take into account LITS thermomechanical strains contribution originated from the aggregates inclusions in the matrix, which lead to concrete microcracking (thermal mismatch), concrete thermal mechanical restraint imposed by the applied load and transient creep acceleration due to aggregate degradation.

Concrete heating leads to thermal mismatch, which, together with concrete thermal differentials (eigenstresses), results in the interfacial transition zone (ITZ) microcracking (tangential and radial cracks around the aggregates) and the later appearance of macrocracks in the cement paste due to microcracks coalescence. In Figure 62, it is possible to observe the crack pattern for a concrete heated up to 600°C.

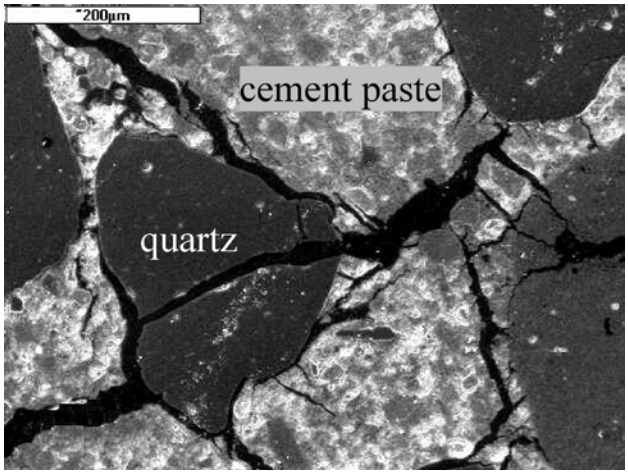

Figure 62 –Microstructure of concrete heated up to 600°C (Hager, [41]).

Moreover, at high temperatures, according to Sygała et al [118] , rocks (coarse aggregates) are subjected to chemical changes – polymorphic transformation, melting and disappearance of certain minerals. The most important processes that lead to geomechanical properties decay occurs between 400°C and 600°C (Sygała et al, [118]). In this temperature interval, rocks are submitted to thermal expansion, decomposition of minerals, dehydration, thermal stresses increase and considerable modification in the internal structure, which causes a change in the mechanical behavior from a brittle to a ductile response with plastic deformations.

Colombo [6] evidenced these thermomechanical damage by ultrasonic wave tests on FRC beams after a complete cycle of heating and cooling. The results, before and after thermal treatment, demonstrated that the mass loss due to concrete dehydration (thermochemical damage) was much lower than the ultrasonic speed reduction.

According to Sygała et al [118], carbonate rocks mineral decomposition occurs at relatively low temperatures, since the bonding between rock minerals exhibits a small

resistance, which causes a decrease in strength from the beginning of heating. On the contrary, sandstones exhibit a pronounced elasticity up to 800°C and an increase in its strength during heating up to 400°C (Sygała et al, [118].

4.3.4 LITS thermochemical strains

LITS thermochemical strains occur due to both concrete free water loss (drying creep) and dehydration. They are seated in the cement paste and, thus, they are insensitive to the type of the aggregate. As a result, an UHPC will develop only thermochemical strains due to the absence of coarse aggregates, which are responsible for LITS acceleration.

Drying creep occurs approximately around 100ºC due to the evaporation of water stored in concrete capillaries (macropores). It is strongly affected by the moisture condition (Gillen, [115]). A pre-dried concrete exhibits no drying creep.

In turn, dehydration occurs above 150ºC due to physical and chemical bound water evaporation from the CSH nano-porous media. It is the leading process of transient creep up to approximately 400ºC, when the aggregates start to become increasingly important, eventually superseding dehydration as the leading process.

4.3.5 Proposed LITS semi-empirical model

A new semi-empirical LITS model is proposed, considering concrete as a heterogeneous biphasic material (aggregates + matrix) and assuming that LITS is the sum of thermomechanical (microcracking, aggregate degradation and thermal expansion restraint) and thermochemical (drying and dehydration creep) strain contributions.

In the first step, LITS for two different concrete mixtures, respectively with (ordinary concrete) and without (UHPC) coarse aggregates are found. Eq. 32 shows LITS model for ordinary concrete, where: v_1 is a variable dependent on the volume of coarse aggregates ($\ln(c.aggr./binder)$); and, $\varphi(T)$ is a polynomial function describing LITS on concretes with coarse aggregates. In this particular case, LITS is the result of the contribution of both thermomechanical and thermochemical strain components, which are respectively explicitly (β_1) and implicitly taken into account.

$$LITS_{OC} = \beta_1 \times \varphi(T) \times \frac{\sigma}{f'_c} \tag{32}$$

Eq. 33 shows LITS model for UHPC, where: β_2 is a variable dependent on the cement content ($\ln(binder/100)$); and, $\vartheta(T)$ is an exponential function describing LITS on concretes without coarse aggregates. In this case, LITS is solely the result of the contribution of thermochemical strains (concrete drying and dehydration), explicitly described by the variable v_2.

$$LITS_{UHPC} = \beta_2 \times \vartheta(T) \times \frac{\sigma}{f'_c} \tag{33}$$

In the second step, the two functions are rewritten (Eq. 34 and Eq. 35) in terms of compliance functions (*J(T)*) in order to keep them independent of the load level, where: $q_1(T)$ is the thermomechanical compliance function and $q_2(T)$ is the thermochemical compliance function.

$$J_{LITS,OC}(T) = \beta_1 \times q_1(T) \quad (34)$$

$$J_{LITS,UHPC}(T) = \beta_2 \times q_2(T) \quad (35)$$

In the third step, the two equations are added (Eq. 36) in order to obtain a general semi-empirical model for plain concrete, such that the total LITS is the sum of the thermomechanical and the thermochemical strain contributions. It is important to underline that Eq. 34 describes explicitly LITS thermomechanical strain evolution, but contains implicitly LITS thermochemical strains. Hence, in order to disregard the thermochemical effects in Eq. 34, a reduction factor (α) was introduced.

$$J_{LITS}(T) = \alpha \times \beta_1 \times q_1(T) + \beta_2 \times q_2(T) \quad (36)$$

The final model, after fitting the parameters to the experimental data, was obtained as shown in Eq. 37, where: β_{tc} is the variable dependent of the cement content (Eq. 41); β_{tm} is the variable dependent of the aggregate volume (Eq. 40); $q_{tm}(T)$ is the thermomechanical compliance function in mm/m (Eq. 38); and, $q_{tc}(T)$ is the thermochemical compliance function in mm/m (Eq. 39).

$$J_{LITS}(T) = \beta_{tm} \times q_{tm}(T) + \beta_{tc} \times q_{tc}(T) \quad (37)$$

$$q_{tm}(T) = (-5.26 \cdot 10^{-5} \cdot T - 9.73 \cdot 10^{-7} \cdot T^2 + 3.23 \cdot 10^{-9} \cdot T^3 - 4.42 \cdot 10^{-12} \cdot T^4) \quad (38)$$

$$q_{tc}(T) = -exp(T^{0.31}) \cdot 0.156^5 \quad (39)$$

$$\beta_{tm} = ln\left(1 + \left({}^{c.agg.}/_{binder}\right)^3\right) \quad (40)$$

$$\beta_{tc} = ln\left({}^{binder}/_{100}\right) \quad (41)$$

In order to take into account the different types of aggregates (recycled, calcareous, siliceous and basalt), which are limited to the range of the samples analyzed, two different thermomechanical compliance functions were derived. This is because recycled aggregates breaks up at about 400°C, while siliceous and calcareous aggregates decompose at 1200°C. For the latter case, the thermomechanical compliance function is described in Eq. 38. For recycled aggregates, the thermomechanical compliance function (mm/m) is shown in Eq. 42.

$$q_{tm,recycled}(T) = (-3.5 \cdot 10^{-7} \cdot T^2 + 1.7 \cdot 10^{-9} \cdot T^3 - 1.3 \cdot 10^{-11} \cdot T^4 + 2.4 \cdot 10^{-14} \cdot T^5) \quad (42)$$

Figure 63 shows a comparison between the two thermomechanical compliance functions.

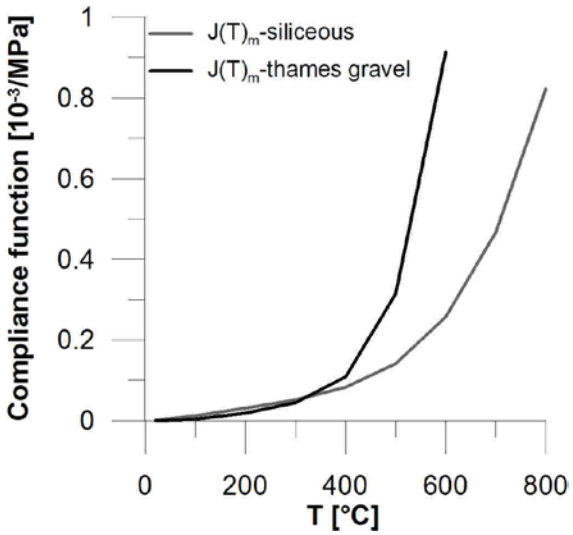

Figure 63 – Comparison between siliceous and Thames gravel LITS compliance functions.

Total LITS (in mm/m), for a determined load level, is calculated according to Eq. 43 and LITS coefficient (φ) is obtained according to Eq. 44.

$$LITS = J_{LITS}(T) \times \sigma \tag{43}$$

$$\varphi_{LITS} = J_{LITS}(T) \times E_c \tag{44}$$

It is important to underline that, as stated by Xing et al [119], recent studies demonstrated that rocks of identical chemical nature can show different behaviors during the temperature increase. Since the aggregate thermal damage process has a direct effect on LITS behavior, the semi-empirical model represents an average value and is limited to the amount of samples used.

4.3.6 The role of the aggregates

One important conclusion obtained from the proposed semi-empirical model is that the aggregates seem to produce a much higher variability on LITS in relation to the cement content. On one hand, the boundary conditions (compressive load and heating) restrains the aggregate expansion (in a lesser degree also the matrix). On the other hand, aggregates chemical transformations, mostly beyond 300°C, lead to an increasing ductile behavior and higher deformations, accelerating LITS.

Figure 64 demonstrates that, as the amount of coarse aggregate increases, its influence becomes gradually more important, since an increase in the cement content causes only a small increase in LITS compared to an increase in the coarse aggregate volume. As a result, the role of the aggregates cannot be disregarded, especially for OC. In HSC and UHPC, dehydration prevails due to the small volume or absence of coarse aggregates in the bulk concrete.

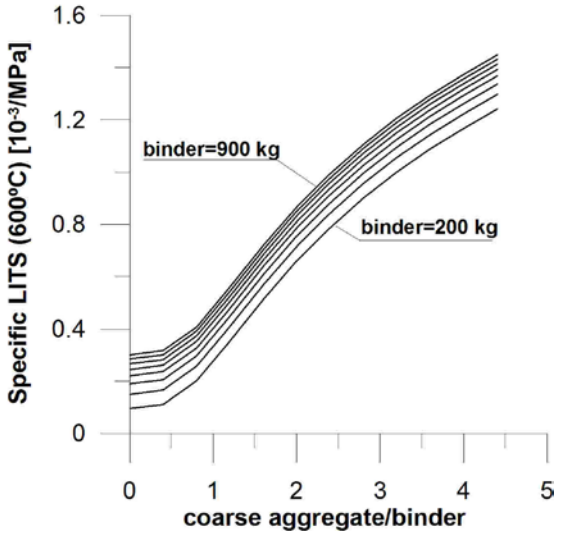

Figure 64 – Cement and coarse aggregate influence on LITS equation.

4.3.7 The role of the age of loading

In literature, there is no noticeable reference (to the best of the author's knowledge) to the role of the age of loading to transient creep behavior. On the contrary, for creep, Eurocode 2 proposes a reduction factor ($\beta(t_0)$) to take into account this effect. Since one of the main mechanisms (microprestress relaxation) of both creep and transient creep are the same, in spite of the different causes, one may expect that the age of loading also have an influence on transient creep. It is important to say that concrete aging increases both the level of the hydrated cement products (solidification process) and the number of bonds of the CSH layers, increasing concrete stiffness, as described in Bazant et al [2].

Comparing the experimental results of 5-year-old concrete from Hager [112] with the proposed semi-empirical model, it is possible to observe that, without incorporating a reduction factor, LITS values are consistently higher, as shown in Figure 65 to Figure 68. Therefore, a reduction factor ($\beta(t_0)$ – Eq. 45) is introduced and a good agreement between the semi-empirical model (Eq. 46) and experimental curves is obtained. Despite that, more tests should be carried out in order to better understand and confirm this assumption.

$$\beta(t_0) = \frac{400}{\left[ln\left(\frac{28}{t_0}\right)\right]^4 + 400} \tag{45}$$

$$J_{LITS}(T) = [\beta_{tm} \times q_{tm}(T) + \beta_{tc} \times q_{tc}(T)] \times \beta(t_0) \tag{46}$$

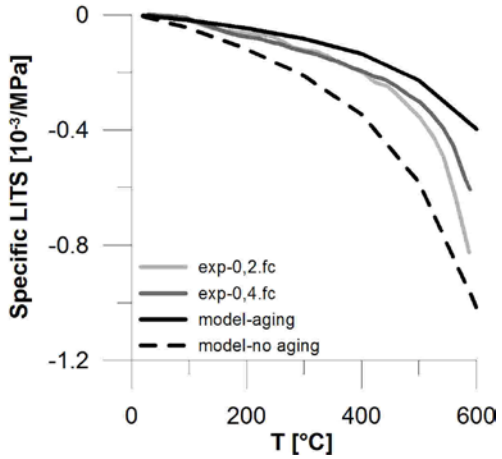

Figure 65 – Comparison with [112] M30C results.

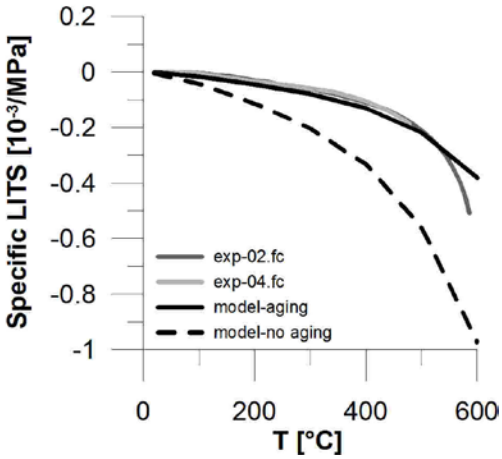

Figure 66– Comparison with [112] M75C results.

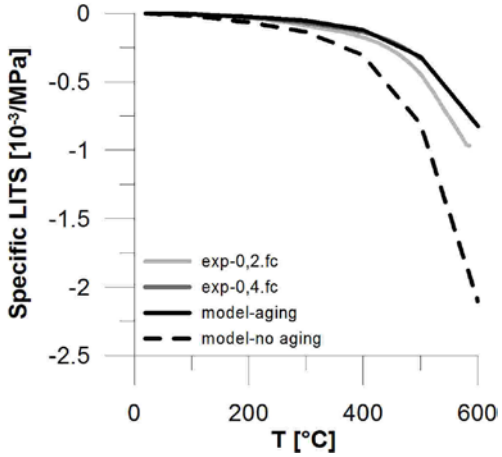

Figure 67 – Comparison with [112] M75SC results.

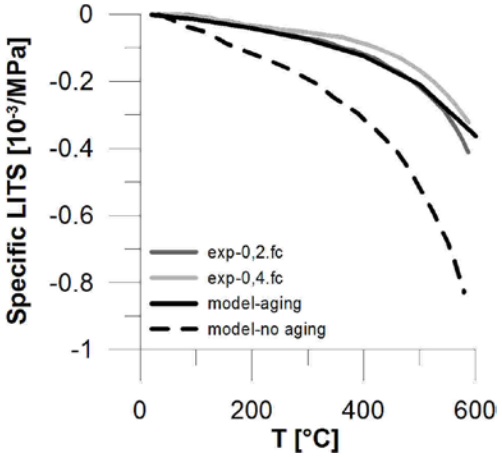

Figure 68 – Comparison with [112] M100C results.

4.3.8 Validation of the proposed semi-empirical model

In order to validate the new semi-empirical model, it was compared with experimental results from other authors. All the values are shown in terms of specific LITS (strain per unit stress).

Figure 69 shows the comparison between the proposed model and Khoury [58] experimental results considering siliceous and calcareous aggregates. From the experimental results, it is possible to observe that the curves for the two types of concrete are practically the same and the model solution has a good approximation.

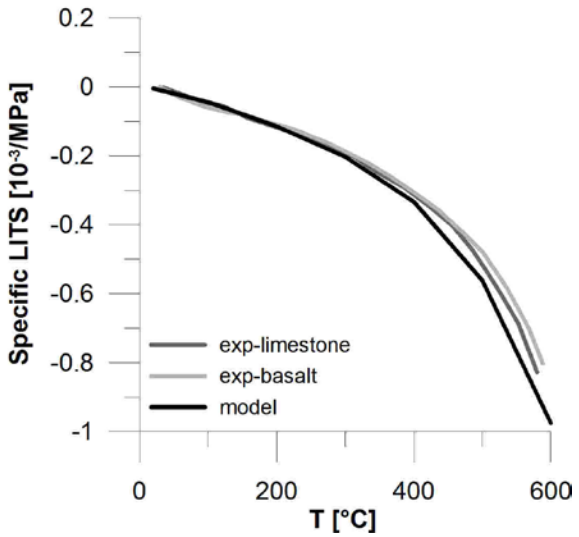

Figure 69 – Khoury [58] experimental results for siliceous and calcareous aggregate types.

Figure 70 shows the comparison with Nielsen [107] green concrete (recycled aggregates). It is possible to notice that the experimental curves with different load levels ($0.11 \cdot f_c$ to $0.44 \cdot f_c$) are practically juxtaposed, indicating the linear relationship between LITS and the stress level. Moreover, the semi-empirical solution, adopting the thermomechanical compliance function given in Eq. 42, has a good approximation with the experimental curves.

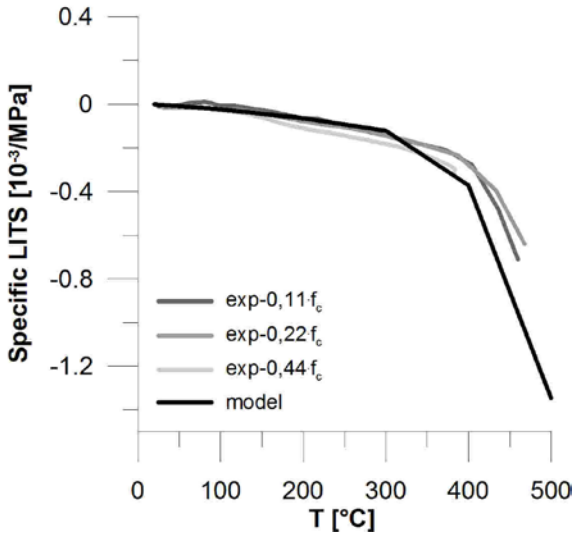

Figure 70 – Comparison with [107] experimental results for green concrete and three types of load.

Figure 71 and Figure 72 show respectively the comparison with Andenberg and Thelandersson [47] and Mindeguia et al [110] experimental results considering two different heating rates. From the experimental results, it is possible to observe that the increase in the heating rate from 1°C/min to 5°C/min has a very small effect on LITS values. A good agreement between the proposed model and the experimental curves was obtained.

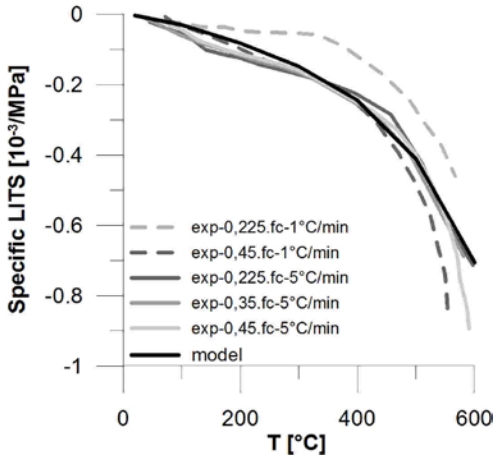

Figure 71 – Comparison with [47] experimental results considering heating rates of 1°C/min and 5°C/min.

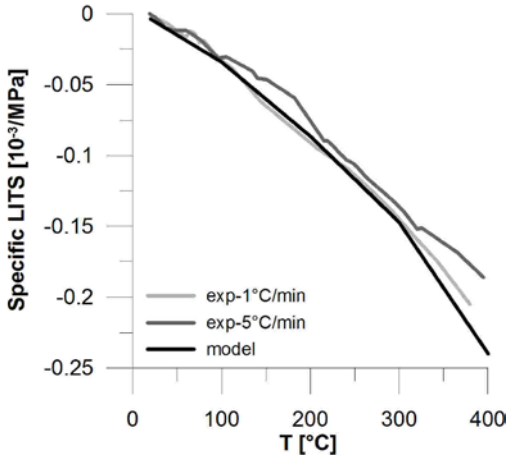

Figure 72 – Comparison with [110] values considering heating rates of 1°C/min and 5°C/min.

Figure 73 shows the comparison with Andenberg and Thelandersson [47] results considering saturated specimens. The proposed semi-empirical model is able to reproduce reasonably the experimental behavior. The difference between the model and experimental curves is due to the fact that, as stated by Sabeur and Colina [117], transient creep is inversely proportional to the w/c ratio and, hence, saturated specimens develop smaller transient creep strains in relation to standard cured ones.

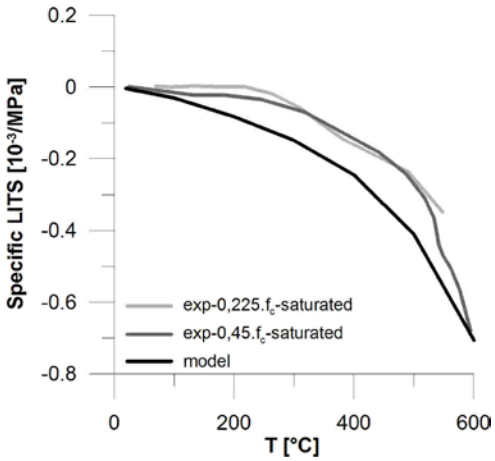

Figure 73 - Comparison with [47] experimental results considering saturated specimens.

Figure 74 shows the comparison with Andenberg and Thelandersson [47] tests taking into account pre-dried specimens. In this case, the experimental result of the specimen loaded at 0.2.fc was higher than the one loaded at 0.4.fc. Despite that, the proposed model can predict the evolution of transient creep behavior in pre-dried concrete.

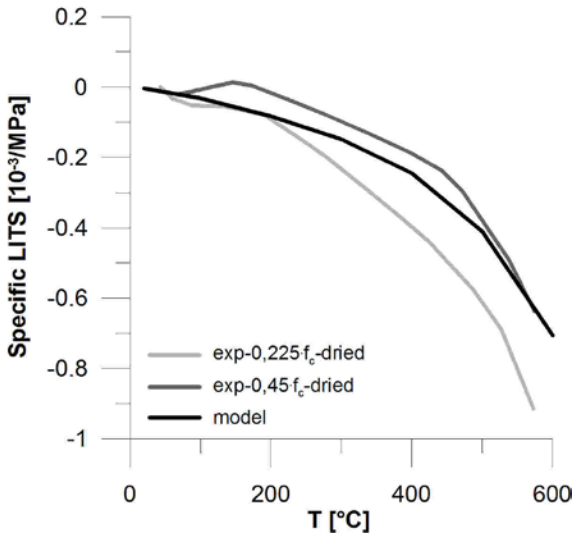

Figure 74 - Comparison with [47] experimental results considering pre-dried specimens.

Figure 75 and Figure 76 show, respectively, the experimental results of UHPC specimens from Diederichs et al [113] and HSC results from Huismann et al [108]. From these results, one can observe a good approximation between the proposed model and the experimental curves.

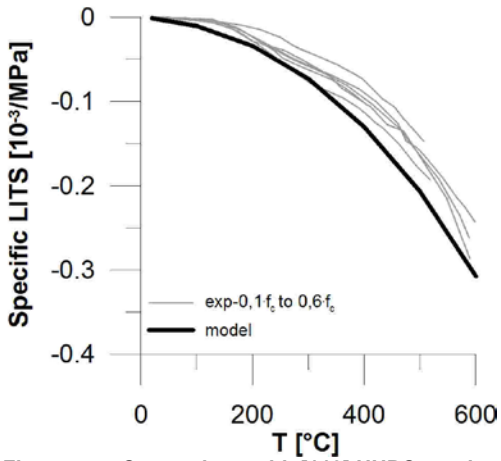

Figure 75 – Comparison with [113] UHPC results.

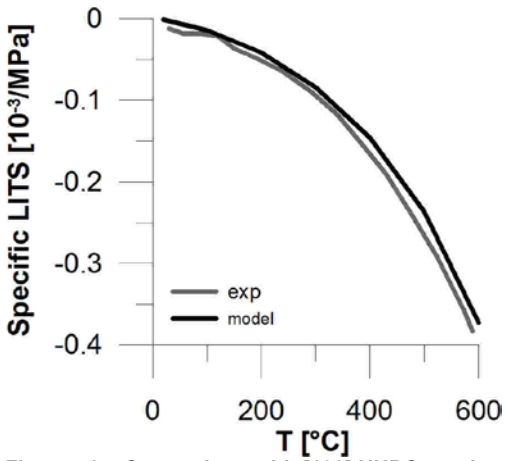

Figure 76 – Comparison with [108] UHPC results.

Figure 77 shows the comparison with SCC (self-compacting concrete) from Tao et al [109]. In this case, the proposed model is able to capture the trend of LITS evolution. However, in the experimental tests, between 200°C and 400°C, LITS slows down and after that, accelerates again. This phenomenon was observed only for this type of concrete. Hence, more tests should be carried out in order to better understand this behavior. It is worth mentioning that SCC mixture differs from those of OC, since it incorporates more powder, less aggregates and a high range of superplasticizers to reduce w/c ratio and increase workability. Also the aggregate shape (angular or rounded) and size distribution are distinct from OC.

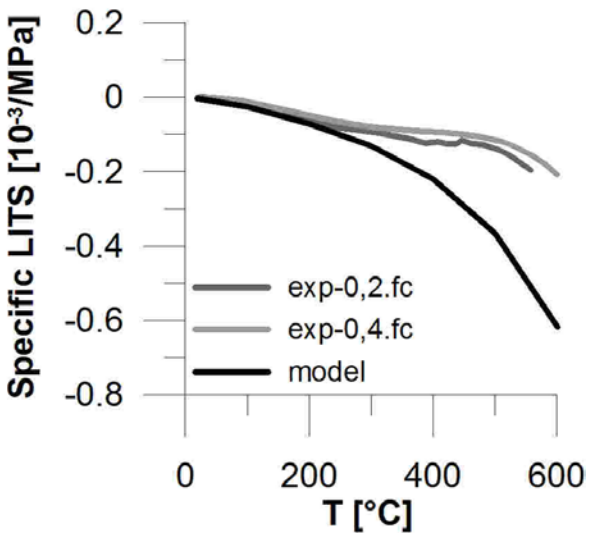

Figure 77 – Comparison with [109] SCC specimens.

A comparison was also made between the proposed semi-empirical model and other empirical equations (Andenberg and Thelandersson, [47]; Schneider, [120]; Tao et al, [109]; Terro, [53]), as shown from Figure 78 to Figure 83. In this case, experimental results obtained by other authors were considered as benchmark. Concrete mechanical properties are shown in Table 5, together with the load level.

The results demonstrate the reliability of the proposed semi-empirical model, which, compared to other empirical ones, has shown the best fitting in relation to the experimental curves.

Table 5 – Concrete properties of the specimens

Reference	f_{ck}	concrete type	stress level	aggregate type	coarse aggregate /binder	concrete age	Figure
Khoury [58]	51	OC	$0.1 \cdot f_c$	calcareous	2.7	5 months	Figure 78
Huismann et al [108]	113	HSC	$0.1 \cdot f_c$	siliceous	0.83	166 days	Figure 79
Tao et al [109]	30	SSC	$0.2 \cdot f_c$	calcareous	1.58	118 days	Figure 80
Mindeguia et al [69]	45.40	OC	$0.4 \cdot f_c$	calcareous	2.2	97 days	Figure 81
Nielsen [107]	35	Green	$0.11 \cdot f_c$	calcareous	4.79	3 months	Figure 82
Andenberg and Thelandersson [47]	43.80	OC	$0.225 \cdot f_c$	siliceous	1.92	5 months	Figure 83

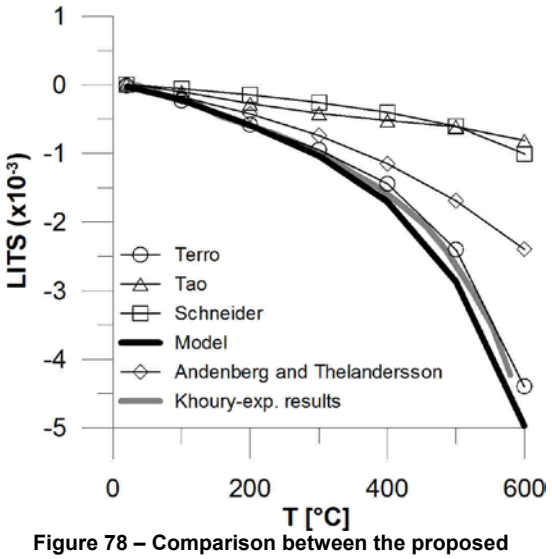

Figure 78 – Comparison between the proposed model and [58] experimental results.

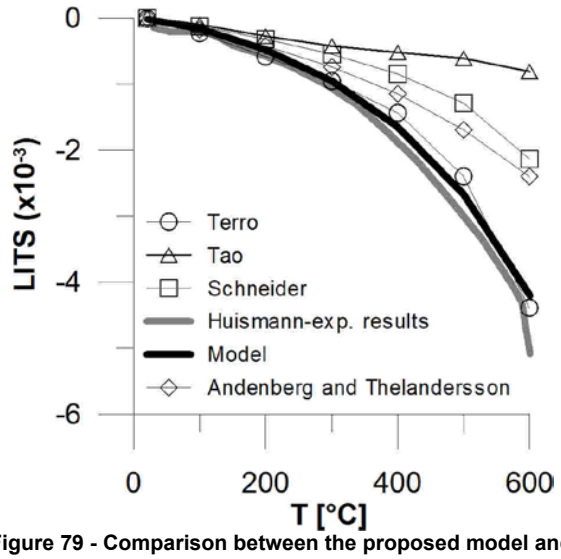

Figure 79 - Comparison between the proposed model and [108] experimental results.

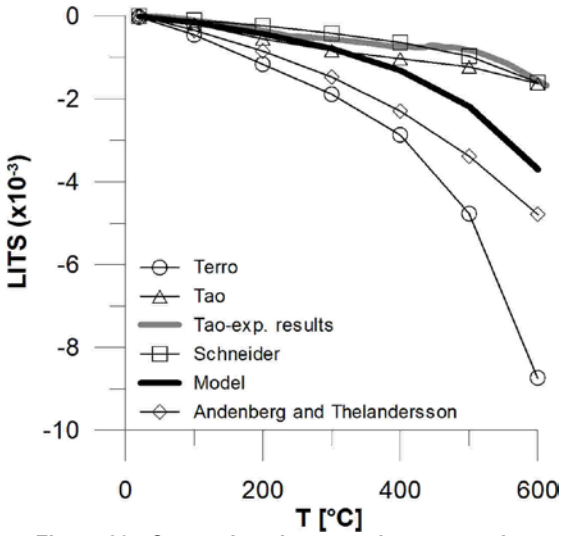

Figure 80 - Comparison between the proposed model and [109] experimental results.

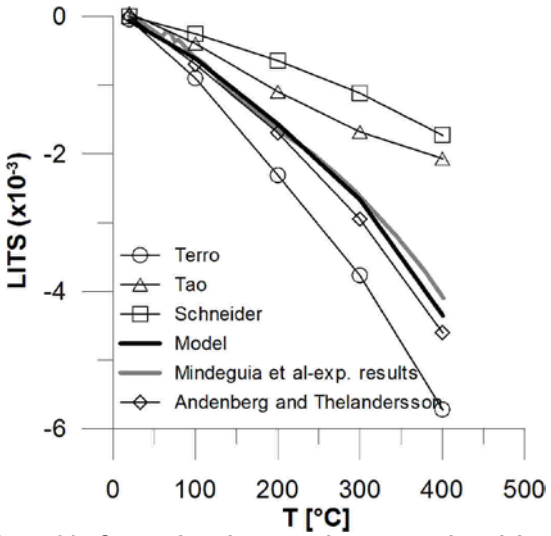

Figure 81 - Comparison between the proposed model and [69] experimental results.

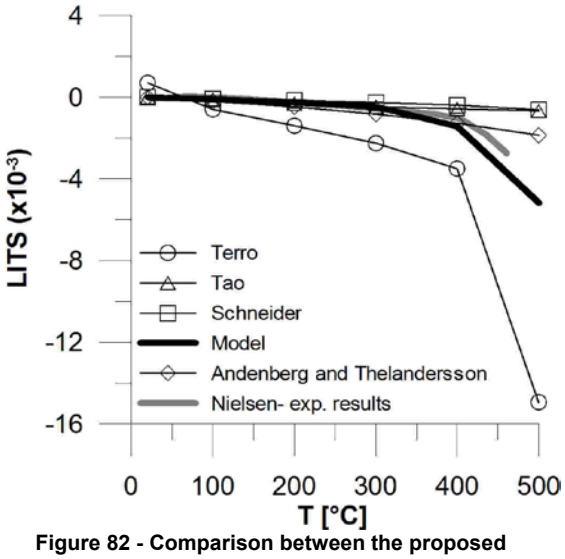

Figure 82 - Comparison between the proposed model and [107] experimental results.

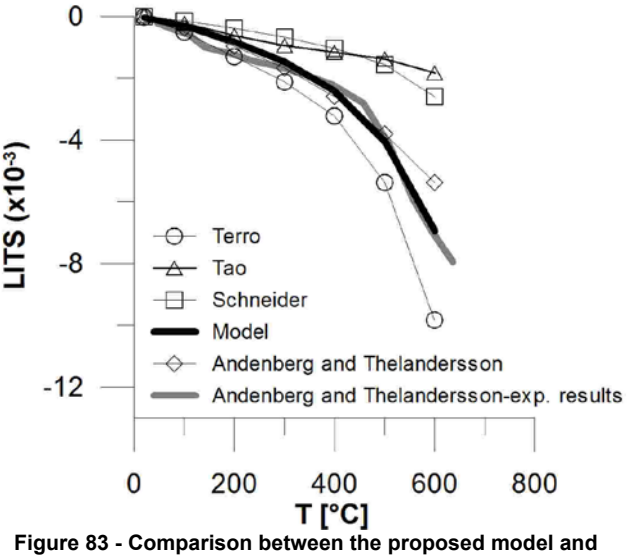

Figure 83 - Comparison between the proposed model and [47] experimental results.

4.4 Final Comments

Andenberg and Thelandersson [47] tests on pre-dried specimens (Figure 74) have shown that LITS was higher in the specimen loaded at 0.225·fc in relation to the one loaded at 0.45·fc. Andenberg and Thelandersson [47] results are similar to the ones obtained from experimental tests at high temperature carried out during the thesis and described in Chapter 7. In the latter case, the tests were performed on 11.5-year-old specimens and one can expect a similar behavior in relation to a pre-dried concrete due to the long period of drying exposure.

Comparing the experimental results from literature, it was observed that LITS increases with the increase in coarse aggregate quantity, which can be attributed to the direct relationship between aggregate volume and concrete thermal expansion. This is the opposite of the assumption of Terro [105] empirical model (Eq. 30), which assumes that the variation of LITS is inversely proportional to the amount of aggregates.

From the comparison of the proposed semi-empirical model with experimental results, one can conclude that the model has a poor agreement with saturated specimens. In order to have a better prediction, the moisture content should be incorporated in the semi-empirical model.

A lack of correlation between the semi-empirical model and SCC experimental results after 200°C occurred. One possible explanation is that SCC mixture differs from those of OC, since it incorporates more powder, less aggregates and a high range of superplasticizers to reduce w/c ratio and increase workability. The aggregate shape (angular or rounded) could be possibly related to this. In any case, Bamonte and Gambarova [17] tests confirmed others experimental results, showing that, although SCC has a tendency to be more heat-sensitive, its behavior is practically the same of normal concrete mixtures (vibrated) in terms of thermomechanical properties decay considering quasi-steady thermal conditions.

In relation to the age of loading, it was observed that the semi-empirical model overestimated the experimental results of 5-year-old specimens. In order to take into account the effect of concrete aging, a reduction factor ($\beta(t_0)$) was introduced.

CHAPTER 5

SFRC mechanical characterization and aging effects

FRC beams used in this investigation and shown in Figure 84 were cast in the same day, in 2004, respecting the same casting procedure. Part of them were tested in 2005 (1-year-old material) during Colombo [6] PhD thesis and the rest in 2014 (10-year-old material), during this thesis. The specimens size are 150x150x600 mm.

Figure 84 - Details of [6] FRC beams.

The beams were cast with 50 kg/m^3 of low carbon steel hooked end fibers, 30 mm long and with an aspect ratio (l_f/d_f) equal to 45. Concrete mixture is described in Table 6.

Table 6 – FRC beams mix design

Material	Type	Quantity [kg/m^3]
Cement	I 52.5R	450
Siliceous agreggates	0 -3 mm 0 -12 mm 8 -15 mm	620 440 710
Plastificizer	Acrylic	5.5
Water		195
Calcareous powder		30
Steel fibers	Low carbon hooked-end	50

The mechanical characterization of the material included ultrasonic wave tests, flexural tests (3PB and 4PB) and indirect DEWS tensile tests.

The change in material mechanical properties due to long-term aging, especially the residual post-cracking tensile strength, is investigated. In order to observe possible changes in the material class through the years, the material classification according to fib Model Code 2010 [78] of 1- and 10-year-old specimens was determined and compared.

The tensile constitutive law of the material at 1 year was obtained according to fib Model Code 2010 [78] and a plane section (PS) numerical analysis in bending was developed.

A comparison of the σ_N-COD curves between direct (UTT and DEWS) and inverse analyses (tensile constitutive law of the material at 1 year) is carried out.

5.1 Ultrasonic wave tests

Ultrasonic tests were carried out in order to determine the Dynamic Modulus of Elasticity. The values were compared with Colombo results [6] to verify the evolution of the material properties through the years.

It is worth mentioning that ultrasonic tests apply pulses (short acoustic waves) with a frequency range between 0.5 and 25 MHz to detect flaws inside the specimen due to wave pattern modifications. Its main advantage is the high precision in comparison with other non-destructive tests. The equipment has high sensibility, being capable to detect microscopic flaws. Besides, it is simple to operate and fast to execute.

Concrete structures with good homogeneity, uniformity and compactness exhibit high speed ultrasonic pulses. Material microstructure defects and flaws, such as microcracks, voids and concrete segregation reduce and distort acoustic waves. Discontinuity evaluation is determined by the comparison of the test results with a reference number.

5.1.1 Experimental results

Overall, twenty FRC beams from Colombo [6] were tested. Two piezoelectric transducers were employed, one transmitter and one receptor, disposed at beam's ends (longitudinally) as shown in Figure 85.

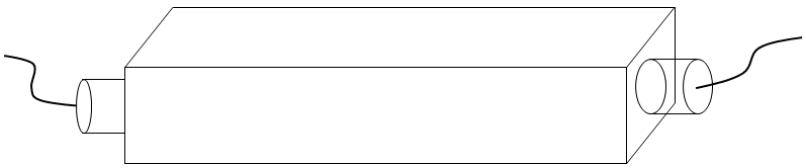

Figure 85 – Ultrasonic test procedure

The test comprised two steps: data collection and posterior data analysis. Firstly, specimens lengths were measured and then, with the experimental apparatus, the time of wave propagation was determined. After that, specimens wave velocities and dynamic modulus of elasticity were calculated. The results are shown in Table 7.

The dynamic modulus of elasticity is directly related to the square of the ultrasonic wave velocity and is computed according to Eq. 47, where v_{el} = ultrasound wave velocity; ρ = concrete specific weight; ν = Poisson ratio.

$$E_d = {v_{el}}^2 \rho \frac{(1+\nu)(1-2\nu)}{(1-\nu)} \quad (47)$$

Table 7 - Ultrasonic test results

nº	length (mm)	time (μs)	vel. (m/s)	Dynamic elasticity modulus
1	620	127.7	4.86	50.916
2	620	130.5	4.75	48.755
3	620	130.2	4.76	48.980
4	600	124.7	4.81	50.006
5	620	128.7	4.82	50.128
6	600	126.1	4.76	48.902
7	600	125.6	4.78	49.292
8	600	126.6	4.74	48.516
9	620	130	4.77	49.130
10	620	128	4.84	50.678
11	620	128.2	4.84	50.520
12	600	127.2	4.72	48.060
13	600	126.5	4.74	48.593
14	620	133	4.66	46.939
15	620	129.2	4.80	49.741
16	620	130.9	4.74	48.457
17	600	128	4.69	47.461
18	620	131.7	4.71	47.870
19	620	132.5	4.68	47.294
20	620	130	4.77	49.130

The results were very close, with a standard deviation of 2.30%, thus, indicating a very good mixture homogeneity and concrete hydration over the period.

After the test, a comparison of the mean dynamic modulus of elasticity with Colombo results [6] was carried out, as shown in Table 8, indicating an increase in the Modulus of Elasticity.

Table 8 – Long term aging evolution of the mean dynamic modulus of elasticity

	Experimental results	Colombo [6] results	Difference
Mean Dynamic Modulus of Elasticity	48968 MPa	44991 MPa	**+8.84%**

5.2 Uniaxial compressive test

The uniaxial compressive test was carried out using a hydraulic press CONTROLS ADVANTEST9 with a maximum loading capacity of 3000 kN and a maximum error in the loading measure lower than 0.01 of the maximum load capacity of the press.

A comparison between the experimental results of 1-year-old (mean value from three tests) and 10-years-old (result from one test) specimens is shown in Figure 86 by means of nominal stress (σ_N = P/A) versus strain curve. The results demonstrate an increase of the compressive strength in the period of approximately 35%.

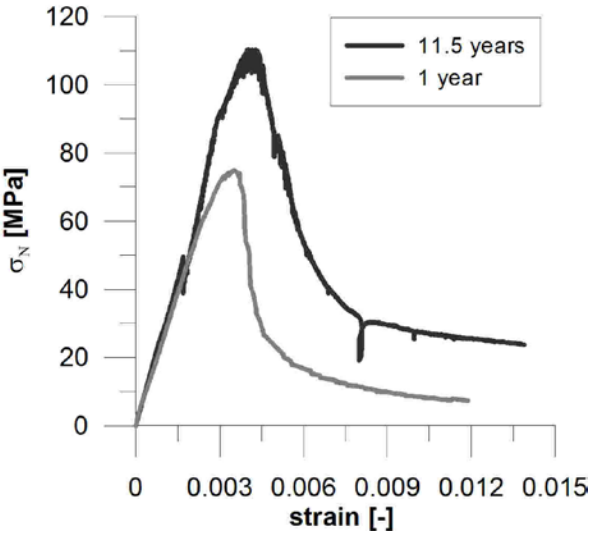

Figure 86 – Comparison between FRC compressive strength at 1 year and 10 years.

5.3 Flexural tests

5.3.1 Bending tests experimental procedures

Three and four-point bending tests on notched beams were carried out, following respectively EN 14651 [121] and UNI 11039 [81] standard procedures, as shown in Figure 87.

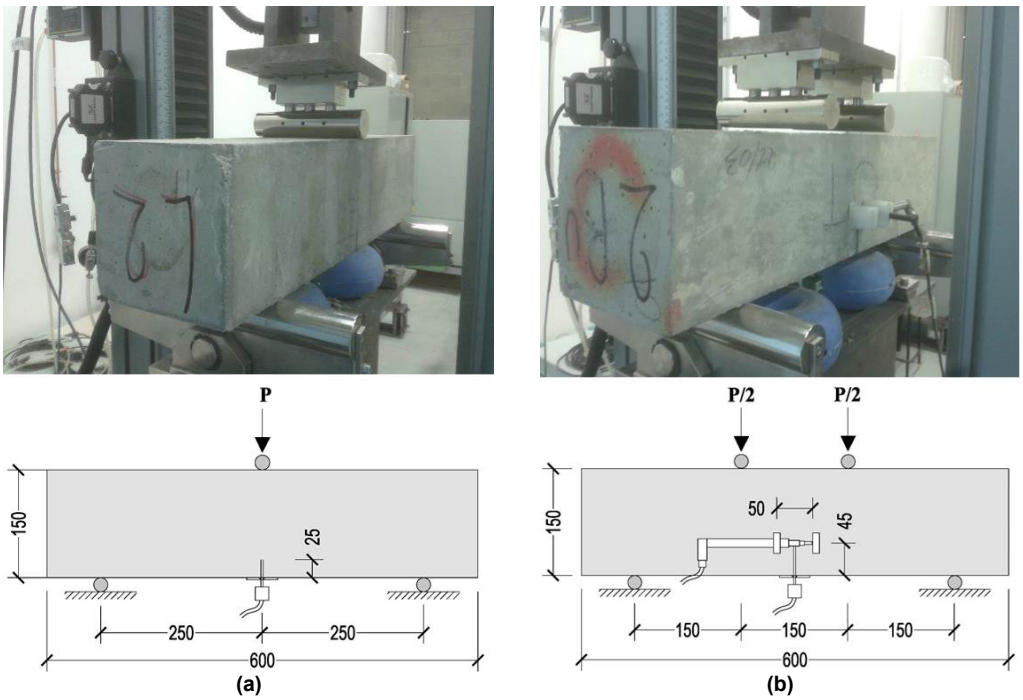

Figure 87 - Flexural test procedures: a) three-point bending test [121]; b) four-point bending test [81].

It is worth mentioning that CTOD values from 4PB tests were determined by the average values of front and rear measurements performed by means of two LVDT's. CMOD values for both tests were measured with a clip gage installed in the center of the mouth of the beam's notch.

The tests were carried out at Politecnico di Milano - Lecco Campus - Laboratory with an electro-mechanical press INSTRON 5867, with a loading capacity of 30 kN and a measurement precision of $\pm$ 0.4%.

Both 3PB and 4PB tests (10-year-old material) were carried out considering nine nominally identical experimental procedures for each case. The 4PB tests (three nominal identical experimental procedures) performed by Colombo [6] (1-year-old material) are also described.

5.3.2 Determination of the characteristic values of the bending tests

In the case investigated, bending tests were carried out at two different ages (1 year and 10 years) using the same material and the same standard test procedures. In this way, V_x is supposed to be unknown at one age and known at the other. Since the tests performed at 10 years have a larger number of specimens and, as a result, a better statistical representation of the material mechanical behavior, V_x was supposed to be unknown and the characteristic values were calculated using the standard deviation directly obtained from those tests. In contrast, for the bending tests at 1 year, V_x was supposed to be known and equal to the largest value measured at 10 years (to remain on the safe side), which corresponds to that obtained for the 3PB tests.

This assumption was made because no discrepancies with regard to variation are expected from one material to the other due to the aging effect. It is important to take into account that all the beams were cast on the same day, adopting the same casting procedure. Moreover, Eurocode [29] states that a known V_x should be used if the

coefficient of variation or a realistic upper bound of it is held from prior knowledge. In this case, the prior knowledge comes from the evaluation of previous tests (at 10 years) in comparable situation (same material and same standard test procedures).

5.3.3 Bending test results from Colombo [6] at 1 year

The results of 4PB tests from Colombo [6] is shown in Figure 88 in terms of nominal stress (σ_N) vs. CTOD.

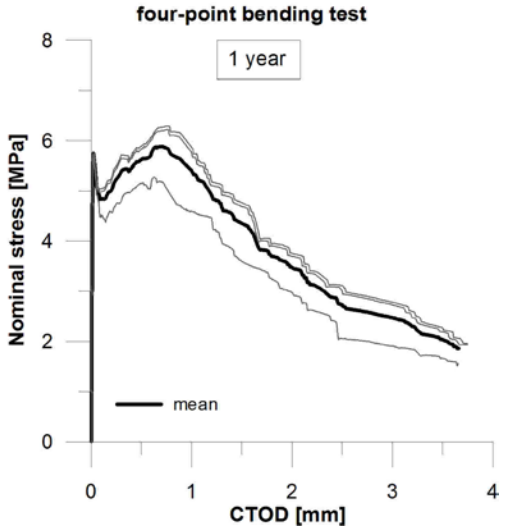

Figure 88 – 4PB experimental results of 1-year-old specimens [6].

The values of the peak flexural strength ($f_{ct,fl}$) and post-peak stresses at serviceability (f_{R1}, w=0.5 mm) and ultimate limit states (f_{R3} w=2.5 mm), together with the coefficient of variation, are summarized in Table 9.

Table 9 - Experimental results of four-point bending tests of 1 year old specimens

Specimen nº.	f_{ctfl} [MPa]	f_{R1} [MPa]	f_{R3} [MPa]
1	5.73	5.70	3.65
2	5.75	5.74	3.71
3	5.75	5.04	2.88
$f_{i,mean}$ (V_x)	5.74 (0.08)	5.49 (0.17)	3.42 (0.26)
$f_{i,k}$	4.87	3.73	1.74

5.3.4 Bending test results at 10 years

Experimental results of three and four-point bending tests in terms of nominal stress *vs*. crack opening displacement related to 10-year-old beams are shown in Figure 89.

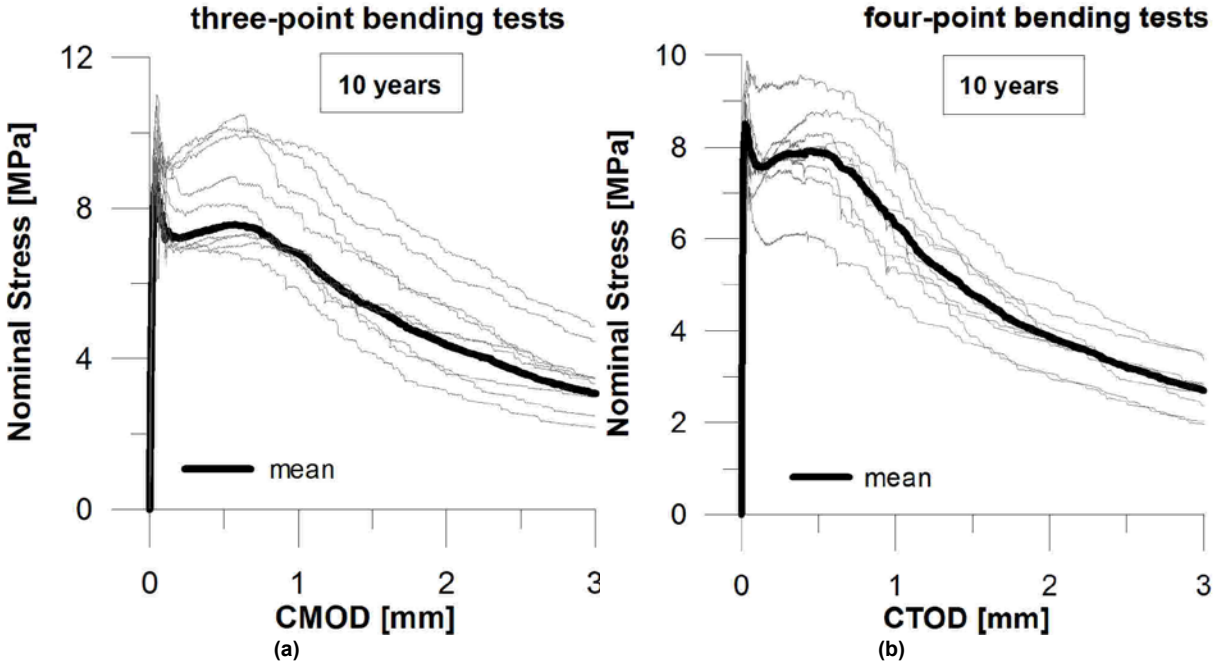

Figure 89 - Flexural tests of 10-year-old specimens: a) three-point bending test [121]; b) four-point bending test [81].

Overall nine tests were carried out for each bending test type. The values of the maximum flexural strength ($f_{ct,fl}$), residual strength at serviceability (f_{R1}, CMOD=0.5 mm) and ultimate limit states (f_{R3}, CMOD=2.5 mm) from 3PB and 4PB tests, accompanied by the standard deviations, are shown respectively in Table 10 and Table 11.

Table 10 - Experimental results of three-point bending tests of 10-year-old specimens

Specimen nº (beam reference)	f_{ctfl} [MPa]	f_{R1} [MPa]	f_{R3} [MPa]
1 (L1)	11.03	10.12	5.31
2 (L2)	8.88	6.98	4.11
3 (L3)	10.14	8.76	4.20
4 (L4)	9.88	7.23	2.91
5 (L5)	10.49	10.26	5.81
6 (L6)	9.04	6.81	2.52
7 (L7)	9.33	7.20	3.93
8 (L8)	10.78	9.87	4.24
9 (L10)	9.35	8.09	3.28
$f_{i,mean}$ (st. dev.)	9.88 (0,78)	8.37 (1.42)	4.04 (1.06)
$f_{i,k}$	8.35	5.59	1.96

Table 11 - Experimental results of four-point bending tests of 10-year-old specimens

Specimen nº	f_{ctfl} [MPa]	f_{R1} [MPa]	f_{R3} [MPa]
1 (U1)	9.14	6.95	3.09
2 (U2)	9.56	9.38	5.33
3 (U3)	8.60	7.72	3.36
4 (U4)	8.17	7.80	4.12
5 (U5)	8.,09	8.02	4.07
6 (U7)	9.15	8.05	4.92
7 (U8)	8,30	7.82	4.98
8 (U9)	7.96	6.09	3.51
9 (U10)	8.27	8.33	5.37
$f_{i,mean}$ (st. dev.)	8.58 (0.56)	7.80 (0.90)	4.30 (0.87)
$f_{i,k}$	7.48	6.02	2.59

A direct comparison of the two tests in terms of nominal stress vs. CMOD is shown in Figure 90. To this aim, 4PB σ_N *vs. CTOD* curve was shifted along the longitudinal axis to be represented in terms of crack mouth opening displacement. A correlation, considering a linear relation between CTOD and CMOD and assuming a linear opening of the crack edges, was adopted (di Prisco et al, [78]). Because of the specimen geometry, in this case, the relationship assumed is: $h_{ref}/h_{net}^{3PB} \cdot CTOD = 150/125 \cdot CTOD \cong 1.2 \cdot CTOD$, which takes into account the 3PB test (EN 14651 [121]) geometry and a mechanism of two blocks causing a linear opening of the crack along the ligament.

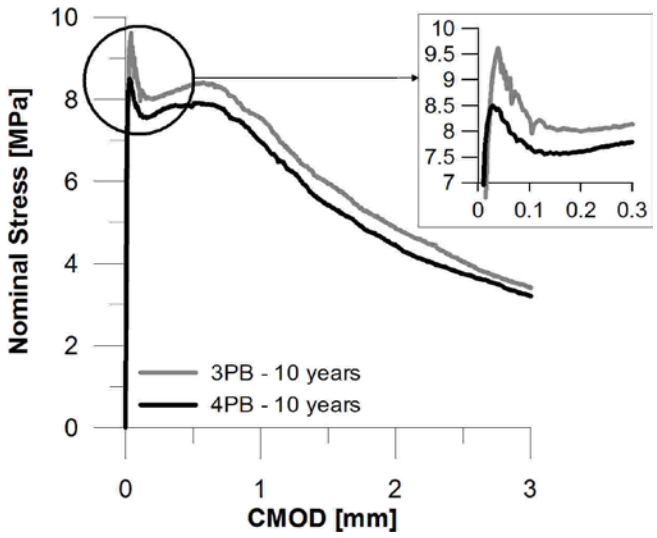

Figure 90 - Comparison between the mean values of three and four-point bending tests.

The results demonstrate that 3PB test has a slightly higher peak load, with a more unstable crack propagation characterized by a steeper slope in the branch immediately after the peak. This fact can be attributed to the stress distribution between the loading points at the 4PB test, which results in a more stable crack propagation. 3PB test has a peak bending moment concentrated at the loading point aligned to the central load knife (crack tip). In the case analyzed, 3PB tests lead to smaller load levels as the ratio of the two nominal strengths ($f_{fl,3PB}$/ $f_{fl,4PB}$) gives a difference of 17.6% for the same load, as shown in Eq. 48.

$$\frac{f_{fl,3PB}}{f_{fl,4PB}} = \frac{M_{3PB}/W_{3PB}}{M_{4PB}/W_{4PB}} = \frac{6 \cdot P \cdot L_{3PB}/4 \cdot b \cdot h_{3PB}^2}{6 \cdot P \cdot L_{4PB}/6 \cdot b \cdot h_{4PB}^2} = \frac{3 \cdot L_{3PB} \cdot h_{4PB}^2}{2 \cdot L_{4PB} \cdot h_{3PB}^2} = 1.176 \quad (48)$$

The fiber pull-out branches of the two bending tests are practically the same, with slightly higher values for the 3PB tests. These results are in agreement with di Prisco et al [78] previous experimental campaign with 3PB and 4PB tests considering different fiber volume percentage and concrete mixes, which has shown very similar pull-out strengths for the two test modalities, with a tendency for 3PB tests to give higher values, justified by the real stress distribution in the tests.

A crucial issue related to FRC, according to di Prisco et al [78], regards the heterogeneity of the material, which can be related to fibers orientation and distribution. FRC heterogeneity leads to a larger scattering in material response that results in a reduction of the characteristic values used for material classification. Even the same material, tested according to different bending test types, could give not-negligible differences in the standard deviation. In fact, in the experimental tests, the standard deviation was higher on the 3PB tests in relation to 4PB tests, thus resulting in a higher class in the latter case.

5.4 Tensile tests

5.4.1 Tensile experimental procedure

The tensile behavior of the material was studied by means of fixed-end uniaxial tensile tests (UTT) for the 1-year-old material (see Colombo [6]) and by means of indirect Double Edge Wedge Splitting (DEWS) test for the 10-year-old material.

DEWS tests were performed on prismatic specimens (Figure 91a) with a width of 30 mm and cut from the beams tested in bending in the longitudinal direction, as shown in Figure 91b. The crack opening was measured with two LVDT's (length = 50 mm) installed on the front and rear surfaces, as shown in Figure 92a.

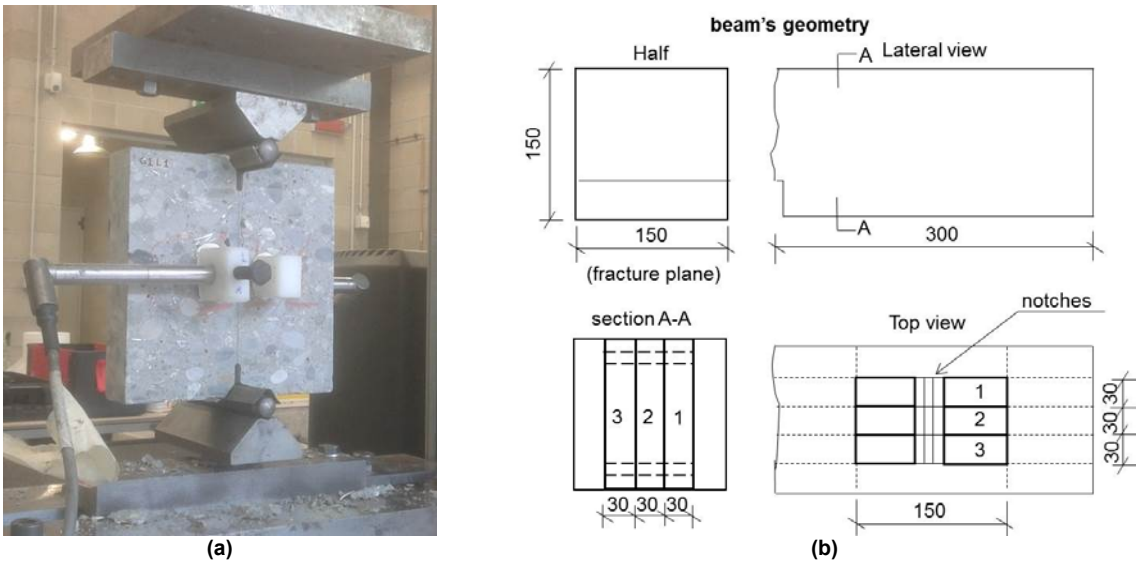

Figure 91 - DEWS testing procedures: a) DEWS experimental apparatus; b) beam's cutting planes (dimensions in mm).

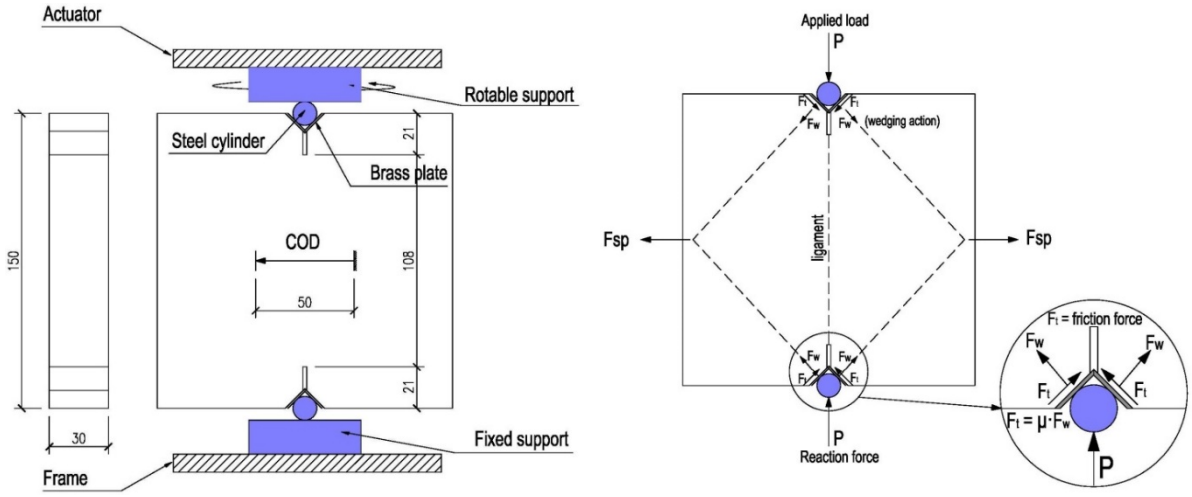

Figure 92 - DEWS experimental details: a) specimen geometry and measuring scheme; b) force diagram.

It is worth mentioning that DEWS gives the uniaxial tensile nominal stress vs. average cracking opening, which corresponds to the assumption of a linear stress distribution along the crack plane. In fact, it allows a direct determination of tensile stress *vs.* crack opening curve in a predetermined orientation. For example, it is possible to cut off a pre-ordained notch in the fracture plane direction and aligned to the principal fibers orientation or in the perpendicular direction, thus, allowing the analysis of stresses in orthotropic planes.

Another important aspect of DEWS test is the fact that the experiment induces a pure mode I fracture state at the critical transverse section (ligament), as shown in Figure 92b. This is made possible due the application of a compressive load, such as the Brazilian test, but, in this particular case, compressive and tensile stresses are completely uncoupled on the ligament cross-section owing to the 45º notch ends.

2.4.2 UTT experimental results from Colombo [6]

The results of direct tensile tests from Colombo [6] are shown in Figure 93 in terms of stress ($\sigma = P/A$) vs. COD (w) curve.

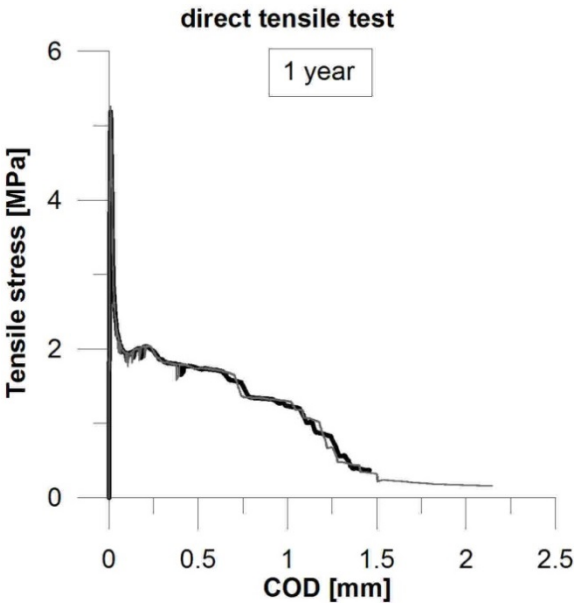

Figure 93 – Direct tensile tests of 1-year-old specimens.

5.4.3 DEWS experimental results

A total of eight specimens from three different beams were tested by means of DEWS [83] methodology. From each beam half, obtained after the flexural tests, three DEWS specimens were obtained (Figure 91b).

The specimens were cut in order to have for both DEWS and bending tests the same tensile stress direction (the longitudinal direction of the beam). Considering that fibers distribution through the beam fracture plane is not homogeneous and the beam cross-section, according to EN 14651 [121], (125 mm x 150 mm = 18750 mm^2) corresponds to about six DEWS specimens (6 x 108 m x 30 mm = 19440 mm^2), a better comparison with the beam ligament can be obtained by averaging the DEWS results coming from the same beam tested in bending, as shown in Figure 94. In subsection 3.3, a comparison between DEWS results and the tensile constitutive law obtained from flexural tests is carried out.

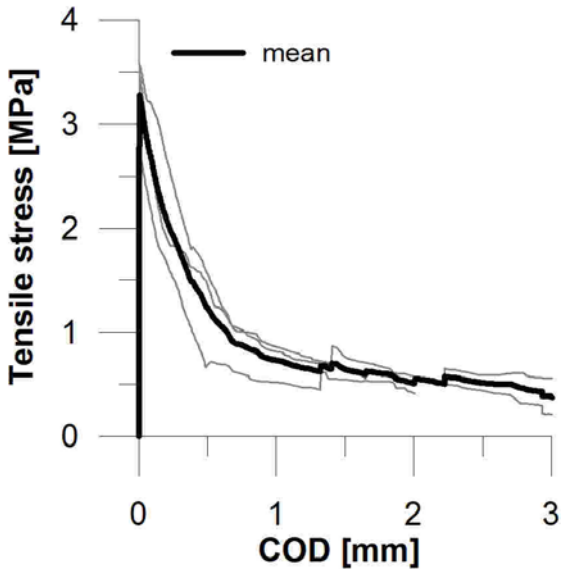

Figure 94 - DEWS experimental results of 10-year-old specimens.

Some important observations coming from the comparison with direct tensile tests of 1-year-old material can be stated looking at the peak tensile strength and at the post-peak softening behavior. In the direct tensile test, in contrary to the indirect tensile test, the entire specimen is subjected to tension. In DEWS test, a tensile stress is induced at the ligament by the application of an external compressive load. In addition, in the UTT, the experiments were performed with specimens glued to fixed-end platens, while in the second case, the specimens were free to develop in- and out of plane rotations. The difference between the flexural stiffness due to the testing procedures explains the relatively higher peak strength of the direct tensile test and also the bump observed on the descending branch of the uniaxial tensile stress *vs.* COD curve.

According to Van Mier [122], the rotational stiffness of the specimen outside the crack zone determines its post-peak behavior. For fixed-end tensile test procedures, a characteristic bump occurs in the softening branch, which is largely dependent on the bending moment produced by the entire specimen-machine system interaction during the crack propagation. In DEWS tests, a gradual descending curve is observed, as occurs for rotational-ends direct tensile tests, as described in Van Mier [122]. Therefore, as stated by di Prisco et al [83], due to the rotations, there will always exist a strain gradient over DEWS ligament which has to be taken into account by making an inverse analysis if an “exact” stress-COD relation according to fracture mechanics concept should be identified.

The post-peak behavior of the two tests is also influenced by the crack opening displacement control adopted in each test. In the direct tensile test, COD values represent the averaged values of three LVDT’s placed astride the specimen (see Colombo [6]). According to the crack opening distribution along the cross-section, qualitatively represented in Figure 95a, these measurements refer to the maximum crack opening available on the cross-section. On the contrary, in DEWS test, COD values are measured at the mid-section, thus reflecting crack opening closed to mean values, as shown in Figure 95b.

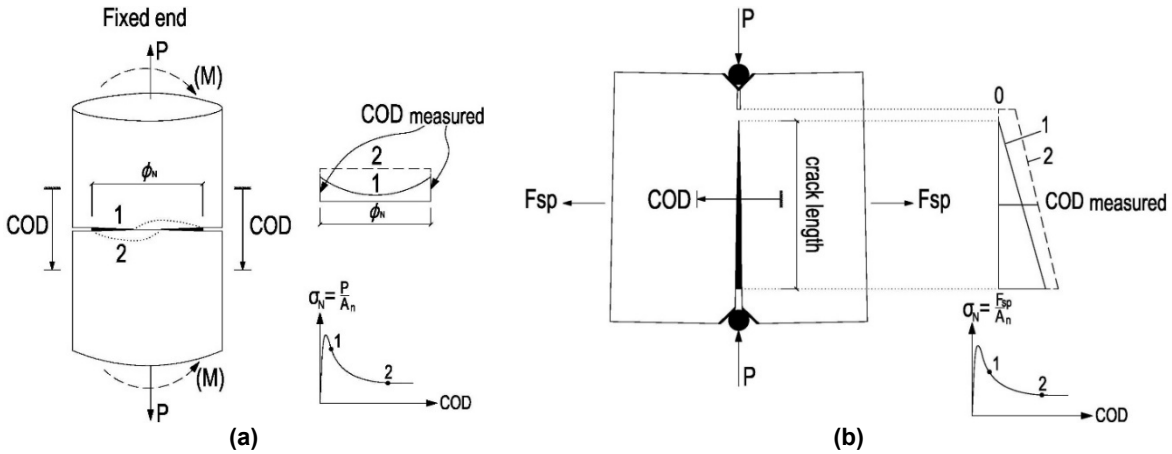

Figure 95 - Crack opening displacement measurements: a) direct tensile test; b) indirect DEWS test.

5.5 Aging effects

Concrete aging is an important characteristic of cementitious materials, which tends to continuously increase its strength over the years due to cement hydration process and CSH bond strength increase. However, the improvement in concrete micromechanical properties does not occur uniformly, since the characteristics of the microstructure of fibers interfacial transition zone (ITZ) differs from the one of the bulk cement. As reported by Chan et al [123], fibers ITZ are markedly weaker compared to the bulk matrix due to the higher porosity and the formation of large CH crystals. Hence, one can expect that the strength gain increases more in the bulk cement in relation to the fiber-matrix interface.

In order to observe aging effect, 4PB average values of beams with 1-year-old (Colombo [6]) and 10-year-old are compared in Figure 96.

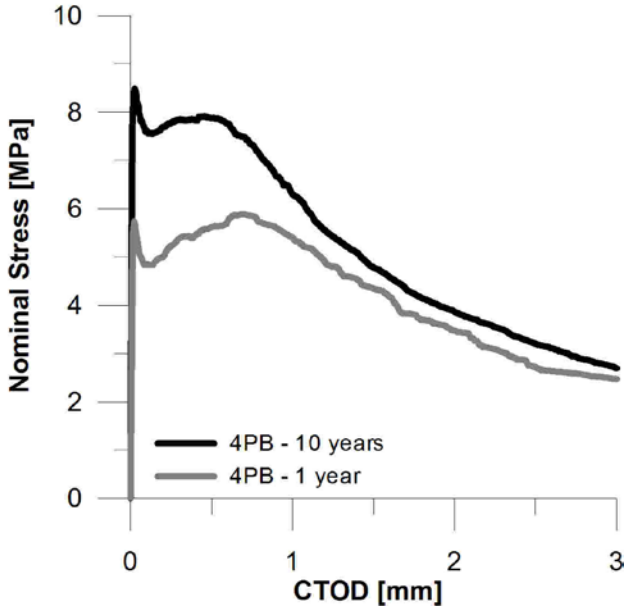

Figure 96 - Comparison between four-point bending tests of 1- and 10-year-old beams.

The comparison shows that the first post-peak slope of the 10-year-old material presents a smaller plateau in relation to the younger material. The peak stress and first

post-peak behavior have a pronounced gain in strength, demonstrating an increase in material toughness. However, this was not true for the softening branch with large crack openings, which shows only a small increase in the residual ULS strength ($f_{r3,k}$, w=2.5 mm). These results demonstrate that final pull-out mechanism is scantly affected by aging.

The increase in the material toughness can also be observed from the results of the tensile tests. Comparing the first branch of the σ_N *vs. COD* post-peak curve (0-0.5 mm) of both direct (Figure 93) and indirect tensile tests (Figure 94), the fracture energy of the 10-year-old material is higher in relation to the 1-year-old. It is important to point out that a direct comparison between the two types of experiments should take into account that DEWS tests reflect COD mean values along the ligament, while direct tensile test measures the maximum crack opening displacement over the cross-section. It is important to note that this difference is important mainly in the first crack propagation.

One important conclusion is that fiber pull-out effectiveness is not reduced due to concrete long-term aging, guarantying a structural ductile response during the whole structure life. In contrast, if a high increase in bond strength would be observed, this could reduce fibers efficiency, since collapse could occur due to fiber failure and not due to fiber continuous bond slip. As a result, the structural behavior could present a progressively embrittlement.

Test results of fiber reinforced shotcrete (FRS) round panels from Bernard [124] have demonstrated that macro-synthetic FRS exhibited a slightly increase in the post-peak strength without any change in the fibers resisting mechanism and in accordance with the experimental results of this thesis. On the contrary, hooked-end steel FRS exhibited a substantial decrease in the post-peak strength at wider crack widths due to a progressively embrittlement with age, leading to fibers rupture.

In conclusion, FRC softening behavior seems to be much less dependent on the contribution of the matrix and much more dependent on fiber bond properties. Concrete peak strength is dependent on the matrix tensile strength, while concrete post-peak strength at SLS (f_{R1}, CMOD=0.5 mm) depends largely on the matrix properties (aggregate interlock) and much less on the fibers due to their progressive activation before the effect of pull-out is fully developed. On the contrary, in the softening branch of the uniaxial tensile stress *vs.* COD curve, fibers are fully engaged and the concrete response depends largely on fiber bond properties, which includes both the physical and chemical adhesion and, in case of hooked-end fibers, the mechanical anchorage. These effects are localized and comprise a much smaller concrete surface area in relation to the bulk matrix.

5.5.1 Material class

The characteristic value (X_k), according to Eurocode [99], was described in subsection 2.1.3 (see Eq. 21) and the material classification, according to fib Model Code 2010, was shown in subsection 2.1.4.

According to Eurocode [99], the coefficient of variation (V_x) can be considered as known or unknown respectively if previously determined experimental results on the same material are available or not. In the case investigated, bending tests were carried out in two different periods of time (1 year and 10 years) using the same material and the same standard test procedures. In this way, V_x is supposed to be unknown in one

period of time and known in the other. Since the tests performed at 10 years have a larger number of specimens and, as a result, a better statistical representation of the material mechanical behavior, V_x was supposed to be unknown. The characteristic values were calculated using the standard deviation obtained from those tests. For the bending tests at 1 year, V_x was supposed to be known and equal to the largest values measured at 10 years (safe side), which corresponds to those obtained for the 3PB tests. The characteristic values were calculated using those V_x values and Km factor corresponding to a known V_x.

This assumption was made because no discrepancies with regard to variation are expected from one material to another due to the aging effect. It is important to take into account that all the beams were cast on the same day, adopting the same casting procedure. Moreover, Eurocode [99] states that a known V_x should be used if the coefficient of variation or a realistic upper bound of it is held from prior knowledge. In this case, the prior knowledge comes from the evaluation of previous tests (at 10 years) in comparable situation (same material and same standard test procedures).

If one considers the coefficient of variation obtained separately from each bending test at 10 years, different classes of material will be attained. In this experimental campaign, a higher class was achieved for the beams in 4PB tests. The values of K_m together with the classification of the materials are shown in Figure 97.

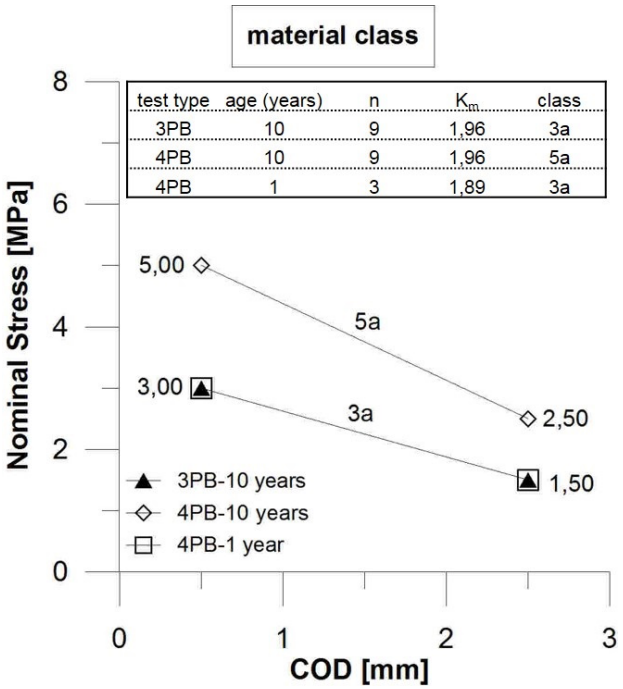

Figure 97 - Classification of the material according to fib Model Code 2010 ([101], [78]).

Finally, it is important to underline that a minimum ratio f_{R3k}/f_{R1k} equal to 0.5 is accepted in the *fib* Model Code 2010 [78] and, therefore, a reduction of f_{R1k} is introduced if f_{R3k}/f_{R1k} is less than 0.5.

Comparing the material evolution through the years, one can observe that the post-peak response does not change and continues in the lower bound limit of the material class. The better performance of the composite is solely due to the increase in the peak strength and first post-peak stress ($f_{R1,k}$). This can be attributed to the

improvements on the matrix properties because of long-term aging, rather than on fibers bonding.

5.6 FRC tensile constitutive law

FRC constitutive law was defined according to *fib* Model Code 2010 ([101], [78]). It is important to underline that the tensile constitutive law, in terms of σ_N *vs. COD,* is based on the 4PB tests for the material at 1 year. The tensile constitutive law was compared with direct and indirect DEWS tensile experimental results respectively at 1 year (see Colombo [6]) and 10 years.

Figure 98a presents a comparison between the tensile constitutive law and direct tensile test results on 1-year-old specimens. Figure 98b shows the comparison between the constitutive law and DEWS experimental results on 10-year-old specimens. In both cases, the tensile constitutive law is described in terms of characteristic and design values ($X_d = X_k/\gamma_F$; $\gamma_F = 1.5$).

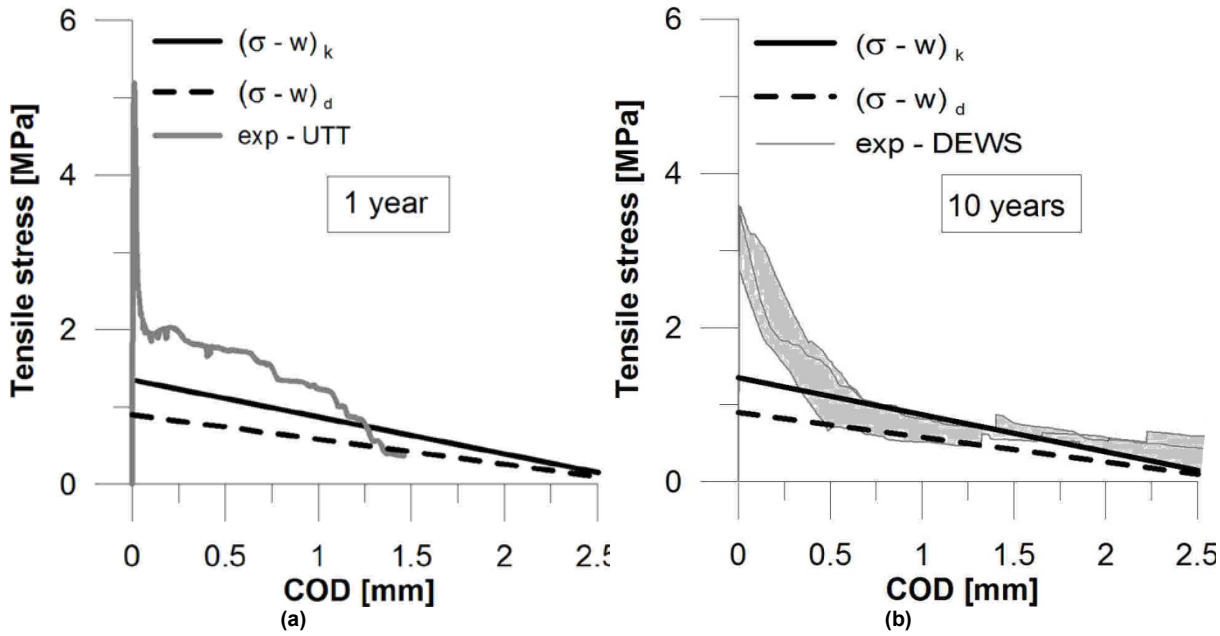

Figure 98 - Comparison between the tensile constitutive law and tensile tests: a) direct tensile test of 1-year-old specimens; b) indirect tensile test (DEWS) of 10-year-old specimens.

It is important to remember that DEWS test type, due to the boundary conditions, has a lower rotational stiffness in relation to fixed end direct tensile tests. In the latter case, the crack propagation is hindered after cracking, due to the additional constrains imposed in the specimen because of the fixed-end platens and the appearance of bending moment reactions (see the effect in Figure 95). On the contrary, DEWS specimens are free to develop in- and out-of-plane rotations and at the onset of cracking, all the potential energy stored in the system is released at once though the entire ligament, leading to a crack propagation throughout the weakest portions of the ligament surface. As a result, a higher decrease of the first slope of the post-peak curve is attained. The bump in the post-peak curve observed in the uniaxial tensile test is due to the closing bending moment acting immediately after crack initiation.

Moreover, the tensile constitutive law obtained from the 4PB tests can only be partially correlated to DEWS σ_N *vs. COD* values since the compared fracture plane area are not the same for the two tests. In the latter case, the results of three specimens are averaged (3 x 108 mm x 30 mm = 9720 mm^2), which corresponds to only 62% (A_{DEWS}/A_{4PB} = *9720/15750*) of the beam fracture area. In this particular case, a close correlation can be obtained with five DEWS specimens (*5 x 108 mm x 30 mm = 16200* mm^2).

In conclusion, it is possible to say that both tests demonstrate that the procedure adopted to find the tensile constitutive law, based on the material classification, are reasonable and on the safe side.

5.7 Plane section prediction

A plane section (PS) non-linear analysis was carried out taking into account the tensile constitutive law derived from the material classification at 1 year. The choice of this approach is due to its simplicity and reliability for determining the mechanical response of composite structural members in bending. The hypotheses considered herein are the Bernoulli law (plane sections remain plane after deformation) and quasi-static monotonic loads.

Regarding the tensile constitutive law, a bilinear stress-strain relation, with a linear elastic pre-peak followed by a linear softening post-peak, was assumed taking into account the material class. The strain was calculated taking into account Hillerborg [125] cohesive-fracture concept generalized by means of the characteristic length ($w=l_{cs}\cdot\varepsilon$) (Bazant and Cedolin, [126]; Barros et al, [127]; Kooiman et al, [128]; Hordjik, [129]). In this case, according to *fib* Model Code 2010, the structural characteristic length is considered equal to the beam depth (di Prisco et al, [78]). Saenz stress-strain model was adopted for the compressive behavior.

The comparison between the predictions and 4PB tests results, considering 1- and 10-year-old materials (Figure 99), demonstrates that the response prediction remains always on the safe side in bending considering both characteristic and design parameters. It is worth noting that the plane section approach does not consider any notch effect and in the pre-peak, the PS model exhibits a lower peak strength value since the contribution of the matrix (f_{ct}) was not taken into account in the constitutive law.

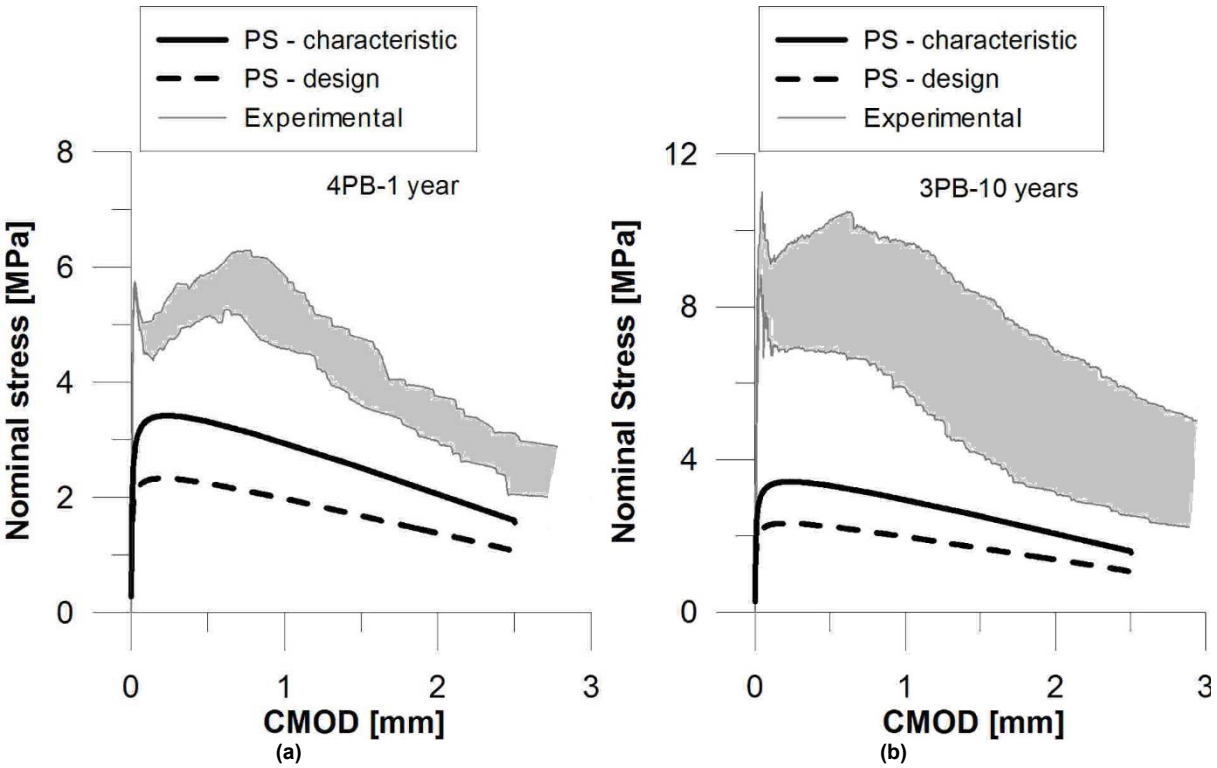

Figure 99 - Comparison between bending tests and numerical plane section analyses: a) 4PB results of 1-year-old specimens; b) 3PB results of 10-year-old specimens.

CHAPTER 6

Mesoscopic numerical modelling

A mesoscopic model has the advantage to incorporate concrete heterogeneous phases, taking into account strain incompatibilities in the aggregate-cement paste interface. As stated by Fu and Li [28], concrete thermal cracking process cannot be numerically modeled without considering concrete heterogeneity and the introduction of a thermo-mechanical damage model at mesoscopic level. Moreover, the different LITS sources (chemical, physical and mechanical processes) developed in the concrete phases (aggregates, matrix, ITZ) can be properly modeled in the mesoscopic level.

In order to better understand transient creep phenomenon, using LITS approach, a 2D three-phase mesoscopic analysis is carried out. It is worth mentioning that LITS strains are originated from concrete physical-chemical transformations during the heating process, as shown in Figure 100.

In the thesis, concrete is recognized as a heterogeneous biphasic material (aggregates + matrix) and LITS is described as the sum of thermochemical (matrix drying and dehydration) and thermomechanical (microcracking, aggregate degradation and thermal expansion restraint) strains.

Concrete thermochemical transformations develop mainly in the cement paste. In turn, microcracking starts in the interfacial transition zone (ITZ), around the aggregates (tangential and radial cracks) due to thermal incompatibilities with the cement paste. At high temperatures, the diffused microcracks coalesce, creating localized macrocracks within the matrix. The aggregate surface is also subjected to microcracking in the early stages of heating. At elevated temperatures, according to Hager [41], its physical-chemical structure changes, giving rise to macrocraks and an increasingly ductile behavior.

In the numerical analyses, LITS is analyzed by uncoupling the different strain contributions (thermochemical and thermomechanical processes) in three components: aggregate geomechanical properties decay with temperature increase, matrix thermomechanical properties decay as function of temperature and the effect of the boundary conditions on concrete (thermal expansion restraint). In this approach, drying creep and microcracking are implicit in the model.

The numerical results are compared with Khoury [116] experimental values in order to validate the model. A comparison between the numerical results and the proposed LITS semi-empirical model is also performed in order to validate the model.

A parametric analysis is carried out in order to identify the most sensitive parameters, taking into account different aggregate distributions and changes in the mechanical properties of the concrete phases.

The path dependence, considering preloaded and preheated specimens, as shown in Figure 101, is studied in order to observe the influence of the thermal expansion restraint on LITS.

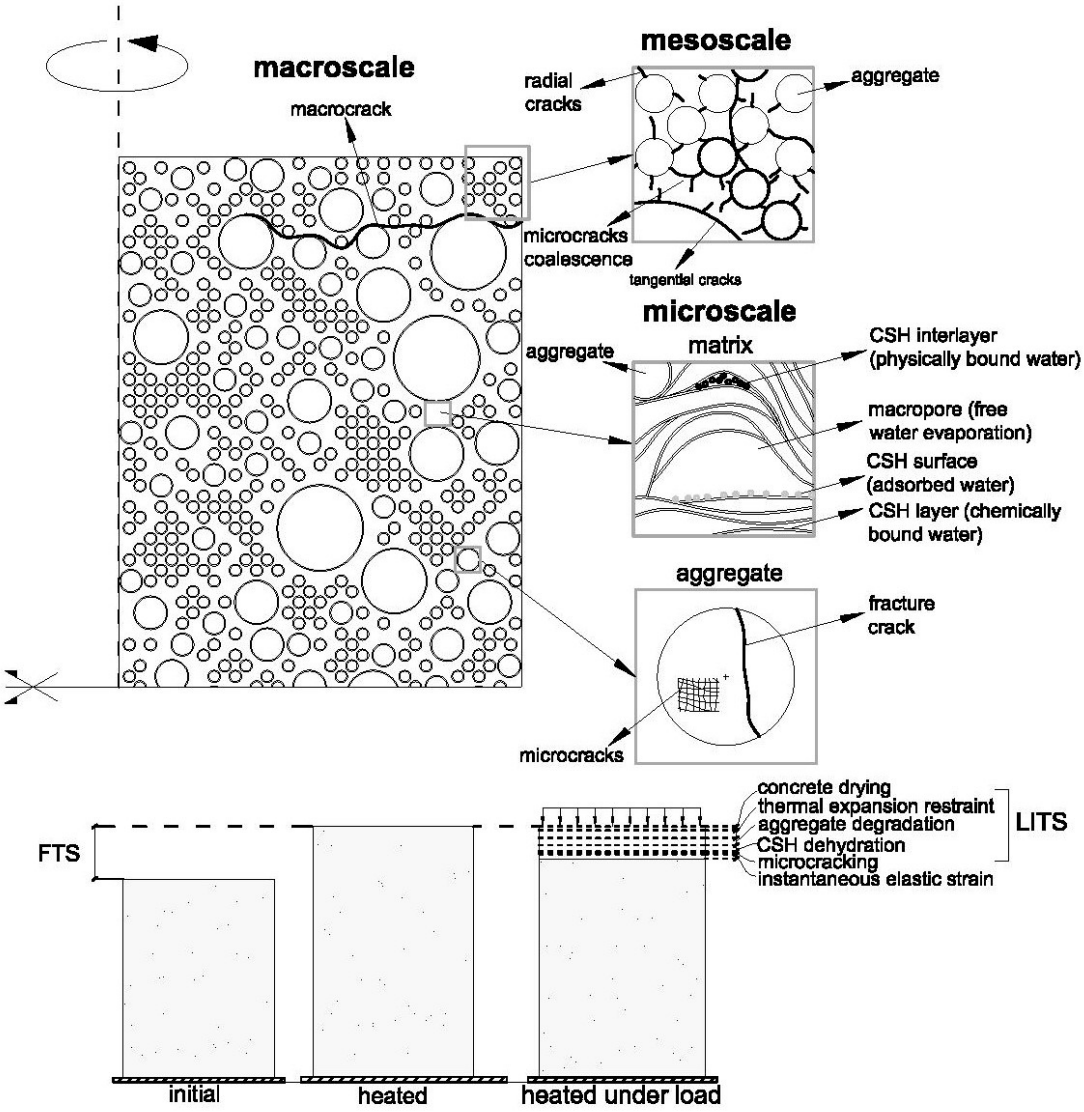

Figure 100 - Concrete physical-chemo-mechanical processes at high temperature.

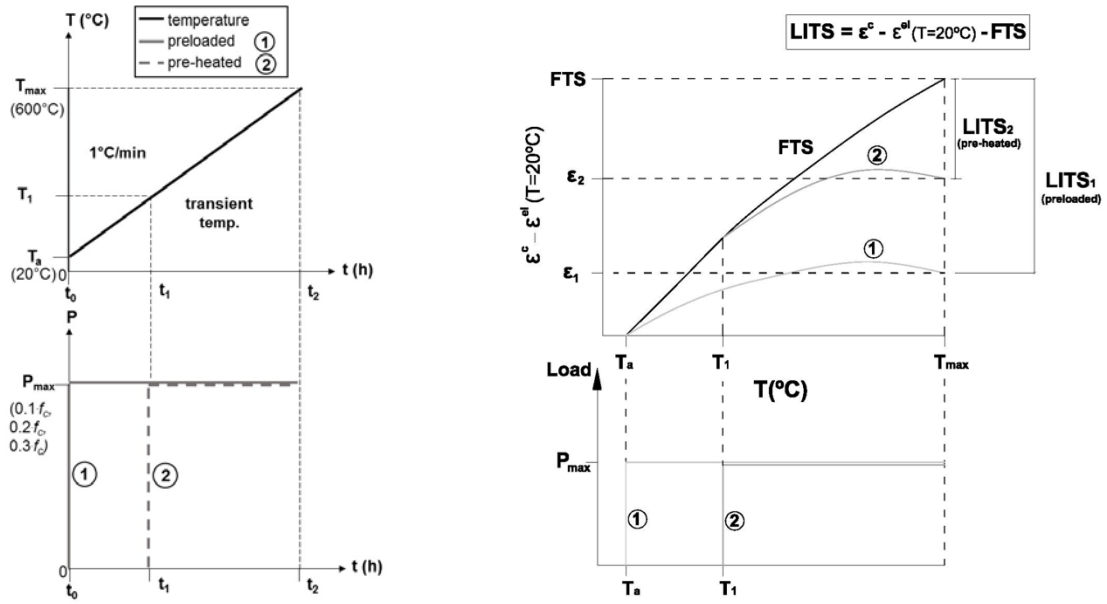

Figure 101 - Numerical analyses considering two load paths.

6.1 Mesoscale modeling

According to Kim et al [130], aggregate volume fraction and ITZ mechanical properties are the key parameters that control the overall macroscopic concrete response and the fracture process evolution. On one hand, the aggregate plays an important role in crack distribution, which tends to be more localized as the aggregate volume increases (Kim et al, [130]). On the other hand, the aggregate distribution has negligible effects on the concrete overall mechanical response. Uniaxial tensile tests using Monte Carlo simulation carried out by Wang et al [131] have shown that the pre-peak and the peak stresses are insensitive to the aggregate distribution, but the post-peak curve is much more sensitive due to microcracks coalescence and macrocracking tortuous propagation around the aggregates.

Aggregate size distribution can be obtained by applying the Fuller curve for 3D models or the cumulative distribution function derived in Walraven [132] for 2D models.

Aggregate spatial distribution can be simulated with two distinct methods, i.e., the “take-and-place” and the “divide-and-fill” methods. In the former case, the aggregates are distributed within the matrix from the largest to the smallest ones following the sieving curve (De Schutter et al, [133]). The latter method divided the model into separated areas, filling them with aggregates according to a predefined grading curve.

Aggregate placing can follow, for example, Bazant [134] procedure, which consists in a normal random generation of particle coordinates, rejecting the overlapping ones (aggregate collision). More refined methods adopt, for example, the Monte Carlo simulation (Wrigger and Moftah [135]; Wang et al, [136]; Wang et al, [131]). In any case, a proper representative volume element (RVE) should be adopted in order to accurately represent concrete microstructure without changing its macroscopic properties.

Aggregate shape can assume circular, quadrangular or polygonal forms. Circular aggregates tend to give a higher strength compared to irregular ones, which are prone to stress concentrations on the edges (Kim et al, [130]; Wang et al, [131]). Besides, as stated by Kim et al [130], a small difference in the predictions of the overall tensile

strength and strain capacity was observed in the numerical analyses with different shapes of aggregates.

The ITZ, according to Kim et al [130], is highly heterogeneous and highly damaged due to pre-existing voids and microcracks and, hence, it is very important to properly define its tensile and compressive behavior. As the strength increases, more cracks are propagated through the matrix, resulting in a more brittle behavior and a linear increase of concrete ultimate tensile strength. Grondin et al [137] demonstrated by 2D three-phase mesoscopic analyses that, when the ITZ has the same tensile strength of the matrix, the results are closer to the macroscopic experimental tests and, when the ITZ has a lower tensile strength compared to the matrix, the results are closer to the microscopic inspection tests.

The ITZ cracking evolution can be modelled by diffuse (smeared crack) or localized (cohesive and discrete crack) models. Cohesive zone modelling imposes major challenges to properly determine the associated material parameters, which are highly dependent of the experimental data of ITZ traction-separation behavior.

It is worth mentioning that ITZ thickness varies from 0.2mm to 0.8mm and increasing the thickness in this range may have no effect to the global concrete strength (Kim et al, [130]).

6.2 Numerical modelling description

A 2D three-phase axisymmetric mesoscopic analysis was performed using *Abaqus* software, where the ITZ corresponds to the interfacial transition zone between the aggregates and the matrix, the inclusions represent the coarse aggregates and the matrix represents the cement paste with fine aggregates. The aim is to observe the contribution of each concrete phase to LITS. The results are compared with experimental data from Khoury [116]. Concrete mix design and aggregate size distribution are shown respectively in Table 12 and Table 13.

Table 12 – Concrete mix design

	fine aggr./cement	**coarse aggr./cement**	**cement (kg/m^3)**	**f_c (MPa)**
Khoury [116]	1.8	2.7	415	61

Table 13 – Aggregate size distribution [116]

Aggregate type	**Unit**	**Content**
coarse (max. 10 mm)	kg/m^3	1120
sand	kg/m^3	750

A Matlab algorithm was developed for the aggregate placing taking into account the “take and place” method. The model adopts circular aggregate shape and a normal random distribution as described in Bazant [134]. From Table 13, aggregate size distribution was calculated according to a cumulative distribution function (P_c) (Walraven, [132]), as shown in Eq. 49, where: D_i is the aggregate diameter in mm; D_{max} is the maximum aggregate diameter in mm; and P_k is the ratio of the total weight of aggregates and concrete weight.

$$P_c = P_k \times \left(1.065 \times \left(\frac{D_i}{D_{max}}\right)^{0.5} - 0.053 \times \left(\frac{D_i}{D_{max}}\right)^{4} - 0.012 \times \left(\frac{D_i}{D_{max}}\right)^{6} - 0.045 \times \left(\frac{D_i}{D_{max}}\right)^{8} - 0.025 \times \left(\frac{D_i}{D_{max}}\right)^{10}\right) \quad (49)$$

From the aggregate size distribution (Eq. 49), aggregate numbering (Table 14) was determined according to Eq. 50, where: ΔP_c is the aggregate volume fraction referred to the aggregate diameter; A_c is the bulk concrete area; and $A_{aggr,i}$ is the area of the referred aggregate. Aggregates smaller than 1 mm are considered implicitly in the matrix.

$$N_i = \Delta P_c \times P_k \times \frac{A_c}{A_{aggr,i}} \quad (50)$$

Table 14 - Aggregate numbering

D(mm)	Number	D(mm)	Number
1	912	6	4
2	66	7	2
3	24	8	2
4	11	9	1
5	6	10	0

The aggregate placing takes into account the “wall effect”, i.e., all aggregates located outside or on the specimen boundaries are relocated within the concrete volume limits, as shown in Figure 102. In order to avoid internal overlapping, new coordinate pairs were generated in case of aggregate collision.

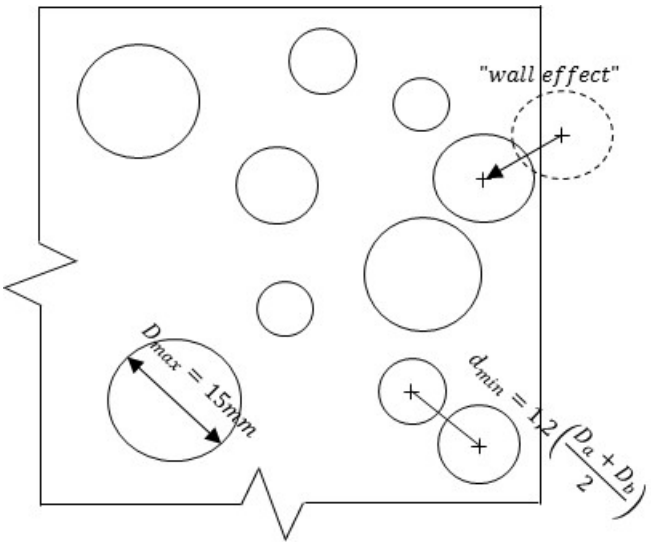

Figure 102 – Aggregate placement.

An ITZ thickness of 0.1 mm was adopted, while the minimum distance between the centers of two aggregates was defined as $1.25 \cdot (D_a+D_b)/2$.

The numerical model dimensions, including aggregate distribution and monitoring points, are shown in Figure 103.

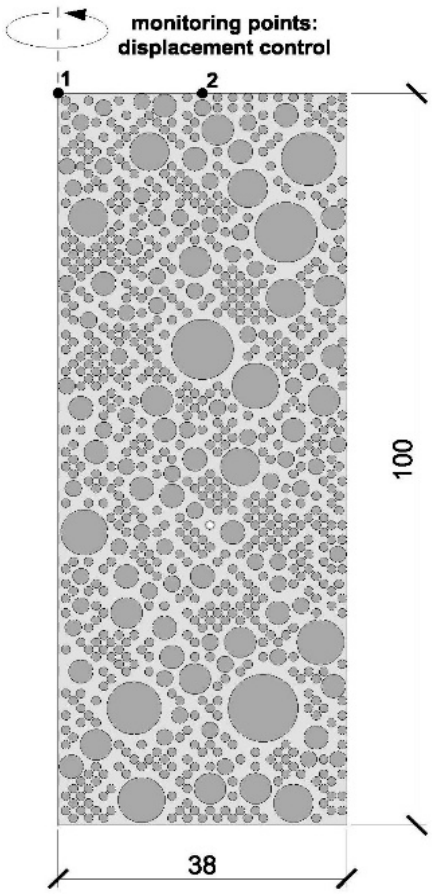

Figure 103 – Abaqus 2D mesoscopic model.

6.3 Concrete thermomechanical properties

The greatest challenge undergone in the numerical analyses was the appropriate definition of the aggregate mechanical parameters, since a large variability among and within the different types of aggregates (limestone, siliceous, basalt, recycled, lightweight) is found in literature. It is important to underline that aggregate mechanical properties decay due to high temperature have a direct effect on LITS behavior, especially LITS acceleration beyond 400ºC due to aggregate physical-chemical transformations (Sygała et al, [118] and JianPing et al, [138]).

The numerical model adopts a bilinear elasto-brittle behavior for the aggregate with a progressive thermomechanical decay. The geomechanical properties were based on Sygala et al [118] taking into account the aggregate type (basalt rocks). In this case, the strength was kept constant up to 400ºC, while the Young's Modulus decreased with temperature in order to represent aggregate softening behavior.

For both the matrix and the ITZ, an elasto-perfectly plastic constitutive law in uniaxial compression was adopted. The mechanical properties of concrete phases are shown in Table 15.

Table 15 – Thermomechanical properties of concrete phases

phase	T (°C)	E (GPa)	f_c (MPa)	ε_u	f_t (MPa)	
matrix	20°C	35	50	0.0035	4	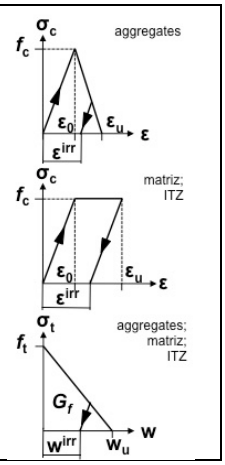
	200°C	29.79	45	0.004	3.4	
	400°C	17.50	39	0.005	2	
	600°C	7	19	0.006	0.6	
aggregate	20°C	80	200	0.005	17	
	200°C	70	200	0.0075	17	
	400°C	55	200	0.01	12	
	600°C	20	120	0.01	4	
ITZ	20°C	27	40	0.0035	3.4	
	200°C	23	38	0.004	2.89	
	400°C	13.50	30	0.005	1.6	
	600°C	5.4	14	0.006	0.51	

Due to the lack of more precise values, a constant fracture energy in uniaxial tension equal to 0.1 N/mm was adopted for the concrete phases. This assumption does not have any impact to the global results, since the cracking strains are very small compared to the total deformation and the crack opening is restrained by the sustained compressive load. Concrete residual properties were based on (Menou et al, [139]; Noumowé et al, [140]; Odelson et al, [141]; and Kim et al [130]).

As stated by Fu [142], no satisfactory model can be used to simulate the thermal cracking process in the heated concrete due to the complexity of the material structure. For example, the introduction of a cohesive crack model needs the implementation of interface elements in the matrix continuum or other complex strategies such as cohesive segments techniques as described in Pérez et al [143] and Remmers et al [144]. Hence, the numerical modeling did not take into account a specific crack model and it is based on *Abaqus* concrete damaged plasticity (parameters are shown in Table 16).

Table 16 – Abaqus concrete damaged plasticity parameters

dilation angle	eccentricity	f_{b0}/f_{c0}	K	viscosity parameter
38	1	1.12	0.6	0

This simplification has limited effects on LITS global numerical results, since, in this particular case, the specimen is subjected to a uniaxial compressive stress state and the total deformation, induced by the boundary conditions (temperature and compressive load), is much higher in relation to the cracking strains. The most important phenomena to be properly modeled are the thermal mismatch due to matrix-aggregate different coefficients of thermal expansion and the thermomechanical properties decay, which is mostly related to the strength decay and the damage evolution of the different concrete phases. These effects can be modeled with good accuracy using concrete plasticity model.

The thermal properties and density of the different concrete phases are shown in Table 17, while the coefficient of thermal expansion (CTE) as function of temperature is shown in Table 18. Aggregate, matrix and ITZ thermal strains, according to their respectively coefficient of thermal expansion, are shown in Figure 104.

Table 17 – Concrete phases thermal properties

Concrete phase	conductivity (N·mm/(mm*C)	specific heat (N·mm·s/(kg*C)	Density (kg/mm^3)
matrix	2	1.17 x 10^6	1.92 x 10^{-6}
ITZ	2	1.17 x 10^6	1.92 x 10^{-6}
aggregate	4	1.17 x 10^6	2.60 x 10^{-6}
Stefan Boltzmann constant (J*m^{-2}*s^{-1}*k^{-4}): 5.67*10^{-8}			

Table 18 – Coefficient of thermal expansion

T (°C)	CTE (x10^{-6})		
	aggregate	matrix	ITZ
20	1.3x10^{-5}	5x10^{-8}	5x10^{-8}
600	3.9x10^{-5}	-5x10^{-8}	-5x10^{-8}

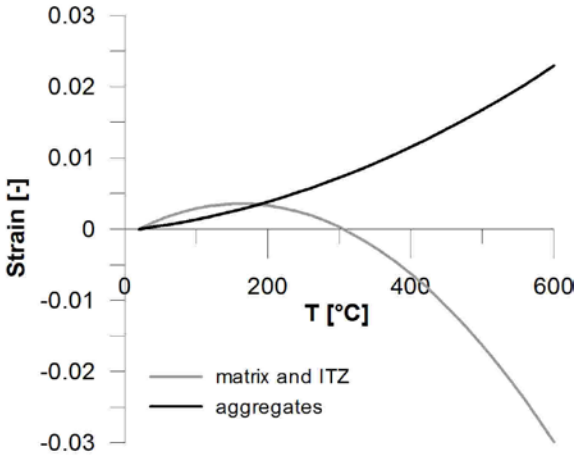

Figure 104 – Concrete phases (aggregate, matrix and ITZ) thermal strains.

A 4-node axisymmetric (CAX4T) FE mesh with coupled temperature-displacement with a global size of approximately 0.8 mm was adopted.

6.4 Numerical results

The numerical investigation includes a parametric study to observe the sensitivity of the model to different parameters, an analysis of the different strain contributions to LITS and the path dependence (load path). A comparison between the numerical results and the proposed LITS semi-empirical model is also carried out in order to validate the model.

It is important to underline that concrete thermo-elasto-plastic behavior was determined based on estimated values due to the lack of information about the thermomechanical properties of Khoury [116] tested specimens. Hence, a better approximation between experimental and numerical global macroscale values are expected in relation to the mesoscale uncoupled strain results.

Moreover, the numerical model does not assume an explicit cracking model (complete separation of the aggregate-matrix interfacial transition zone), neither takes into account the fluid transport phenomena. As a result, cracking strain and drying creep are considered implicitly in the model.

6.4.1 Parametric analysis

Overall 11 numerical analyses were carried out considering different aggregate distributions and different variations on the mechanical properties of the concrete phases, as described in Table 19. In all cases, the load level was equivalent to $0.2 \cdot f_c$.

Table 19 - Description of the numerical analyses

	phase	condition	n° models
random aggregate generation	-	-	5
mechanical properties variation (f_c, f_t, E)	ITZ	ITZ = matrix	1
		ITZ > matrix	1
	matrix	+ 25%	1
		- 25%	1
	aggregate	+ 25%	1
		- 25%	1

A comparison between the numerical analyses and the experimental results from Khoury [116] in terms of total strains - $\varepsilon^c(T)$ - minus the initial elastic one - $\varepsilon^{el}(T = 20°C) = \sigma/E_0$ -, considering five different aggregate random distributions and three load levels ($0.1 \cdot f_c$, $0.2 \cdot f_c$, $0.3 \cdot f_c$) are shown in Figure 105a, together with the coefficient of variation (CoV). A good agreement between experimental and numerical values was obtained. The highest coefficient of variation was found for specimens loaded at $0.1 \cdot f_c$ (CoV > 64%) and the smallest ones were obtained for unloaded and loaded specimens at $0.3 \cdot f_c$ (CoV < 20%).

If the results are compared in terms of LITS, as shown in Figure 105b, the CoV decreases significantly. For an equivalent load of $0.1 \cdot f_c$, the CoV was smaller than 20%, while for higher load levels, the CoV remained below 10%. Hence, the high scattering observed in the total strain values due to different aggregate distributions had a small impact on LITS results.

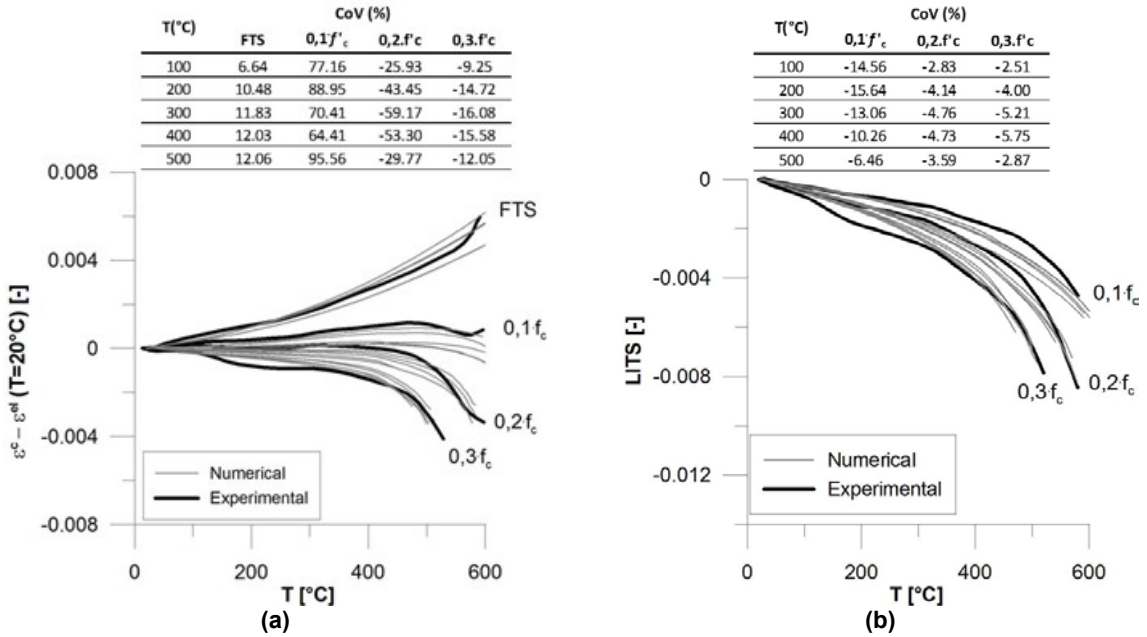

Figure 105 - Comparison between experimental [116] and numerical results for different aggregate distributions: a) total strain minus initial elastic one at 20°C versus temperature; b) LITS versus temperature.

A comparison considering variations on the mechanical properties of the aggregates, matrix or ITZ in terms both of total strains minus the initial elastic one at 20°C and LITS are shown respectively in Figure 106 and Figure 107. The reference is the same numerical model with the same aggregate distribution before the variation of concrete mechanical properties. On one hand, changes in the mechanical properties of the ITZ (increase in the strength and Elastic Modulus respectively by +25% and +56% compared to the reference model) lead to a comparable increase in the total strains, as shown in Figure 106a. On the other hand, LITS results were scantly affected, as shown in Figure 107a.

The highest sensitivity was observed in the total strains due to changes in the matrix and aggregate mechanical properties. In these two cases, a variation of ±25% in the mechanical properties led to a difference higher than 40% in the total strain, reaching 70% in the case of the aggregates (Figure 106b) and 109% in the case of the matrix (Figure 106c). On the contrary, in both cases, LITS scattering remained relatively small (less than 10%), as shown in Figure 107b and Figure 107c.

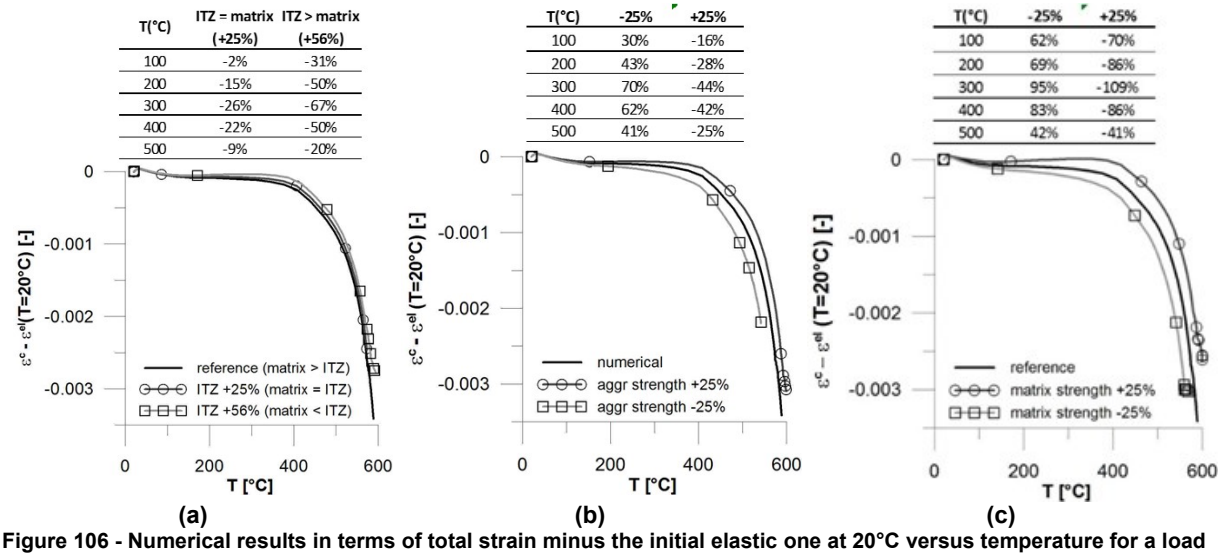

Figure 106 - Numerical results in terms of total strain minus the initial elastic one at 20°C versus temperature for a load level of 0.2·f_c:and different mechanical properties: a) ITZ; b) aggregate; c) matrix.

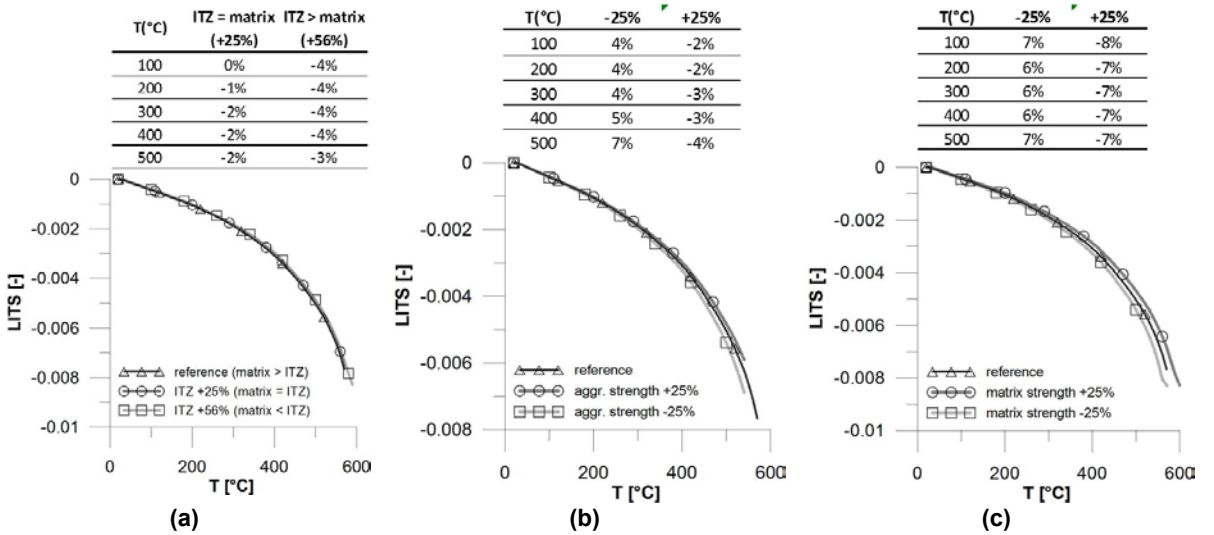

Figure 107- LITS results for a load level of 0.2·f_c and considering different mechanical properties: a) ITZ; b) aggregate; c) matrix.

In all these cases, the free thermal strain (FTS) had a negligible variation, as shown in Figure 108, since the thermal stresses (self-equilibrated) developed in the concrete during heating remained in the elastic limit (Figure 109a). In contrast, loaded specimens have shown high stress levels (Figure 109b to Figure 109d) with progressively more damage in the matrix as the stress level increases. For an equivalent load of $0.3 \cdot f_c$, high localized stresses in the aggregates were developed due to the confinement effect imposed by both the compressive load and the thermal incompatibilities between aggregate expansion and matrix shrinkage.

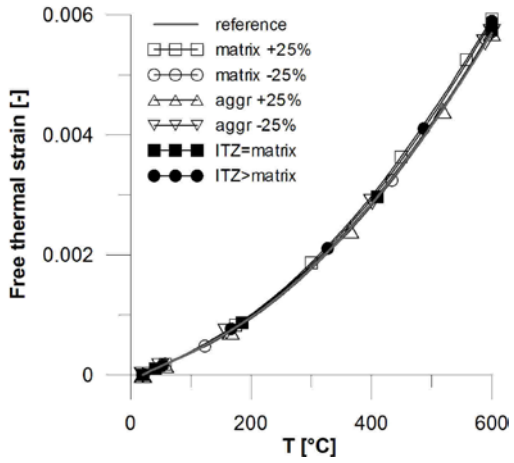

Figure 108 - FTS curves of the numerical analyses.

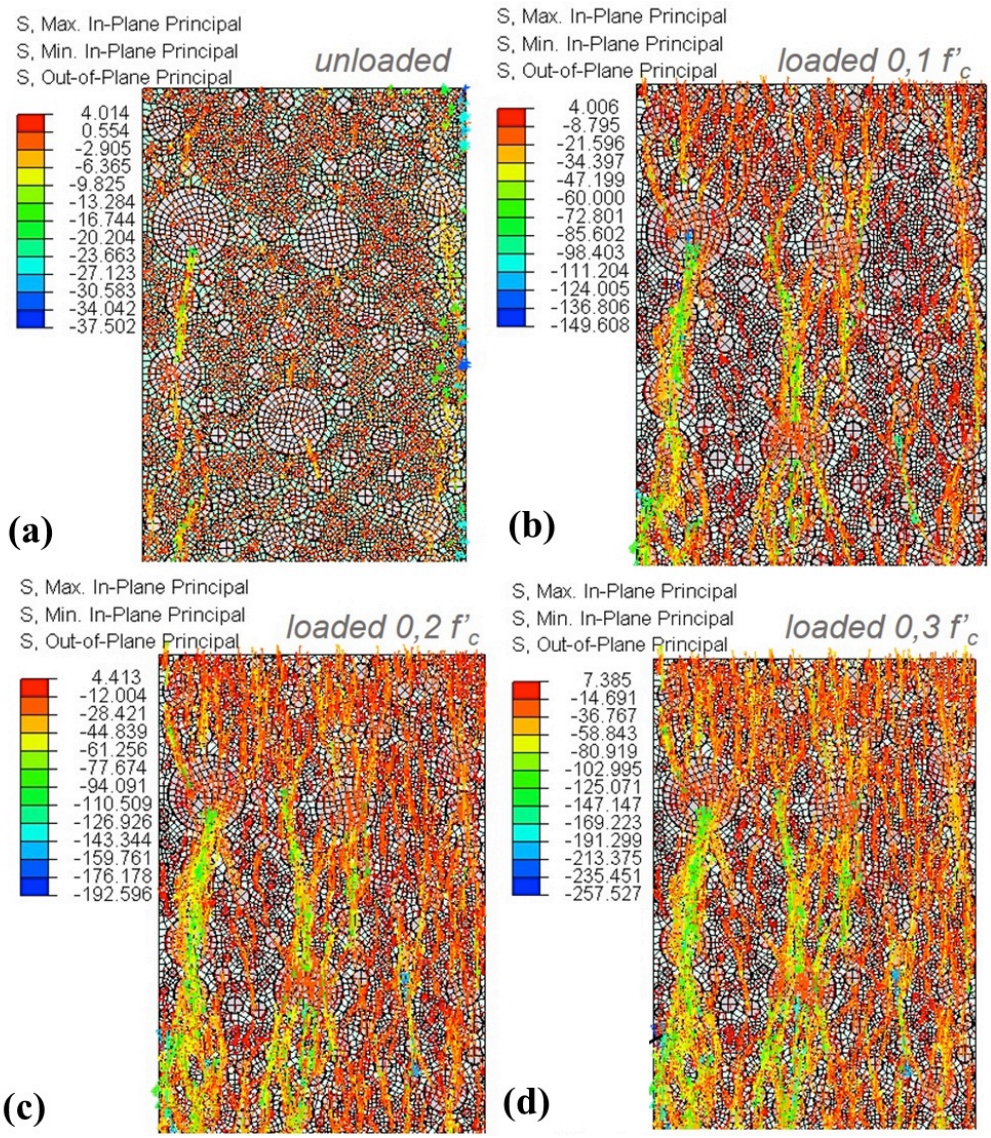

Figure 109 – Specimens stress distribution: a) unloaded; b) loaded at 0.1·f_c; c) loaded at 0.2·f_c; d) loaded at 0.3·f_c.

In conclusion, it is possible to state that variations on the mechanical properties of the concrete phases lead to a much higher scattering on the total strain values in relation to LITS. Moreover, both the matrix and the aggregates had the most sensitive response to variations on their mechanical properties in relation to the ITZ, which has shown the smallest variability.

6.4.2 LITS strain components

The aim is to uncouple LITS into three main components by means of a 2D three-phase mesoscopic analysis, as described in Eq. 51, where: $LITS_{agg}$ is the effect on LITS of aggregate geomechanical properties decrease as function of temperature; $LITS_{mat}$ is the effect on LITS of matrix thermomechanical properties decrease as function of temperature; $LITS_{bc}$ is the effect of the boundary conditions on concrete which imposes a thermal expansion restraint due to the application of a sustained

compressive load, neglecting any effect of the temperature on the matrix and aggregates.

$$LITS = LITS_{agg} + LITS_{mat} + LITS_{bc} \quad (51)$$

The aggregates (basalt, siliceous and calcareous), up to 600°C, do not exhibit a significant strength decay. However, due to physical-chemical changes in their microstructure, their behavior becomes increasingly ductile. In the numerical model, the softening behavior is modeled considering a decrease in the Modulus of Elasticity with the temperature and a strength decay above 400°C. In fact, the Modulus of Elasticity experiences a large decline between 400°C and 600°C, as described by Takarli et al [145] and Sygała et al [146].

In order to determine the aggregate and the matrix contributions to LITS, two independent analyses were carried out for each case, considering respectively the mechanical properties of the aggregate and the matrix dependent or independent on the temperature. By the difference between these two numerical results, the aggregate ($LITS_{agg}$) and matrix ($LITS_{mat}$) contributions to LITS were quantified. In Figure 110a, it is possible to observe the increase in the total strain due to aggregate thermomechanical decay, while in Figure 110b, LITS acceleration due to aggregate increasingly ductile behavior is clearly demonstrated.

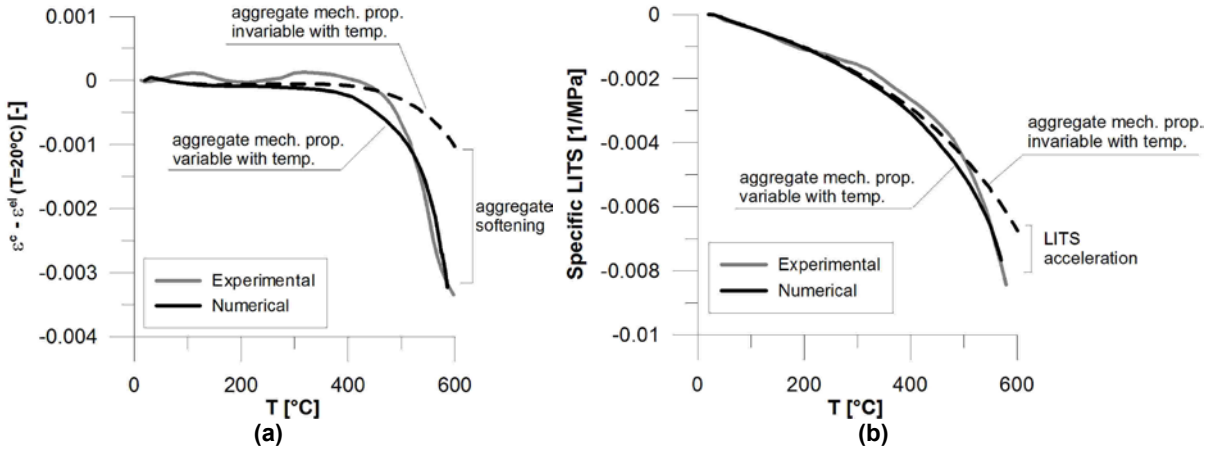

Figure 110 - Comparison between numerical and experimental [106] results for an equivalent load of 0.2.f_c: a) total strain minus the initial elastic one at 20°C versus temperature; b) LITS versus temperature.

The contribution of concrete thermal expansion restraint to LITS ($LITS_{bc}$) was determined by the difference between the numerical results in unloaded and loaded specimens, considering concrete mechanical properties independent of the temperature. In this approach, the effects of concrete softening behavior (thermomechanical decay) can be disregarded and the confinement behavior imposed by the boundary conditions can be isolated.

It is important to underline that changes in the mechanical properties of one concrete phase influences the overall behavior of the bulk concrete due to stress redistributions. Moreover, as the temperature increases, concrete behavior becomes increasingly inelastic (visco-plastic deformation). Hence, this method can lead to an overestimation of the total strain values. In order to check the reliability of this approach, the uncoupled LITS strains were added and compared to the results of the reference model. The reference is the same numerical model with the same aggregate distribution before the

variation of concrete mechanical properties. Table 20 shows the values of the uncoupled strains and the total strains for different load levels. LITS values correspond to the reference model and to the sum of the uncoupled strains.

Table 20 – LITS normalized numerical values: uncoupled and total strain values for different load levels

T(°C)	load level	$LITS_{bc}$	$LITS_{agg}$	$LITS_{mat}$	LITS (sum)	LITS (reference)
100	$0.1 \cdot f_c$	0.078	0.0005	0.005	0.083	0.084
	$0.2 \cdot f_c$	0.078	0.001	0.004	0.084	0.084
	$0.3 \cdot f_c$	0.068	0.0016	0.007	0.073	0.076
200	$0.1 \cdot f_c$	0.192	0.002	0.017	0.210	0.212
	$0.2 \cdot f_c$	0.188	0.005	0.015	0.205	0.207
	$0.3 \cdot f_c$	0.160	0.005	0.015	0.176	0.180
300	$0.1 \cdot f_c$	0.329	0.009	0.050	0.386	0.388
	$0.2 \cdot f_c$	0.320	0.012	0.044	0.371	0.376
	$0.3 \cdot f_c$	0.272	0.013	0.041	0.318	0.326
400	$0.1 \cdot f_c$	0.490	0.028	0.112	0.633	0.630
	$0.2 \cdot f_c$	0.483	0.031	0.097	0.605	0.611
	$0.3 \cdot f_c$	0.413	0.037	0.089	0.536	0.540
500	$0.1 \cdot f_c$	0.679	0.095	0.225	1.028	1
	$0.2 \cdot f_c$	0.680	0.114	0.206	1.013	1
	$0.3 \cdot f_c$	0.589	0.219	0.192	1.106	1

From the results, it is possible to observe that, at 500°C, there is an overestimation of about 10% of LITS for an equivalent load of $0.3 \cdot f_c$. In spite of that, up to 400°C, the values of the sum of the uncoupled strains are very close to the LITS reference values.

LITS uncoupled strains, normalized with respect to the peak LITS value at 500°C, are shown in Figure 111.

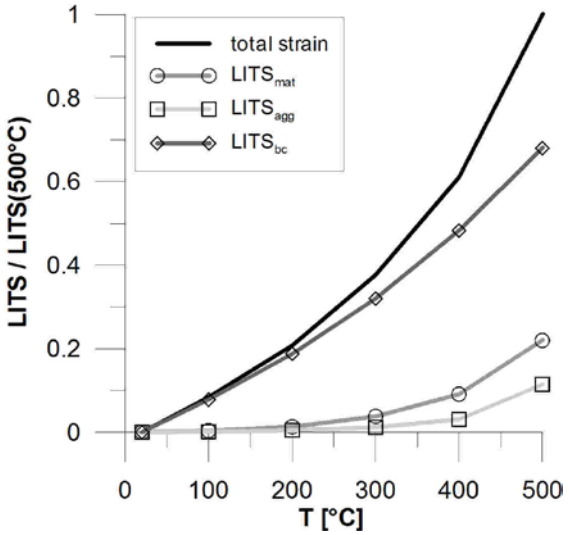

Figure 111 - Uncoupled normalized LITS for an equivalent load of $0.2 \cdot f_c$.

The normalized uncoupled LITS contributions due to aggregate performance on temperature - $LITS_{agg}$ ($LITS_{agg}/LITS(400°C)$) -, matrix performance on the

temperature - $LITS_{mat}$ ($LITS_{mat}/LITS(400°C)$) – and the effects of the boundary conditions - $LITS_{bc}$ ($LITS_{bc}/LITS(400°C)$) - are shown respectively in Figure 112a, Figure 112b and Figure 112c.

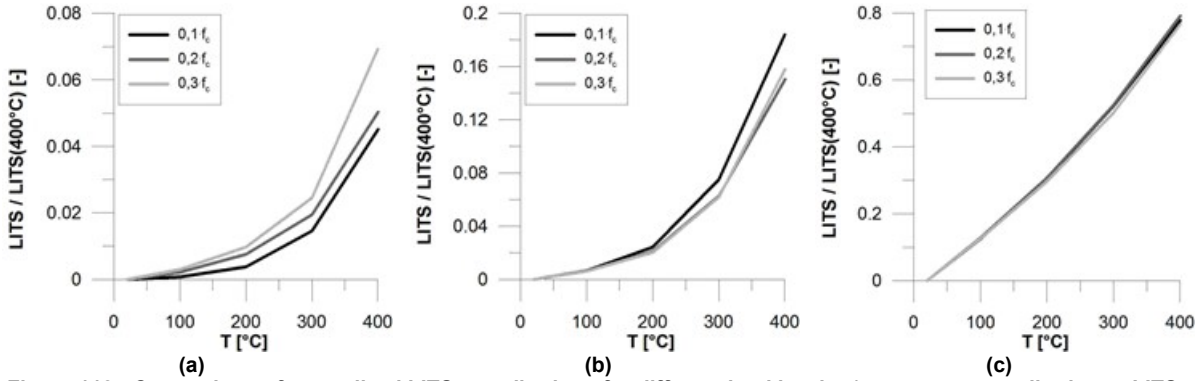

Figure 112 - Comparison of normalized LITS contributions for different load levels a) aggregate contribution to LITS ($LITS_{agg}$); b) matrix contribution to LITS ($LITS_{mat}$); c) thermal expansion restraint contribution to LITS ($LITS_{bc}$).

The results demonstrate that, for this type of concrete, the thermal expansion restraint ($LITS_{bc}$) is responsible for the largest contribution to LITS, followed respectively by the matrix ($LITS_{mat}$) and aggregate ($LITS_{agg}$) contributions. These results are in agreement with Mindeguia et al [69] conclusions, which state that the physical origins of transient creep, up to 400°C, are mainly the result of drying and dehydration processes, and, after that, increasingly due to concrete thermomechanical damage. According to Mindeguia et al [69], below 300°C, transient creep is mainly the result of thermo-hygral process and the nature of the aggregate does not influence transient creep behavior. Above 300°C, the effect of aggregates begins to appear as a thermomechanical process. In fact, analyzing the numerical results (Figure 111), one can notice that the contribution of the aggregates to LITS is not relevant up to 400°C. After that, its contribution increases exponentially.

Furthermore, the impact of the thermal expansion restraint imposed by the boundary conditions (uniaxial compressive stress state) is highly relevant both to the total strain and to LITS. In the numerical case analyzed, it has the largest contribution to LITS.

Another important observation is that LITS can be considered linearly dependent of the stress level, despite the small variations observed in the numerical and experimental results, as shown in Figure 113.

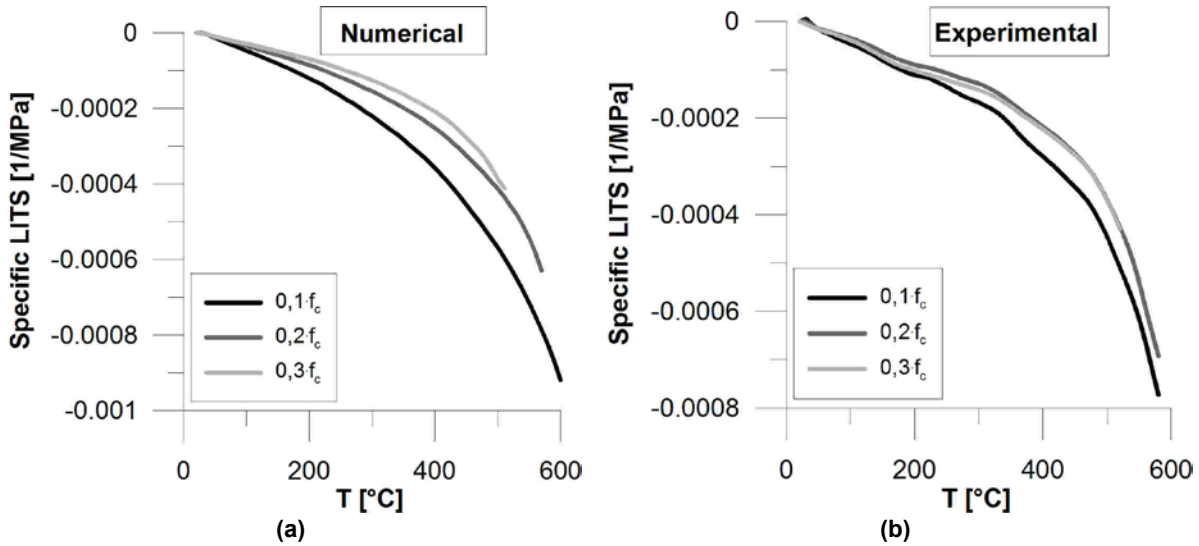

Figure 113 - LITS in terms of specific values for different load levels: a) numerical results; b) experimental results.

6.4.3 Comparison between the numerical results and the proposed semi-empirical model prediction

A comparison between numerical results the proposed LITS semi-empirical model prediction was carried out in order to validate the model. The results were compared in terms of LITS and with respect to thermomechanical and thermochemical strains.

In the proposed model, the thermomechanical ($LITS_{tm} = \beta_{tm} \times q_{tm}(T) \times \sigma$) and thermochemical ($LITS_{tc} = \beta_{tc} \times q_{tc}(T) \times \sigma$) strain components are uncoupled. The latter corresponds to concrete drying and dehydration, while the former corresponds to the contributions of the aggregate degradation, microcracking and thermal expansion restraint. Drying creep is implicit in the model, since it does take into account explicitly concrete moisture content.

In the numerical analyses, LITS was uncoupled into $LITS_{agg}$, $LITS_{mat}$ and $LITS_{bc}$ (see Figure 111). The thermomechanical strain was determined by adding the contributions to LITS of the aggregate and the thermal expansion restraint ($LITS_{tm} = LITS_{agg} + LITS_{bc}$, while the thermochemical strain was considered equal to the matrix contribution to LITS ($LITS_{tc} = LITS_{mat}$).

Figure 114a and Figure 114b show respectively a comparison between the numerical and the proposed model results in terms of LITS and normalized LITS with respect to the peak value at 500°C. In the former case, the proposed model prediction is in good agreement with the numerical results. In the latter case, both curves show a simple juxtaposition, indicating that, in this case, the proposed model is able to predict with high accuracy LITS evolution.

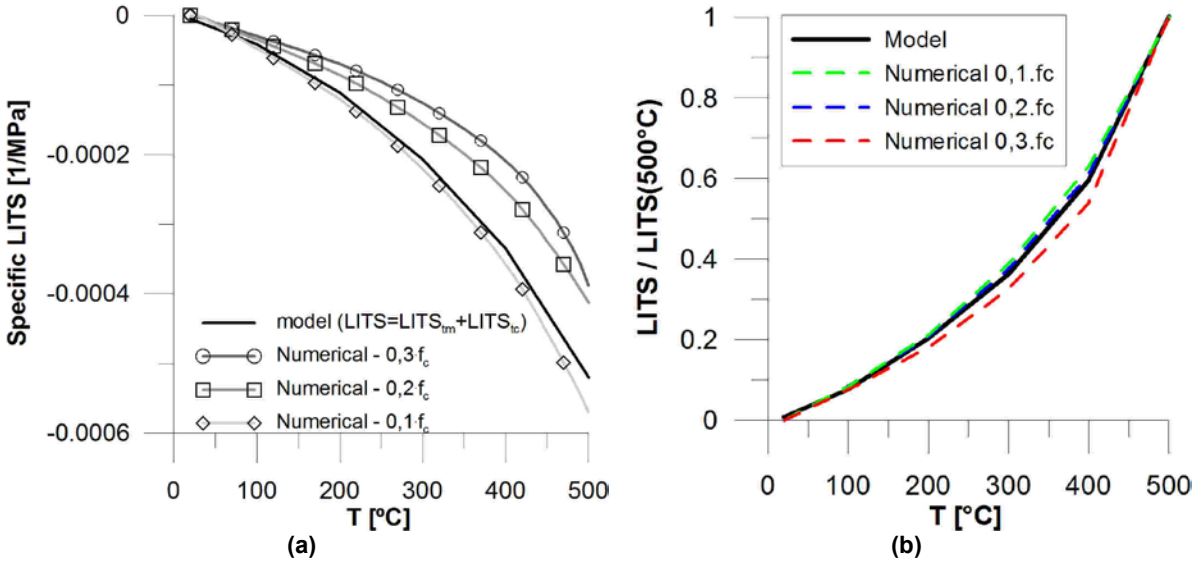

Figure 114 - Comparison between the proposed model and the numerical results: a) LITS values; b) normalized LITS values.

A comparison between numerical and predicted model results in terms of thermomechanical and thermochemical strains is important to validate the proposed semi-empirical model predictions. The results of both cases in terms of normalized LITS(500°C) are shown respectively in Figure 115a and Figure 115b, demonstrating that the semi-empirical model solution has a good correlation with the numerical values. It is important to remember that the thermomechanical properties of the numerical model were determined based on estimated values from the literature and, thus, the results do not reflect with high accuracy the real material response.

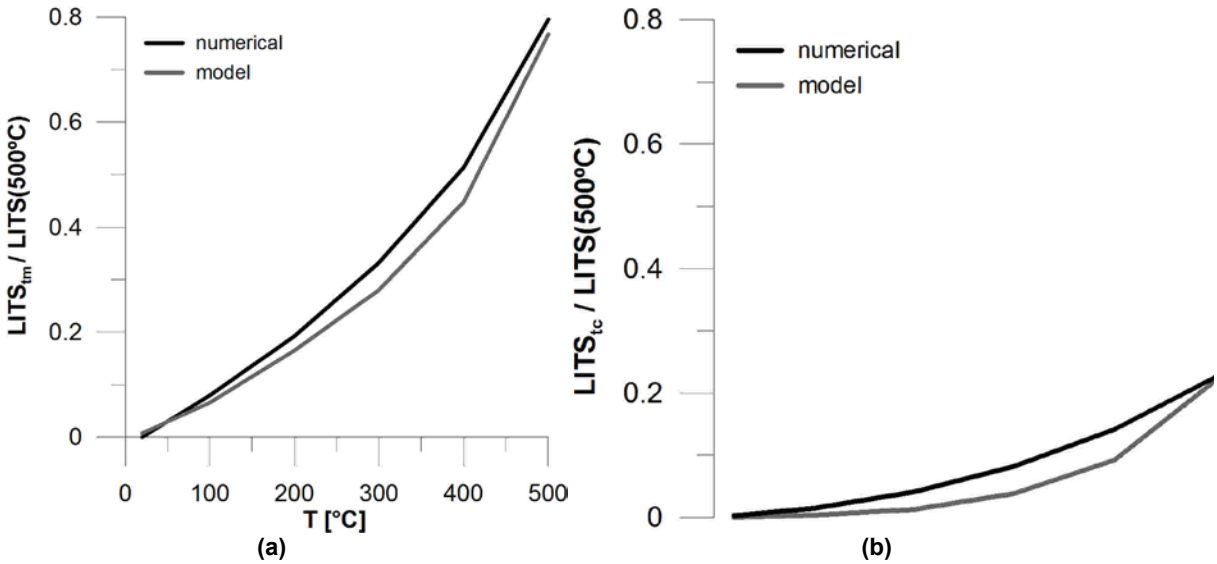

Figure 115 - Comparison between numerical results and model prediction in terms of normalized LITS versus temperature for an equivalent load of 0.2·f_c: a) thermomechanical strain; b) thermochemical strain.

From the numerical results, it is also possible to derive the constitutive equations of $LITS_{agg}$ and $LITS_{bc}$. In this way, in the LITS semi-empirical model, the thermomechanical strain ($LITS_{tm}$) can be described as the sum of two compliance functions dependent on the temperature, as shown in Eq. 52, where: $J_{LITS;agg}$ = LITS aggregate compliance function; $J_{LITS;bc}$ = boundary condition LITS compliance function;

$q_{agg}(T)$ = aggregate LITS exponential function, as shown in Eq. 53; and $q_{bc}(T)$ = boundary condition LITS power function, as shown in Eq. 54.

$$LITS_{tm} = (J_{LITS,agg} + J_{LITS,bc}) \times \sigma = (\beta_{tm} \times (q_{agg}(T) + q_{bc}(T)) \times \sigma \quad (52)$$

$$q_{agg}(T) = exp(T^{0.42}) \cdot 0.055^{6} \quad (53)$$

$$q_{bc}(T) = 9.5^{-5} \cdot T^{1.46} \quad (54)$$

Figure 116 shows a comparison between numerical results and the proposed model prediction in terms of the contribution of the aggregate and the thermal expansion restraint to LITS, considering their specific values (LITS per unit stress).

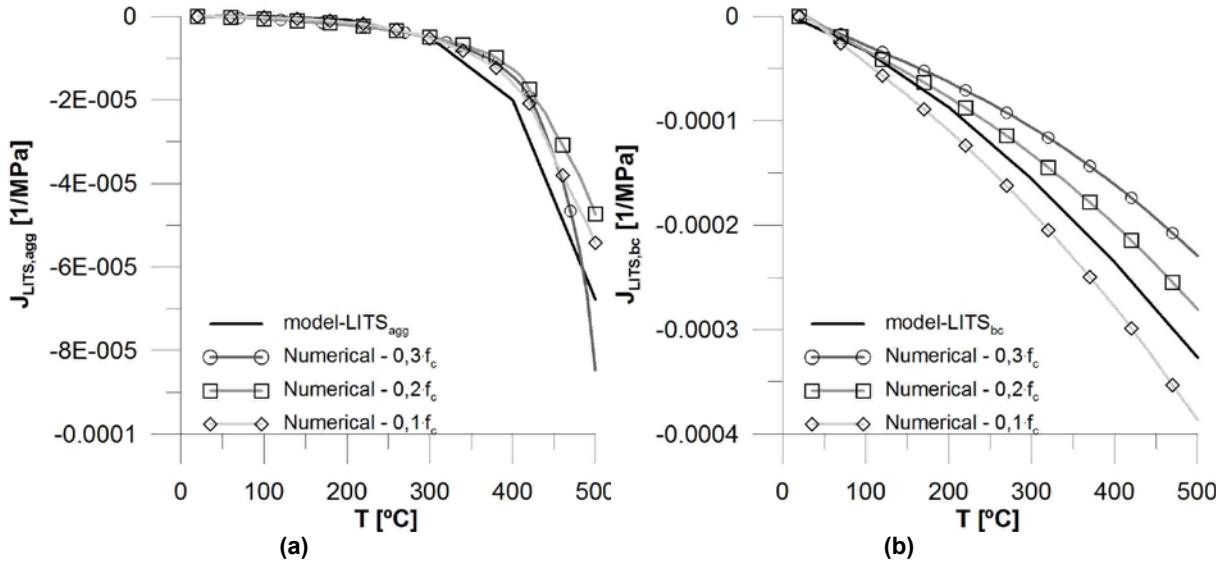

Figure 116 – Comparison between numerical and proposed model results: a) aggregate contribution ($LITS_{agg}$); b) thermal expansion restraint contribution ($LITS_{bc}$).

Figure 117 shows a comparison between numerical results and the proposed model prediction results in terms of thermomechanical strain and LITS specific values, where: $J_{LITS,tm} = J_{LITS,agg} + J_{LITS,bc}$ and $J_{LITS} = J_{LITS,agg} + J_{LITS,bc} + J_{LITS,tc}$.

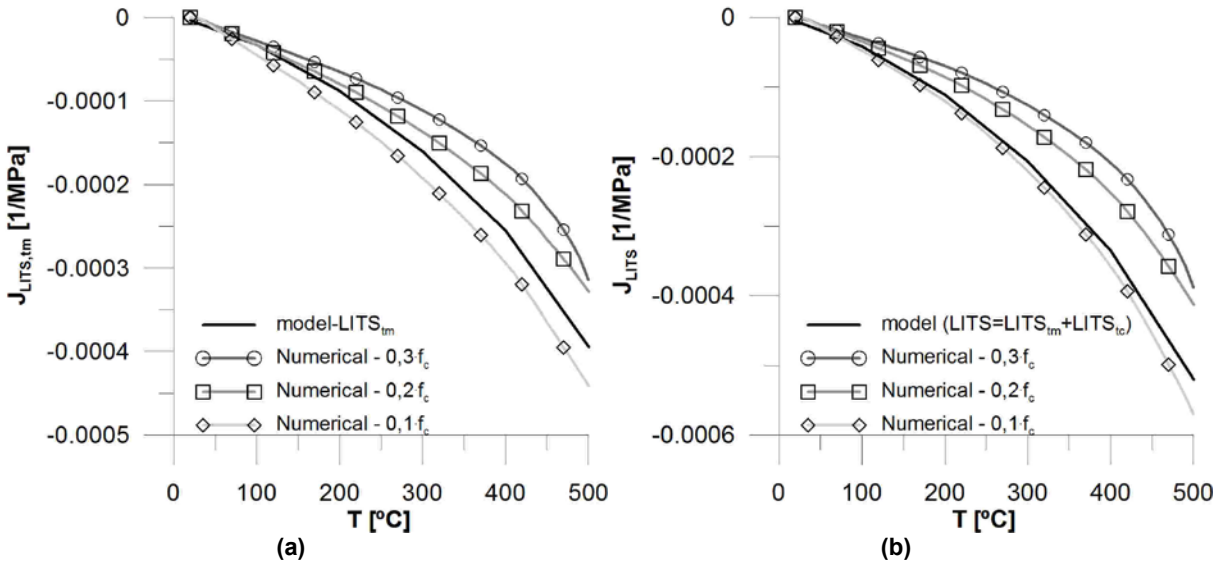

Figure 117 - Comparison between numerical and proposed model results: a) thermomechanical strain; b) LITS.

It is important to mention that the equations above (Eq. 53 and Eq. 54) were derived considering just one type of concrete. Further analyses should be carried out with different concrete mixtures in order to validate these equations for other concrete mixtures.

6.4.4 Path dependence

LITS considers transient thermal conditions and it is determined in preloaded specimens or pre-heated ones when the load is applied at a certain temperature level. It is worth mentioning that LITS behavior is quasi-instantaneous and continues after temperature stabilization due to concrete physical-chemical transformations (Khoury, [116]).

LITS in pre-heated specimens was analyzed by Mindeguia et al [69]. From the experimental results (Figure 118), it is possible to observe that the total strain is affected by preheating.

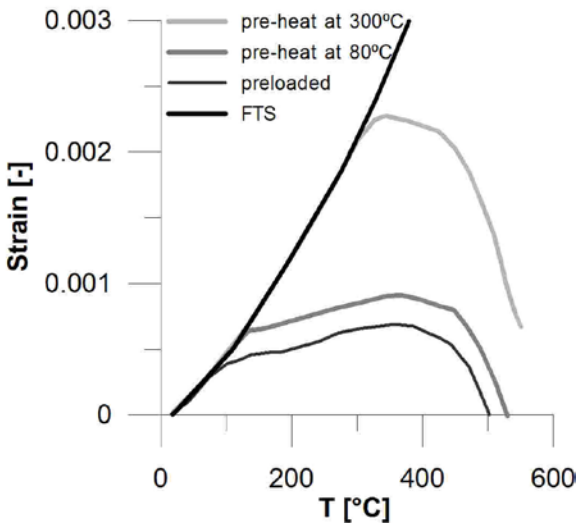

Figure 118 - Total strains from the experimental tests of [69] for preloaded and pre-heated specimens.

In order to better understand the effects of concrete preheating, twelve numerical analyses were carried out adopting the same mesoscopic model of the previous studies. In this case four different temperatures (100°C, 200°C, 300°C, 400°C) and three load levels (0.1·f_c, 0.2·f_c, 0.3·f_c,) were considered.

The comparison between preloaded (20°C) and preheated (100°C, 200°C, 300°C, 400°C) specimens, in terms of total strain (ε^c) minus the initial elastic one at 20°C - $\varepsilon^{el}(T = 20°C)$ - versus temperature, is shown in Figure 119.

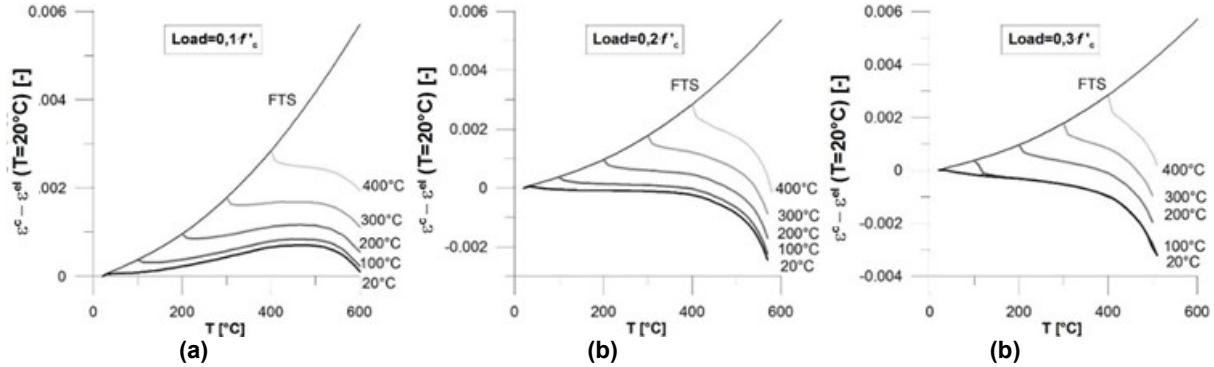

Figure 119 - Numerical results of preloaded and preheated specimens for different load levels in terms of total strain minus the initial elastic one at 20°C versus temperature: (a) 0.1·*f*c; (b) 0.2·*f*c; (c) 0.3·*f*c.

It is important to mention that the preloaded specimen is subjected to both thermal (self-equilibrated) and mechanical (compressive load) stresses from the beginning of the heating process, which induces thermomechanical damage and stresses redistribution within the bulk concrete. In contrast, preheated specimens are subjected only to thermal stresses before the application of the load, which restricts the total damaged area. As a result, immediately after the application of the load, the preheated specimens, on one side, show relatively lower internal stress values in relation to the preloaded one, and, on the other side, they are prone to higher damage as the temperature rises. Table 21 shows the maximum and minimum principal stresses of both preloaded and preheated specimens at different temperatures. It is possible to observe that the internal stresses (max./min.) of preheated specimens are lower in relation to the preloaded one immediately after loading, with a tendency of convergence at the maximum temperature analyzed (540ºC).

Table 21 - Maximum and minimum principal stresses (MPa) for preloaded and preheated specimens at different temperatures and an equivalent load of 0.2·f_c

T(°C)	unloaded	preloaded	pre-heated			
			100°C	200°C	300°C	400°C
120	17 / -50	16 / -111	16 / -87	-	-	-
220	17 / -75	17 / -192	17 / -171	16 / -99	-	-
320	14 / -84	14 / -240	14 / -229	14 / -195	14 / -112	-
420	12 / -76	12 / -260	12 / -257	12 / -236	11 / -196	11 / -108
540	6 / -49	6 / -230	6 / -226	6 / -216	6 / -197	6 / -168

In order to quantitatively analyze the effect of the thermal expansion restraint in preloaded and preheated specimens, the effect of the boundary conditions - $LITS_{bc}$ - (see Table 20), at the moment of the application of the load, was added to the total

strain values on preheated specimens. The comparison of the results both in terms of total strains (ε^c) minus the initial elastic one at 20°C - $\varepsilon^{el}(T = 20°C)$ - and LITS, considering two load levels, are shown respectively in Figure 120 and Figure 121.

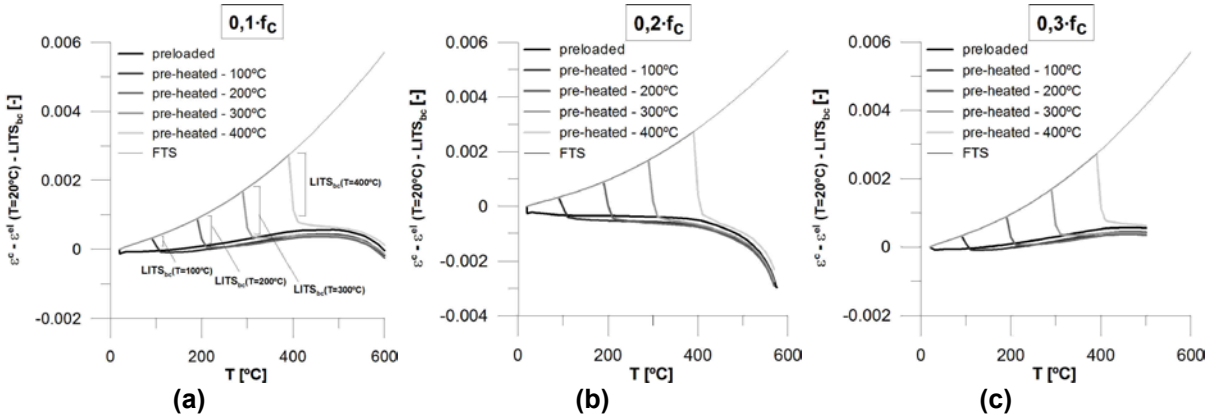

Figure 120 – Total strain minus the initial elastic one at 20°C and including the effect of the boundary conditions ($LITS_{bc}$) for preloaded and pre-heated specimens for different load levels: a) 0.1·f_c; b) 0.2·f_c; c) 0.3·f_c.

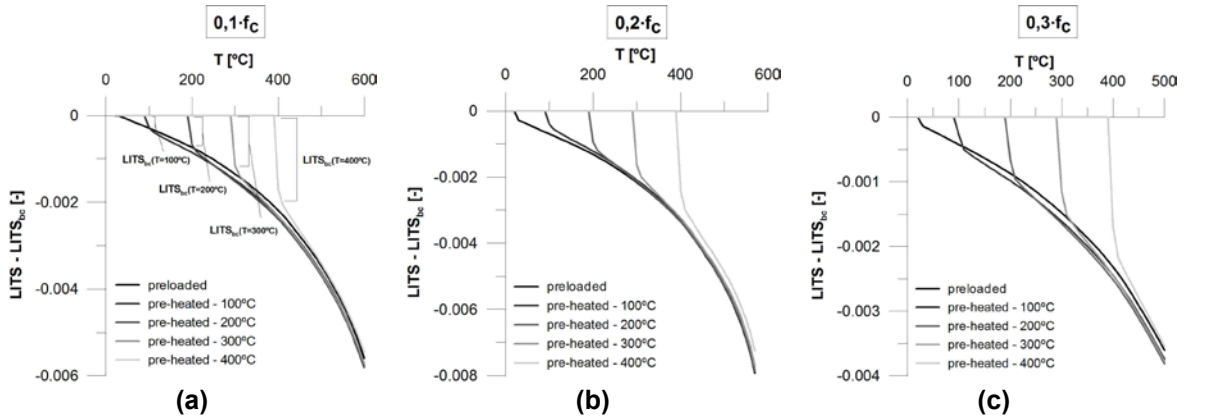

Figure 121 – LITS values including the effect of the boundary conditions ($LITS_{bc}$) for preloaded and pre-heated specimens for different load levels: a) 0.1·f_c; b) 0.2·f_c; c) 0.3·f_c.

From the results, it is possible to observe that the difference among LITS values from preloaded and preheated specimens seems to be due to the thermal expansion restraint imposed by the boundary conditions, which occurs at the structural level and, hence, it is not related to an intrinsic property of the material. As a result, one can conclude that, contrary to LITS, transient creep is not affected by the load path (pre-heating), since it is function of concrete physical-chemical transformations (aggregate degradation, concrete drying and cement paste dehydration) at the material level due to the high temperature exposure.

In conclusion, the mesoscopic analyses demonstrated that the numerical modeling can predict accurately concrete behavior of preloaded and preheated specimens. In the latter case, immediately after loading, the specimen shows a higher potential energy in relation to the preloaded one due to the relatively lower damage in the bulk concrete. Moreover, the difference between LITS values from preloaded and preheated specimens seems to be result of the thermal expansion restraint imposed by the boundary conditions at the structural level.

(This page intentionally left blank)

CHAPTER 7

Creep tests at high temperature

The hot tests were carried out at Politecnico di Milano - Lecco Campus – Laboratory using an electrical oven. The main objective is to analyze SFRC transient creep (during heating) and basic creep (after heating, at constant temperature).

The 11.5-year-old cylindrical specimens of 75 mm x 100 mm were cored from Colombo FRC beams [6] with a handheld drill after the mechanical characterization of the material. Table 22 shows the reference of the cylindrical specimens to the original beams (see Table 10 and Table 11).

Table 22 – Specimens reference to the original beams.

	specimen reference	beam reference		specimen reference	beam reference
Transient temperature	PL-20-200-1	U4	**Constant temperature**	PH-20-200-1	U3
	PL-20-200-2	U5		PH-20-200-2	U1
	PL-40-200-1	U7		PH-40-200-1	U3
	PL-40-200-2	L1		PH-40-200-2	-
	PL-20-400-1	U6		PH-20-400-1	U10
	PL-20-400-2	U7		PH-20-400-2	-
	PL-40-400-1	U5		PH-40-400-1	U6
	PL-40-400-2	U10		PH-40-400-2	-

The nomenclature adopted for the specimens used in the experimental tests is described below:

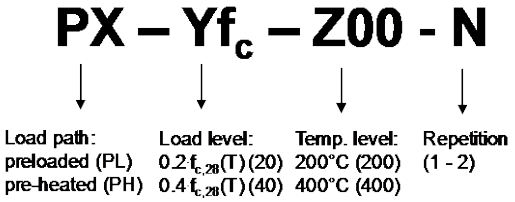

7.1 Experimental procedure

The experimental procedure is shown in Figure 122 and considered two different temperatures (200°C and 400°C), two different load levels – $0.2 \cdot f_{c,28}(T)$ and $0.4 \cdot f_{c,28}(T)$ - and two load paths (preload and pre-heat), where: $f_{c,28}(T)$ = residual compressive strength at 28 days. Concrete mechanical properties at 28 days were obtained from

Colombo [6], assuming that concrete residual strength is equal to the one at hot condition.

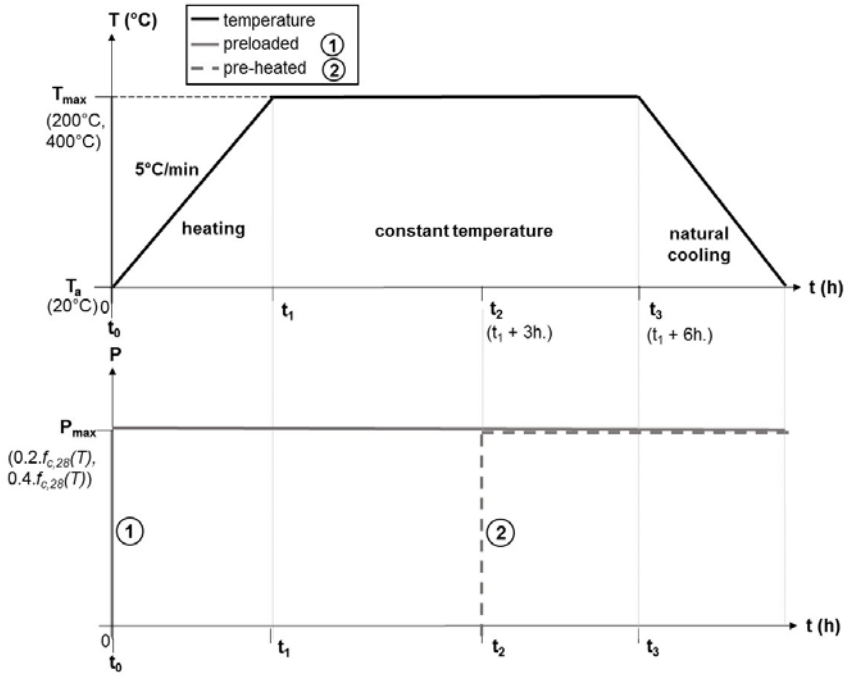

Figure 122 – Experimental procedure considering different load paths, temperatures and load levels.

Overall 16 tests were performed, according to Table 23.

Table 23 – Description of the tests procedure

test 1 – preloaded (x2)		test 2 – preloaded (x2)		test 3 – pre-heated (x2)		test 4 – pre-heated (x2)	
temp.	load level	temp.	load level	temp.	load level	temp.	load level
200°C	0.2·$f_{c,28}$(T) ≈13 MPa	400°C	0.2·$f_{c,28}$(T) ≈12 MPa	200°C	0.2·$f_{c,28}$(T) ≈13 MPa	400°C	0.2·$f_{c,28}$(T) ≈12 MPa
	0.4·$f_{c,28}$(T) ≈26 MPa		0.4·$f_{c,28}$(T) ≈24 MPa		0.4·$f_{c,28}$(T) ≈26 MPa		0.4·$f_{c,28}$(T) ≈24 MPa

The strain under sustained load was measured during the heating phase in preloaded specimens and at constant temperature in preloaded and pre-heated specimens.

Transient creep tests were carried out with a heating rate of 5°C/min. Basic creep (creep at constant temperature) tests in pre-heated specimens started after 3 hours of the temperature stabilization in order to guarantee a uniform temperature distribution inside the specimen. This procedure prevents the coupling behavior between basic creep and transient creep, which continues even after temperature stabilization, until all concrete physical-chemical reactions are completed.

The free thermal strain (FTS) was measured during the heating phase in unloaded specimens. LITS was determined by the difference between the total strain during heating in preloaded specimens and the free thermal strain, disregarding the initial elastic deformation. Basic creep was determined by the difference between the total strain and the free thermal strain at constant temperature, excluding the initial elastic deformation.

Concrete displacements (ε^c) were determined from the experimental results after removing the effect of the test setup on the specimen. In this case, the total displacement measured from three LVDT's included both the displacements of concrete and steel rods (see Figure 123). Concrete total strain (ε^c) was calculated according to Eq. 55, where: δ_t = total displacement measured with the LVDT's; δ_s = steel rod displacement, calculated according to Eq. 56; h_c = height of the specimen; P = applied load; l_s = length of the two steel rods; A_s = cross-sectional area of the steel rod; E_s = steel Elastic Modulus.

$$\varepsilon_c = \frac{\delta_t - \delta_s}{h_c} \tag{55}$$

$$\delta_s = \frac{P \times l_s}{A_s \times E_s} \tag{56}$$

7.2 Test set-up

The experimental device is shown in Figure 123. The load system consists in a compressor that provides the oil pressure to the hydraulic jack, moving the piston, which is responsible for the application of the load on the specimen. The load level was continuously measured by means of a load cell fixed at the bottom of the steel frame. The electric oven was mounted on the center of the steel frame and a thermocouple monitored the temperature inside the furnace during the tests.

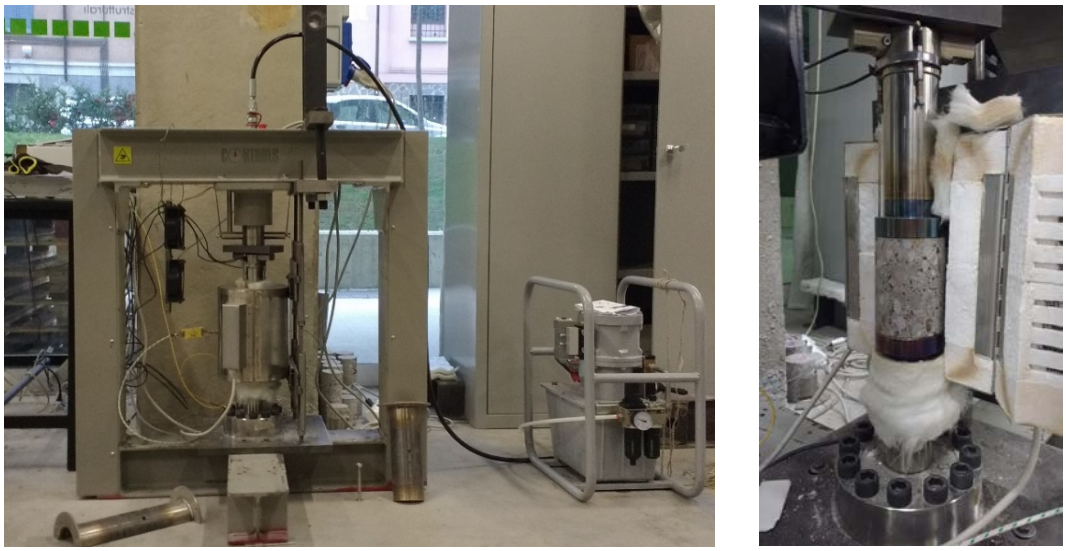

Figure 123 – Hot tests setup.

In order to support high temperatures without loss of data acquisition, the displacements were measured with three LVDT's placed outside the oven and not subjected to high temperatures. To read the longitudinal displacements, three tempered glass cylinder bars were fixed, on one side, to the specimen's top surface, and, on the other side, to the LVDT's.

7.3 Preliminary test – creep at room temperature

A preliminary creep test at room temperature was carried out with a duration of three days. From the experimental result, the Kelvin-Voigt model (Eq. 57) was adopted to predict SFRC creep behavior under a compressive sustained load equivalent to $0.2 \cdot f_{c,28}$. In this case, the best fitting was obtained by adopting the following values: ϕ_∞ =0.16; β =4.

$$\varepsilon^{cr}(t, t_0) = \frac{\sigma}{E}(1 + \phi_\infty \cdot (1 - e^{-\beta \cdot (t - t_0)}) \quad (57)$$

A comparison between experimental and predicted values is shown in Figure 124, demonstrating a good approximation of the Kelvin-Voigt approach. In contrast, the Model Code 2010 (MC2010) [101] underestimates the experimental results. One important observation is that, in this case, creep reached much faster a value close to the asymptotic one when compared to young specimens. This effect, which could be prevalent on old specimens with an age of loading higher than 10 years, is not predicted on Eurocode 2 [103] and MC2010 [101].

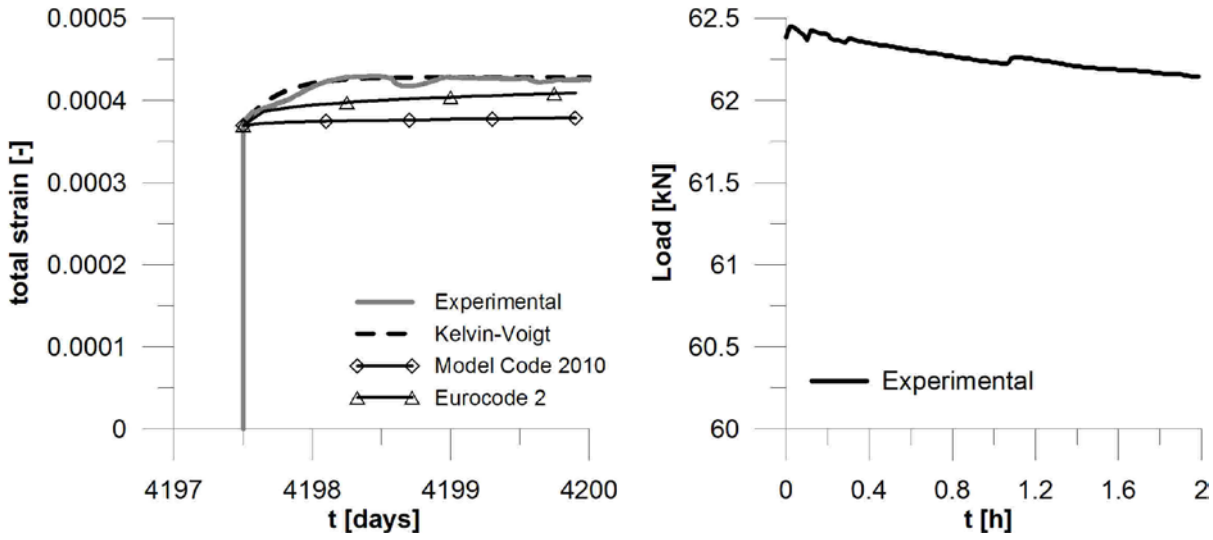

Figure 124 – Comparison between creep experimental result and Kelvin-Voigt model.

7.4 Experimental results at high temperature

7.4.1 Calibration tests

Calibration tests were carried out in order to measure the thermal effects of the test setup on the measured values of specimen tests. In this case, two tests were performed, considering a maximum temperature of 200°C and 400°C. The tests were developed without the specimen, measuring the displacements (free thermal expansion) at the bottom steel rod with three LVDT's, as shown in Figure 125. The results in terms of displacements *versus* time are shown in Figure 126.

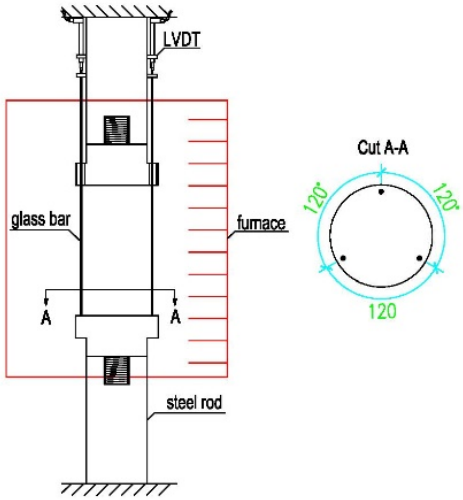

Figure 125 – Calibration tests measurement procedure.

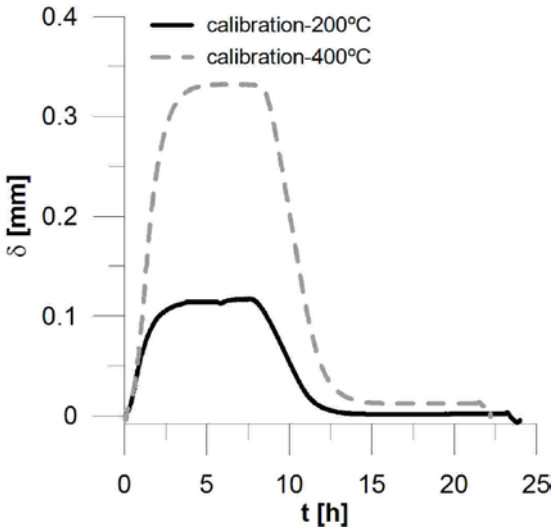

Figure 126 – Results of the calibration tests.

7.4.2 Free thermal strains

The free thermal strains were measured in pre-heated specimens. In order to remove the thermal effects of the test setup from the results, the values of the calibration test were subtracted from the measured concrete thermal displacements as described in Eq. 58, where: ε^{th} = concrete thermal strain; δ_c^{th} =concrete thermal displacements; δ_s^{th} = steel rod thermal displacements; h_c =specimen height.

$$\varepsilon^{th} = \frac{\delta_c^{th} - \delta_s^{th}}{h_c} \tag{58}$$

The experimental results, together with the thermal strain prediction by means of both the Eurocode 2 (EC-2) [103] and the Model Code 2010 (MC 2010), are shown in Figure 127. The temperature evolution refers to the one of the specimen (Figure 128). In the case of MC2010, the coefficient of thermal expansion adopted was equal to $1x10^5$. The results show that EC-2 is in the upper bound limit and MC2010 is in the lower bound limit.

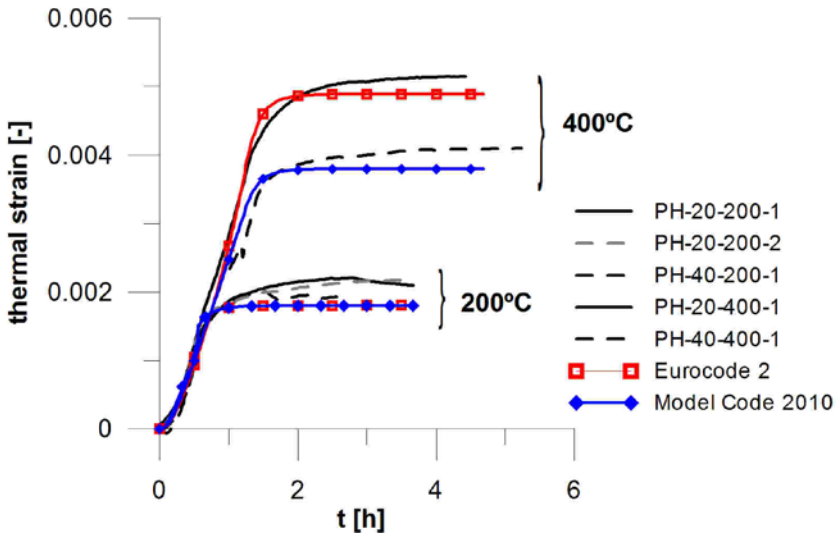

Figure 127 - Free thermal strains from pre-heated specimens.

7.4.3 Preloaded specimens

Concrete total strains (ε^c) minus the initial elastic deformation (ε^{el}), corresponding to 0.2·$f_{c,28}$(T) *and* 0.4·$f_{c,28}$(T), are presented both in terms of strain *versus* temperature of the specimen and strain *versus* time. In order to obtain the temperature in the center of the specimen, a numerical thermal analysis was carried out using the finite element software Abaqus, as shown in Figure 128.

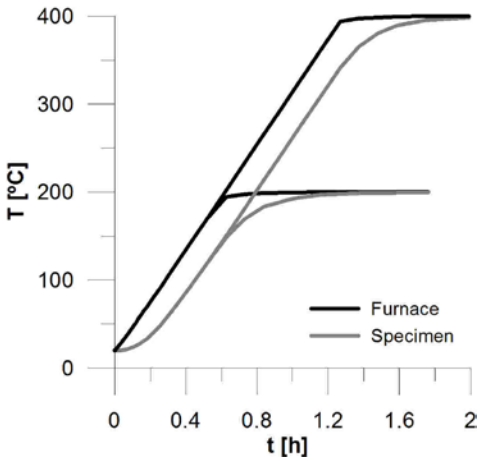

Figure 128 – Evolution of temperature as function of time on the oven and in the center of the specimen.

The results considering a stress level of 0.2·$f_{c,28}$(T) are shown in Figure 129 and the results for the specimen loaded at 0.4·$f_{c,28}$(T) are shown in Figure 130. From the experimental results, one can observe that most of concrete deformation during heating in preloaded specimens was recovered after cooling. This phenomenon can be attributed to the positive effect of the smeared steel fibers in the bulk concrete, which were able to keep the matrix cohesion, reducing the deleterious effect of thermal mismatch during the thermal cycle. As a result, despite the decrease of the Elastic Modulus at high temperature, the residual thermomechanical damage was much smaller than the one expected for plain concrete.

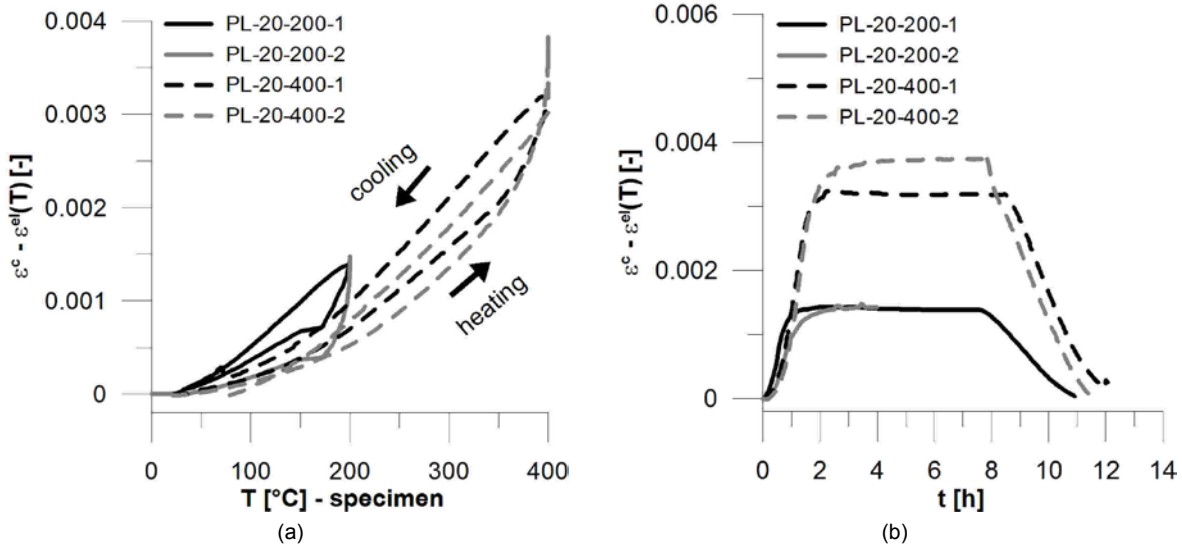

Figure 129 – Concrete strains of preloaded specimens considering a load level equivalent to 0.2·$f_{c,28}$(T): a) total strain minus initial elastic one vs. temperature; b) total strain minus initial elastic one vs. time.

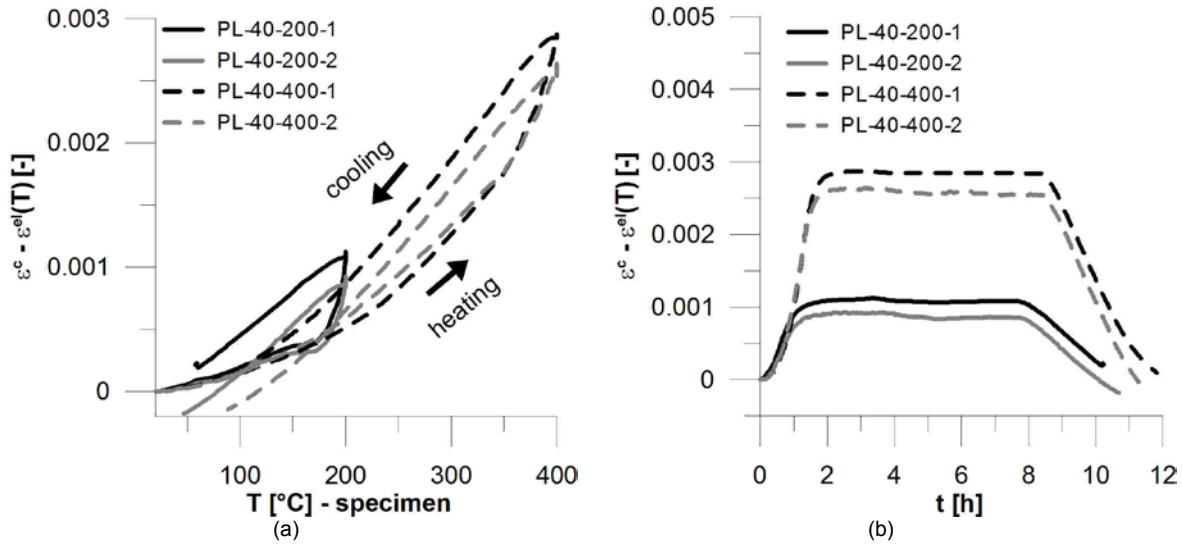

Figure 130 – Concrete strains of preloaded specimens considering a load level equivalent to 0.4·$f_{c,28}$(T): a) total strain minus initial elastic one vs. temperature; b) total strain minus initial elastic one vs. time.

Creep strains were determined according to Eq. 59, where: $\varepsilon^{cr}(t, t_0, T)$ = creep strain during heating and at constant temperature; $\varepsilon^{c}(T)$ = concrete total strain; $\varepsilon^{th}(T)$ = free thermal strain; $\varepsilon^{el}(T) = \sigma(T)/E_T$ = elastic strain at high temperature. The results in terms of creep *versus* time for specimens loaded at 0.2·$f_{c,28}$(T) and 0.4·$f_{c,28}$(T) are shown in Figure 131.

$$\varepsilon^{cr}(t, t_0, T) = \varepsilon^{c}(T) - \varepsilon^{th}(T) - \varepsilon^{el}(T) \quad (59)$$

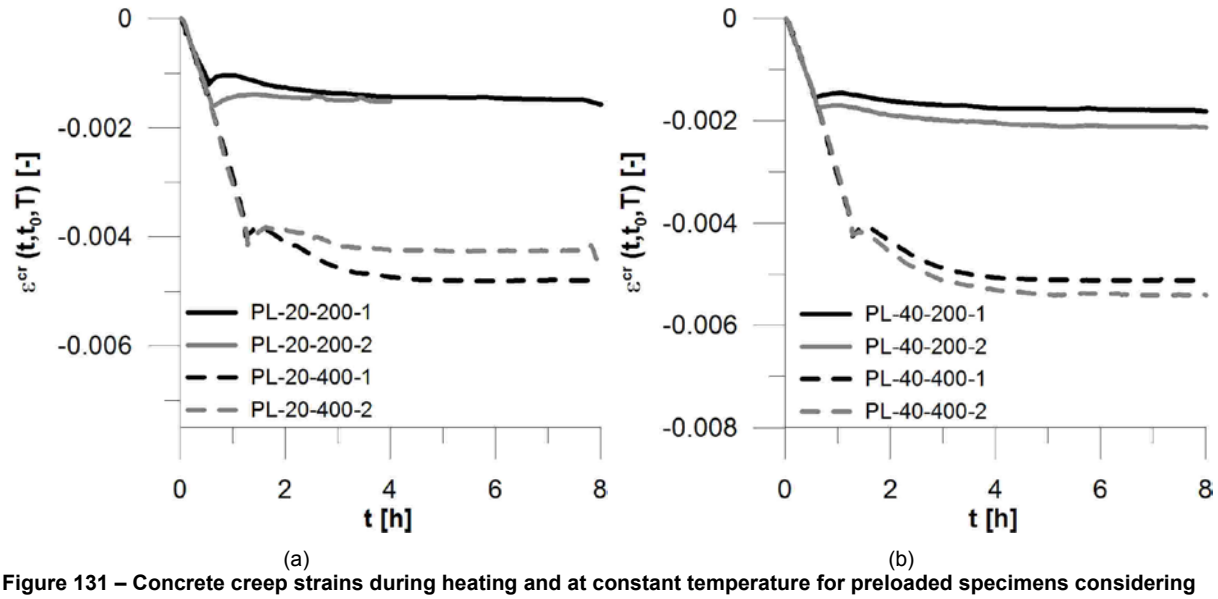

Figure 131 – Concrete creep strains during heating and at constant temperature for preloaded specimens considering an equivalent load of: a) 0.2·$f_{c,28}(T)$; b) 0.4·$f_{c,28}(T)$.

Due to the characteristics of the test setup (see Figure 123), the load level was not kept perfectly constant during the experimental tests, as one can observe in Figure 132. This is because, during heating, concrete thermal expansion produced a pullback force opposite to the applied load, leading to an increase in the pressure of the air in the compressor and, as a result, increasing the oil pressure in the hydraulic jack and the stress level on the specimen. In contrast, during constant temperature and cooling, there was a relaxation of the pressure of the system, resulting in a decrease of the air pressure and accordingly, to a decrease of the oil pressure and the stress level.

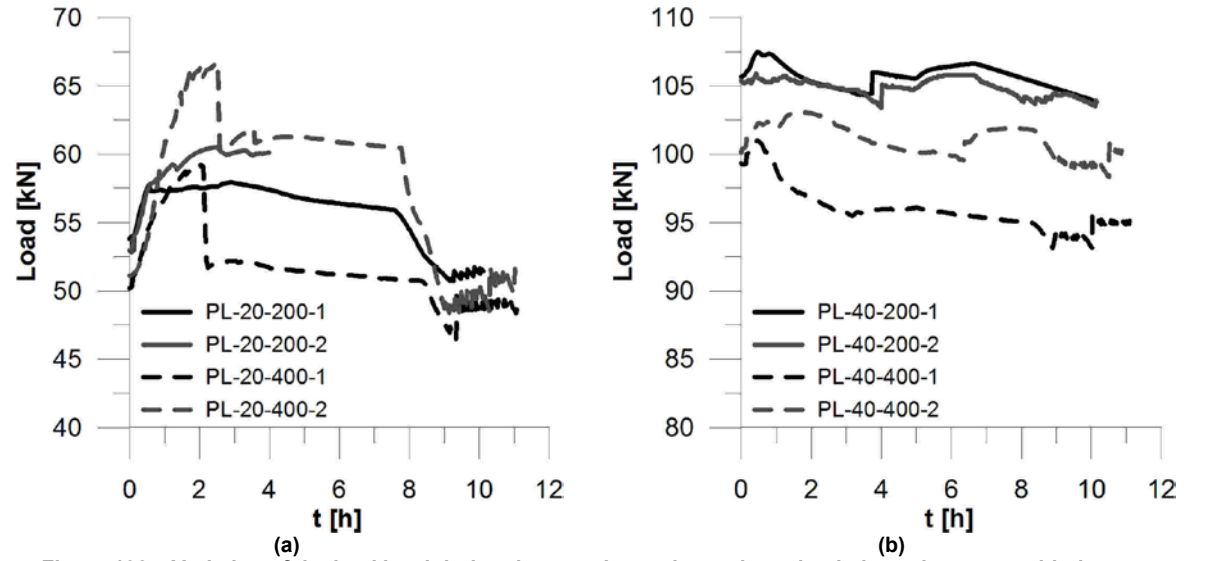

Figure 132 – Variation of the load level during the experimental tests in preloaded specimens considering an equivalent load of: a) 0.2·$f_{c,28}(T)$; b) 0.4·$f_{c,28}(T)$.

The variation of the load in the tests stressed at 0.4·$f_{c,28}(T)$ was not as significant as the one observed in the tests loaded at 0.2·$f_{c,28}(T)$. In the latter case, there was a variation up to 30% in the applied load. In order to remove the effects of the stress variation on the results, the creep function values – $v(t,t_0,T)$ - were calculated according to the Volterra integral as described in Eq. 60, where: $\varepsilon_k^c(t,t_0)$ = concrete

total strain at the time step k; $J_0(t_0) = 1/E_0$ = initial elastic value; σ_0 = initial stress level; $J_{ki}(t_k, t_i, T)$ = creep per unit stress; $\Delta\sigma_k = \sigma_i - \sigma_{i-1}$ = variation of the stress level between two consecutive time steps.

$$\varepsilon_k^c(t, t_0, T) = J_0(t_0) \cdot \sigma_0 + \frac{1}{2} \cdot \sum_{i=1}^{k} [J(t_k, t_i, T) + J(t_k, t_{i-1}, T)] \cdot \Delta_i \sigma \quad (60)$$

The results in terms of $J(t, t_0, T)$ *versus* time are shown in Figure 133, indicating a small variation among the results for the specimens tested at the same maximum temperature, except for the case of the specimen PL-20-400-1. The highest variation occurred in the tests loaded at 0.2·$f_{c,28}$(T). This fact can be attributed to the increase of the load level during heating, which reached a peak with the attainment of a uniform temperature distribution inside the specimen. The increase in the stress level led to an increase in the total strains during heating, magnifying the creep values.

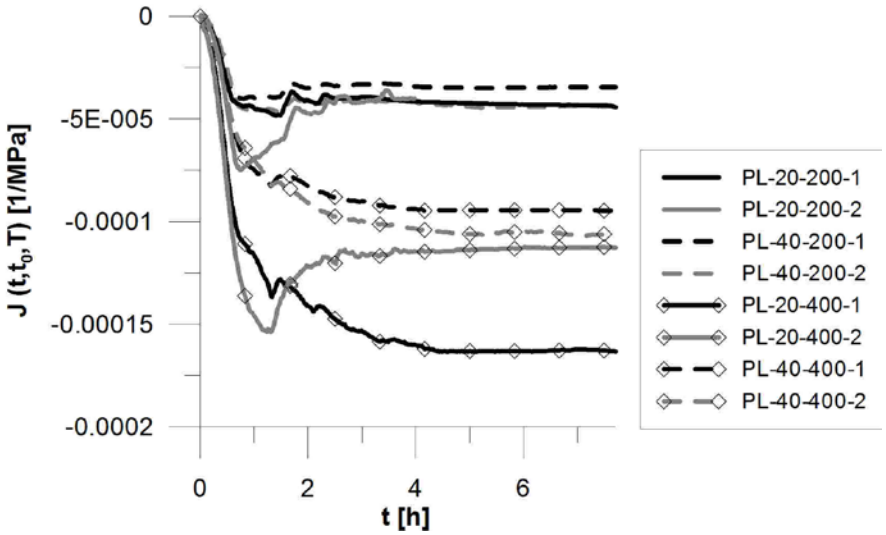

Figure 133 –Comparison among the results of preloaded specimens in terms of creep during heating and at constant temperature.

7.4.4 Pre-heated specimens

The apparent Modulus of Elasticity at 200ºC and 400ºC are shown in Table 24. The values were calculated according to Eq. 61 and were obtained during the loading phase in pre-heated specimens for a load level equivalent to 0.4·f_c(T), as shown in Figure 134.

Table 24 – Modulus of Elasticity at high temperature

Temperature	Modulus of Elasticity
200ºC	40000 MPa
400ºC	33000 MPa

$$E_c(T) = \frac{(P_{max} - P_{20})/A_c}{(\delta_{max} - \delta_{20})/h_c} \quad (61)$$

where: P_{max} =maximum load level; P_{40} =load equal to 20 kN; A_c =concrete cross-section area; δ_{max} =concrete maximum displacement; δ_{40} = concrete displacement at P=20 kN; h_c =specimen height.

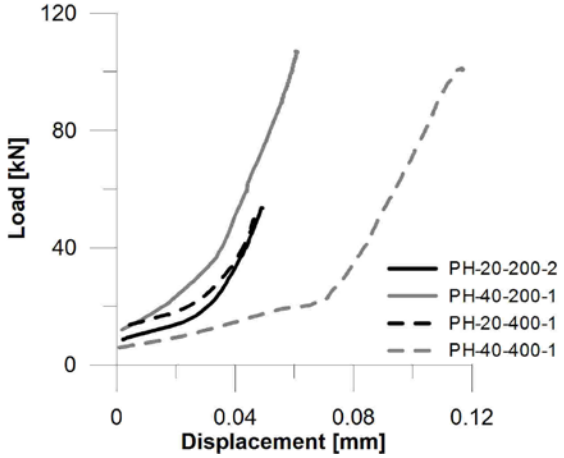

Figure 134 – Load versus temperature on pre-heated specimens.

Concrete total strains ($\varepsilon^c(T)$) minus the initial elastic value at high temperature ($\varepsilon^{el}(T)$), for two load levels – 0.2·$f_{c,28}$(T) *and* 0.4·$f_{c,28}$(T) -, are shown in Figure 135.

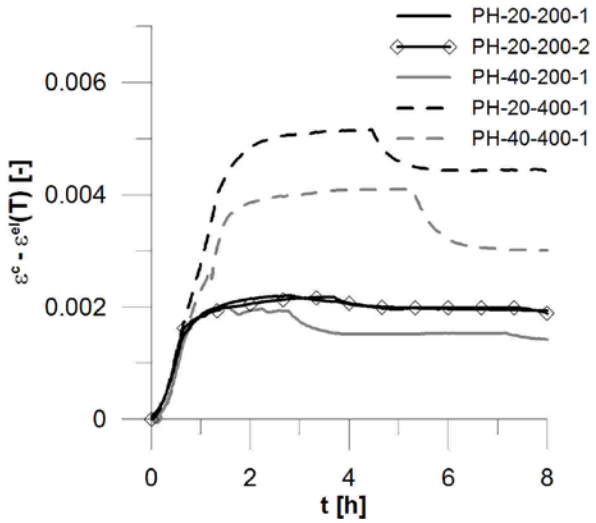

Figure 135 - Concrete experimental results of pre-heated specimens in terms of total strain minus the initial elastic one versus time.

The load and temperature profiles of the pre-heated tests are shown in Figure 136.

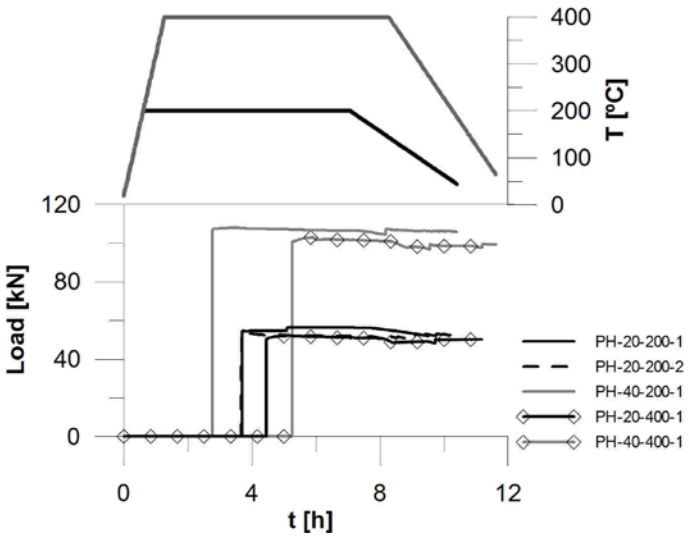

Figure 136 – Load and temperature profiles of pre-heated tests.

The experimental results in terms of creep per unit stress are shown in Figure 137. The values were determined according to Eq. 62, where: $J(t,t_0,T) =$ creep per unit stress; $\varepsilon^c(T) =$ concrete total strain; $\varepsilon^{th}(T) =$ concrete thermal strain; $\varepsilon^{el}(T) =$ elastic strain at high temperature; $\sigma(T) =$ stress level.

$$J(t,t_0,T) = \frac{\varphi(t,t_0,T)}{E_c(T)} = \frac{\varepsilon^c(T) - \varepsilon^{th}(T) - \varepsilon^{el}(T)}{\sigma(T)} \quad (62)$$

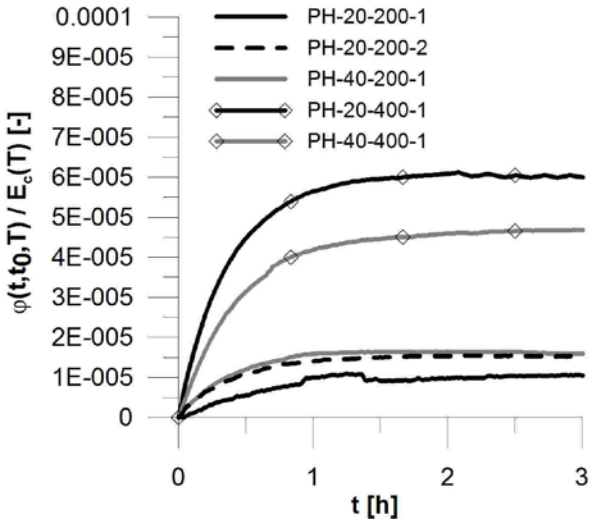

Figure 137 – Experimental results of pre-heated specimens in terms of creep per unit stress versus time.

The experimental results in terms of the creep coefficient for three different temperatures (20ºC, 200ºC and 400ºC) are shown in Figure 138. At 20°C, the Kelvin-Voigt prediction is presented, while, at high temperature, the creep coefficient was calculated according to Eq. 63, where: $J(t,t_0,T) =$ creep per unit stress; $E_T =$ Elastic Modulus at high temperature as shown in Table 24. In this case, a linear interpolation was adopted to determine the Elastic Modulus at different temperatures.

$$\phi(t, t_0, E_T) = J(t, t_0, T) \cdot E_T \quad (63)$$

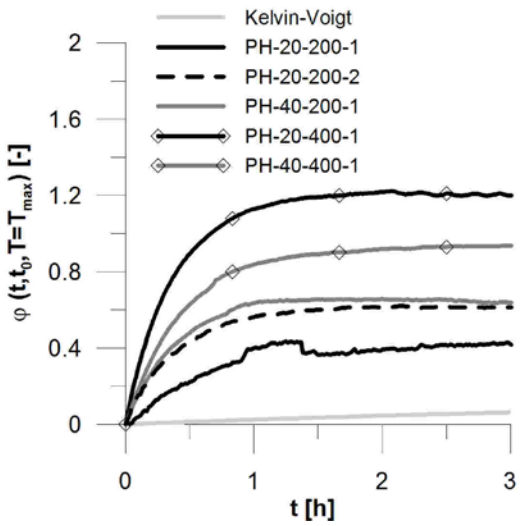

Figure 138 – Experimental results of pre-heated tests in terms of creep coefficient versus time at three different temperatures: 20ºC, 200ºC and 400ºC.

7.4.5 Path dependence

The values of preloaded and pre-heated specimens in terms of total strain versus time is shown in Figure 139.Figure 140 From the comparison of the results, it is possible to notice that, as expected, the two load path has an effect on creep, which is also valid for steel fiber reinforced concrete.

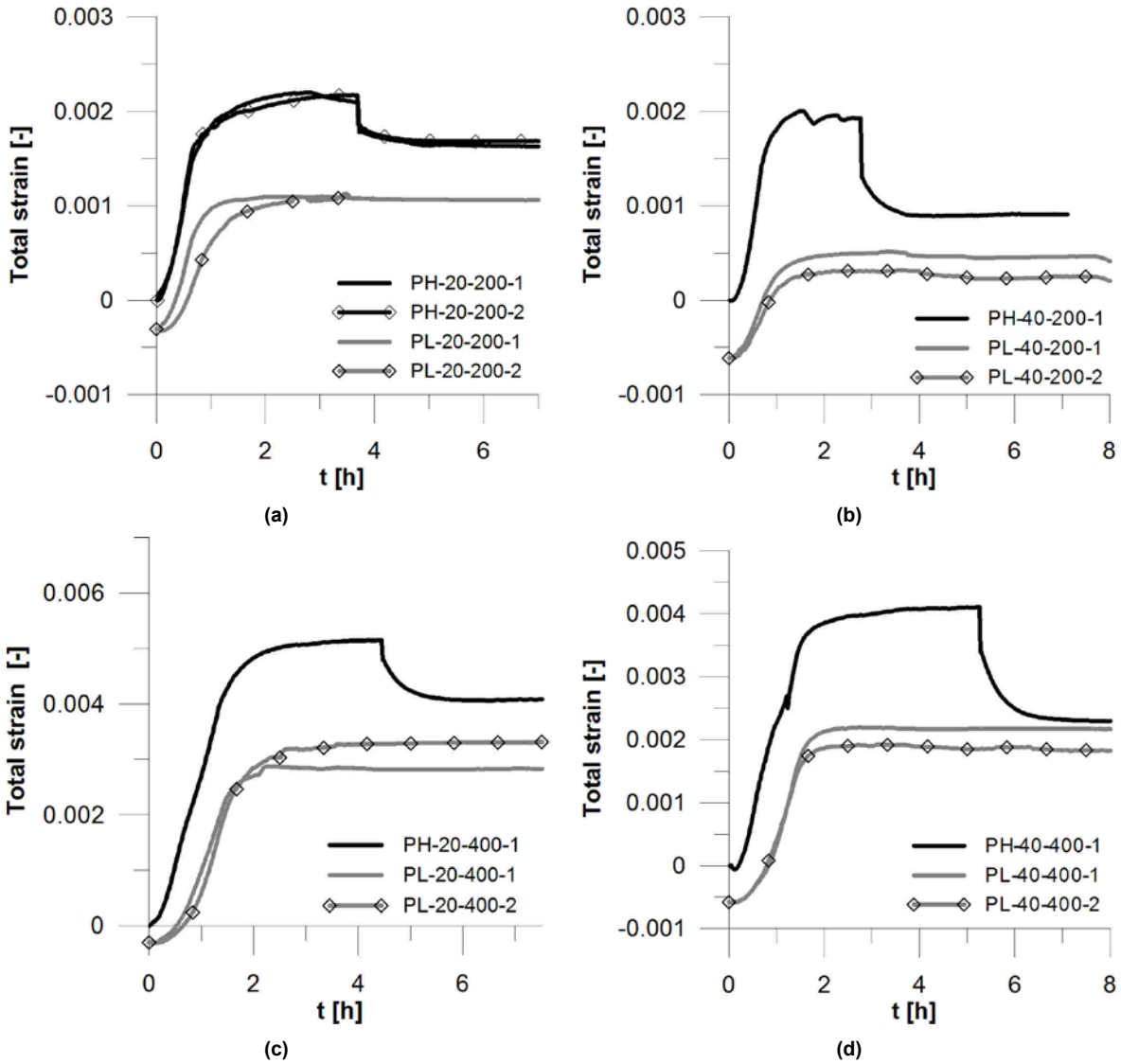

Figure 139 – Experimental results of preloaded and pre-heated specimens in terms of total strain versus time: a) 0.2.fc,28(T) and 200ºC; b) 0.4.fc,28(T) and 200ºC; c) 0.2.fc,28(T) and 400ºC; d) 0.4.fc,28(T) and 400ºC.

(This page intentionally left blank)

CHAPTER 8

Discussion of the experimental results

8.1 The role of the boundary conditions (path dependence)

From the experimental results in preloaded and pre-heated specimens, it is possible to notice the path dependence, which is also valid for steel fiber-reinforced concrete. The difference between the total strains in the two different load paths can be attributed to the thermal expansion restraint. In Chapter 6, the restraint effect imposed by the boundary condition ($LITS_{bc}$) was evidenced by LITS uncoupling and a equation to predict this effect was derived.

A comparison between experimental and predicted values is carried out. The experimental results are shown in Figure 140. In this case, the same thermal strain values were adopted for all tests in order to guarantee the same initial base of comparison. The values of the two nominally identical preloaded tests were averaged. The predicted values were calculated according to Eq. 66, as described in section 6.4.3.

$$LITS_{bc} = \left[\beta_{tm} \cdot q_{bc}(T)\right] \cdot \beta(t_0) \cdot \sigma \quad (64)$$

$$q_{bc}(T) = 9.5^{-5} \cdot T^{1.46} \quad (65)$$

where: $LITS_{bc} =$ the effect of the boundary condition on concrete; $q_{bc}(T) =$ boundary condition power function; $\beta(t_0) =$ reduction factor to take into account the age of loading; and $\sigma =$ stress level.

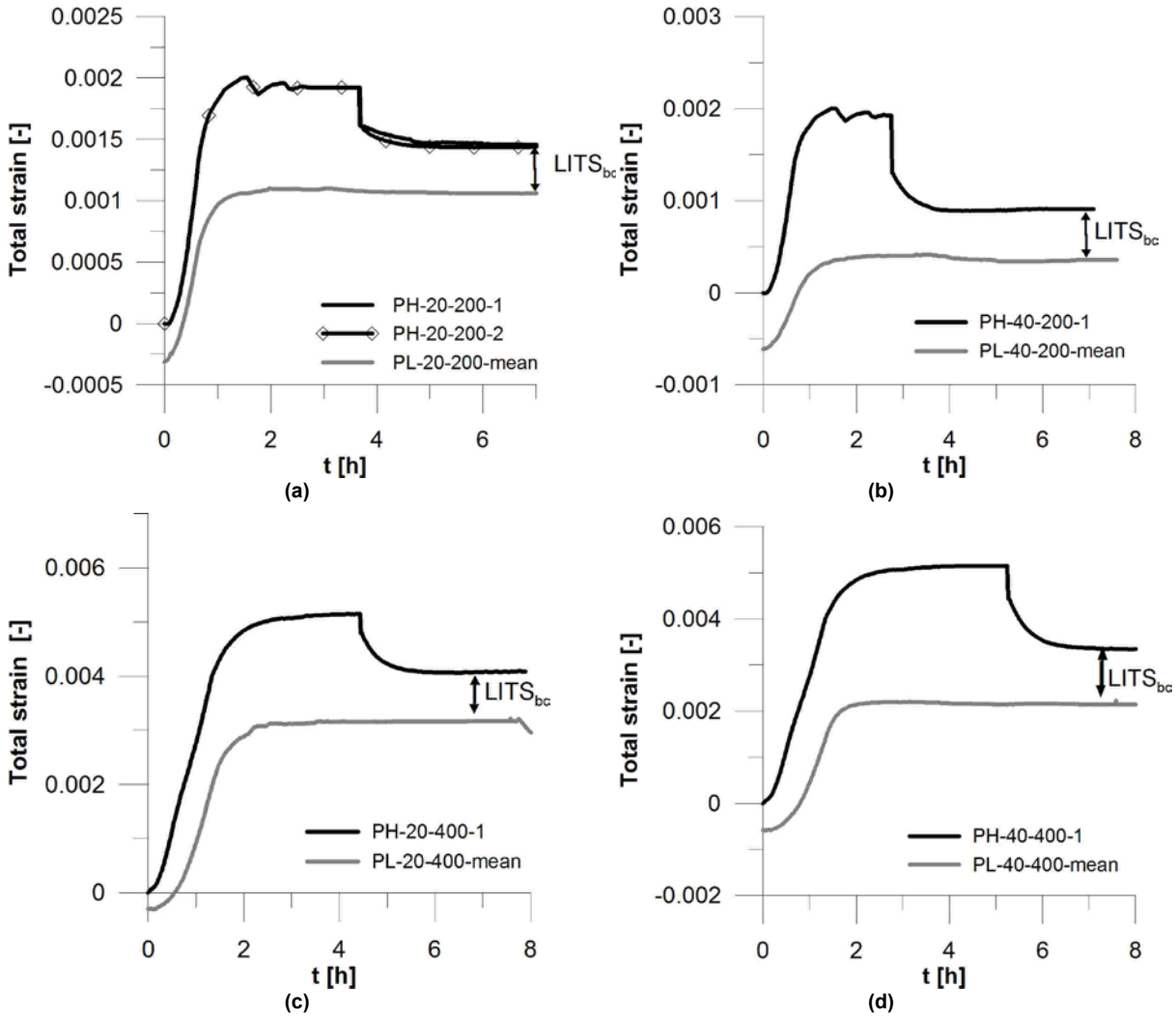

Figure 140 – Comparison between preloaded and pre-heated specimens: a) 0.2·$f_{c,28}$(T) and 200ºC; b) 0.4·$f_{c,28}$(T) and 200ºC; c) 0.2·$f_{c,28}$(T) and 400ºC; d) 0.4·$f_{c,28}$(T) and 400ºC.

The comparison between experimental and predicted values are shown in shown in Table 25. The experimental values were obtained from the difference of preloaded and pre-heated results after 7 hours of the start of the tests.

Table 25 – Experimental and predicted values of thermal expansion restraint after 7 hours of the start of the tests.

	experimental	**predicted ($LITS_{bc}$)**
0.2·f_c(T) and 200ºC	0.00039	0.00043
0.4·f_c(T) and 200ºC	0.00051	0.00082
0.2·f_c(T) and 400ºC	0.0009	0.00107
0.4·f_c(T) and 400ºC	0.001225	0.00213

The comparison indicates that the equation ($LITS_{bc}$) can predict with acceptable accuracy the thermal expansion restraint effects on preloaded specimens, although for the specimens loaded at 0.4·$f_{c,28}$(T) it overestimates the results. One possible explanation is that the mechanical strain seems to be not strictly linear to the load level (see Figure 116b in chapter 6)

8.2 Load Induced Thermal Strain (LITS)

A comparison between the experimental results and the LITS semi-empirical model proposed in this thesis and described in details in Chapter 3 was carried out. The proposed model is shown in Eq. 66, where: β_{tc} is the variable dependent of the cement content (Eq. 70); β_{tm} is the variable dependent of the aggregate volume (Eq. 69); $q_{tm}(T)$ is the thermomechanical compliance function in mm/m (Eq. 67); $q_{tc}(T)$ is the thermochemical compliance function in mm/m (Eq. 68); and $\beta(t_0, T)$ is the reduction factor to take into account the age of loading (Eq. 71).

$$J_{LITS}(T) = (\beta_{tm} \times q_{tm}(T) + \beta_{tc} \times q_{tc}(T)) \times \beta(t_0, T) \quad (66)$$

$$q_{tm}(T) = (-5.26 \cdot 10^{-5} \cdot T - 9.73 \cdot 10^{-7} \cdot T^2 + 3.23 \cdot 10^{-9} \cdot T^3 - 4.42 \cdot 10^{-12} \cdot T^4) \quad (67)$$

$$q_{tc}(T) = -exp(T^{0.31}) \cdot 0.156^5 \quad (68)$$

$$\beta_{tm} = ln\left(1 + \left({}^{c.agg.}/_{binder}\right)^3\right) \quad (69)$$

$$\beta_{tc} = ln\left({}^{binder}/_{100}\right) \quad (70)$$

$$\beta(t_0) = \frac{400}{\left[ln\left(\frac{28}{t_0}\right)\right]^4 + 400} \quad (71)$$

The results in terms of specific values (LITS per unit stress) are shown in Figure 141. LITS model values considered two cases: one including the effect of the age of loading ($\beta(t_0)$) and the other disregarding it. In general, a better prediction was achieved with the introduction of the reduction factor. From the experimental results, one can notice that there is not a strictly linear variation between LITS and the stress level, which in part can be attributed to the highest variation of the load level of the specimens tested at $0.2 \cdot f_{c,28}(T)$. Moreover, LITS values on specimens loaded at $0.2 \cdot f_{c,28}(T)$ were higher than the ones loaded at $0.4 \cdot f_{c,28}(T)$. This difference was also obtained by Andenberg and Thelandersson [47] tests on pre-dried specimens (see Figure 74).

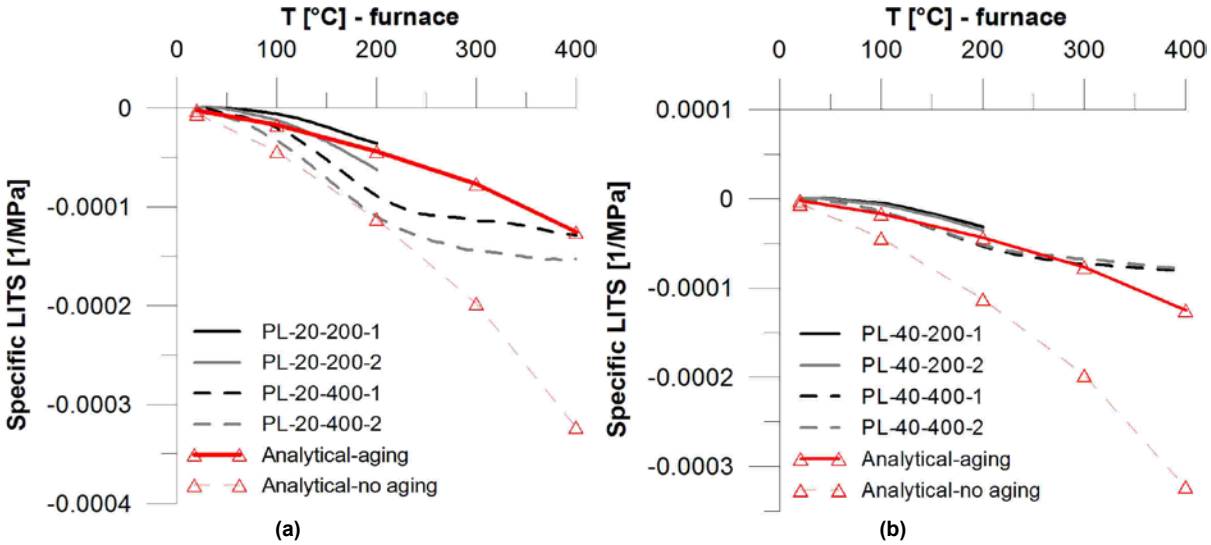

Figure 141 - Comparison of specific LITS values for preloaded specimens considering an equivalent load of: a) $0.2 \cdot f_{c,28}(T)$; b) $0.4 \cdot f_{c,28}(T)$.

8.3 Basic creep (constant temperature)

At high temperature, creep is increased due to the acceleration of moisture diffusion (water evaporation below 100ºC) and CSH bond breakages (concrete dehydration above 150º). As a result, the time of development of primary creep is reduced and creep values are increased. In this case, when the values at room temperature are compared with the ones at high temperature, one can observe a reduction of the time of the primary creep development of about 16 times and an increase of the creep coefficient ($\phi(t, t_0, T)$) by 4 times at 200ºC and by 6 times at 400ºC. These results are in agreement with Gillen [115] tests, which have shown that the primary creep was developed during the first hour and creep strains at 316°C were 5 times to 10 times greater than the ones measured at ambient temperature.

From the experimental results, a correlation among basic creep values at different temperatures was derived using an adapted Kelvin-Voigt model as described in Eq. 72, where: $\phi_{bc}(t, t_0, T) =$ adapted Kelvin-Voigt model to include the effects of high temperature; $A(T) =$ temperature adjusted parameter to take into account the effect of high temperature on creep (Eq. 73).

$$\phi_{bc}(t, t_0, T) = \left[A(T) \cdot \phi_\infty \cdot (1 - e^{-\beta(T)\cdot(t-t_0)}\right] \quad (72)$$

$$A(T) = 0.165 \cdot T^{0.6} \quad (73)$$

Table 26 shows the values of creep parameters for the best fitting with the experimental results for three different temperatures.

Table 26 – Creep parameters adopted in the adapted Kelvin-Voigt model.

	20ºC	**200ºC**	**400ºC**
ϕ_∞	0.16	0.16	0.16
$\beta(T)$	4	64	64

A comparison between experimental and LITS model values is shown in Figure 142, demonstrating a good approximation of the results, except for the specimens PH-20-400-1 and PH-20-200-1.

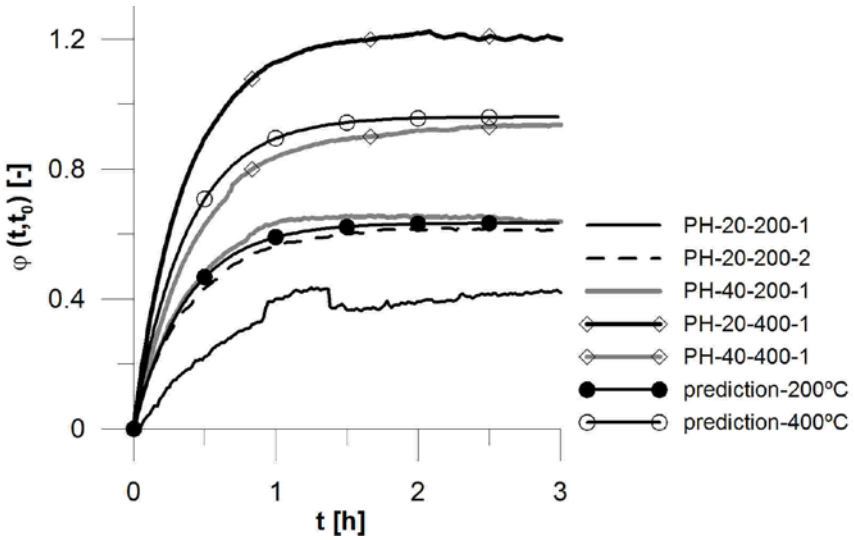

Figure 142 – Comparison between experimental and predicted (adapted Kelvin-Voigt model) creep values at constant temperature.

8.4 Creep at high temperature (LITS and basic creep)

In Chapter 6, LITS values are uncoupled by means of a 2D three-phase mesoscopic analysis and the effect of the boundary conditions on concrete (thermal expansion restraint) was defined according to Eq. 74, where: $LITS_{bc}$ = the effect of the boundary condition on concrete; $q_{bc}(T)$ = boundary condition power function; $\beta(t_0)$ = reduction factor to take into account the age of loading; and σ = stress level.

$$LITS_{bc} = \left[\beta_{tm} \cdot q_{bc}(T)\right] \cdot \beta(t_0) \cdot \sigma \quad (74)$$

$$q_{bc}(T) = 9.5^{-5} \cdot T^{1.46} \quad (75)$$

By introducing the effect of the boundary conditions on concrete, creep at high temperature for preloaded specimens can be predicted using the adapted Kelvin-Voigt approach, as described in Eq. 76. The Modulus of Elasticity was obtained from Table 24 and a linear interpolation was adopted to determine the Elastic Modulus at different temperature levels.

$$\phi(t, t_0, T) = \left[A(T) \cdot \phi_\infty \cdot \left(1 - e^{-\beta(T)\cdot(t-t_0)}\right)\right] + LITS_{bc} \cdot \frac{E_T}{\sigma} \quad (76)$$

A comparison between experimental and predicted (adapted Kelvin-Voigt approach and LITS semi-empirical model) values in terms of creep coefficient versus time is shown in Figure 143. In this case, it was assumed that concrete behavior remains in the viscoelastic regime even at the maximum high temperature analyzed. This assumption is possible since the maximum load applied was lower than $0{,}4 \cdot f_c(T)$ ($0{,}4 \cdot f_{c,28}(T) \approx 0{,}3 \cdot f_c(T)$), which is generally the accepted threshold of concrete viscoelastic regime. After that, there is a progressive plastic behavior as a result of concrete damage.

The results demonstrate that both the proposed LITS semi-empirical model and the adapted Kelvin-Voigt approach can predict with acceptable accuracy creep behavior

during heating and at constant temperature. The “bump” observed in the curves at the peak value can be attributed partially to the variation of the stress level, especially in the specimens loaded at 0.2·$f_{c,28}$(T), and partially to the fact that the residual Elastic Modulus (E_T) is assumed to be the same in all the bulk concrete. Thus, the prediction did not take into account the specimen thermal gradient during heating. As a result, at the end of the heating phase, the variation of the strain level was smaller than the variation of the Elastic Modulus, which could cause a mismatch and a higher deviation of the creep coefficient.

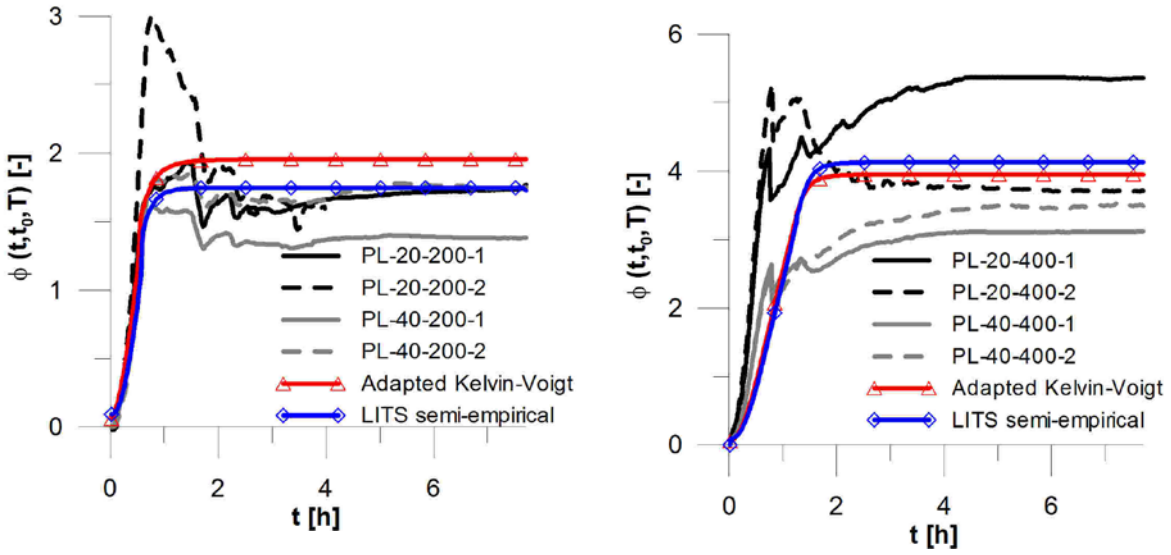

(a) (b)

Figure 143 – Comparison between preloaded experimental and predicted (adapted Kelvin-Voigt and LITS semi-empirical model) values for a maximum temperature of: a) 200°C; b) 400°C.

8.5 The role of the fibers

One important observation from the experimental results is that most of concrete deformation during heating in preloaded specimens was recovered after cooling, indicating that most of the concrete deformation were viscoelastic and not originated from concrete damage (irrecoverable mechanical strain). This phenomenon can be attributed to the positive effect of the smeared steel fibers in the bulk concrete, which were able to keep the matrix cohesion, reducing the deleterious effect of thermal mismatch during heating and cooling. As a result, despite the reduction of the Modulus of Elasticity with the temperature increase, the residual thermomechanical damage was much smaller than the one expected for plain concrete.

The curvature of the experimental LITS compliance (J_{LITS}) curve is modified after 200°C (reduction of LITS growth rate), as one can notice in Figure 141. This effect was not observed on plain concrete (see the comparison between LITS model and experimental results from others in section 4.3.8), where LITS growth rate is always increasing with respect to temperature. This could be an effect introduced by steel fibers which contribute to reduce concrete damage (control of microcracking and crack propagation). In fact, comparing these results with the residual compressive strength of the same material at 1-year-old (see Colombo et al [50] results in Figure 37), one can notice that, between 200°C and 400°C, the strength decay is very low.

CHAPTER 9

Conclusions and future perspectives

9.1 Conclusions

A new semi-empirical model was proposed and compared both with experimental data and empirical models from other authors who worked on plain concrete. Important findings were obtained and the main conclusions are described below.

- The LITS semi-empirical model proposed recognizes concrete as a heterogeneous biphasic material (aggregates + matrix) and describes LITS as the sum of thermomechanical (microcracking, thermal expansion restraint and aggregate degradation) and thermochemical (concrete drying and dehydration) strains.
- The model was compared with experimental results from others, showing its reliability. The great advantage of this model is that it could be adopted for different types of plain concrete (NSC, HSC, UHPC) and SFRC and can be used for design engineers and researches to have a preliminary and straightforward value of the load induced thermal strain (LITS), without the necessity of complicated numerical analyses.
- LITS is directly proportional to the volume of aggregates, which leads to concrete microcracking due to thermal mismatch, thermal expansion restraint imposed by the compressive sustained load and higher deformations as a result of aggregate thermal damage and increasingly ductile behavior.
- As expected, the aggregate type has a direct influence on LITS behavior. While recycled aggregates breaks up at about 400°C, siliceous and calcareous aggregates decompose at 1200°C. In order to account for this effect, two compliance functions were derived to be used in the proposed semi-empirical model.

A 2D three-phase mesoscopic numerical modeling was carried out, LITS strains were uncoupled and the path dependence was analyzed. The model was validated with Khoury [116] experimental results. A parametric study was developed in order to investigate the sensitivity of the model to variations in the concrete mechanical properties and aggregates distribution. The main conclusions are described below.

- A good agreement was obtained between the experimental results and the 2D three-phase mesoscopic modeling both in terms of total strains and LITS.
- A parametric study shows that changing the mechanical properties (strength and elastic modulus) of the aggregates or the matrix by ±25% lead to a much

higher variability in the total strain values (up to 109%) in comparison to LITS (less than 10%). The least sensitive response, both in terms of total strain and LITS, was obtained by changes in the mechanical properties of the ITZ.

- Different aggregate distributions, on one hand, produced a high scattering in the total strain values (CoV ranging from 9% to 95%) and, on the other hand, had a very small impact on LITS behavior (maximum CoV of 15%).
- LITS was uncoupled into three components: the effect of the aggregate geomechanical properties decay with temperature ($LITS_{agg}$), the effect of the matrix thermomechanical properties decay ($LITS_{mat}$) and the restraint effect imposed by the boundary conditions ($LITS_{bc}$). The results have shown that $LITS_{bc}$ plays a very important role in ordinary concrete, superseding dehydration ($LITS_{agg}$) as the leading process of LITS.
- A comparison between numerical and the proposed LITS model, in terms of thermomechanical and thermochemical strains, demonstrated that the model has a good correlation with the numerical results.
- From the numerical analyses, the constitutive equations for both $LITS_{agg}$ and $LITS_{bc}$ were derived. Further analyses should be carried out with different concrete mixtures in order to validate these equations for other concrete types.
- An analysis of the path dependence taking into account preloaded and preheated specimens have shown that, immediately after loading, preheated specimens show a higher potential energy in relation to the preloaded one due to the relatively lower damage in the bulk concrete. Moreover, the difference between LITS values from preloaded and preheated specimens seems to be result of the thermal expansion restraint imposed by the boundary conditions.

In the experimental campaign, a comparison between the mechanical properties of 1- and 10-year-old SFRC was carried out in order to study the long-term aging properties of the material. Some considerations regarding the differences between 3PB and 4PB tests and their implications to the material classification were addressed. A comparison between fixed-end uniaxial tensile tests and DEWS tests was developed. The main conclusions are described below.

- Long-term aging on FRC material result in a significant increase in fiber SLS strength contribution. A comparison between 1-year-old and 10-year-old materials has shown a large increase in the peak and SLS post-peak strength (roughly by 50%), which can be attributed to matrix improvements, while fiber pull-out resistance affecting ULS strength was barely increased ($f_{R3,av}$ was roughly augmented by 15%).
- Due to the localized effects of the mechanical anchorage of the hooked-end steel fiber, which comprises a much smaller concrete surface area in relation to the bulk matrix, the upgrade in the material class can be attributed mainly to the matrix contribution with the increase in the peak and in the SLS post-peak strengths.
- The high heterogeneity of FRC mechanical behavior in the post-cracking regime significantly penalizes the material classification. For example, 3PB first post-peak strength (f_{R1}) resulted in an average value of 8.37MPa, with a characteristic one of 5.59 MPa and a classification as 3a material in order to respect the limitations for structural use.
- The Model Code approach, passing from the classification to the tensile constitutive law, was confirmed by the comparison of the uniaxial tensile

constitutive law (stress-COD curve) with direct and indirect tensile test results and by the comparison of the bending test results with the prediction of the bending moment versus CMOD curve.

Creep tests at high temperature considering both preloaded and pre-heated specimens were performed. Creep at high temperature was predicted both in preloaded (LITS) and preheated (basic creep) specimens by means of an adapted Kelvin-Voigt model. The model takes into account the effect of creep acceleration due to the temperature increase by means of a temperature-adjusted parameter. The proposed LITS semi-empirical model was also validated with the experimental results. The main conclusions are described below.

- A comparison between creep experimental result at room temperature and predicted values using the Kelvin-Voigt approach, Eurocode 2 and Model Code 2010 was carried out. In this case, for a 11.5-year-old specimen, the Kelvin-Voigt model demonstrated a good agreement with the experimental values, while the Model Code 2010 underestimated the results. One important observation is that creep reached a value close to the asymptotic one in less than two days. This effect, which could be prevalent in old specimens with an age of loading higher than 10 years, was not predicted both in the case of the Eurocode 2 [103] and the Model Code 2010 [101].
- At high temperature, creep (measured in pre-heated specimens and loaded after the temperature stabilization) is increased due to the acceleration of moisture diffusion (water evaporation below 100ºC) and CSH bond breakages (concrete dehydration above 150º). As a result, the time of the development of primary creep is reduced and creep values are increased. In this case, when the values at room temperature are compared with the ones at high temperature, it was observed a reduction of the time of the primary creep development of about 16 times and an increase of the creep coefficient by 4 times at 200ºC and by 6 times at 400ºC
- A good approximation between LITS experimental results and the proposed semi-empirical model was obtained. In this case, a better prediction of LITS was achieved when the age of loading was taken into account by means of the introduction of a beta factor proposed by the author. This indicates that concrete long-term aging has an influence on LITS.
- The curvature of the experimental LITS compliance (J_{LITS}) curve is modified after 200°C (reduction of LITS growth rate) and this could be an effect introduced by steel fibers. This effect was not observed in plain concrete, where LITS growth rate is always increasing with respect to temperature.
- Both the proposed LITS semi-empirical model and the adapted Kelvin-Voigt approach were able to predict with good accuracy creep behavior in preloaded specimens. Moreover, the adapted Kelvin-Voigt model has shown a good approximation with the experimental results of pre-heated specimens.
- One important conclusion that comes from the experimental results is that most of concrete deformation during heating in preloaded specimens was recovered after cooling, indicating that most of concrete deformation were reversible and not originated from concrete damage (irrecoverable mechanical strain). This phenomenon can be attributed to the positive effect of the 3D-distribution of

steel fibers in the bulk concrete, which were able to keep the matrix cohesion, reducing the deleterious effect of thermal mismatch during heating and cooling.

9.2 Future work and perspectives

The researches on this area are converging towards a consolidation of the main theoretical aspects, especially regarding the better understanding of the main mechanisms of LITS activation. New experimental tests developed in recent years allow the creation of a database that can subsidize new studies, giving valuable information about LITS behavior on different types of concrete. The major challenge is to develop a transient creep model that can be reliable to be used with any type of concrete.

Future work in this area could focus, for example, on the role of the moisture content to transient creep. An equation to describe drying creep during heating considering different moisture conditions is still to be formulated. Experimental tests taking into account specimens with different w/c ratios can give more information about transient creep evolution during the initial stages of heating (20°C to 150°C).

The role of fibers (steel polypropylene, carbon, etc.) has just started to be investigated. A few researches on transient creep in compression were carried out on concrete reinforced with PP fibers in the recent years, indicating an increase of transient creep due to the higher concrete porosity induced by fibers melting. However, tests with steel fibers (SFRC) and textile (TRC) are still to be done. Experimental tests in tension should also be developed, especially in post-cracked specimens in order to investigate fibers viscous-shear pull-out effect.

DEWS tests should offer a good approach to investigate thermal transient creep in uniaxial tension.

By means of both experimental and numerical mesoscopic analyses, it is possible to uncouple LITS thermomechanical strain into aggregate ($LITS_{agg}$) and thermal expansion restraint ($LITS_{bc}$) effects. Further experimental analyses could be able to uncouple the thermochemical strain into drying creep and dehydration creep.

Bibliography

[1] EN 1992-1: “Eurocode 2: Design of concrete structures. Part 1-2 - General rules - Structural Fire Design”. British Standards, 2004.

[2] Bazant, Z. P.; Hauggaard, A. B.; Baweja, S. and Ulm, F.-J.: “Microprestress-Solidification Theory for Concrete Creep. I: Aging and Drying Effects”. Journal of Engineering Mechanics, November, pp. 1188-1194, 1997.

[3] Sabeur, H and Meftah, F: “Dehydration creep of concrete at high temperatures”. Materials and Structures, vol. n. 3, April 2008, pp. 17-30, 2008.

[4] Benboudjema, F.; Meftah, F. and Torrenti, J. M.: “Interaction between drying shrinkage, creep and cracking phenomena in concrete”. Engineering Structures, n° 27, pp. 239-250, 2005.

[5] Sabeur, H.; Meftah, F.; Colina, H. and Platret, G.: “Correlation between transient creep of concrete and its dehydration”. Magazine of Concrete Research, n° 3, April, 2008, pp. 157-163, 2008.

[6] Colombo, M.: “FRC Bending Behaviour: a Damage Model for High Temperatures”. Starrylink Editrice, 2007 (PhD Thesis).

[7] Kim, Y.-S.; Lee, T.-G. and Kim, G.-Y.: “An experimental study on the residual mechanical properties of fiber reinforced concrete with high temperature and load”. Materials an Structures, vol. 46, pp. 607-620, 2013.

[8] Allen, A. J.; Thomas, J. J. and Jennings, H. M.: “Composition and density of nanoscale calcium-silicate-hydrate in cement”: Nature materials, vol. 6, pp. 311-316, 2007.

[9] Alonso, C. and Fernandez, L.: “Dehydration and rehydration processes of cement paste exposed to high temperature environments”. Journal of Materials Science, nº 39, pp. 3015-3024, 2004.

[10] Arioz, O.: “Effects of elevated temperatures on properties of concrete”. Fire Safety Journal, nº 42, pp. 516-522, 2007.

[11] Khoury, G. A.; Sullivan, P. J. E. and Grainger, B. N.: “Radial temperature distributions within solid concrete cylinders under transient thermal states”. Magazine of Concrete Research, vol. 36, pp. 146-156, 1984.

[12] Thienel, K.-C.; and Rostasy, F. S.: “Transien creep of concrete under biaxial stress and high temperature”. Cement and Concrete Research, vol. 26, nº 9, pp. 1409-1422, 1996.

[13] Giaccio, G. M. and Zerbino, R. L.: “Mechanical behaviour of thermally damaged high-strength steel fibre reinforced concrete”. Materials and Structures, vol. n. 38, April 2005, pp. 335-342, 2005.

[14] Y-Sun, K.; T-Gyu, L. and G-Yong, K.: “An experimental study on the residual mechanical properties of fiber reinforced concrete with high temperature and load”. Materials and Structures, n°46, pp. 607-620, 2013.

[15] 50-FMC Draft Reccomendation: “Determination of the fracture energy of mortar and concrete by means of three-point bend tests on notched beams”. RILEM Publications SARL, vol. 18, nº 106, pp. 287-290, 1985.

[16] Nielsen, C. and Bicanic, N.: “Residual fracture energy of high-performance and normaal concrete subjected to high temperatures”. Materials and Structures, vol. 36, nº October 2003, pp. 515-521, 2003.

[17] Bamonte, P and Gambarova, P. G.: “A study on the mechanical properties of self-compacting concrete at high temperature and after cooling”. Materials and Structures, nº 45, pp. 1375–1387, 2012.

[18] Peng, G.-F.; Yang, W.-W.; Zhao, J.; Liu, Y.-F.; Bian, S.-H. and Zhao, L.-H.: “Explosive spalling and residual mechanical properties of fiber toughened high-performance concrete subjected to high temperatures”. Cement and Concrete Research, vol. 36, pp. 723-77, 2006.

[19] Yu, J.; Yu, K. and Lu, Z.: “Residual fracture properties of concrete subjected to elevated temperatures”. Materials and Structures, nº 45, pp. 1155-1165, 2012.

[20] Reis, M. L. B. C.; Neves, I. C.; Tadeu, A. J. B. and Rodrigues, J. P. C.: “High temperature compressive strength of steel fiber high strength concrete”. Journal of Materials in Civil Engineering, n° 13, pp. 230-234, 2001.

[21] Poon, C.-S.; Azhar, S.; Anson, M. and Wong, Y.-L.: “Strength and durability recovery of fire-damaged concrete after post-fire-curing”. Cement and Concrete Research, n° 31, pp. 1307-1318, 2001.

[22] Mindeguia, J.-C.; Pimienta, P.; Noumowe, A. and Kanema, M.: “Temperature pore pressure and mass variation of concrete subjected to high temperature - Experimental and numerical discussion on spalling risk”. Cement and Concrete Research, n° 40, pp. 477-487, 2010.

[23] Neville, A. M. and Dilger, W.: “Creep of Concrete: Plain, Reinforced, Prestressed”. Amsterdam: North-Holland, 1970.

[24] Bazant, Z. P.: “Theory of Creep and Shrinkage in Concrete Structures: A Précis of Recent Developments”. Mechanics Today, vol. 2, pp. 1-93, 1975.

[25] Phan, L. T.: “Pore pressure and explosive spalling in concrete”. Materials and Structures, n° 41, pp. 1623-1632, 2008.

[26] van der Heijden, G. H. A.; Pel, L. and Adan, O. C.: “Fire spalling of concrete, as studied by NMR”. Cement and Concrete Research, vol. 42, pp. 265-271, 2012.

[27] Zeiml, M.; Leithner, D.; Lackner, R. and Mang, H. A.: “How do polypropylene fibers improve the spalling behavior of in-situ concrete”. Cement and Concrete Research, n°. 36, pp. 929-942, 2006.

[28] Fu, Y. and Li, L.: “Study on mechanism of thermal spalling in concrete exposed to elevated temperatures”. Materials and Structures, n° 44, pp. 361-376, 2011.

[29] Sa, C. and Benboudjema, F.: “Modeling of concrete nonlinear mechanical behavior at high temperatures with different damage-based approaches”. Materials and Structures, n° 44, pp. 1411-1429, 2011.

[30] Lau, A. and Anson, M.: “Effect of high temperatures on high performance SFRC”. Cement and Concrete Research, n° 36, pp. 1698-1707, 2006.

[31] Chan, Y. N.; Luo, X. and Sun, W.: “Compressive strength and pore structure of high-performance concrete after exposure to high temperature up to 800ºC”. Cement and Concrete Research, vol. 30, pp. 247-251, 2000.

[32] Biolzi, L.; Cattaneo, S. and Rosati, G.: “Evaluating residual properties of thermally damaged concrete”. Cement and Concrete Composites, vol. 30, pp. 907-916, 2008.

[33] Kalifa, P.; Chene, G. and Galle, C.: “High-temperature behaviour of HPC with polypropilene fibres”. Cement and Concrete Research, vol. 31, pp. 1487-1499, 2001.

[34] Heo, Y.-S.; Sanjayan, G.; Han, C.-G. and Han, M.-C.: “Limited effect of diameter of fibres on spalling protection of concrete in fire”. Materials and Structures, n° 45, pp. 325-335, 2012.

[35] Bilodeau, A.; Kodur, V. K. R. and Hoff, G. C.: “Optimization of the type and amount of polypropilene fibres for preventing the spalling of lightweight concrete subjected to hydrocarbon fire”. Cement and Concrete Composites, vol. 26, pp. 163-174, 2004.

[36] Bazant, Z. P.; Cusatis, G. and Cedolin, L.: “Temperature Effect on Concrete Creep Modeled by Microprestress-Solidification Theory”. Journal of Engineering Mechanics - ASCE, June, pp. 691-699, 2004.

[37] United States Department of Transportation - Federal Highway Administration: “Portland Cement Concrete Pavements Research”. Available: http://www.fhwa.dot.gov/publications/research/infrastructure/pavements/pccp/thermal.cfm. [Access in 27/11/2013].

[38] Bazant, Z. P. and Kaplan, M. F.: “Concrete at High Temperatures: Material Properties and Mathematical Models”. London: Longman, 1996.

[39] Lie, T. T. and Kodur, V. K. R.: “Thermal and mechanical properties of steel-fibre-reinforced concrete at elevated temperatures”. Canadian Journal of Civil Engineering, vol. 23, pp. 511-517, 1996.

[40] Kodur, V. and Khaliq, W.: “Effect of Temperature on Thermal Properties of Different Types of High Strength Concrete,” Journal of Materials in Civil Engineering, vol. 23, June, pp. 793-801, 2011.

[41] Hager, I.: “Behaviour of cement concrete at high temperature”. Bulletin of the Polish Academy of Sciences, vol. 61, nº 1, pp. 145-154, 2013.

[42] Schneider, U.: “Modelling of concrete behaviour at high temperatures”. Design of Structures Against Fire, Elsevier Applied Science, 1986, pp. 53-69.

[43] Ellobody, E. and Bailey, G.: “Modelling of unbounded post-tensioned concrete slabs under fire conditions”. Fire Safety Journal, vol. 44, pp. 159-167, 2009.

[44] Khan, M. I.: “Factors affecting the thermal properties of concrete and applicability of its prediction models”. Building and Environment, vol. 37, pp. 607-614, 2002.

[45] Youssef, M. A. and Meftah, M.: “General stress-strain relationship for concrete at elevated temperatures”. Engineering Structures, vol. 29, pp. 2618-2634, 2007.

[46] Khenane, A and Baker, G.: “Uniaxial model for concrete under variable temperature and stress”. Journal of Engineering Mechanics, vol. 119, pp. 1507-1525, 1993.

[47] Anderberg, Y. and Thelandersson, J.: “Stress and deformation characteristics of concrete at high temperatures”. Technical report, Lund Institute of Technology, 1976.

[48] Felicetti, R.; Gambarova, P. G.; Sora, M. N. and Khoury, G.: “Mechanical behaviour of HPC and UHPC in direct tension at high temperature and after cooling”. In Proceedings of the 5th Symposium on Fibre-Reinforced Concrete - BEFIB, Lyon, France, 2000.

[49] Hertz, K. D.: “Concrete strength for fire safety design”. Magazine of Concrete Research, vol. 57, pp. 445-453, 2005.

[50] Colombo, M.; di Prisco, M. and Felicetti, R.: “Mechanical properties of steel fibre reinforced concrete exposed at high temperatures.” Materials and Structures, nº 43, pp. 475–491, 2010.

[51] Li, L.-Y. and Purkiss, J.: “Stress-strain constitutive equations of concrete material at elevated temperatures”. Fire Safety Journal, vol. 40, pp. 669-686, 2005.

[52] Bazant, Z. P. and Chern, J.-C.: “Triple Power Law for Concrete Creep”. Journal of Engineering Mechanics, ASCE, nº 111, pp. 63-83, 1985.

[53] Terro, M. “Numerical Modeling of teh Behavior of Concrete Structures in Fire,” ACI Structural Journal, vol. 95, pp. 183-193, 1998.

[54] Scott, B. D.; Park, R. and Priestley, J. N.: “Stress-strain behaviour of concrete confined by overlapping hoops at low and high strain rates”. ACI Journal Proceedings, vol. 79, pp. 13-27, 1982.

[55] Mander, J. B.; Priestley, M. J. N. and Park, R.: “Theoretical Stress-Strain Model for Confined Concrete”, Journal of Structural Engineering, vol. 114, pp. 1804-1825, 1988.

[56] Felicetti, R and Gambarova, P. G.: “Effects of High Temperature on the Residual Compressive Strength of High-Strength Siliceous Concretes”. ACI Materials Journal, vol. 95, nº 4, 1998.

[57] Collins, M. P. and Mitchell, D.: “Prestressed Concrete Basics”. Ottawa: Canadian Prestress Concrete Institute, 1994.

[58] Khoury, G. A.: “Strain of heated concrete during two thermal cycles. Part 1: strain over two cycles, during first heating and at subsequent constant temperature”. Magazine of Concrete Research, nº 6, pp. 367-385, 2006.

[59] RILEM TC 107-CSP: Creep And Shrinkage Prediction Models: Principles Of Their Formation: “Measurement of time-dependent strains of concrete”. Materials and Structures, vol. 31, pp. 507-512, 1998.

[60] ACI 318/318-R08: “ACI Comitee 318: Building code and commentary”. ACI Farmington Hills, MI, 2008.

[61] RILEM TC 129-MHT: Test Methods For Mechanical Properties Of Concrete At High Temperatures: “Recommendations: Part 7: Transient Creep for service and accident conditions”. Materials and Structures, vol. 31, pp. 290-295, 1998.

[62] Willan, K.; Xi; Y.; Lee, K. and Kim, B.: “Thermal response of reinforced concrete structures in nuclear power plants”. University of Colorado at Boulder, Colorado, 2009.

[63] Rossi, P.; Godart, N.; Robert, L.; Gervais, J. P. and Bruhat, D.: “Investigation of the basic creep of concrete by acoustic emission”. Materials and Structures, nº 27, pp. 510-514, 1994.

[64] Ranaivomanana, N.; Multon, S. and Turatsinze, A.: “Basic creep of concrete under compression, tension and bending”. Construction and Building Materials, n° 38, pp. 173-180, 2013.

[65] Atrushi, D. S.: “Tensile and Compressive Creep of Early Age Concrete: Testing and Modelling”. Trondheim, Norwey: The Norwegian University of Science an Technology, 2003.

[66] Acker, P. and Ulm, F.: “Creep and shrinkage of concrete - physical origins and practical measurements”. Nuclear Engineering and Design, vol. 203, pp. 143-158, 2001.

[67] Bazant, Z. P. and Carol, I.: “New test method to separate microcracking from drying creep: curvature creep at equal bending moment and various axial forces”. Proceedings of the Fifth International Rilem Symposium: Creep and shrinkage of concrete, pp. 77-82, 1993.

[68] Thelandersson, S.: “Modeling of Combined Thermal and Mechanical Action in Concrete”: Journal of Engineering Mechanics, pp. 893-906, June 1987.

[69] Mindeguia, J.-C.; Hager, I.; Pimienta, P.; Carré, H. and La Borderie, C.: “Parametrical study of transient thermal strain of ordinary and high performance concrete”. Cement and Concrete Research, nº 48, pp. 40-52, 2013.

[70] Sadaoui, A. and Khennane, B. “Effect of Transient Creep on Behavior of Reinforced Concrete Beams in a Fire”. ACI Materials Journal, Nov-Dec, pp. 607-616, 2012.

[71] Altoubaut, S. and Lange, D.: “The Pickett effect at early age and experiment separating its mechanisms in tension”. Materials and Structures, vol. 35, pp. 211-218, 2002.

[72] Bissonette, B.; Pigeon, M. and Vaysburd, A. M.: “Tensile Creep of Concrete: Study of Its Sensitivity to Basic Parameters”. Materials Journal, vol. 104, nº 4, pp. 360-368, 2007.

[73] Bissonnette, B and Pigeon, M.: “Tensile creep at early ages of ordinary, silica fume and FRC”. Cement and Concrete Research, vol. 25, nº 5, pp. 1075-1085, 1995.

[74] Kovler, K.: “Interdependence of Creep and Shrinkage for Concrete under Tension”. Journal of Materials in Civil Engineering, May, pp. 96-101, 1995.

[75] Kovler, K.: “A New Look at the Problem of Drying Creep of Concrete under Tension”. Journal of Materials in Civil Engineering, nº 11, pp. 84-87, 1999.

[76] Reinhardt, H.-W. and Rinder, T.: “Tensile Creep of High Strength Concrete”. Journal of Advanced Concrete Technology, vol. 4, nº 2, pp. 277-283, 2006.

[77] Naaman, A. E. and Reinhardt, H. W.: “Proposed classification of HPFRC composites based on their tensile response”. Materials and Structures, nº 39, pp. 547–555, 2006.

[78] di Prisco, M.; Colombo, M. and Dozio, D.: “Fibre-reinforced concrete in fib Model Code 2010: principles, models and test validation”. Structural Concrete, vol. 14, pp. 342-361, 2013.

[79] ASTM C1150: Standard Test Method for Flexural Toughness of Fiber Reinforced Concrete (Using Centrally Loaded Round Panel), 2008.

[80] RILEM TC 162-TDF: “Recommendations of RILEM TC 162-TDF: Test and design methods for steel fibre reinforced concrete”. Materials and Structures, vol. 33, nº 225, pp. 3-5, 2000.

[81] UNI11039: “Concrete Renforced with Steel Fibres. Part II: Test Method for the Determination of First Cracking Strength and Ductility Indexes”. 2003.

[82] Denneman, E; Kearsley, E. P. and Visser, A. T.: “Splitting tensile test for fibre reinforced concrete”. Materials and Structures, nº 44, pp. 1441–1449, 2011.

[83] di Prisco, M.; Ferrara, L. and Lamperti, M. G. L.: "Double edge wedge splitting (DEWS): an indirect tension test to identify post-cracking behaviour of fibre reinforced cementitious composites". Materials and Structures, February, pp. 28, 2013.

[84] Laranjeira, F; Grunewald, S.; Walraven, J; Blom, C; Molins, C and Aguado, A.: “Characterization of the orientation profile of steel fiber reinforced concrete”. Materials and Structures, nº 44, pp. 1093–1111, 2011.

[85] Linsbauer, H. N. and Tschegg, E. K.: “Fracture energy determination of concrete with cube-shaped specimens”. Zement und Beton, nº 31, pp. 31-40, 1986.

[86] Bruhwiler, E. and Wittmann, F. H.: “The wedge splitting test, a new method of performing stable fracture mechanics test”. Engineering Fracture Mechanics, vol. 35, nº 1/2/3, pp. 117-125, 1990.

[87] Logfren, I.; Stang, H. and Olesen, J. S.: “The WST method, a fracture mechanics test method for FRC”. Materials and Structures, nº 41, pp. 197-211, 2008.

[88] di Prisco, M.; Felicetti, R.; Iorio, F and Gettu, R: “On the identification of SFRC tensile constitutive behaviour”. Fracture Mechanics of Concrete Structures, pp. 541-548, 2001.

[89] Qian, S. and Li, V. C.: “Simplified Inverse Method for Determining the Tensile Strain Capacity of Strain Hardening Cementitious Composites”. Journal of Advanced Concrete Technology, vol. 5, nº 4, pp. 235-246, 2007.

[90] Ferrara, L and di Prisco, M.: “Three- vs. four-point bending tests: a numerical investigation on plain concrete”. Studies and Research - Graduate School in Concrete Structures - Fratelli Presenti, vol. 22, pp. 73-117, 2001.

[91] Montaignac, R; Massicotte, B; Charron, J-P and Nour, A.: “Design of SFRC structural elements: post-cracking tensile strength measurement”. Materials and Structures, nº 45, pp. 609-622, 2012.

[92] Carmona, S; Aguado, A and Molins, C.: “Characterization of the properties of steel fiber reinforced concrete by means of the generalized Barcelona test”. Construction and Building Materials, nº 48, pp. 592–600, 2013.

[93] Aenor (2004), UNE 83 – 510: “Hormigones con fibras. Determinación del índice de tenacidad y resistencia a primera fisura”. Madrid, España, pp. 6.

[94] Mobasher, B.; Bakhshi, M and Barsby, C.: “Back calculation of residual tensile strength of regular and high performance fiber reinforced concrete from flexural tests”. Construction and Building Materials, nº 70, pp. 243–253, 2014.

[95] Sousa, J. L. A. O. and Ravindra, G.: “Determining the Tensile Stress-Crack Opening Curve of Concrete by Inverse Analysis”. Journal of Engineering Mechanics, nº 132, pp. 141-148, 2006.

[96] Godde, L. and Strack, M: “Conversion factors for the determination of the tensile behaviour of steel fibre reinforced concrete from bending tests”. BEFIB-2008, Chennai, India, 2008.

[97] fib - Internationl Federation for Concrete Structures: “Fib Model Code for ConcreteStructures 2010”. Berlin, Verlag Ernst and Sohn, 2013.

[98] Amin, A; Foster, S. J. and Muttoni, A.: “Derivation of the σ-w relationship for SFRC from prism bending tests”. Structural Concrete, pp. 93-105, 2015.

[99] EN 1990: “Eurocode: Basis of Structural Design”, 2002.

[100] Soetens, T. and Matthys, S.: “Different methods to model the post-cracking behaviour of hooked-end steel fibre reinforced concrete”: Construction and Building Materials, nº 73, p. 458–471, 2014.

[101] fib - Internationl Federation for Concrete Structures: “Fib Model Code for ConcreteStructures 2010”. Berlin, Verlag Ernst and Sohn, 2013.

[102] Askin, B. and Sigin, A.: “Preliminary Assessment of Transient Creep on Fibre-Reinforced Concrete”. Master Dissertation, Politecnico di Milano, 2014.

[103] EN 1992-1: “Eurocode 2: Design of concrete structures. Part 1-1 - General rules and rules for buildings”. British Standards, 2004.

[104] Diederichs, U.: “Modelle zur Beschreibung der Betonverformung bei instantionaren,” em Abschlubkolloquium Bauwerke unter Brandeinwirkung, Braunschweig, Technische Universitat, pp. 25-34.

[105] Terro, M. J.: “Numerical modeling of thermal & structural response of reinforced concrete structures in fire” PhD Thesis, Department of Civil Engineering, Imperial College, 1991.

[106] Khoury, G. A.; Grainger, B. N. and Sullivan, P. J. E.: “Strain of concrete during first heating to 600°C under load”. Magazine Concrete Research, nº 37, pp. 195-215, 1985.

[107] Nielsen, C. V.: “Experimental Investigation of Combined Thermal and Mechanical Behaviour of Danish and Swedish Concrete subject to High Temperatures”. Norsk Forening for Betongrehabilitering, 2008.

[108] Huismann, S; Weise, F.; Meng, B. and Schneider, U.: “Transient strain of high strength concrete at elevated temperatures and the impact of polypropylene fibers”. Materials and Structures, nº 45, pp. 793-801, 2012.

[109] Tao, J.; Liu, X.; Yuan, Y. and Taerwe, L.: “Transient strain of self-compacting concrete loaded in compression heated to 700°C”. Materials and Structures, nº 46, pp. 191-201, 2013.

[110] Mindeguia, J-C., Pimienta, P.; Hager, I.; La Borderie, B. and Carre, H.: “Experimental study of transient thermal strain and creep of an ordinary concrete at high temperatures”. Fourth International Workshop - Structures in Fire, Aveiro, Portugal, 2006.

[111] Wu, B.; et. al.: “Creep Behavior of High-Strength Concrete with Polypropylene Fibers at Elevated Temperatures”. ACI Materials Journal, March-April, pp. 176-184, 2010.

[112] Hager, I.: “Thermal behavior of high performance concretes at high temperature - evolution of mechanical properties”. PhD Thesis, l’Ecole Nationale des Ponts et Chaussées, 2005.

[113] Diederichs, U. and Mertzsch, O.: “Behavior of Ultra High Strength Concrete at High Temperatures”. Ultra High Performance Concrete (UHPC): Proceedings of the Second international Symposium on Ultra High Performance Concrete, Kassel, Kassel university Press, 2008, pp. 347-354.

[114] Cheyrezy, M.; Khoury, G. A. and Behloul, M.: “Mechanical Properties of Four High-Performance Concretes in Compression at High Temperatures”: Revue Française de Génie Civil, nº 5:8, pp. 1159-1180, 2001.

[115] Gillen, M.: “Short-term Creep of Concrete at Elevated Temperatures”. Fire and Materials, vol. 5, nº 4, pp. 142-148, 1981.

[116] Khoury, G.: “Strain of heated concrete during two thermal cycles. Part 3: isolation of strain components and strain model development”. Magazine of Concrete Research, nº 7, pp. 421-435, 2006.

[117] Sabeur, H. and Colina, H.: “Effect of heating–cooling cycles on transient creep strain of high performance, high strength and ordinary concrete under service and accidental conditions”. Materials and Structures, 2014.

[118] Sygała, A.; Bukowska, M. and Janoszek, T.: “High temperature versus geomechanical parameters of selected rocks - the present state of the research”. Journal of Sustainable Mining, vol. 12, nº 4, pp. 45-51, 2013.

[119] Xing, Z.; et al.: “Influence of aggregate’s nature on their instability at elevated temperature”. 2nd International RILEM Workshop on Concrete Spalling due to Fire Exposure, 2011.

[120] Schneider, U and Schneider, M.: “Experimental Study of the Advanced Transient Concrete Model on Reinforced Concrete Columns During Fire Exposure”. The Open Construction and Building Technology Journal, nº 4, pp. 79-87, 2010.

[121] EN 14651: “Test method for metallic fibered concrete - Measuring the flexural tensile strength (limit of proportionality (LOP), residual)”. Eurpean Comettee for Standardization, 2005.

[122] Van Mier, J. G. M.: “Mode I behavior of concrete influence of the rotational stiffness outside the crack zone”. Rilem proceedings 6: Analysis of concrete structures by fracture mechanics, 1991, pp. 16-25.

[123] Chan, Y.-W. and Li, V. C.: “Age effect on the characteristics of fibre/cement interfacial properties”. Journal of Materials Science, nº 32, pp. 5287-5292, 1997.

[124] Bernard, E. S.: “Age-dependent changes in post-crack performance of fibre reinforced shotcrete linings”. Tunneling and Underground Space Technology, nº 49, pp. 241-248, 2015.

[125] Hillerborg, A, Modeer, M. and Petersson, P-E.: “Analysis of crack formation and crack growth by means of fracture mechanics and finite elements”. Cement and Concrete Research, nº 6, pp. 773-782, 1976.

[126] Bazant, Z. P. and Cedolin, L.: “Stability of Structures: Elastic, Inelastic, Fracture and Damage Theories”. New York: Oxford University Press, 2003.

[127] Barros, J. A. O.; Cunha, V. M. C. F.; Ribeiro, A. F. and Antunes, J. A B.: “Post-cracking behaviour of steel fibre reinforced concrete”. Materials and Structures, nº 38, pp. 47-56, 2005.

[128] Kooiman, A. G.; Van der Veen, C. and Walraven, J. C.: “Modelling the post-cracking behaviour of steel fibre reinforced concrete for structural design purposes”. Heron, vol. 45, nº 4, pp. 275-307, 2005.

[129] Hordjik, D. A.: “Local approach to fatigue of concrete”. Delft university of Technology, 1991 (PhD Thesis).

[130] Kim, S.-M.; Al Rub, R. K. A.: “Meso-scale computational modeling of the plastic-damage response of cementitious composites”. Cement and Concrete Research, nº 41, pp. 339-358, 2011.

[131] Wang, X. F.; et. al.: “Monte Carlo simulations of mesoscale fracture modelling of concrete with random aggregates and pores”. Construction and Building Materials, nº 75, pp. 35-45, 2015.

[132] Walraven, J.: “Aggregate interlock: a theoretical and experimental analysis”. Delft University Press, 1980 (PhD Thesis).

[133] De Schutter, G. and Taerwe, L.: “Random particle model for concrete based on Delaunay triangulation”. Materials and Structures, nº 26, pp. 67-73, 1993.

[134] Bazant, Z. P.: “Random particle model for fracture of aggregate or fiber composites”. Journal of Engineering Mechanics, nº 116, pp. 1686-1705, 1990.

[135] Wrigger, P and Moftah, S. O.: “Mesoscale models for concrete: Homogenisation and damage behaviour”. Finite Elements in Analysis and Design, nº 42, p. 623 – 636, 2006.

[136] Wang, Z. M.; Kwan, A. K. H. and Chan, H. C.: “Mesoscopic study of concrete I: generation of random aggregate structure and finite element mesh”. Computers and Structures, nº 70, pp. 533-544, 1999.

[137] Grondin, F. and Matallah, M.: “How to consider the Interfacial Transition Zones in the finite element modelling of concrete?”. Cement and Concrete Research, nº 58, pp. 67-75, 2014.

[138] JianPing, Z. HePing, X. and HongWei, Z.: “Investigation of meso-failure behavior of rock under thermal-mechanical coupled effects based on high temperature SEM”. Science China Press and Springer-Verlag Berlin Heidelberg, vol. 55, nº 10, p. 1855–1862, 2012.

[139] Menou, A., Mounajed, G.; Boussa, H.; Pineaud, A. and Carre, H.: “Residual fracture energy of cement paste, mortar and concrete subject to high temperature”. Theoretical and Applied Fracture Mechanics, nº 45, p. 64–71, 2006.

[140] Noumowé, A.; Siddique, R. and Ranc, G.: “Thermo-mechanical characteristics of concrete at elevated temperatures up to 310°C”. Nuclear Engineering and Design, nº 239, p. 470–476, 2009.

[141] Odelson, J. B., Kerr, E. A.; Wilasa, V-V.: “Young's modulus of cement paste at elevated temperatures”. Cement and Concrete Research, nº 37, p. 258–263, 2007.

[142] Fu, Y.-F.: “Thermal stresses and associated damage in concrete at elevated temperatures”. PhD Thesis, Hong Kong Polytrechnic University, 2003.

[143] Pérez, A.; Rodriguez, M.; Lopez, C. M. and Carol, I.: “3D-mesomechanical analysis of cracking and spalling of concrete subjected to high temperatures”. XII International Conference on Computational Plasticity. Fundamentals and Applications, Barcelona, 2013.

[144] Remmers, J. C.; et. al.: “The cohesive segment method for the simulation of dynamic fracture”. IUTAM Symposium on discretization for evolving discontinuities, Lyon, 2006.

[145] Takarli, M. and Prince-Agbodjan, W.: “Temperature Effects on Physical Properties and Mechanical Behavior of Granite: Experimental Investigation of Material Damage”. Journal of ASTM International, vol. 5, nº 3, 2008.

[146] Sygała, A.; Bukowska, M. and Janoszek, T.: “High temperature versus geomechanical parameters of selected rocks - the present state of research”. Journal of Sustainable Mining, vol. 12, nº 4, pp. 45–51, 2013.